NANOHYBRIDS OF $BiVO_4$ WITH TWO DIMENSIONAL TITANATE AND HEXANIOBATE NANOSHEETS FOR THE PHOTOCATALYTIC DYE DEGRADATION

THESIS SUBMITTED TO

D. Y. PATIL EDUCATION SOCIETY

(DEEMED TO BE UNIVERSITY), KOLHAPUR

FOR THE DEGREE OF

DOCTOR OF PHILOSOPHY

IN

PHYSICS

UNDER THE FACULTY OF

INTERDISCIPLINARY STUDIES

SUBMITTED BY

Ms. SHIRIN PRASAD KULKARNI

M.Sc. (Physics)

UNDER THE GUIDANCE OF

Dr. JAYAVANT L. GUNJAKAR

M.Sc., Ph.D. (Physics)

ASSOCIATE PROFESSOR

CENTRE FOR INTERDISCIPLINARY RESEARCH,

D. Y. PATIL EDUCATION SOCIETY

(DEEMED TO BE UNIVERSITY), KOLHAPUR- 416 006, MS, (INDIA)

2024

DECLARATION

I hereby declare that the thesis entitled **"Nanohybrids of $BiVO_4$ with two dimensional titanate and hexaniobate nanosheets for the photocatalytic dye degradation"** submitted for the degree of **Doctor of Philosophy in Physics (Ph.D.)** in the **Centre for Interdisciplinary Research** faculty of the **D. Y. Patil Education Society (Deemed to be University), Kolhapur** is completed and written by me, has not before made the basis for the award of any degree/diploma/other related headings of this or any other university in India/any other country/examining body to the best of my knowledge. Further, I assert that I have not dishonored any of the requirements under the copyright and piracy/cyber/IPR act amended by UGC from time to time.

Place: Kolhapur **Ms. Shirin Prasad Kulkarni**

Date: **(Research Student)**

D. Y. Patil Education Society (Deemed to be University), Kolhapur

Centre for Interdisciplinary Research

Certificate

This is to certify that the thesis entitled ***"Nanohybrids of $BiVO_4$ with two dimensional titanate and hexaniobate nanosheets for the photocatalytic dye degradation"*** which is being submitted herewith for the award of the Degree of ***Doctor of Philosophy (Ph.D.)*** in ***Physics*** at ***D. Y. Patil Education Society (Deemed to be University), Kolhapur***, is the result of the original research work completed by ***Ms. Shirin Prasad Kulkarni*** under my supervision and guidance. To the best of my knowledge and belief the work embodied in this thesis has not formed earlier the basis for the award of any Degree or similar title of this or any other University or examining body.

Place: **Kolhapur** Research Guide

Date: / /**20**

Dr. Jayavant L. Gunjakar
(Associate Professor)

Forwarded through,
Prof. C. D. Lokhande
Dean and Research Director,
Centre for Interdisciplinary Research

ACKNOWLEDGEMENT

Apart from the efforts of myself, the success of this work depends largely on the encouragement and support of many others. I take this opportunity to express my gratitude to the people who have been instrumental in successfully completing this project. First and foremost, I would like to thank the almighty for his guidance and spiritual comfort in making this quest for knowledge possible.

At the completion of my Ph.D. thesis, I would like to express my sincere gratitude towards my guide, **Dr. J. L. Gunjakar** [Associate professor, Centre for Interdisciplinary Research (CIR), D. Y. Patil Education Society (Deemed to be University), Kolhapur] for the continuous support during my Ph.D. study and related research, for his motivation and immense knowledge. I thank him not only for the guidance he rendered in the field of research but also for enlightening the path of my life with a deep love for science. With his support, I could overcome my personal and scientific problems in writing scientific papers, including this Ph.D. thesis. This work could not have been completed without his inspiring guidance and constant encouragement during my research tenure.

I sincerely acknowledge the wholehearted help, valuable discussions, guidelines and suggestions provided by **Prof. C. D. Lokhande**, Dean and Research Director, Centre for Interdisciplinary Research (CIR). He provided a fruitful discussion and helpful guidance for time management regarding my Ph.D. progress.

I would like to express my sincere thanks to Vice-Chancellor **Prof. R. K. Mudgal** and Registrar **Dr. V. V. Bhosale** for the inspiration and support. I thank **Dr. Umakant Patil, Dr. Sharad Patil** and **Dr. Vishwajeet Khot,** who helped me to analyze the results with their empathy and cooperative mind. I also thank **Dr. Amol Pawar, Dr. Dhanaji Malvekar, Dr. H. M. Pathan** and **Dr. S. D. Sartale** for providing me very important sample characterization data during the entire research work.

I would like to express sincere thanks to my seniors **Dr. Shrikant Sadavar, Dr. Navnath Padalkar**, **Dr. Rohini Shinde**, **Dr. Sachin Pujari, Dr. Satish Jadhav, Dr. Suraj Khalate** and **Dr. Shivaji Ubale** for insightful guidelines, scientific discussions and valuable suggestions on the present work.

I owe a word of thanks to all my friends and research colleagues from the CIR department, viz. **Vikas Magdum, Yogesh Chitare, Prashant Sawant, Shweta Talekar, Shraddha Pawar, Mayura Medhekar, Sayali Kulkarni, Dr. Prity Bagwade, Vinod Patil, Shraddha Bhosale, Sambhaji Kumbhar, Ranjit Nikam, Ketaki kadam, Satish Falake, Manohar Lad** and **Sambhaji Khot**. Thanks for providing a great work environment and for the help and discussions. I am also thankful to the non-teaching staff of the CIR Department for their kind co-operation during my research work.

My heartfelt gratitude goes out to my Father **(Pappa)**, Mother **(Aai)**, Sisters **Shraddha** and **Srushti**, as well as all of my family members for their constant support, encouragement, love and affection towards me to cruise through the difficulties to bring me at this position.

Some people contributed indirectly to this work. For those people, I might have forgotten you, but you can have sure that this won't be forever. Your contribution is important to my research career.

Thank you!

~Shirin

Place: Kolhapur

Date:

SUMMARY OF RESEARCH WORK

A) Granted/Published (Indian) Patents:

1) Title of Invention: Infrared (IR) cut-off water filter assembly
(Application no: 407337-001; Date: 12/02/2024)
Inventors: Jayavant L. Gunjakar, Yogesh M. Chitare, Vikas V. Magdum, ***Shirin P. Kulkarni***, Akash S. Patil, Abhaya S. Patil
Status: Design Granted
2) Title of Invention: A method for depositing uniform coating of 2D titanate nanosheets
(Application no: 202421035776; Date: 06/05/2024)
Inventors: Jayavant L. Gunjakar, Vikas V. Magdum, Yogesh M. Chitare, ***Shirin P. Kulkarni***, Chandrakant D. Lokhande
Status: Published

B) Papers Published/Submitted at International Journals:

1) ***Shirin P. Kulkarni***, Yogesh M. Chitare, Vikas V. Magdum, Prashant D. Sawant, Shweta V. Talekar, Shraddha A. Pawar, Umakant M. Patil, Kishor V. Gurav, Dhanaji B. Malavekar, Amol U. Pawar, Jayavant L. Gunjakar, "Chemically synthesized facet-controlled visible light active $BiVO_4$ thin films for photoelectrochemical water splitting", *Appl. Phys. A, 2023, 129, 876*, https://doi.org/10.1007/s00339-023-07164-1 **(I. F. – 2.6)**.
2) ***Shirin P. Kulkarni,*** Vikas V. Magdum, Yogesh M. Chitare, Prashant D. Sawant, Shweta V. Talekar, Shraddha A. Pawar, Amol U. Pawar, Dhanaji B. Malavekar, Shrikrishna D. Sartale, Ayman A. Ghfar, Jayavant L. Gunjakar, "Modified successive ionic layer adsorption and reaction for interconnected bismuth vanadate nanograins: Highly active visible light harvesting photoanodes", *J. Photochem. Photobiol. A: Chem., 2024, 454, 115737*, https://doi.org/10.1016/j.jphotochem.2024.115737 **(I. F. – 4.1)**.
3) ***Shirin P. Kulkarni,*** Yogesh M. Chitare, Vikas V. Magdum, Prashant D. Sawant, Shweta V. Talekar, Shraddha A. Pawar, Dhanaji B. Malavekar, Sabah Ansar, Jin H. Kim, Jayavant L. Gunjakar, "Nanohybrids of layered titanate and bismuth vanadate as visible light driven photocatalysts for the degradation of dyes and antibiotic", *ACS Appl. Nano Mater., 2024,* 7, 11411-11422, https://doi.org/10.1021/acsanm.4c01039 **(I. F. – 5.3)**.
4) Pramod A. Koyale, ***Shirin P. Kulkarni***, Jayavant L. Gunjakar, Tukaram D. Dongale, Santosh S. Sutar, Saurabh S. Soni, Yash G. Kapdi, Swapnajit V. Mulik, Sagar D. Delekar "ZnO nanorod/multiwalled carbon nanotube composites sensitized with Cu-based metal organic frameworks as photoanodes for solar-driven water splitting", *ACS Appl. Nano Mater., 2024, 7, 2662-2674*, https://doi.org/10.1021/acsanm.3c04694 **(I. F. – 5.3)**.
5) Yogesh M. Chitare, Vikas V. Magdum, ***Shirin P. Kulkarni***, Shweta V. Talekar, Shraddha A. Pawar, Prashant D. Sawant, Dhanaji B. Malavekar, Umakant M. Patil, Jin H. Kim, Sabah Ansar, Jayavant L. Gunjakar, "Vertically aligned interlocked tungsten oxide nanosheet thin film for photocatalytic application: Effect of deposition cycles", *J. Mater. Sci.: Mater. Electron., 2024, 35, 1436*, https://doi.org/10.1007/s10854-024-13184-1 **(I. F. – 2.7)**.

6) Vikas V. Magdum, Yogesh M. Chitare, ***Shirin P. Kulkarni***, Dhanaji B. Malavekar, Amol U. Pawar, Ravindra N. Bulakhe, Chandrakant D. Lokhande, Umakant M. Patil, Sharad B. Patil, Jayavant Gunjakar, "Tailoring the physicochemical properties of chemically deposited MoS_2 thin films for photocatalytic dye and TC degradation: Effect of different cationic precursors", *J. Mater. Sci.: Mater. Electron., 2024, 35, 1433*, https://doi.org/10.1007/s10854-024-13186-z **(I. F. – 2.7)**.

7) Yogesh M. Chitare, Vikas V. Magdum, ***Shirin P. Kulkarni***, Shweta V. Talekar, Shraddha A. Pawar, Prashant D. Sawant, Dhanaji B. Malavekar, Umakant M. Patil, Chandrakant D. Lokhande, Jayavant L. Gunjakar, "Preferentially oriented m-tuned WO_3 thin-films photocatalysts for the multitargeted degradation of organic molecules", *Appl. Surf. Sci. Adv., 2024, 19, 100573,* https://doi.org/10.1016/j.apsadv.2024.100573 **(I. F. – 7.5)**.

8) Vikas V. Magdum, Yogesh M. Chitare, ***Shirin P. Kulkarni***, Prashant D. Sawant, Shraddha A. Pawar, Shweta V. Talekar, Chandrakant D. Lokhande, Umakant M. Patil, Sharad B. Patil, Jayavant L. Gunjakar, "Versatility of group VI layered metal chalcogenide thin films synthesized by solution-based deposition methods", *J. Mater. Chem. C, 2023, 11, 9768-9786,* https://doi.org/10.1039/D3TC01470C **(I. F. – 5.7)**.

9) Navnath S. Padalkar, Chae H. Cho, Vikas V. Magdum, Yogesh M. Chitare, ***Shirin P. Kulkarni***, Umakant M. Patil, Jong P. Park, Jayavant L. Gunjakar, "Self-assembled architecture of 2D layered double hydroxide pillared with 0D polyoxomolybdate anions: High performance redox-type cathode for solid-state asymmetric supercapacitor", *J. Energy Storage, 2023, 74, 109538,* https://doi.org/10.1016/j.est.2023.109538 **(I. F. – 8.9)**.

10) Navnath S. Padalkar, Shrikant V. Sadavar, Rohini B. Shinde, Akash S. Patil, Umakant M. Patil, Vikas V. Magdum, Yogesh M. Chitare, ***Shirin P. Kulkarni***, Ravindra N. Bulakhe, Vinayak G. Parale, Jayavant L. Gunjakar, "2D-2D nanohybrids of Ni-Cr-layered double hydroxide wrapped with graphene oxide nanosheets: Electrode for hybrid asymmetric supercapacitors", *Electrochim. Acta, 2022, 424, 140615*, https://doi.org/10.1016/j.electacta.2022.140615 **(I. F. – 5.5)**.

11) Rohini B. Shinde, Navnath S. Padalkar, Shrikant V. Sadavar, Akash S. Patil, Shital B. Kale, Vikas V. Magdum, Yogesh M. Chitare, ***Shirin P. Kulkarni***, Umakant M. Patil, Vinayak G. Parale, Jayavant L. Gunjakar, Lattice engineering route for self-assembled nanohybrids of 2D layered double hydroxide with 0D isopolyoxovanadate: Chemiresistive SO_2 sensor, *Mater. Today Chem., 2022, 24, 100801*, https://doi.org/10.1016/j.mtchem.2022.100801 **(I. F. – 6.7)**.

12) Rohini B. Shinde, Navnath S. Padalkar, Shrikant V. Sadavar, Shital B. Kale, Vikas V. Magdum, Yogesh M. Chitare, ***Shirin P. Kulkarni***, Umakant M. Patil, Vinayak G. Parale, Hyung-Ho Park, Jayavant L. Gunjakar, 2D-2D Lattice engineering route for intimately coupled nanohybrids of layered double hydroxide and potassium hexaniobate: Chemiresistive SO_2 sensor, *J. Hazard. Mater., 2022 432, 128734,* https://doi.org/10.1016/j.jhazmat.2022.128734 **(I. F. – 12.2)**.

13) Shrikant V. Sadavar, Navnath S. Padalkar, Rohini B. Shinde, Akash S. Patil, Umakant M. Patil, Vikas V. Magdum, Yogesh M. Chitare, ***Shirin P. Kulkarni***, Ravindra N. Bulakhe, Vinayak G. Parale, and Jayavant L. Gunjakar, Graphene oxide an efficient hybridization matrix for exploring electrochemical activity of 2D cobalt-chromium-layered double hydroxide based nanohybrids, *ACS Appl. Energy Mater., 2022, 5, 2083-2092***,** https://doi.org/10.1021/acsaem.1c03619 **(I. F. – 5.4)**.

14) Shrikant V. Sadavar, Navnath S. Padalkar, Rohini B. Shinde, Akash S. Patil, Umakant M. Patil, Vikas V. Magdum, Yogesh M. Chitare, ***Shirin P. Kulkarni***,

Ravindra N. Bulakhe, Saji T. Kochuveedu, Jayavant L. Gunjakar, Lattice engineering exfoliation-restacking route for 2D layered double hydroxide hybridized with 0D polyoxotungstate anions: Cathode for hybrid asymmetric supercapacitors, *Energy Storage Mater., 2022, 48, 101-113*, https://doi.org/10.1016/j.ensm.2022.03.005 **(I. F. – 18.9)**.

15) ***Shirin P. Kulkarni***, Vikas V. Magdum, Yogesh M. Chitare, Dhanaji B. Malavekar, Jin H. Kim, Sultan Alshehri, Jayavant L. Gunjakar, Shashikant P. Patole, "2D porous hexaniobate-bismuth vanadate hybrid photocatalyst for photodegradation of aquatic refractory pollutants", *Heliyon* (Under review) **(I. F. – 3.4)**.

16) Vikas V. Magdum, Yogesh M. Chitare, ***Shirin P. Kulkarni***, Sultan Alshehri, Sharad B. Patil, Jayavant L. Gunjakar, "Efficient photocatalytic decomposition of tetracycline hydrochloride by chemically grown MoS_2 nanospheres", *Emergent Mater.* (Under review) **(I. F. – 4.8)**.

17) Vikas V. Magdum, Yogesh M. Chitare, ***Shirin P. Kulkarni***, Dhanaji B. Malavekar, Jin H. Kim, Jayavant L. Gunjakar, "MoS_2 nanospheres anchored 2D exfoliated titanate nanosheet hybrid photocatalyst thin films for efficient photocatalytic degradation of organic pollutants", *Mater. Sci. Eng. B* (Submitted) **(I. F. – 3.9)**.

18) Vikas V. Magdum, Yogesh M. Chitare, ***Shirin P. Kulkarni***, Shraddha A. Pawar, Shweta V. Talekar, Prashant D. Sawant, Dhanaji B. Malavekar, Jin H. Kim, Hemraj M. Yadav, Jayavant L. Gunjakar, "MoS_2 decorated titanate nanosheets hybrid photocatalyst thin films for enhanced photodegradation of organic contaminants", *J. Ind. Eng. Chem.* (Submitted) **(I. F. – 5.9)**.

19) Yogesh M. Chitare, Vikas V. Magdum, ***Shirin P. Kulkarni***, Ravindra N. Bulakhe, Dhanaji B. Malavekar, Umakant M. Patil, Jin H. Kim, Sultan Alshehri, Jayavant L. Gunjakar, "Lattice engineered two-dimensional titanate and tungsten oxide hybrid heterostructure thin films for visible light driven photooxidation of organic compounds", *J. Mater. Chem. C* (Submitted) **(I. F. – 5.7)**.

20) Yogesh M. Chitare, Vikas V. Magdum, ***Shirin P. Kulkarni***, Sohel B. Shaikh, Dhanaji B. Malavekar, Jin H. Kim, Deu S. Bhange, Sultan Alshehri, Jayavant L. Gunjakar, "Heterolayered photocatalyst thin films of stratified 2D-titanate and tungsten oxide for degradation of organic contaminants", *Appl. Mater. Today* (Submitted) **(I. F. – 7.2)**.

21) Shraddha A. Pawar, Shweta V. Talekar, Prashant D. Sawant, Vikas V. Magdum, ***Shirin P. Kulkarni***, Yogesh M. Chitare, Chandrakant D. Lokhande, Jayavant L. Gunjakar, Hemraj M. Yadav, "Water exfoliated ultrathin 2D cobalt-iron-layered double hydroxide nanosheets for electrocatalytic oxygen evolution reaction", *Colloids Surf. A: Physicochem. Eng. Asp.* (Submitted) **(I. F. – 4.9)**.

C) Book Chapters Published/Submitted:

1) ***S. P. Kulkarni***, A. S. Patil, V. V. Patil, U. M. Patil, J. L. Gunjakar, "Nanosheet-derived porous materials and coatings for energy storage applications" in 'Chemically Deposited Nanocrystalline Metal Oxide Thin Films', Springer Nature (2021), 431-467.

2) Y. M. Chitare, V. V. Magdum, S. B. Jadhav, ***S. P. Kulkarni***, C. D. Lokhande, J. L. Gunjakar, "Rare earth element-based nonenzymatic glucose sensor" in 'Chemically Deposited Metal Chalcogenide-based Carbon Composites for Versatile Applications' Springer Nature (2023), 393-410.

3) S. V. Talekar, ***S. P. Kulkarni***, S. B. Wategaonkar, J. L. Gunjakar, "Engineering of POM-based materials for photo-/electro-catalysis" in 'Polyoxometalate-based Materials and Applications' Elsevier (2024) (Revision submitted).

D) Papers/Poster Presented at National/International Conferences:

1) Attended the Asian e-Conference on 'Engineered Science' 2020 held online on 5th to 6th December 2020.
2) ***S. P. Kulkarni***, Y. M. Chitare, V. V. Magdum, J. L. Gunjakar, Oral presentation "Effect of precursor variation on visible light induced photoelectrochemical characteristics of SILAR deposited bismuth vanadate photoanodes", at 2nd Asian e-Conference on Engineered Science, 5th to 6th December, 2021.
3) ***S. P. Kulkarni***, Y. M. Chitare, V. V. Magdum, J. L. Gunjakar, Poster presentation "Photo-functional characteristics of visible light active bismuth vanadate thin films deposited by facile chemical route", at International Conference on Advanced Materials Synthesis, Characterization and Applications (AMSCA-2022) held on 18th to 20th October, 2022 organized by Department of Physics, Savitribai Phule Pune University, Pune, India.
4) ***S. P. Kulkarni***, V. V. Magdum, Y. M. Chitare, J. L. Gunjakar, Oral presentation "Multifunctionality of bismuth vanadate thin films deposited by modified chemical solution deposition for solar assisted water splitting and multitargeted degradation", at International Conference on Nanotechnology Addressing the Convergence of Materials Science, Biotechnology, and Medical Science (IC-NACMBM 2024) held on 12th to 14th February, 2024 organized by Centre For Interdisciplinary Research, D. Y. Patil Education Society (Deemed to be University), Kolhapur, India.

LIST OF ABBREVIATIONS

Name	Abbreviation
Bismuth vanadate	$BiVO_4$
Chemical bath deposition	CBD
Conduction band	CB
Crystal violet	CV
Cyclic voltammetry	CV
Double distilled water	DDW
Electrophoretic deposition	EPD
Energy dispersive spectroscopy	EDS
Field emission scanning electron microscopy	FESEM
Fourier transform infrared spectroscopy	FTIR
Inorganic nanosheets	INs
Indium doped tin oxide	ITO
Layered double hydroxide	LDH
Metal oxide nanosheets	MONs
Methylene blue	MB
Methyl orange	MO
Nanosheets of hexaniobate	NS-hexaniobate
Nanohybrids of $BiVO_4$ with nanosheets of hexaniobate	NS-hexaniobate-$BiVO_4$
Nanosheets of titanate	NS-titanate
Nanohybrids of $BiVO_4$ with nanosheets of titanate	NS-titanate-$BiVO_4$
Photoelectrochemical	PEC
Rhodamine-B	Rh-B
Successive ionic layer adsorption and reaction	SILAR
Three-dimensional	3D
Two-dimensional	2D
Ultraviolet-visible diffuse reflectance spectroscopy	UV-vis DRS
Valence band	VB
X-ray photoelectron spectroscopy	XPS
X-ray diffraction	XRD

CONTENTS

CHAPTER-1

General Introduction and Literature Survey

CHAPTER-1

General Introduction and Literature Survey

1.1 General Introduction:

The most urgent issue facing humanity in the 21st century is increasing global environmental pollution. During the last few decades, the development of various industries and technologies has given rise to water pollution because of the heavy discharge of industrial pollutants into the water resources. Thus, natural water resources such as lakes, rivers and seas have drastically enhanced water pollution, which is now the second most crucial issue next to air pollution. Textile dyes, paint, paper manufacturing, cosmetics, food and oil production are significant resources for water contamination [1]. The hazardous effects of pollution not only affect the environment but also human health and animals as well. Hence, there is a strong need to develop environmentally friendly and harmless technologies to overcome the global issue of water pollution.

Compared with other industries, the textile industry uses plenty of water for different purposes such as cooling, processing, cleaning and rinsing [2]. Traditionally, the coloring of fabrics was achieved with natural dyes obtained from vegetables, flowers and fruits [3]. However, chemical dyes are nowadays preferred due to their low cost and fast processing [4]. From the survey, it is seen that textile industries alone use around 3600 types of chemical dyes. Also, about ten thousand commercially available dyes are produced yearly, and more than 15% of dye effluents are disposed directly in water resources. Most industries are located near natural water resources. Thus, natural water resources are highly polluted by these industries. According to the view of the World Bank, nearly 20% of the total industrial water contamination is caused by the textile industries alone [5].

1.1.1 Dyes:

Dye is a chemical compound applied to the fabric or any other colored object. All aromatic compounds generally absorb electromagnetic radiation, but few can absorb visible light and exhibit specific colors. Every dye has the delocalized electron system named chromophore group (-NO_2, -N=N-, -C=O, -C=N- and C=C-) responsible for the dye color [6]. The color of the chromophore is intensified by its electron donor or acceptor substituents. The total energy of the electron system is influenced by these auxo-chromes (-NH_3, -COOH, -SO_3H and -OH groups). The interaction of polar auxo-chromes with an oppositely charged group of specific compounds binds the dye molecules with that compound [7].

1.1.2 Classification of Dyes:

Dyes are categorized into different types based on the chromophore present in the molecules. Every dye has unique features like structure, chemical composition, nature of the nuclear structure, and bonding properties. Generally, dyes are classified into two main types: natural and synthetic [8]. Natural dyes are extracted from plants and animals like roots, berries, bark, leaves, wood, fungi, lichens and sea snails. Also, they are often negatively charged, which means the colored part of the dye molecule is in the anionic state. However, the synthetic dyes are developed from the organic or inorganic chemical compounds. Further, synthetic dyes are classified into two main types, namely (a) non-azo dyes and (b) azo dyes. Acid dyes, basic dyes, reactive dyes, dispersive dyes, sulfur dyes and vat dyes are the types of azo dyes [9]. The schematic representing the different types of dyes is shown in **Fig. 1.1**.

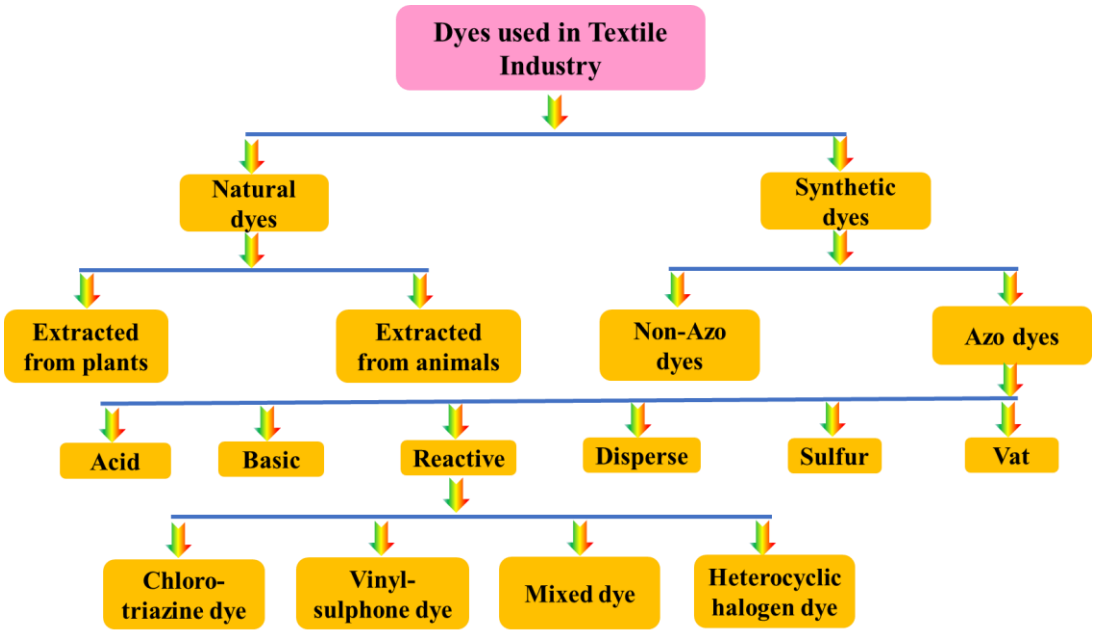

Fig. 1.1: Classification of dyes.

1.1.3 Methylene Blue (MB):

MB is a synthetic dye with the chemical formula $C_{16}H_{18}ClN_3S$ appearing in the shades of blue. MB is an organic chloride salt used as a dye and medication. The absorption spectra of MB lie within the visible range of the solar spectrum with an absorption wavelength of 664 nm, as represented in **Fig. 1.2** [10]. It is soluble in glacial acetic acid, water, ethanol, chloroform and glycerol. It is a neuroprotective agent, tracer, acid-base indicator, histology dye, fluorochrome, etc. It is a thiazine dye that has cardioprotective and antioxidant effects. It is also used as an antimalarial and antidepressant.

Although MB is used in medication, it has certain side effects, such as vomiting, high blood pressure, headache, serotonin syndrome, shortness of breath, red blood cell breakdown, confusion, etc.

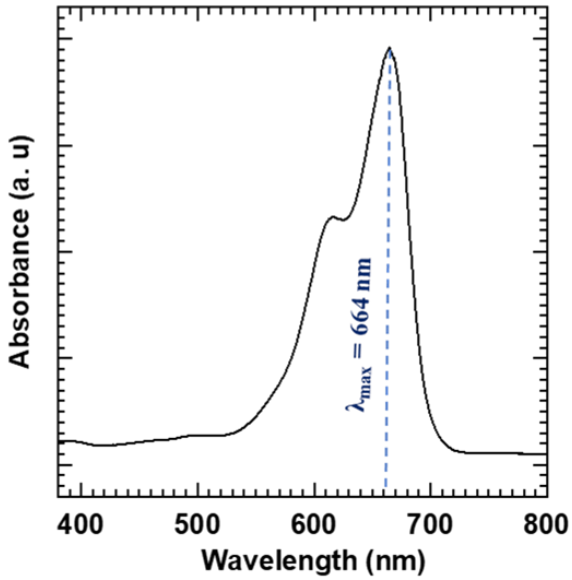

Fig. 1.2: MB dye absorbance spectrum.

1.1.4 Rhodamine B (Rh-B):

Rh-B is a highly stable organic synthetic dye with the chemical formula $C_{28}H_{31}ClN_2O_3$, appearing in shades of red and violet. It is water soluble and frequently used as a tracer dye in the water to detect the flow, transport rate and direction. Rh-B acts as the active medium in continuous and pulsed wave dye LASER. The absorption spectra of Rh-B lie within the visible range of the solar spectrum with an absorption wavelength of 552 nm, as represented in **Fig. 1.3** [11]. Rh-B is soluble in water and acidic solution with solubility of ~50 g L^{-1} and ~400 g L^{-1}, respectively. As temperature increases, the fluorescence intensity of Rh-B will decrease. Rh-B is widely used in leather, paint, paper, printing industries, dyeing in textiles, etc.

Rh-B is one of the highly toxic dyes. Its toxicity comprises chronic effects (carcinogen), mutagenic effects (genotoxicity), teratogenic effects (fetotoxicity), aquatic toxicity, respiratory tract irritation, skin irritation, eye impairment, acute effects on target organs (liver spleen), digestive system discomfort, poor reproductive, and lethal effects in animals. It is harmful when swallowed, inhaled, or ingested.

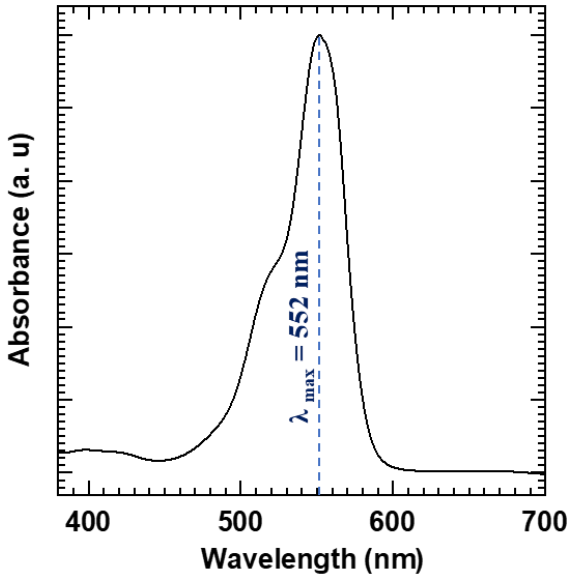

Fig. 1.3: Rh-B dye absorbance spectrum.

1.2 Methods of Dye Removal:

Frequently, the textile industries store dye effluents as industrial waste, and without proper treatment, these products are directly released into water resources. These consequences of water pollution are harmful to the environment and living organisms [12-15]. The dye waste present in the water can block the photosynthesis process occurring under the water. Also, the development of a visible dye layer on the surface of water blocks the penetration of sunlight, which is essential for aquatic living organisms [16]. Furthermore, dye waste harms soil productivity if it comes in contact with forests or agricultural fields. In rural areas, rivers are the primary resources for agricultural production; hence, the contaminated water has hazardous effects on agricultural fields. When dye-polluted water comes into contact with the human body, hazards like skin irritation, burning of the eyes, or even permanent eye injuries may be caused. Also, difficulty in breathing occurs due to reduced inhalation caused by chemically treated dye wastewater. Occasionally, consumption of dyes can cause sweating, confusion, mouthburn, nausea, and vomiting [17-19]. Hence, extracting dye effluents from the wastewater is crucial to protecting the ecosystem from dye contamination.

During the past few decades, people have not been concerned about selecting dyes based on their composition and environmental hazards. During that time, there were no discharge limits for industrial dye waste. However, in 1980, people started to think about the dangerous effects of dye waste discharge in water sources on human health and began to pay attention to removing dye contamination. In the first stage, dye

wastewater was treated with various physical methods such as sedimentation and total dissolved solids (TDS). Afterwards, for the removal of dyeing wastewater, filters and aerobic biodegradation processes were employed [20].

Usually, the wastewater treatment includes pre-treatment, in which industrial wastewater is pre-treated before discharge using a neutralization process. Following this, primary treatment is used to treat wastewater, where suspended solids are eliminated using chemical or physical separation techniques. The secondary treatment comprises the biological process in which bacteria stabilize the waste compounds. The third process in wastewater treatment is physical-chemical treatment, including ion exchange, chemical oxidation, membrane separation, stripping and adsorption [20].

In this section, some of the methods for wastewater removal are briefly explained.

1.2.1 Sedimentation:

Sedimentation is a primary process for wastewater treatment that involves settling suspended particles using sedimentation basins, clarifiers and chemical flocculants. It is widely used for treating domestic and industrial wastewater [20].

1.2.2 Filtration:

Dye removal is typically achieved through filtration processes such as microfiltration, ultrafiltration and reverse osmosis. However, microfiltration is unsuitable for wastewater treatment due to its larger pore size [21]. Also, this method requires high working pressure with more energy consumption, a short lifetime, and a high membrane cost. On the other hand, reverse osmosis is the most effective decolourizing method for desalting wastewater, as it breaks down the salts rather than non-ionized weak bases and acids [20].

1.2.3 Chemical treatment:

The coagulation or flocculating process is treated as an effective technique for degrading industrial dyes. In this process, the dye effluents are mixed with aluminium (Al) or calcium (Ca) ions, resulting in flocculation. The overall cost of this process depends upon the cost of chemicals; hence, it may be expensive in some cases. However, this method is ineffective for azo, reactive, acid and highly soluble dyes due to its pH dependency and restriction imposed by sludge production [22].

1.2.4 Oxidation process:

During the oxidation process, contaminated water is reacted with different oxidizing agents. The two primary types of this technique are chemical oxidation and ultraviolet (UV) assisted oxidation. In the second case, dye effluents are treated with chlorine, hydrogen peroxide, Fenton's reagent and ozone. This method is fast and has fewer requirements; hence, it is mainly used for dye removal. The oxidizing agents in this method accomplish complete dye degradation, provided that pH and catalyst are the two key factors that play a vital role in the oxidation process [23].

1.2.5 Advanced oxidation process:

There is a strong need to develop an effective and eco-friendly system that overcomes the drawbacks of conventional water-treatment methods to remove hard-to-treat pollutants. Consequently, the advanced oxidation process is developed to overcome the demerits of conventional systems. This method can completely degrade many dye effluents, organic pollutants, heavy metals and microbial substances. In many instances, the complete degradation of effluents in a single oxidation process is insufficient; in those cases, more oxidation processes are preferred. This process comprises many oxidation techniques, including Fenton's reagent oxidation process, UV photolysis and sonolysis. These methods are highly effective for degrading dyes at ambient pressure and normal temperature. The advanced oxidation process frequently results in the oxidation of organic compounds to CO_2. Numerous sophisticated oxidation techniques are currently in use, including chemical oxidation procedures that use ozone, combined ozone, peroxide and UV light [20-24].

1.2.6 Photocatalysis:

In recent years, light-assisted photocatalysis has attracted enormous research interest as it is a very efficient technique for degrading harmful and non-biodegradable pollutants from the environment. Photocatalysis is one of the environmentally friendly techniques utilized to degrade contaminants present in wastewater using a proper photocatalyst. During photocatalytic reactions, when a photocatalyst is exposed to solar irradiation, effluent degradation occurs via reactive oxidizing species production. Solar-assisted photocatalysis can be used to degrade non-biodegradable and hazardous substances; hence, it is treated as a very effective technique for removing hazardous effluents from contaminated wastewater [25]. Photocatalysis is one of the environmentally friendly processes for complete effluent degradation by converting

hazardous chemicals into water, CO_2, and mineral acids under the exposure of light irradiation. The photocatalytic degradation method has significant advantages, including cost-effectiveness, eco-friendly nature, reusability, sustainability, and no risk of producing secondary pollutants.

1.3 Photocatalysts for Photocatalytic Dye Degradation:

Photocatalysis is a green process because it uses natural sunlight to decompose toxic and hazardous organic water pollutants. Heterogeneous photocatalysis comprises the acceleration of a photoreaction in the presence of a semiconductor photocatalyst [26]. Heterogeneous semiconductor photocatalysis has been extensively studied, and it is a cost-effective and promising approach for the decomposition of a large number of organic pollutants by harvesting solar energy. Compared with other renewable energy sources, solar energy is one of the clean and sustainable sources that can replace fossil fuels and provide energy when needed [27]. During the past few years, the research interest has been focused on developing various photocatalyst materials due to their suitable band structure, composition, and optical properties beneficial for solar-assisted photocatalysis.

1.3.1 Bismuth vanadate ($BiVO_4$):

Photocatalyst materials with narrow band gaps are desirable to enhance photocatalytic activity. Among the metal oxides, wide band gap semiconducting oxides such as zinc oxide (ZnO), niobium oxide (Nb_2O_5) and titanium dioxide (TiO_2) have been extensively studied as photocatalysts due to their high chemical stability and non-toxicity. Still, their performance is restricted due to the wide band gap (absorbs only UV radiations; <4% of solar spectrum). Consequently, many efforts were made on narrow band gap semiconductors like metal chalcogenides, (oxy)nitride/oxysulfide, doped metal oxides, etc [28]. However, most of these narrow band gap semiconductor photocatalysts do not possess enough photoactivity because they suffer from high recombination rates of excitons, low electrical conductivity, low surface area, non-porous morphology and limited photostability. Among them, the narrow band gap (2.4 eV) $BiVO_4$ is one of the highly studied photocatalysts due to its high photostability, non-toxicity, low photo-corrosion, well-suited band structure, high optical absorption coefficient (10^4-10^5 cm^{-1} at 350-520 nm) and favorable flat band potential (<200mV) positive to hydrogen evolution reaction [29].

$BiVO_4$ naturally occurs in an orthorhombic structure with mineral pucherite form. Monoclinic scheelite structure (m-$BiVO_4$), tetragonal scheelite (ts-$BiVO_4$) structure, and tetragonal zircon type structure (tz-$BiVO_4$) are three crystalline phases of $BiVO_4$. Among these three crystal structures, the absorption edge of the tetragonal phase lies in the UV region, whereas the absorption edge of the m-$BiVO_4$ with a band gap energy of 2.4 eV lies within the visible region of the solar spectrum [30]. The common thing in all three crystal structures of $BiVO_4$ is that eight oxygen atoms are co-ordinally bonded to each bismuth ion, and four oxygen atoms in a tetrahedral site are co-ordinally bonded to each vanadium ion. The zircon and scheelite crystal structures differ in such a way that the bismuth ion is bound to six VO_4 ions in a zircon-type structure, whereas each bismuth ion is bound to eight VO_4 tetrahedral units in a scheelite structure. Crystal structures of monoclinic scheelite and tetragonal scheelite $BiVO_4$ are not similar because, as compared to $BiVO_4$ tetragonal phase, local environments of vanadium and bismuth ions are distorted in monoclinic phase [31,32]. A schematic representation of three crystal structures of $BiVO_4$ is displayed in **Fig. 1.4**.

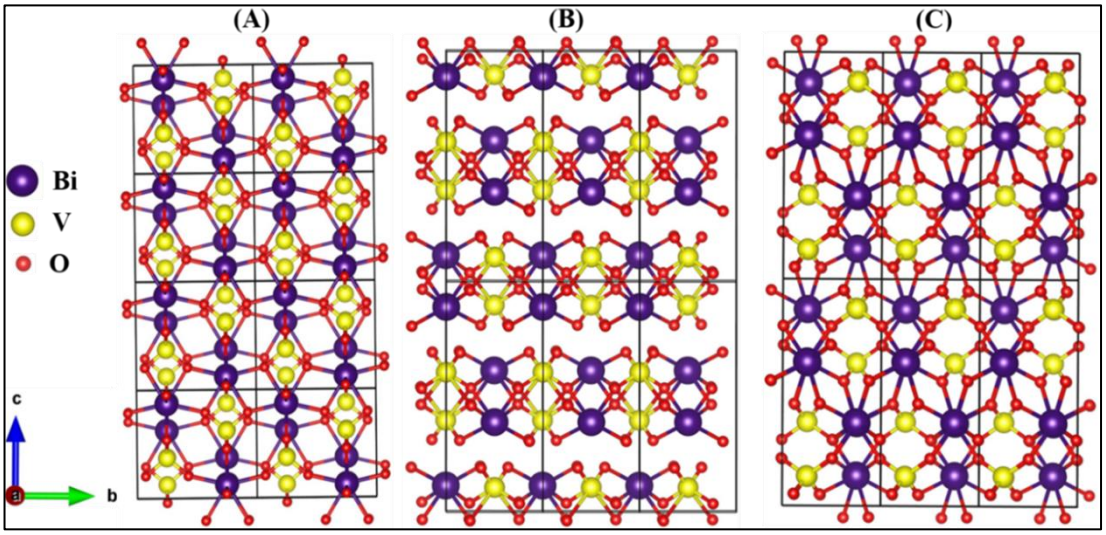

Fig. 1.4: Schematic representation of crystal structures of $BiVO_4$ drawn from Vesta Software: (A) tetragonal zircon, (B) monoclinic scheelite and (C) tetragonal scheelite.

Interconversion between three crystalline phases of $BiVO_4$ is possible by tuning the synthesis temperature. Low-temperature synthesis methods produce the tz-$BiVO_4$ phase. At a higher temperature of 670-770 K (397-497°C), the m-$BiVO_4$ phase is produced from the tz-$BiVO_4$ phase, whereas the phase transition between m-$BiVO_4$ and ts-$BiVO_4$ achieves reversibly at a temperature of 528 K (255°C) [31]. Among all other crystal structures of $BiVO_4$, superior performance for all photo-functional applications is obtained for m-$BiVO_4$ owing to its excellent visible light absorption.

1.3.2 2D Layered Metal Oxide Nanosheets (MONs):

Numerous low-dimensional nanostructured semiconductive materials are developed and investigated as photocatalysts. Current research interest has been focused on developing two-dimensional (2D) nanostructured inorganic solids due to their superior functionalities. "Inorganic nanosheets" (INs) refer to inorganic plate-like particles with lateral sizes hundreds to thousands of times greater than their thickness, typically at the nanometer scale. Nanosheets (NSs) are particles with a thickness ranging from 1 nm to sub-nm. Monolayered INs can be obtained through the exfoliation of inorganic layered crystals. The INs are atomically thin monolayers with few nanometres of thickness. Even though a monolayer of these inorganic crystals is the ideal realization of NSs, pristine layered crystals with one or more layers are practically considered as NSs. Since the parent layered inorganic crystals from which NSs are produced have a wide variety of structural frameworks and chemical compositions, the corresponding INs also have a wide variety of structural and chemical diversity [33]. **Fig. 1.5** depicts a few typical monolayer INs of MnO_2, lepidocrocite-type layered titanate (TiO_2), MoS_2, layered double hydroxide (LDH) and graphene NSs.

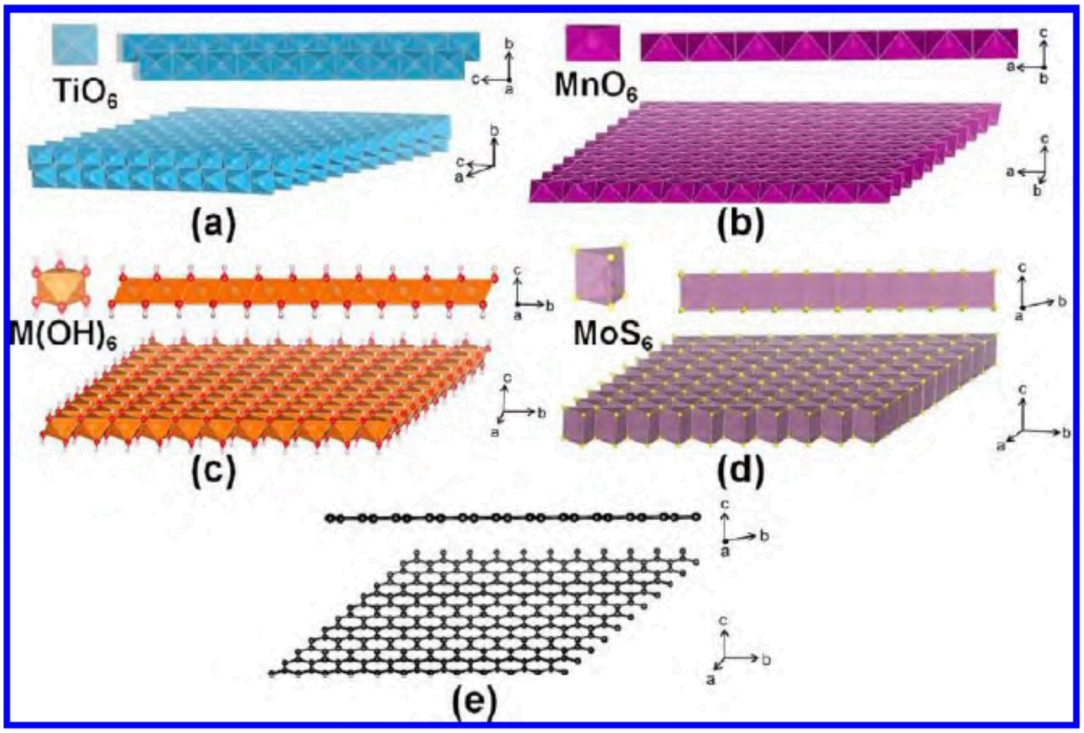

Fig. 1.5: Schematic structural representation of (a) lepidocrocite-type titanate NS, (b) MnO_2 NS, (c) LDH NS, (d) MoS_2 NS and (e) graphene NS [34].

Properties of NSs and NSs-Based Hybrids:

Anisotropic morphology and flexibility:

The characteristics of the exfoliated 2D INs change with diverse crystallographic directions due to their 2D morphological features. Additionally, these 2D INs display a scrolling behavior along a specific crystallographic axis to reduce surface stresses and energy.

Exceptionally thin thickness:

Exfoliated 2D INs revealed monolayer morphology having an extremely thin thickness in the 0.5-2.0 nm range [35]. As a result, most of the component ions are exposed on the surface of INs, which is crucial for their hybridization with other guest species. This results in significant electronic coupling with the hybridized species. The effective electronic coupling and chemical interaction of 2D NSs with hybridized species enhance the several functionalities of 2D NSs for numerous applications.

Photoinduced surface properties:

Interestingly, INs exhibit photoinduced superhydrophilicity, which is highly desired for photocatalytic self-cleaning and antifogging coatings. With the phenomena mentioned above, exploring the mechanism and origin of the photogenerated superhydrophilicity of the NS surface is possible.

Compositional flexibility:

The exfoliated INs can be prepared with various crystal shapes and chemical compositions based on the composition and structure of the parent host layered crystals used in the exfoliation protocol [36]. Thus, INs with a variety of chemical compositions can be possible.

Surface charge:

Most layered inorganic solids have charge-compensating ionic species in their intergallary spacings, producing INs having an inherent surface charge. The excellent processability of INs is facilitated by their inherent surface charge, which minimizes self-agglomeration and results in very stable colloidal suspension. When such INs are used to develop nanohybrid materials, the chemical interaction between the surface-charged INs and oppositely charged guest species leads to a well-ordered nanohybrid structure.

Expanded surface area:

INs have expanded surface area because of their unusual 2D anisotropic surface morphology. Most of the constituent ions are present on the surface, which significantly increases the potential for functionalizing INs by anchoring various functional groups [37]. Because of the highly anisotropic 2D morphology of the exfoliated NSs, different functional groups can be attached to the 2D INs with improved surface area.

By soft-chemically exfoliating the pristine layered materials, sub-nanometre-thick 2D NSs of layered metal oxides can be produced. Many exfoliated wide band gap layered MONs can be used as photocatalysts for water splitting and the photodegradation of organic pollutant molecules [38]. These wide band gap 2D MONs can be useful for coupling with narrow band gap semiconductors. Compared to other materials, MONs act as fundamental building blocks for the fabrication of nanohybrid photocatalysts with characteristic physicochemical features due to their improved surface area and thin thickness.

The 2D titanate NSs (NS-titanate) and hexaniobate NSs (NS-hexaniobate) derived by the exfoliation of their respective pristine layered crystals are excellent due to the exceptionally high anisotropy in their crystal structure and morphology (NS-titanate and NS-hexaniobate imply the exfoliated NSs derived from the bulk cesium titanate ($Cs_{0.7}Ti_{1.825}\square_{0.175}O_4$) and potassium hexaniobate ($K_4Nb_6O_{17}$) crystals by the reported protocol of exfoliation) [35-38]. NS-titanate and NS-hexaniobate are selected due to their highly anisotropic 2D morphology, suitable band positions for reducing hydroxyl ions and oxidation of H_2O, and high chemical stability.

1.3.3 Nanohybrids based on $BiVO_4$ and 2D Layered MONs:

Due to the wide band gap energy, low photostability and inappropriate electronic band positions for the reduction of protons and the oxidation of oxide ions, most inorganic photocatalysts are unsuitable for visible-light-driven photocatalysis. To increase the photocatalytic activity, attempts are being made to hybridize two different types of photocatalysts to overcome the limitations of these materials. Thus, the approach of developing nanostructures and electronic coupling between semiconducting materials is explored [34].

Several coupled semiconductors are explored as a photocatalyst. Most of them used nanocrystalline TiO_2 as a wide-bandgap semiconductor and metal chalcogenides as a narrow-bandgap material. Still, the coupled semiconductor photocatalyst system

suffers from limited efficiency and stability. To enhance photoactivity and overcome the above problems, an intimate electronic coupling between photocatalyst materials is necessary. Considering highly anisotropic 2D morphology, suitable band positions and high chemical stability of NS-titanate and NS-hexaniobate, these NSs can be used as effective building blocks for developing nanohybrid photocatalyst materials. In these nanostructures, all the ions in the sub-nanometre-thick 2D NSs are exposed to its surface and can significantly alter electronic interactions between hybridized guest species. In this context, nanohybrids made up of $BiVO_4$ with suitable band positions and NS-titanate or NS-hexaniobate can provide 1) enhanced photocatalytic activity as a result of strong electronic coupling between the hybridized species, 2) expanded surface area caused by the development of a mesoporous house of cards type structure and 3) tunable chemical composition to accomplish desire photo-physicochemical characteristics.

1.4 Mechanism of Photocatalytic Dye Degradation:

The two reaction mechanisms are involved in the photodegradation or bleaching of the toxic dyes [39,40]. These mechanisms are briefly discussed below.

1.4.1 Direct mechanism for dye degradation:

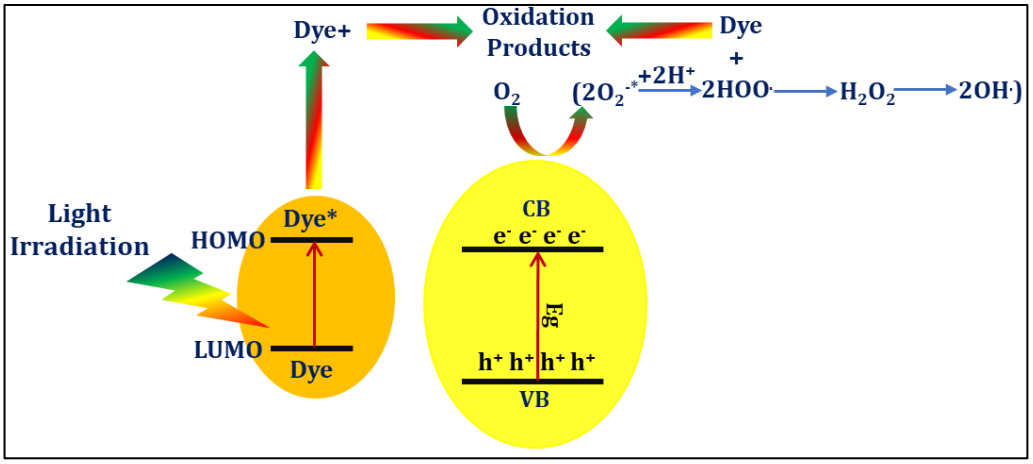

Fig. 1.6: Schematic of direct dye degradation mechanism.

This dye degradation mechanism occurs when the dye can absorb some visible light. In this type, when the dye absorbs visible light (λ>400 nm), dye excitation occurs from the ground state (Dye) to the excited triplet state (Dye*). Further, the (Dye*) species gets transformed into semi-oxidized cation (Dye^+) radicals due to the injection of electrons into the conduction band (CB) of the semiconductor. Finally, as shown in

Fig. 1.6, superoxide (O_2^{*-}) and hydroxyl (OH^-) radicals can form by the reaction of trapped electrons and dissolved oxygen in the system.

$$Dye + h\nu \rightarrow Dye^* \quad (1.1)$$

$$Dye^* + semiconductor \rightarrow Dye^+ + semiconductor^- \quad (1.2)$$

1.4.2 Indirect mechanism for dye degradation:

An indirect dye degradation mechanism can occur via four steps, as shown in **Fig. 1.7**.

(A) Photoexcitation: The photons get absorbed when a semiconductor photocatalyst is exposed to electromagnetic radiation with photon energy equal to or greater than its band gap. As a result, valence band (VB) electrons get excited to their CB by forming photoexcited electrons in CB and holes in VB. An electron-hole pair is formed when the excitation process leaves a hole in the VB, indicated by the following equation,

$$semiconductor + h\nu \rightarrow semiconductor\ [e^-(CB) + h^+(VB)] \quad (1.3)$$

(B) Water Ionization: Photogenerated holes at the VB reacted with water by creating hydroxyl (OH*) radicals.

$$H_2O(ads) + h^+(VB) \rightarrow OH^*(ads) + H^+(ads) \quad (1.4)$$

The OH* radicals produced on the irradiated semiconductor surface are powerful oxidizing agents that attack organic molecules non-selectively to mineralize them to an extent.

(C) Oxygen ionosorption: On the other hand, photoexcited electrons get absorbed by oxygen and anionic superoxide radicals (O_2^{-*}) are produced.

$$O_2 + e^-(CB) \rightarrow O_2^{-*}(ads) \quad (1.5)$$

These superoxide ions maintain electron neutrality by preventing the recombination of electrons and holes.

(D) Superoxide Protonation: The created superoxide O_2^{-*} undergoes protonation to make hydroperoxyl radicals (HOO*), followed by the formation of H_2O_2 that further dissociates to become an extremely reactive OH* radicals.

$$O_2^{-*}(ads) + H^+ \rightarrow HOO^*(ads) \quad (1.6)$$

$$2HOO^{*}(ads) \rightarrow H_2O_2(ads) + O_2 \quad (1.7)$$

$$H_2O_2(ads) \rightarrow 2OH^{*}(ads) \quad (1.8)$$

$$Dye + OH^{*} \rightarrow CO_2 + H_2O\ (dye\ intermediates) \quad (1.9)$$

$$Dye + h^{+}(VB) \rightarrow oxidation\ products \quad (1.10)$$

$$Dye + e^{-}(CB) \rightarrow reduction\ products \quad (1.11)$$

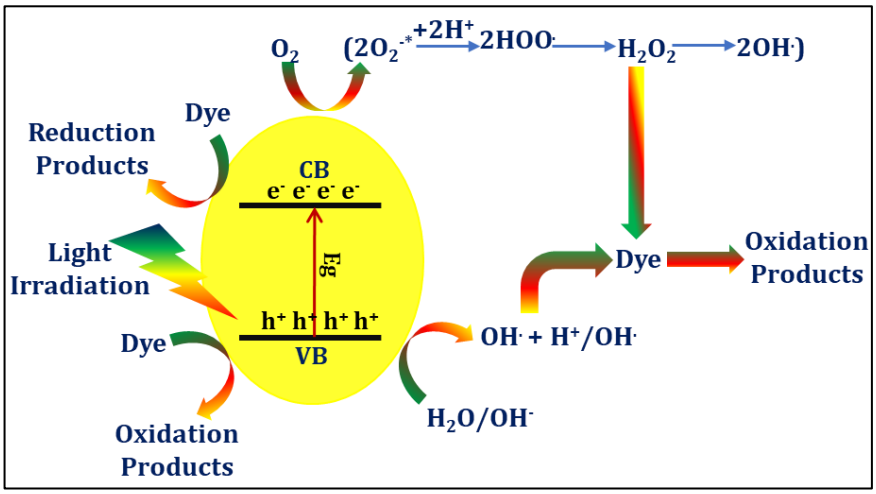

Fig. 1.7: Schematic of indirect dye degradation mechanism.

During the past few decades, various semiconducting materials have been employed as photocatalysts for visible light photocatalysis. Many of them suffer from low photocatalytic performance due to the wide band gap energy. Their light absorption behavior is restricted to the UV region of the total solar spectrum, which accounts for only 4% of the total solar spectrum. Among many nanocrystalline oxides, nanostructured TiO_2 and potassium hexaniobate have been considered as stable materials for photocatalysis. Bulk TiO_2 and Nb_2O_5-based composite materials are investigated for photocatalytic applications. However, their optimum performance is restricted by the difficulty in controlling crystallite size and limited electronic coupling due to the large crystallites. Thus, the coupling strategy of wide band gap semiconductor photocatalysts with other narrow band gap semiconductors is recommended to overcome the above issues. Also, such a strategy can collect the photogenerated holes/electrons or to channelize them [34]. Considering the issues mentioned above, there is a strong need to design and develop novel types of NS-titanate and NS-hexaniobate-based hybrids, which can lead to the formation of a highly porous house-

of-cards-type stacking structure and a controlled alteration of the electronic structure that enables an optimization of the physicochemical characteristics and applicability of NSs based hybrid in solar assisted photocatalysis with high stability and efficiency.

1.4.3 Photocatalytic degradation of MB and Rh-B:

In the present work, the narrow band gap $BiVO_4$ is hybridized with the wide band gap NS-titanate and NS-hexaniobate. Coupling of $BiVO_4$ with NS-titanate and NS-hexaniobate can lead to visible light active photocatalysts with enlarged surface area and improved photoactivity by strong electronic coupling between the hybridizing species. Also, the chemically stable NS-titanate and NS-hexaniobate hybridized with $BiVO_4$ led to the overall increase in the chemical stability of the nanohybrid photocatalyst. The plausible dye degradation mechanism is proposed in **Fig. 1.8**.

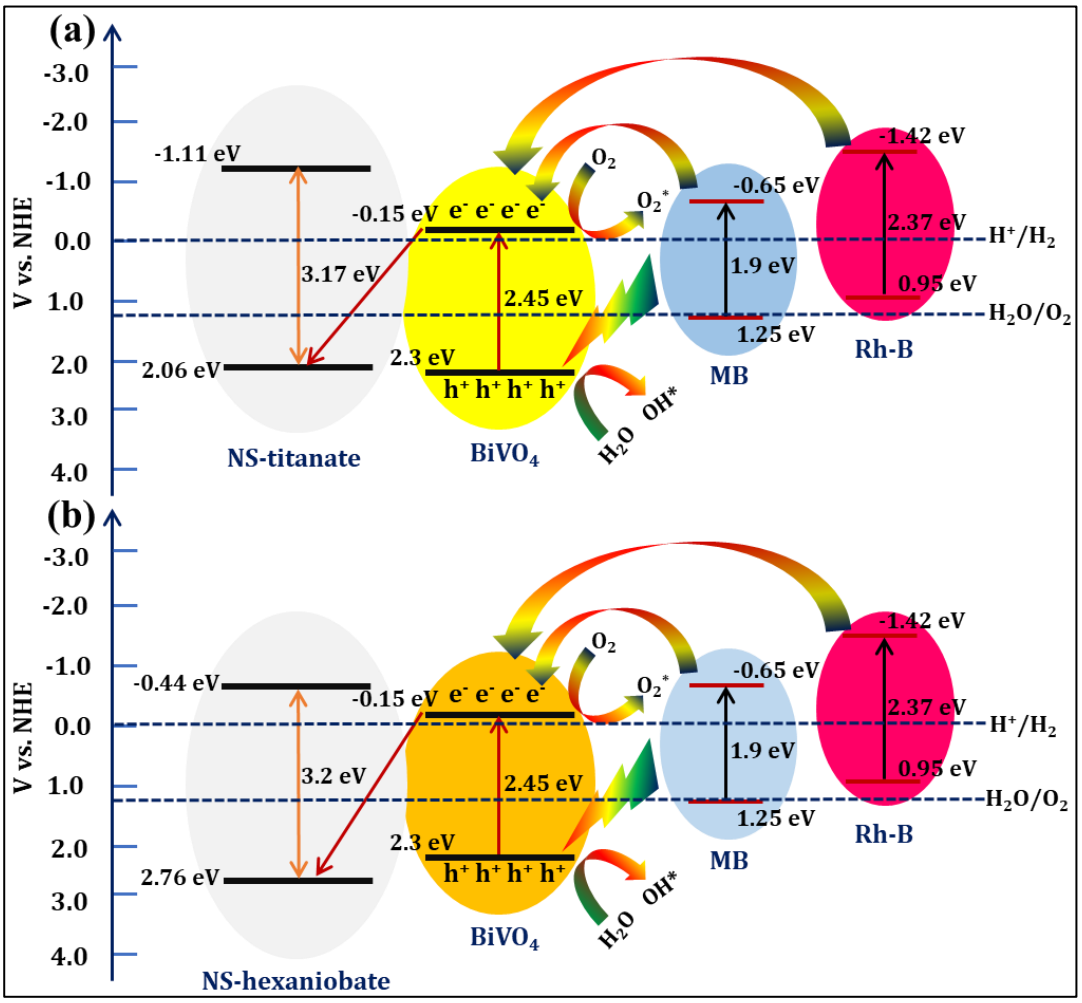

Fig. 1.8: Plausible dye degradation mechanism for (a) $BiVO_4$ hybridized with NS-titanate for degradation of MB, Rh-B and (b) $BiVO_4$ hybridized with NS-hexaniobate for degradation of MB, Rh-B.

1.5 Review of Literature:

1.5.1 Literature survey of $BiVO_4$ for photocatalytic dye degradation:

Nanocrystalline metal oxide attracts great attention in the field of photocatalytic dye degradation as well as photocatalytic and photoelectrochemical (PEC) water splitting due to their nanosized surface morphology, tunable band structure, large surface area, well-defined crystal structure and high photostability. Among different semiconducting metal oxides used in photocatalysis, $BiVO_4$ is the most widely used photocatalyst due to its low band gap energy (2.4 eV), superior photostability and resistance to photo-corrosion [41]. Therefore, $BiVO_4$ is the vividly exploited photocatalyst for the photodegradation of various dyes.

In one instance, the wet solution method was employed to prepare porous $BiVO_4$ hollow spheres and applied for the photocatalytic degradation of methyl orange (MO) in visible light illumination [42]. The formation of $BiVO_4$ hollow spheres with narrow band gaps increases visible light absorbance, resulting in enhanced degradation efficiency. $BiVO_4$ hollow spheres showed improved MO degradation performance of 95.3% after 180 min of light exposure. Ultrasonic assisted strategy was followed to synthesize $BiVO_4$ crystals (Sono $BiVO_4$), and its photodegradation activity for MO degradation was tested under visible light illumination [43]. The Sono $BiVO_4$ displayed 99% MO degradation after 180 min.

Moreover, the $BiVO_4$ thin films deposited by the solution combustion method were examined for photocatalytic Rh-B degradation [44]. The photocatalytic characteristics of $BiVO_4$ thin films were evaluated by varying the calcination temperature. The optimized $BiVO_4$ thin film displays 86.67% Rh-B degradation in 50 min. Further, the hydrothermal process was employed for synthesizing $BiVO_4$ nanoparticles and their photocatalytic activity for degradation of MB was examined [45]. The photocatalytic activity of $BiVO_4$ nanoparticles was tested with the effect of the amount of catalyst loading, the effect of dye concentration and the effect of pH. The optimized $BiVO_4$ thin film showed a superior MB photodegradation performance of 91.9% after 90 min of light exposure.

Similarly, the hydrothermal method was employed to synthesize $BiVO_4$ powder photocatalysts and used for the photodegradation of MB, MO, Rh-B and crystal violet (CV) dyes [46-51]. Among the four dyes, $BiVO_4$ powder photocatalyst showed an excellent photodegradation performance of 99% for MB degradation in 90 min of light

exposure [47]. $BiVO_4$ photocatalysts prepared via microwave-assisted route and precipitation method were used for the photocatalytic degradation of Rh-B and MB dyes [52-54]. $BiVO_4$ displays a maximum Rh-B and MB degradation performance of 94 and 92.25% in visible-light illumination.

On the other hand, $BiVO_4$ thin films deposited by electrophoretic deposition (EPD) were utilized for the visible-light-driven photodegradation of MO, MB and phenol [55]. Among the three dyes, $BiVO_4$ exhibited an excellent photodegradation performance of 97% for MB degradation. $BiVO_4$ photocatalysts synthesized by hydrothermal, solvothermal and Rf-sputtering techniques were employed for the photodegradation of Rh-B, MB and rhodamine 6G (Rh-6G) dyes [56-58]. $BiVO_4$ displays improved photocatalytic activity with degradation rates of 60, 81 and 95% for Rh-B, MB and Rh-6G, respectively. The spray pyrolysis method was adopted to synthesize $BiVO_4$ thin films, and the obtained thin films were used to photodegrade Rh-B and MO dyes [59-61]. The optimized $BiVO_4$ thin film displayed improved Rh-B photodegradation of 96% under visible light illumination [60]. Furthermore, $BiVO_4$ samples synthesized via solvothermal and urea hydrolysis methods were applied for the photodegradation of MB and Rh-B dyes, respectively [62,63]. $BiVO_4$ shows superior degradation performance of 91 and 55.1% for MB and Rh-B degradation, respectively. The literature survey of photodegradation performance for $BiVO_4$ photocatalysts is summarized in **Table 1.1**.

Table 1.1: Brief literature review of $BiVO_4$ photocatalysts for visible-light-driven photodegradation of dyes.

Sr. no.	**Photocatalyst**	**Method of synthesis**	**Target dye**	**λ (nm)**	**Percentage degradation**	**Ref.**
1	$BiVO_4$	Wet-solution	MO	500	95.3%; 180 min	42
2	$BiVO_4$	Ultrasonic-assisted	MO	465	99%; 180 min	43
3	$BiVO_4$	Solution combustion	Rh-B	553	86.67%; 50 min	44
4	$BiVO_4$	Hydrothermal	MB	664	91.9%; 90 min	45
5	$BiVO_4$	Hydrothermal	MB	664	88.86%; 60 min	46
6	$BiVO_4$	Hydrothermal	MB	664	99%; 90 min	47

7	$BiVO_4$	Hydrothermal	MO	-	94%; 60 min	48
8	$BiVO_4$	Hydrothermal	Rh-B, CV	553, 583	64.81%; 210 min 96.23%; 120 min	49
9	$BiVO_4$	Microwave-hydrothermal	Rh-B	553	95%; 200 min	50
10	$BiVO_4$	Hydrothermal	CV	590	98.21%; 120 min	51
11	$BiVO_4$	Microwave-assisted	Rh-B	554	90.8%; 180 min	52
12	$BiVO_4$	Precipitation	Rh-B	553	94%; 220 min	53
13	$BiVO_4$	Precipitation	MB	664	92.25%; 120 min	54
14	$BiVO_4$	EPD	MO, Phenol, MB	-	39.8%, 63.7%, 97%	55
15	$BiVO_4$	Hydrothermal	Rh-B	554	60%; 240 min	56
16	$BiVO_4$	Solvothermal	MB	664	81%; 120 min	57
17	$BiVO_4$	Rf-sputtering	Rh 6G	527	95%; 240 min	58
18	$BiVO_4$	Spray pyrolysis	Rh-B, MO	-	86%, 93%	59
19	$BiVO_4$	Spray pyrolysis	Rh-B	552	96%; 180 min	60
20	$BiVO_4$	Spray pyrolysis	Rh-B	553	95%; 180 min	61
21	$BiVO_4$	Solvothermal	MB	668	91%; 60 min	62
22	$BiVO_4$	Urea hydrolysis	Rh-B	553	55.1%; 75 min	63

1.5.2 Literature survey of TiO_2 and Nb_6O_{17}-based nanohybrids for photocatalytic dye degradation:

Despite extensive research, the majority of inorganic photocatalysts ever designed are ineffective for visible-light-driven photocatalysis. To overcome the limitations of these materials, attempts have been made to couple two different types of photocatalysts. Additionally, an alternate method for boosting the photocatalytic activity of semiconductive materials is the development of nanostructures. As photocatalysts, numerous low-dimensional nanostructured semiconducting materials are being developed and investigated. The 2D nanostructured inorganic solids are being studied due to their nanostructured morphology. The number of exfoliated layered MONs can

be used as photocatalysts for the photodegradation of organic pollutant molecules. The hybridization of 2D NS-titanate and NS-hexaniobate with $BiVO_4$ can enhance the photocatalytic dye degradation activity.

In one instance, $BiVO_4/TiO_2$ composite thin films were synthesized by coating $BiVO_4$ layers on the surface of TiO_2 thin films deposited by successive ionic layer adsorption and reaction (SILAR) method. The photoactivity of $BiVO_4/TiO_2$ composite thin films for degradation of Rh-6G was tested [39]. The $BiVO_4/TiO_2$ composite films showed enhanced photocatalytic performance compared with pristine TiO_2 and $BiVO_4$ thin films. Further, the $BiVO_4/TiO_2$ composite thin films were deposited by sol-gel followed by the doctor blade method and the obtained films were used for visible-light-induced MB degradation [64]. Enhanced MB degradation obtained for composite thin films can attributed to improved charge transfer kinetics. Solvothermal and hydrothermal methods were used to synthesize $BiVO_4/TiO_2$ composites, and their photocatalytic activity for photodegradation of Rh-B and MB dyes was checked [65,66]. The $BiVO_4/TiO_2$ composites show improved photocatalytic degradation of 92 and 92.7% for Rh-B and MB, respectively. The hybrid photocatalysts composed of reduced graphene oxide (rGO), $BiVO_4$ and TiO_2 were developed by wet-chemical method and applied for photocatalytic degradation of MB [67]. The optimized rGO-$TiO_2/BiVO_4$ photocatalyst showed complete degradation of MB after 120 min of light exposure.

Similarly, $BiVO_4/TiO_2$ composite thin film photocatalysts were synthesized by hydrothermal and sol-gel methods and their photoactivity for photocatalytic degradation of Rh-B, 4-nonylphenol, acid blue (AB-113) was examined [68-70]. Among the three pollutants, the $BiVO_4/TiO_2$ composite thin film displays complete degradation of Rh-B in 80 min of light exposure [68]. Likewise, $TiO_2/BiVO_4$ composite photocatalysts synthesized via hydrothermal and wet-impregnation methods displayed almost complete degradation of Rh-B and MB after 18 and 150 min of light exposure, respectively [71,72]. Hydrothermally deposited $BiVO_4/TiO_2$ composite thin films were used for photocatalytic degradation of MB [73]. The optimized thin film showed superior photocatalytic performance (99%) for MB degradation in 60 min of light exposure. $BiVO_4/TiO_2$ composite photocatalysts were synthesized by combining metal-organic decomposition (MOD) and sol-gel methods and obtained thin films were used for the photodegradation Rh-B [74]. The optimized $BiVO_4/TiO_2$ composite displays superior photocatalytic activity with a rate constant (k) of 0.0073 min^{-1}.

Moreover, the $BiVO_4/TiO_2$ hybrids were developed by sol-gel and electrostatic self-assembly methods, and their photoactivity for degradation of MO and Rh-B dyes was tested [75,76]. The $BiVO_4/TiO_2$ hybrids show improved photocatalytic performance of 99.78 and 93% for MO and Rh-B degradation, respectively. The wet-chemical method was used to synthesize $TiO_2/BiVO_4$ composite photocatalysts and applied for photodegradation of Rh-B [77]. The $TiO_2/BiVO_4$ composite photocatalyst displays enhanced Rh-B degradation performance of 69% in 105 min of light exposure. The $BiVO_4$-TiO_2-$BiVO_4$ three-layer composite thin film photocatalyst was synthesized via the facile sol-gel method [78]. It showed superior photocatalytic activity for MB (95%) and Rh-B (91%) degradation under 180 and 300 min of light exposure, respectively. Further, the $TiO_2/BiVO_4$ thin film photocatalysts were epitaxially deposited on yttrium-stabilized zirconia substrates by pulsed laser deposition (PLD) method and obtained thin films were used for photocatalytic degradation of Rh-B [79]. The optimized $TiO_2/BiVO_4$ photocatalyst shows improved photocatalytic activity with a k value of 0.0015 min^{-1}. The photocatalytic degradation performance of composite photocatalysts composed of $BiVO_4$ and TiO_2 is summarized in **Table 1.2**.

Furthermore, the Ag@AgBr intercalated $K_4Nb_6O_{17}$ composite was deposited by the ion exchange route and utilized for the photodegradation of Rh-B in visible light illumination [80]. Almost 96% of Rh-B was degraded under visible light exposure. The photocatalyst composed of CdS loaded on $K_4Nb_6O_{17}$ was synthesized by the microemulsion method [81]. The CdS-loaded $K_4Nb_6O_{17}$ showed enhanced visible-light-driven photocatalysis for the decomposition of Rh-B with 90% degradation after 120 min. The PbS-sensitized $K_4Nb_6O_{17}$ nanocomposite was deposited using microemulsion and applied for photocatalytic degradation of Rh-B [82]. The PbS-sensitized $K_4Nb_6O_{17}$ nanocomposite with 25% of PbS showed 71% of Rh-B degradation after 120 min under visible light illumination.

Table 1.2: Brief literature review of TiO_2 and Nb_6O_{17}-based nanohybrids for visible-light-induced photodegradation of dyes.

Sr. no.	**Photocatalyst and method of synthesis**	**Target dye**	**λ (nm)**	**Percentage degradation or K**	**Ref.**
1	$BiVO_4/TiO_2$ by SILAR	Rh-6G	525	0.004 min^{-1}	39

2	$BiVO_4/TiO_2$ by sol-gel followed by doctor blade	MB	664.5	1.568 h^{-1}	64
3	$BiVO_4/TiO_2$ by solvothermal	Rh-B	554	92%; 240 min	65
4	$BiVO_4/TiO_2$ by hydrothermal	MB	664	92.7%; 30 min	66
5	rGO-$TiO_2/BiVO_4$ by wet-impregnation	MB	-	100%; 120 min	67
6	$BiVO_4/TiO_2$ by hydrothermal	Rh-B	-	100%; 80 min	68
7	$BiVO_4/TiO_2$ by hydrothermal	4-nonyl phenol	-	1.19 h^{-1}	69
8	$BiVO_4/TiO_2$ by sol-gel	AB-113	568	82%; 120 min	70
9	$TiO_2/BiVO_4$ by hydrothermal	Rh-B	553	99%; 18 min	71
10	$TiO_2/BiVO_4$ by wet-impregnation	MB	-	100%; 150 min	72
11	$BiVO_4/TiO_2$ by hydrothermal	MB	665	99%; 60 min	73
12	$BiVO_4/TiO_2$ by MOD, sol-gel	Rh-B	554	0.0073 min^{-1}	74
13	$BiVO_4/TiO_2$ by sol-gel	MO	-	99.78%; 140 min	75
14	$BiVO_4/TiO_2$ by self-assembly	Rh-B	-	93%; 150 min	76
15	$TiO_2/BiVO_4$ by wet-chemical	Rh-B	554	69%; 105 min	77
16	$BiVO_4$-TiO_2-$BiVO_4$ by sol-gel	MB, Rh-B	664, 553	95%; 180 min, 91%; 300 min	78
17	$TiO_2/BiVO_4$ by PLD	Rh-B	554	0.0015 min^{-1}	79
18	Ag@AgBr-$K_4Nb_6O_{17}$ by ion exchange	Rh-B	554	96%	80
19	CdS@$K_4Nb_6O_{17}$ by microemulsion	Rh-B	554	90%; 120 min	81
20	PbS@$K_4Nb_6O_{17}$ by microemulsion	Rh-B	554	71%; 120 min	82

The above literature survey clearly indicated that $BiVO_4$ demonstrated enhanced photocatalytic activity when coupled with wide-bandgap semiconductors. TiO_2 is a highly suitable wide-bandgap semiconductor for coupling with $BiVO_4$. Along with TiO_2, $K_4Nb_6O_{17}$ is another wide-bandgap semiconductor for coupling with various

narrow-bandgap semiconductor photocatalysts like CdS and PbS. However, the efficient photocatalyst based on $BiVO_4$ has not been realized in practical application. It is also clear that the nanocrystalline hybridization strategy is highly desirable to achieve the intimate electronic coupling between the semiconductor photocatalysts. The NS-titanate and NS-hexaniobate evoke high research interest as a fundamental component of the hybrid photocatalysts due to their high anisotropy, extremely thin thickness, high surface area, electrostatic surface charge and high mechanical flexibility.

1.6 Orientation and Purpose of Thesis:

Water pollution has severely threatened the global environment and living organisms. One of the major reasons behind water pollution is contamination caused by industrial organic dyes. These dyes can affect aquatic life and lead to serious harm to people and animals through infection of the liver, central nervous system, reproductive system, brain and kidney. Therefore, an efficient and eco-friendly process for dye effluent degradation is essential. Among numerous wastewater treatment methods, heterogeneous photocatalysis has emerged as one of the most promising technologies for wastewater purification.

The process of acceleration of photoreaction in the presence of a semiconductor photocatalyst is known as heterogeneous photocatalysis. Despite extensive investigation, most inorganic photocatalysts are unsuited for visible-light-induced photocatalysis due to their wide band gap energy, least photostability and inappropriate band positions for proton reduction and water oxidation. Lots of efforts were put forward on narrow band gap semiconductors like metal chalcogenides, (oxy)nitride/oxysulfide, doped metal oxides, etc. Still, these semiconductor photocatalysts suffer from high recombination rates and limited photostability. Thus, attempts were made to hybridize two different types of photocatalysts to overcome the limitations of these materials. A hybridization strategy of coupling narrow-band gap photocatalysts with wide-bandgap materials is necessary to overcome the aforementioned issues and enhance photocatalytic performance. Still, the coupled semiconductor photocatalyst systems suffer from limited efficiency and stability.

MONs are an excellent choice for fabricating nanohybrid photocatalysts with distinctive physicochemical features due to their enlarged surface area and thin thickness. The 2D NS-titanate and NS-hexaniobate produced by the exfoliation protocol

from their respective parent crystals are distinct due to their surface topography and exceptionally high anisotropy. Therefore, these materials can be useful for coupling with narrow band gap $BiVO_4$. Specifically, NS-titanate and NS-hexaniobate are selected due to their highly anisotropic 2D morphology, suitable band positions for reducing hydroxide ions and oxidation of H_2O, and high chemical stability. On the other hand, $BiVO_4$ is selected due to its narrow band gap, high photostability, low photo corrosion, and low environmental toxicity.

In this context, NS-titanate and NS-hexaniobate hybridized with $BiVO_4$ are proposed for photocatalytic dye degradation. The chemical bath deposition (CBD) and SILAR methods are the best choices for coating $BiVO_4$ on NS-titanate and NS-hexaniobate. Until now, no previous work exists on NS-titanate and NS-hexaniobate hybridized with $BiVO_4$ for photocatalytic application. The present work to hybridize $BiVO_4$ with NS-titanate and NS-hexaniobate can lead to 1) improved photoactivity as a result of strong electronic coupling between the hybridized species, 2) enlarged surface area caused by the development of a mesoporous house of cards type structure and 3) tunable chemical composition to achieve desired physicochemical features.

Thus, the present work focuses on the chemically synthesized nanohybrids of $BiVO_4$ with 2D NS-titanate and NS-hexaniobate for photocatalytic dye degradation. The NS-titanate-$BiVO_4$ and NS-hexaniobate-$BiVO_4$ nanohybridthin films are synthesized by the coating of $BiVO_4$ on NS-titanate and NS-hexaniobate, respectively. Initially, NS-titanate and NS-hexaniobate thin films are deposited on conducting substrates via the EPD method. Over electrophoretically deposited NS-titanate and NS-hexaniobate thin films, the narrow band gap $BiVO_4$ is deposited by both CBD and SILAR methods.

Various physicochemical characterization techniques are applied to investigate the different properties of synthesized nanohybrid thin films. The crystal structure (phase identification) of the pristine $BiVO_4$, NS-titanate, NS-hexaniobate and their nanohybrid thin films is analyzed using the X-ray diffraction (XRD) technique. The optical properties of pristine and nanohybrid material thin films are investigated with Ultraviolet-visible diffuse reflectance spectroscopy (UV-vis DRS). The chemical bonding nature of the present nanohybrid thin films is examined with Fourier-transform infrared (FTIR) spectroscopy and Micro-Raman spectroscopy analysis. The surface morphologies of pristine $BiVO_4$, NS-titanate/NS-hexaniobate and respective nanohybrid

thin films are scrutinized with Field emission scanning electron microscopy (FESEM). The elemental composition and distribution of the elements present in nanohybrid thin films are examined with energy-dispersive X-ray spectroscopy (EDS) and elemental mapping analysis. The chemical oxidation states of the elements present on the surface of $BiVO_4$ and its nanohybrid thin films are probed with the X-ray photoelectron spectroscopy (XPS) technique.

The photoactivity of the pristine NS-titanate, NS-hexaniobate, $BiVO_4$ thin films and all nanohybrid thin films for photodegradation of dyes is evaluated with UV-vis absorption spectroscopy analysis. MB and Rh-B are used as target dyes for the decomposition. The photocatalytic performance of synthesized pristine and nanohybrid thin films is measured with a percentage degradation study using the formula,

$$\text{dye degradation } (\%) = \frac{C_0 - C_t}{C_0} \times 100 \quad (1.12)$$

where C_0 denotes the initial absorption and C_t denotes the absorption at time t.

A pseudo-first-order kinetic model is used to explore dye degradation dynamics further. The following equation describes a pseudo-first-order reaction:

$$q_t = (1 - e^{-k_1 t}) \quad (1.13)$$

where k_1 and t are rate constant and time, q_e denotes adsorption at equilibrium and q_t is adsorption at time t.

Furthermore, a recyclability study is conducted to check the industrial usefulness of nanohybrid thin films.

1.7 References:

1. E. Forgacs, T. Cserhati, G. Oros, Removal of synthetic dyes from wastewaters: A review, Environ. Int. 30 (2004) 953-971.
2. V. Zaffalon, Climate change, carbon mitigation and textiles, Text. World 160 (2010) 34-35.
3. R. Kant, Textile dyeing industry an environmental hazard, Nat. Sci. 4 (2012) 22-26.
4. S. Benkhaya, S. M'rabet, A.E. Harfi, A review on classifications, recent synthesis and applications of textile dyes, Inorg. Chem. Commun. 115 (2020) 107891.
5. V.C. Santos-Ebinuma, I.C. Roberto, M.F.S. Teixeira, A.P. Jr, Improving of red colorants production by a new Penicillium purpurogenum strain in submerged culture and the effect of different parameters in their stability, Biotechnol. Prog. 29 (2013) 778-785.
6. K. Ahmouda, M. Boudiaf, B. Benhaoua, A novel study on the preferential attachment of chromophore and auxochrome groups in azo dye adsorption on different greenly synthesized magnetite nanoparticles: Investigation of the influence of the mediating plant extract's acidity, Nanoscale Adv. 4 (2022) 3250-3271.

7. S. Kaur, S. Rani, R. Mahajan, M. Asif, V.K. Gupta, Synthesis and adsorption properties of mesoporous material for the removal of dye safranin: Kinetics, equilibrium and thermodynamics, J. Ind. Eng. Chem. 22 (2015) 19-27.
8. Gregory, P. (1990). Classification of dyes by chemical structure. In D.R. Waring, & G. Hallas (Eds.), The chemistry and application of dyes: Topics in applied chemistry (pp. 17-47). Boston, MA: Springer.
9. N.R.J. Hynes, J.S. Kumar, H. Kamyab, J.A.J. Sujana, O.A. Al-Khashman, Y. Kuslu, A. Ene, B.S. Kumar, Modern enabling techniques and adsorbents-based dye removal with sustainability concerns in textile industrial sector: A comprehensive review, J. Clean. Prod. 272 (2020) 122636.
10. I. Khan, K. Saeed, I. Zekker, B. Zhang, A.H. Hendi, A. Ahmad, S. Ahmad, N. Zada, H. Ahmad, L.A. Shah, Review on methylene blue: Its properties, uses, toxicity and photodegradation, Water 14 (2022) 242.
11. A.K. Al-Buriahi, A.A. Al-Gheethi, P.S. Kumar, R.M.S.R. Mohamed, H. Yusof, A.F. Alshalif, N.A. Khalifa, Elimination of rhodamine B from textile wastewater using nanoparticle photocatalysts: A review for sustainable approaches, Chemosphere 287 (2022) 132162.
12. S. Rodriguez-Couto, J.F. Osma, J.L. Toca-Herrera, Removal of synthetic dyes by an eco-friendly strategy, Eng. Life Sci. 9 (2009) 116-123.
13. M. Solis, A. Solis, H.I. Perez, N. Manjarrez, M. Flores, Microbial discoloration of azo dyes: A review, Process Biochem. 47 (2012) 1723-1748.
14. A. Maleki, U. Sadeghi, H. Daraei, B. Hayati, F. Najafi, G. McKay, R. Rezaee, Amine functionalized multi-walled carbon nanotubes: Single and binary systems for high-capacity dye removal, Chem. Eng. J. 313 (2017) 826-835.
15. G. Zeng, Z. Ye, Y. He, X. Yang, J. Ma, H. Shi, Z. Feng, Application of dopamine-modified halloysite nanotubes/PVDF blend membranes for direct dyes removal from wastewater, Chem. Eng. J. 323 (2017) 572-583.
16. J.T. Chacko, S. Kalidass, Enzymatic degradation of azo dyes: A review, Int. J. Env. Sci. 1 (2011) 1250-1260.
17. A. Ahmad, S.H. Mohd-Setapar, S.C. Chuo, A. Khatoon, W.A. Wani, R. Kumar, M. Rafatullah, Recent advances in new generation dye removal technologies: Novel search of approaches to reprocess wastewater, RSC Adv. 5 (2015) 30801-30818.
18. M. Joshi, R. Bansal, R. Purwar, Colour removal from textile effluents, Indian J. Fibre Text. Res. 29 (2004) 239-259.
19. L. Tang, J. Yu, Y. Pang, G. Zeng, Y. Deng, J. Wang, X. Ren, S. Ye, B. Peng, H. Feng, Sustainable efficient adsorbent: Alkali-acid modified magnetic biochar derived from sewage sludge for aqueous organic contaminant removal, Chem. Eng. J. 336 (2018) 160-169.
20. V.K. Gupta, A. Suhas, Application of low-cost adsorbents for dye removal: A review, J. Environ. Manage. 90 (2009) 2313-2342.
21. S.A. Avlonitis, I. Poulios, D. Sotiriou, M. Pappas, K. Moutesidis, Simulated cotton dye effluents treatment and reuse by nanofiltration, Desalination 221 (2008) 259-267.
22. F.I. Hai, K. Yamamoto, K. Fukushi, Hybrid treatment systems for dye wastewater, Crit. Rev. Env. Sci. Technol. 37 (2007) 315-377.
23. J.L. Wang, L.J. Xu, Advanced oxidation process for wastewater treatment: Formation of hydroxyl radical and application, Crit. Rev. Env. Sci. Technol. 42 (2012) 251-325.

24. M.M. Mahlambi, C.J. Ngila, B.B. Mamba, Recent developments in environmental photocatalytic degradation of organic pollutants: The case of titanium dioxide nanoparticles- A review, J. Nanomater. 2015 (2015) 790173.
25. D. Ravelli, D. Dondi, M. Fagnoni, A. Albini, Photocatalysis - A multi-faced concept for green chemistry, Chem. Soc. Rev. 38 (2009) 1999-2011.
26. C. Lavanya, R. Dhankar, S. Chhikaral, S. Sheoran, Degradation of toxic dyes: A review, Int. J. Curr. Microbiol. App. Sci. 3 (2014) 189-199.
27. R.L. Singh, P.K. Singh, R.P. Singh, Enzymatic decolorization and degradation of azo dyes: A review, Int Biodeterior. Biodegradation 104 (2015) 21-31.
28. M.K.H.M. Nazri, N. Sapawe, A short review on photocatalytic toward dye degradation, Mater. Today: Proc. 31 (2020) A42-A47.
29. J.H. Kim, J.S. Lee, Elaborately modified $BiVO_4$ photoanodes for solar water splitting, Adv. Mater. 31 (2019) 1806938.
30. S. Chen, D. Huang, P. Xu, X. Gong, W. Xue, L. Lei, R. Deng, J. Li, Z. Li, Facet-engineered surface and interface design of monoclinic scheelite bismuth vanadate for enhanced photocatalytic performance, ACS Catal. 10 (2020) 1024-1059.
31. H.L. Tan, R. Amal, Y.H. Ng, Alternative strategies in improving the photocatalytic and photoelectrochemical activities of visible-light-driven $BiVO_4$: A review, J. Mater. Chem. A 5 (2017) 16498-16521.
32. T.D. Nguyen, V.H. Nguyen, S. Nanda, D.N. Vo, V.H. Nguyen, T.V. Tran, L.X. Nong, T.T. Nguyen, L.G. Bach, B. Abdullah, S.S. Hong, T.V. Nguyen, $BiVO_4$ photocatalysis design and applications to oxygen production and degradation of organic compounds: A review, Environ. Chem. Lett. 18 (2020) 1779-1801.
33. T.W. Kim, S.J. Hwang, Y. Park, W. Choi, J.H. Choy, Chemical bonding character and physicochemical properties of mesoporous zinc oxide-layered titanate nanocomposites, J. Phys. Chem. C 111 (2007) 1658-1664.
34. J.L. Gunjakar, I.Y. Kim, J.M. Lee, Y.K. Jo, S.J. Hwang, Exploration of nanostructured functional materials based on hybridization of inorganic 2D nanosheets, J. Phys. Chem. C 118 (2014) 3847-3863.
35. Y. Yao, G.S. Chaubey, J.B. Wiley, Fabrication of nano-peapods: Scrolling of niobate nanosheets for magnetic nanoparticle chain encapsulation, J. Am. Chem. Soc. 134 (2012) 2450-2452.
36. T.W. Kim, H.W. Ha, M.J. Paek, S.H. Hyun, I.H. Baek, J.H. Choy, S.J. Hwang, Mesoporous iron oxide-layered titanate nanohybrids: Soft-chemical synthesis, characterization, and photocatalyst application, J. Phys. Chem. C 112 (2008) 14853-14862.
37. J.L Gunjakar, T.W. Kim, I.Y. Kim, J.M. Lee, S.J. Hwang, Highly efficient visible-light-induced O_2 generation by self-assembled nanohybrids of inorganic nanosheets and polyoxometalate nanoclusters, Sci. Rep. 3 (2013) 2080.
38. J.L Gunjakar, T.W. Kim, H.N. Kim, I.Y. Kim, S.J. Hwang, Mesoporous layer-by-layer ordered nanohybrids of layered double hydroxide and layered metal oxide: Highly active visible light photocatalysts with improved chemical stability, J. Am. Chem. Soc. 133 (2011) 14998-15007.
39. G. Odling, N. Robertson, $BiVO_4$-TiO_2 composite photocatalysts for dye degradation formed using the SILAR method, Chem. Phys. Chem. 19 (2016) 2872-2880.
40. A. Ajmal, I. Majeed, R. Malik, H. Idriss, M. Nadeem, Principles and mechanisms of photocatalytic dye degradation on TiO_2 based photocatalysts: A comparative overview, RSC Adv. 4 (2014) 37003-37026.
41. G.S. Kamble, T.S. Natarajan, S.S. Patil, M. Thomas, R.K. Chougale, P.D. Sanadi, U.S. Siddharth, Y.-C. Ling, $BiVO_4$ as a sustainable and emerging photocatalyst:

Synthesis methodologies, engineering properties, and its volatile organic compounds degradation efficiency, Nanomaterials 13 (2023) 1528.
42. J. Mao, Q. Wu, F. Tao, W. Xu, T. Hong, Y. Dong, Facile fabrication of porous $BiVO_4$ hollow spheres with improved visible-light photocatalytic properties, RSC Adv. 10 (2020) 6395-6404.
43. S.S. Han, J.Y. Park, H.S. Hwang, H.R. Choe, K.M. Nam, E.J. Cho, Facile synthesis of $BiVO_4$ for visible-light-induced C-C bond cleavage of alkenes to generate carbonyls, Chem. Sus. Chem. 12 (2019) 3018-3022.
44. Y. Qi, M. Wang, Y. Zhang, T. Zhu, Effect of calcination temperature on the structure and photocatalytic performance of $BiVO_4$ prepared via an improved solution combustion method, Micro Nano Lett. 13 (2018) 1017-1020.
45. M. Arumugam, M.Y. Choi, Effect of operational parameters on the degradation of methylene blue using visible light active $BiVO_4$ photocatalyst, Bull. Korean Chem. Soc. 41 (2020) 304-309.
46. J.S. Roy, S. Morency, Y. Messaddeq, Ultrafast cleaning of methylene blue contaminated water accelerating photocatalytic reaction rate of the $BiVO_4$ nanoflakes under highly intense sunlight irradiation, J. Photochem. Photobiol. 7 (2021) 100037.
47. S. Tang, Z. Wang, D. Yuan, Y. Zhang, J. Qi, Y. Rao, G. Lu, B. Li, K. Wang, K. Yin, Enhanced photocatalytic performance of $BiVO_4$ for degradation of methylene blue under LED visible light irradiation assisted by peroxymonosulfate, Int. J. Electrochem. Sci. 15 (2020) 2470-2480.
48. Y.T. Niu, G.B. Guo, Synthesis, characterization and photocatalytic activities of $BiVO_4$ by carbon adsorption hydrothermal method, Z. Anorg. Allg. Chem. 646 (2020) 1661-1665.
49. M.M. Sajid, N. Amin, N.A. Shad, S.B. Khan, Y. Javed, Z. Zhang, Hydrothermal fabrication of monoclinic bismuth vanadate (m-$BiVO_4$) nanoparticles for photocatalytic degradation of toxic organic dyes, Mater. Sci. Eng.: B 242 (2019) 83-89.
50. T.S. Dabodiya, P. Selvarasu, A.V. Murugan, Tetragonal to monoclinic crystalline phases change of $BiVO_4$ via microwave-hydrothermal reaction: In correlation with visible-light-driven photocatalytic performance, Inorg. Chem. 58 (2019) 5096-5110.
51. Y.M. Hunge, A. Uchida, Y. Tominaga, Y. Fujii, A.A. Yadav, S.W. Kang, N. Suzuki, I. Shitanda, T. Kondo, M. Itagaki, M. Yuasa, S. Gosavi, A. Fujishima, C. Terashima, Visible light-assisted photocatalysis using spherical-shaped $BiVO_4$ photocatalyst, Catalysts 11 (2021) 460.
52. F. Chen, X. Zhang, Y. Tang, X. Wang, K. Shu, Facile and rapid synthesis of a novel spindle-like heterojunction $BiVO_4$ showing enhanced visible-light-driven photoactivity, RSC Adv. 10 (2020) 5234-5240.
53. S. Song, H. Yang, C. Zhou, J. Cheng, Z. Jiang, Z. Lu, J. Miao, Underwater superoleophobic mesh based on $BiVO_4$ nanoparticles with sunlight-driven self-cleaning property for oil/water separation, Chem. Eng. J. 320 (2017) 342-351.
54. M. Ganeshbabu, N. Kannan, P.S. Venkatesh, G. Paulraj, K. Jeganathan, D.M. Ali, Synthesis and characterization of $BiVO_4$ nanoparticles for environmental applications, RSC Adv. 10 (2020) 18315-18322.
55. M. Chahkandi, M. Zargazi, New water based EPD thin $BiVO_4$ film: Effective photocatalytic degradation of amoxicillin antibiotic, J. Hazard. Mater. 389 (2020) 121850.

56. C. Yanga, C. Qin, J. Zhong, J. Li, S. Huang, Q. Wang, L. Ma, Photocatalytic enhancement mechanism insight for $BiVO_4$ induced by plasma treatment under different atmospheres, J. Alloys Compd. 890 (2022) 161883.
57. G. Zhao, X. Zheng, J. Qian, M. Wang, X. Cao, H. Teng, W. Liu, 1D rodlike m-$BiVO_4$ mesocrystals: Preparation, formation mechanism and photocatalytic performance, Chemistry Select 4 (2019) 6930-6944.
58. R. Venkatesan, S. Velumani, K. Ordon, M. Janusik, G. Corbel, A. Kassiba, Nanostructured bismuth vanadate ($BiVO_4$) thin films for efficient visible light photocatalysis, Mater. Chem. Phys. 205 (2018) 325-333.
59. D. Arivukarasan, C.R. Dhas, R. Venkatesh, S.E. Monica, A.J. Josephine, K.C. Gnanamalar, B. Subramanian, Template-free and cost-effective nebulizer spray-coated $BiVO_4$ nanostructured thin films for photocatalytic applications, Appl. Phys. A 126 (2020) 86.
60. C.R. Dhas, D. Arivukarasan, R. Venkatesh, A.J. Josephine, K.C. Malara, S.E. Monica, B. Subramanian, Influence of precursor aging time period on physical and photocatalytic properties of nebulizer spray coated $BiVO_4$ thin films, Solid State Sci. 92 (2019) 36-45.
61. C. Ravidhas, D. Arivukarasan, R. Venkatesh, E.S. Suresh, B. Anitha, A.J. Josephine, A.A. Raj, K.S. Ravichandran, C. Gopalakrishnan, C. Sanjeeviraja, Substrate temperature induced (040) growth facets of nebulizer sprayed $BiVO_4$ thin films for effective photodegradation of rhodamine B, Cryst. Res. Technol. 54 (2019) 1700257.
62. G.S. Kamble, Y.C. Ling, Solvothermal synthesis of facet-dependent $BiVO_4$ photocatalyst with enhanced visible-light-driven photocatalytic degradation of organic pollutant: Assessment of toxicity by zebrafish embryo, Sci. Rep. 10 (2020) 12993.
63. Y. Zhang, H. Gong, Y. Zhang, K. Liu, H. Cao, H. Yan, J. Zhu, The controllably synthesized octadecahedron-$BiVO_4$ with exposed {111} facets, Eur. J. Inorg. Chem. 2017 (2017) 2990-2997.
64. K. Pingmuang, J. Chen, A. Nattestad, W. Kangwansupamonkon, S. Phanichphant, Photocatalytic degradation of methylene blue by innovative $BiVO_4/TiO_2$ composite films under visible light irradiation, Int. Res. J. Environ. 3 (2014) 69-76.
65. Z. Guo, P. Li, H. Che, G. Wang, C. Wu, X. Zhang, J. Mu, One-dimensional spindle-like $BiVO_4/TiO_2$ nanofibers heterojunction nanocomposites with enhanced visible light photocatalytic activity, Ceram. Int. 42 (2016) 4517-4525.
66. X. Zhu, F. Zhang, M. Wang, X. Gao, Y. Luo, J. Xue, Y. Zhang, J. Ding, S. Sun, J. Bao, C. Gao, A shuriken-shaped m-$BiVO_4$/{001}-TiO_2 heterojunction: Synthesis, structure and enhanced visible light photocatalytic activity, Appl. Catal. A: Gen. 521 (2016) 42-49.
67. M.F.R Samsudin, A. Mahmood, S. Sufian, Enhanced photocatalytic degradation of wastewater over rGO-$TiO_2/BiVO_4$ photocatalyst under solar light irradiation, J. Mol. Liq. 268 (2018) 26-36.
68. M. Zalfani, Z.-Y. Hu, W.-B. Yu, M. Mahdouani, R. Bourguiga, M. Wu, Y. Li, G.V. Tendeloo, Y. Djouede, B.-L. Su, $BiVO_4$/3DOM TiO_2 nanocomposites: Effect of $BiVO_4$ as highly efficient visible light sensitizer for highly improved visible light photocatalytic activity in the degradation of dye pollutants, Appl. Catal. B: Environ. 205 (2017) 121-132.
69. H. Li, H. Yu, X. Quan, S. Chen, H. Zhao, Improved photocatalytic performance of heterojunction by controlling the contact facet: High electron transfer capacity

between TiO_2 and the {110} facet of $BiVO_4$ caused by suitable energy band alignment, Adv. Funct. Mater. 25 (2015) 3074-3080.
70. K.T. Drisya, M. Solis-Lopez, J.J. Rios-Ramirez, J.C. Duran-Alvarez, A. Rousseau, S. Velumani, R. Asomoza, A. Kassiba, A. Jantrania, H. Castaneda, Electronic and optical competence of TiO_2/$BiVO_4$ nanocomposites in the photocatalytic processes, Sci. Rep. 10 (2020) 13507.
71. B. Cao, J. Peng, Y. Xu, Simulated sunlight-driven degradation of rhodamine B by porous peanut-like TiO_2/$BiVO_4$ composite, J. Clust. Sci. 24 (2013) 771-785.
72. M.F.R. Samsudin, S. Sufian, R. Bashiri, N.M. Mohamed, L.T. Siang, R.M. Ramli, Optimization of photodegradation of methylene blue over modified TiO_2/$BiVO_4$ photocatalysts: Effects of total TiO_2 loading and different type of co-catalyst, Mater. Today: Proc. 5 (2018) 21710-21717.
73. S. Mansour, R. Akkari, S.B. Chaabene, M.S. Zina, Effect of surface site defects on photocatalytic properties of $BiVO_4$/TiO_2 heterojunction for enhanced methylene blue degradation, Adv. Mater. Sci. Eng. 2020 (2020) 6505301.
74. O. Monfort, T. Roch, M. Gregor, L. Satrapinskyy, D. Raptis, P. Lianos, G. Plesch, Photooxidative properties of various $BiVO_4$/TiO_2 layered composite films and study of their photocatalytic mechanism in pollutant degradation, J. Environ. Chem. Eng. 5 (2017) 5143-5149.
75. R. Rahimi, S. Zargari, M.M. Moghaddas, $BiVO_4$-TiO_2 nanocomposite: Synthesis and photocatalytic investigation, Adv. Mat. Res. 702 (2013) 172-175.
76. L. Gao, J. Du, T. Ma, Photocatalytic activity enhanced by 1D TiO_2 nanobelts and 2D $BiVO_4$ nanosheets heterostructures, Micro Nano Lett. 12 (2017) 580-584.
77. M.J. Madiabu, J. Gunlazuardi, Preparation and characterization of TiO_2/$BiVO_4$ composite: Can this photocatalyst, under visible light, be able to eliminate rhodamine B from water and why?, AIP Conf. Proc. 2023 (2018) 020079.
78. M. Wang, W. Li, Y. Zhao, S. Gu, F. Wang, H. Li, X. Liu, C. Ren, Synthesis of $BiVO_4$-TiO_2-$BiVO_4$ three-layer composite photocatalyst: Effect of layered heterojunction structure on the enhancement of photocatalytic activity, RSC Adv. 6 (2016) 75482-75490.
79. Q. Yu, G. Li, F. Zhang, Enhanced photocatalytic activity and charge transfer of TiO_2/$BiVO_4$ nanostructured composite, Catal. Sci. Technol. 9 (2019) 5333-5338.
80. C. Wenquan, W. Huan, L. Yinghua, H. Bingxu, L. Li, H. Jinshan, Microwave-assisted synthesis of Ag@AgBr-intercalated $K_4Nb_6O_{17}$ composite and enhanced photocatalytic degradation of Rhodamine B under visible light, Int. J. Chem. Eng. 230 (2013) 10-18.
81. L. Yinghua, S. Meiyi, C. Wenquan, L. Li, M.J. Joanne, Photocatalytic degradation of rhodamine B by CdS-loaded $K_4Nb_6O_{17}$ nanocomposites prepared via reverse microemulsion, Mol. Catal. A Chem. 370 (2013) 87-94.
82. C. Wenquan, S. Meiyi, L. Li, L. Yinghua, R. Dipak, Enhanced visible-light-responsive photocatalytic property of PbS-sensitized $K_4Nb_6O_{17}$ nanocomposite photocatalysts, Appl. Surf. Sci. 276 (2013) 823-831.

CHAPTER-2

Theoretical Background of Synthesis Methods and Characterization Techniques

CHAPTER-2

Theoretical Background of Synthesis Methods and Characterization Techniques

2.1 Introduction:

The most critical challenge in the 21st century is to battle against ever-increasing environmental pollution. Dyes, pesticides, surfactants, antibiotics, chloro-organics, etc., are major effluents responsible for water pollution. Heterogeneous semiconductor photocatalysis has been extensively studied for the degradation of organic molecules. It is a cost-effective and promising approach for degrading many organic pollutants by harvesting solar energy [1]. Even after extensive research, most inorganic photocatalysts are unsuitable for visible-light-driven photocatalysis due to their wide band gap energy, low photostability and inappropriate band positions for proton reduction and water oxidation. Various types of nanostructure photocatalysts have been developed to overcome the limitations of these materials. Moreover, attempts are made to develop hybrid photocatalysts to reduce electron-hole recombination via strong electronic coupling between hybridized species [2].

Though many low-dimensional nanostructured semiconducting materials are being developed as photocatalysts, 2D nanostructured inorganic solids attract special research attention due to their excellent features. These wide band gap 2D MONs can be useful for coupling with narrow band gap semiconductors. MONs are the most suited alternatives for developing nanohybrid photocatalysts with distinctive physicochemical features owing to their enlarged surface area and thin thickness [3]. Various narrow band gap semiconductors were coated on MONs using hydrothermal, solvothermal, ultrasonication, CBD, SILAR methods. The proposed work to hybridize $BiVO_4$ with NS-titanate and NS-hexaniobate will lead to 1) improved photocatalytic activity payable to the effective electronic coupling between the hybridized species, 2) enlarged surface area by the formation of highly porous house-of-card type structure and 3) tunable chemical composition to achieve desire photo-physicochemical properties.

The theoretical background of several synthesis methods used to synthesize pristine $BiVO_4$, MONs (NS-titanate and NS-hexaniobate) and nanohybrids of $BiVO_4$ with MONs (NS-titanate-$BiVO_4$ and NS-hexaniobate-$BiVO_4$) is described in this chapter. It also includes the theoretical background of numerous characterization techniques (structural, compositional, morphological, optical, etc.) used to investigate the physicochemical characteristics of nanohybrid thin films.

2.2 Thin film deposition methods:

A layer of material having a thickness of several nanometers to a few micrometers is referred to as a thin film. Deposition of thin film is nothing but the process of thin film formation over any desired surface. The synthesis process significantly influences the properties of thin films; hence, choosing the proper deposition method can tune their different physicochemical properties [4]. The schematic classifying several thin film deposition methods is represented in **Fig. 2.1**. Depending upon the synthesis approach, thin film depositions are broadly classified into chemical and physical methods [5]. The chemical deposition methods are again classified into gas-phase and liquid-phase methods [6]. In liquid-phase chemical methods, the thin films are coated on the desired substrates from the chemical solutions. The liquid phase chemical methods include CBD, electrodeposition, EPD, spray pyrolysis, SILAR, hydrothermal, sol-gel process, spin coating, reflux, dip coating, etc. On the other hand, vacuum evaporation and sputtering are the two main types of physical deposition methods. The solution phase chemical methods have various advantages over physical methods, such as the simplicity of deposition, cost-effectiveness and suitability for large-area coating over various substrates [5,6]. Hence, chemical methods are mostly preferred to synthesize nanostructured materials for versatile applications.

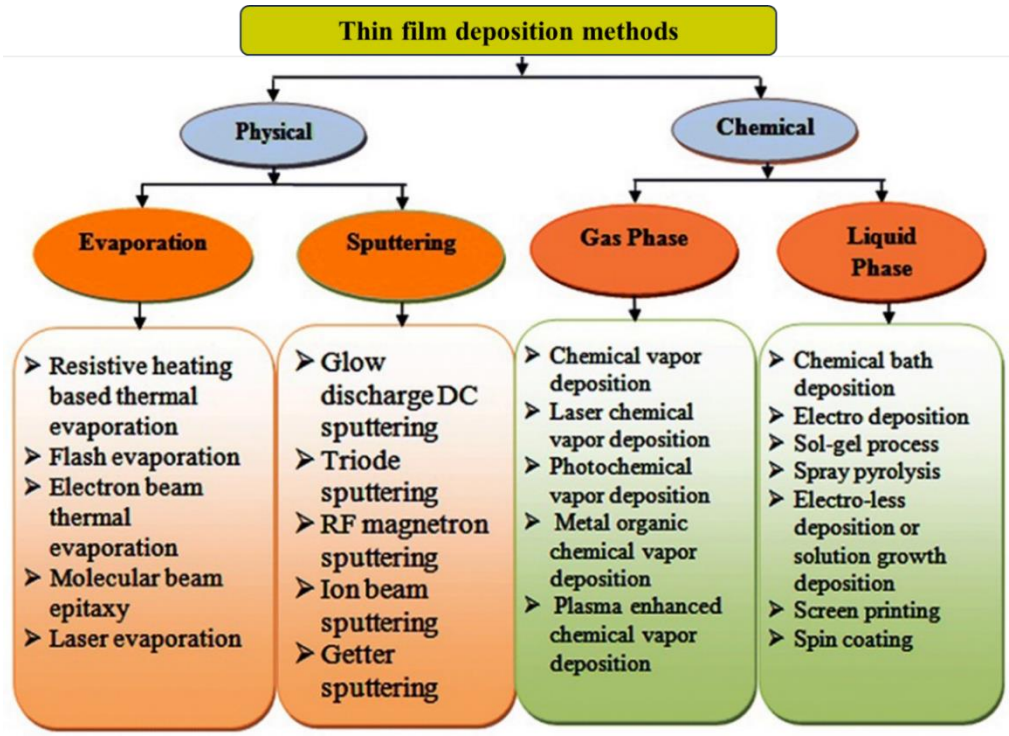

Fig. 2.1: Schematic classifying several thin film deposition methods [7].

2.2.1 CBD method:

All the chemical synthesis methods utilize the thermodynamic equilibrium and kinetic approaches for thin film deposition. Among the several chemical deposition techniques available, CBD is one of the most significant methods for depositing semiconductor thin films on various substrates. CBD is based on the principle of the thermodynamic approach in which film formation takes place via supersaturation, nucleation and succeeding growth processes. In CBD, the nanostructured material from a chemical solution is coated on the surface of the desired substrate. CBD describes depositions from solutions (often aqueous) where the deposit is chemically produced and deposited in the same bath [8].

Among many methods for thin film deposition, CBD has the potential for low-cost fabrication. CBD is an easy and convenient method for coating large-area thin films on various substrates, even at room temperature. There is no vacuum requirement at any deposition stage. It enables pinhole-free deposition with superior grain structure and better crystallite orientation. The stoichiometry of deposits can be precisely controlled because ions are the fundamental building blocks rather than atoms. Hazardous or pyrolyzed gases or organometallic solvents are not released during CBD [9].

(a) CBD: Basic principle:

The thin film deposition via the CBD method depends on the principle of controlled precipitation of the required material over the surface of the desired substrate. Generally, the deposition of thin films via CBD follows the formation of solid phase from a solution, which involves two steps: nucleation and particle growth [10,11]. In CBD, supersaturation or precipitate formation occurs when the ionic product (IP) exceeds the solubility product (SP) [10]. When merely solvable salt (AB) is added to the solvent, it results in a saturated solution with ions (A^+ and B^-) and an undissolved solid (AB). The expression for the equilibrium among the solid phase and the ions in the solution is,

$$AB_{(S)} \rightarrow A^+ + B^- \tag{2.1}$$

By the law of mass action to the equilibrium state,

$$K = \frac{C_A^+ C_B^-}{C_{AB}(S)} \tag{2.2}$$

Where $C_A{}^+$ is the concentration of A^+ ions, $C_B{}^-$ is the concentration of B^- ions and C_{AB} is the concentration of AB compound in solution.

The concentration of the pure solid phase is a constant, which is denoted as C_{AB} (S) = constant = K' then,

$$K = \frac{C_A^+ C_B^-}{K'} \quad (2.3)$$

$$KK' = C_A^+ C_B^- \quad (2.4)$$

In this equation, both K and K' are constants, and the product of KK' is constant, represented by K_s. Therefore, the above equation becomes,

$$K_s = C_A^+ C_B^- \quad (2.5)$$

where K_s and $C_A^+C_B^-$ represent SP and IP, respectively. When IP of the compound is the same as the SP of ions in solution, saturation occurs. For precipitation to occur, IP should exceed SP (IP/SP = S > 1), and the solution becomes supersaturated, which results in the creation of nuclei both on the substrate surface (heterogeneous) and in the solution (homogeneous) [9].

During the CBD experiment, a substrate is immersed in a chemical bath containing cations and anions. When the supersaturated state is reached, a heterogeneous reaction occurs, and these ions form nuclei on the surface substrate. Without supersaturation, thin film deposition by the CBD method is impossible.

(b) CBD: Preparative parameters:

The well-adherent and uniform thin film formation relies on the rate of chemical reactions. In CBD, the deposition rate and film thickness depend upon the degree of supersaturation and the number of nucleation centers produced. The growth kinetics mainly depend on the number of ions, their movement, nucleation and growth processes. The impact of different preparative parameters on the growth mechanism of CBD is explained below:

- *Precursor solution pH**:***

The supersaturation condition affects both the deposition rate and the reaction rate. The metal ion complex gets more stable as the pH of the solution rises. Alternatively, the concentration of metal ions reduces with increased pH, leading to a sluggish reaction rate and, hence, a slower film formation rate.

- *Complexing agent:*

The role of the complexing agent is to avoid bulk precipitation of the material by decreasing the concentration of free metal ions by complex formation. As the concentration of the complexing agent increases, the free metal ion concentration

reduces. Subsequently, reaction rate and bulk precipitation decrease, which affects the particle size of the deposited material.

- *Temperature:*

The rate of dissociation of the complex depends on the bath temperature. Higher temperatures cause the dissociation of the complex to occur more quickly, which speeds up deposition. The terminal film thickness depends on the degree of supersaturation and bath temperature. At higher temperatures, the thermal dissociation rate of complexes is higher, hence achieving higher film thickness. It also affects other properties, such as less adherence due to powdery film formation.

- *Nature of substrate:*

The nature of the substrate significantly influences film adhesion and reaction kinetics. The availability of plenty of nucleation centers on the substrate surface is crucial for the initial nucleation and subsequent growth of the film. Film growth is also significantly influenced by substrate lattice parameters. Single crystal film formation can be formed when the substrate lattice and the deposition material have similar lattices.

2.2.2 SILAR method:

Film formation in CBD depends on the principle of supersaturation. Film formation in CBD occurs when the IP is larger than the SP, resulting in unnecessary bulk precipitation and material wastage due to homogeneous precipitation. To address this drawback, CBD is modified to the SILAR method. In the SILAR method, thin films are produced by dipping the substrate in cationic and anionic precursors placed apart, followed by rinsing with double-distilled water (DDW). The rate of homogeneous bulk precipitation is controlled in SILAR due to the adsorption and the reaction of the ions from the solutions and consecutive rinsing. Hence, the key factor in the SILAR method is the adsorption of ions on the substrate surface. In the SILAR method, pre-adsorbed cations react with newly adsorbed anions to produce films [12].

Among the liquid-phase chemical deposition methods, SILAR is one of the renowned low-temperature processes for coating semiconductor thin films on various substrates. SILAR is a facile, energy-saving, inexpensive chemical method for coating uniform and well-adherent large-area thin films. Doping elements in different proportions is possible with SILAR by adding it to a precursor solution. The rate of deposition and film thickness can be precisely controlled over an extensive span by fine tuning of preparative parameters [12].

(a) SILAR: Basic principle:

Deposition of the thin film via the SILAR method relies on the reaction of the preadsorbed cations on the substrate surface with freshly adsorbed anions from the solutions followed by consecutive rinsing in DDW after each immersion. The consecutive reaction steps lead to film formation on the substrate surface [13]. Notably, the issue of bulk precipitation is avoided with the rinsing step; thus, there is a heterogeneous reaction between the solvated ions in the solution and the solid phase. The SILAR method aims to deposit thin films of water-insoluble compounds of the KpAa type through a heterogeneous chemical reaction at the interface of the solid solution between adsorbed cations, $p\mathrm{K_a}^{+}$ and anions, $a\mathrm{K_p}^{-}$, as represented in the following reaction,

$$\left(pK_{aq}^{a+} + qX_{aq}^{b-}\right) + \left(b'Y_{aq}^{q'+} + aA^{p-}\right) \rightarrow K_pAa_s \downarrow + qX_{aq}^{b-} + b'Y_{aq}^{q'} \quad (2.6)$$

with ap = bq = b'q'

where K: cation (Co^{2+}, Mn^{2+}, Ni^{2+}, etc.), p: number of cations, a: numerical value of charge on cation, X: ion in cationic precursors with a negative charge (X = NO_3^{2-}, Cl^{-}, SO_4^{2-}, etc.), q: number of 'X' in cationic precursors and b: numerical value of charges on 'X'. Also, b: number of 'Y' in the anionic solutions, q': numerical value of charge on 'Y', Y: ion which is attached to chalcogen ion, A: anion (OH^{-}, O^{-}, Te, S and Se) and a: number of anions.

In detail, the film formation in SILAR takes place by following four steps: a) adsorption, b) 1st rinsing, c) reaction and d) 2nd rinsing [13]. In the experimental setup, 1st and 3rd beakers consist of cationic and anionic precursors, respectively, whereas 2nd and 4th beakers contain DDW for rinsing. During the deposition process, the substrate is consecutively immersed in each beaker, starting from 1st beaker.

a) Adsorption:

The first step of the SILAR method is the adsorption of cations. Cations are adsorbed on the substrate surface when it is immersed in cationic solution, resulting in the creation of a Helmholtz electric double layer. The inner (positively charged) layer is made up of cations, and the outer (negatively charged) layer of this layer comprises their counter ions.

b) 1st rinsing:

Rinsing prevents homogenous precipitation caused by an instantaneous interaction between previously adsorbed cations and incoming anions. This process

removes excess and loosely bound cations from the diffusion layer, creating a saturated electrical double layer.

c) Reaction:

Here, the system is exposed to the anions from the anionic solution. Pre-adsorbed cations react with freshly adsorbed anions, forming a solid compound on the substrate surface.

d) 2nd rinsing:

Finally, the excessive and unreacted species and any reaction by-products are entirely removed from the substrate at 2nd rinsing. In this stage, a monolayer of the desired material gets deposited on the substrate surface.

A single SILAR deposition cycle is completed by successively following these four steps. The film thickness is controlled by varying deposition cycles. The superiority of deposited film depends on the time required for adsorption, reaction and rinsing.

(b) SILAR: Preparative parameters:

In the SILAR method, the growth rate of the deposited thin film is based on precursor solution concentration, pH values, adsorption, reaction, rinsing times, complexing agent, etc. The effect of various preparative parameters on the film growth is explained as follows:

- *Precursor solution concentration:*

The surface density of adsorbed ions relies highly on the precursor solution concentration. Hence, thicker films can be obtained for concentrated precursor solutions, whereas the film thickness is decreased for lower concentrations of precursors.

- *Complexing agent:*

A complexing agent controls the concentration of free metal ions in the precursor solution. During chemical reactions, complex compound formation decreases the growth rate of the film. Hence, a complexing agent is mainly utilized to control the growth kinetics of deposited films.

- *Temperature:*

The rate of complex dissociation is influenced by solution temperature. The rate of complex dissociation is greater at higher temperatures, which increases the free metal ion concentration in the solution, leading to an increased deposition rate.

- *Adsorption time and reaction time:*

The adsorption and the reaction times significantly influence material deposition on a substrate surface. The precise control over adsorption and reaction times exhibited

reliable chemical reaction and consistent growth, offering uniform thin film deposition on the surface of the desired substrate [14].

- *Rinsing time:*

The homogeneous precipitation during the deposition is controlled with precise control of rinsing time. Also, rinsing enables the removal of loosely bound and unreacted species from the surface of a substrate.

2.2.3 EPD method:

EPD is a method where charged particles in a stable colloidal suspension are moved through the solvent due to an electric field and deposited on an oppositely charged conductive substrate, forming the layer of material to be deposited. In EPD cells, the deposition of charged particles in a stable colloidal suspension takes place on a conductive substrate, which acts as either a cathode or anode. The EPD can be classified into two types, depending on which electrode deposition can occur. When the deposition of positively charged particles occurs on the surface of the cathode, the process is called cathodic EPD. On the other hand, anodic EPD is the process in which the deposition of negatively charged particles occurs on the surface of a positive electrode (anode) [15,16].

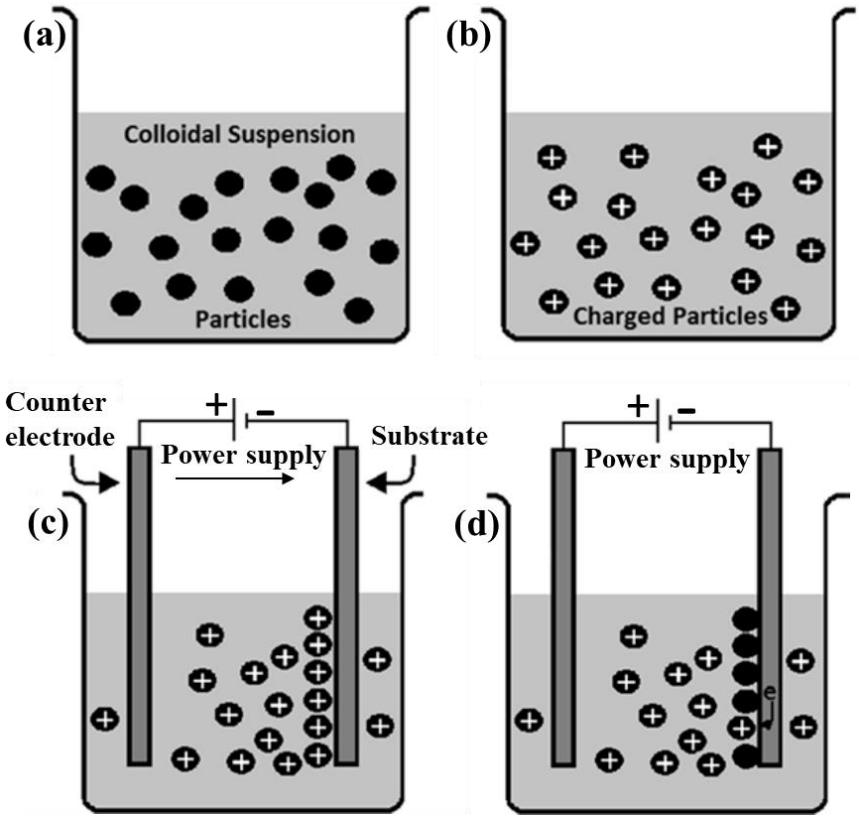

Fig. 2.2: Steps involved in EPD film formation: (a) dispersion, (b) electrochemical charging, (c) electrophoresis and (d) deposition [16].

The EPD cell consists of a working electrode (substrate on which material to be deposited), a counter electrode, colloidal suspension and AC or DC power supply. The EPD is viewed as a two-step process in which particles first migrate to the substrate by applying an electric field. Subsequently, after complex electrochemical reactions and aggregation, the film is deposited on the substrate surface [15,16]. **Fig. 2.2** shows the schematic representation of the steps involved in EPD film formation. The steps involved in EPD film formation are (a) dispersion of colloidal particles in solvent suspension, (b) electrochemical equilibrium between highly dispersed colloidal particles and solvent, resulting in electrochemical charging of colloidal particles, (c) attraction of charged particles in the solvent suspension to the surface of the oppositely charged electrode (substrate) and (d) deposition of charged particles on the surface of a substrate in the form of deposited film [16,17].

Factors affecting EPD:

- *Effect of applied electric field:*

Ideally, the rate of deposition in EPD increases with an increase in the applied electric field. The much lower electric field is not capable of triggering the electrophoresis. On the contrary, applying a high electrical field affects the quality of the deposits. The high electric field can cause turbulence in the suspension, affecting the quality of the deposited film. Conclusionally, the best quality of deposits is obtained at a moderate applied electric field [16,17].

- *Effect of deposition time:*

In EPD, the deposition rate initially increases with an increase in deposition time. Afterwards, it lowers with the increase in deposition time until the deposited film is thick enough and the deposition rate reaches a plateau at high deposition times [16].

- *Conductivity of substrate:*

In EPD, the quality of the deposited film is highly dependent on the conductivity of the substrate. Low substrate conductivity resulted in nonuniformity and slow deposition of the deposited film [17].

2.3 Synthesis of 2D MONs:

The synthesis method strongly influences different physicochemical characteristics and functionalities of 2D INs. 2D INs can be mainly prepared by two

methods: 1) bottom-up and 2) top-down [18]. In the bottom-up approach, the synthesis of 2D materials is achieved by chemical interactions between respective precursors. On the other hand, in a top-down approach, the 2D INs can be obtained from their pristine bulk materials using an exfoliation process.

2.3.1 Bottom-up approach:

In a bottom-up approach, 2D INs can be synthesized by chemical growth processes like chemical vapor deposition (CVD), wet chemical methods, and atomic and molecular condensation. The 2D INs synthesized by the bottom-up approach possess the advantages of large-scale production with cost-effectiveness. Also, these INs are utilized in biological and chemical sectors for different applications. Various organic surfactants are primarily used to synthesize 2D INs in the bottom-up approach. Thus, the removal of such organic surfactants is necessary for their application. Though ample reports are available on the 2D INs synthesized by the bottom-up approach, this approach can only produce multi-layered INs [19,20].

2.3.2 Top-down approach:

2D INs can be obtained by a top-down approach via physical or chemical methods. The physical top-down exfoliation procedure produces monolayer INs against Vander-Waals forces holding the stacked layers of bulk parent layered crystals together. The top-down approach is convenient in various applications owing to its high production yield [19-21].

The highly crystalline pristine host layered materials can be produced using solid-state calcination at extremely high temperatures.

(a) Scotch tape method:

In this method, monolayers of 2D INs can be obtained simply by applying external force through scotch tape. When the external force is applied through scotch tape, the single layers of bulk pristine layered materials can be peeled off from the host layered crystals [22]. This method does not require any chemicals or surfactants for synthesis; hence, it can produce phase-pure and high-quality INs. The schematic representation of the production of 2D INs via the scotch tape method is depicted in **Fig. 2.3**.

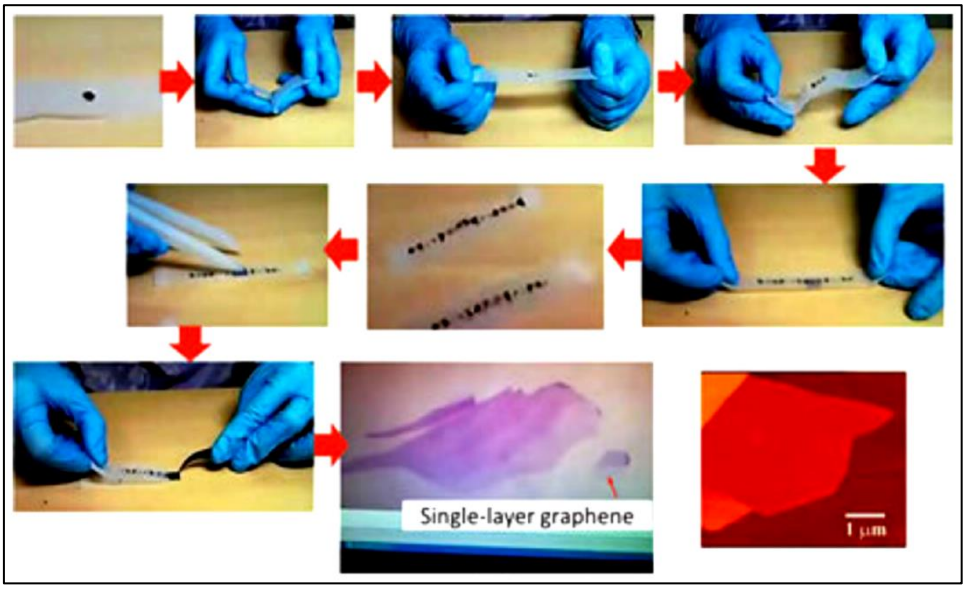

Fig. 2.3: Diagram showing production of 2D INs via scotch tape method [23].

(b) Ultrasonic exfoliation process:

Monolayers or a few layers of 2D INs can be easily obtained via the ultrasonic exfoliation process, as shown in **Fig. 2.4**. Compared to mechanical exfoliation, this method has a higher yield of NSs production. For the production of exfoliated 2D INs, the highly crystalline particles of layered compounds are dispersed in appropriate solvents, and ultrasonication is used to achieve exfoliation. In this process, exfoliation yield is highly dependent on the nature of the solvent used, as solvent plays a very significant role in exfoliation [24,25].

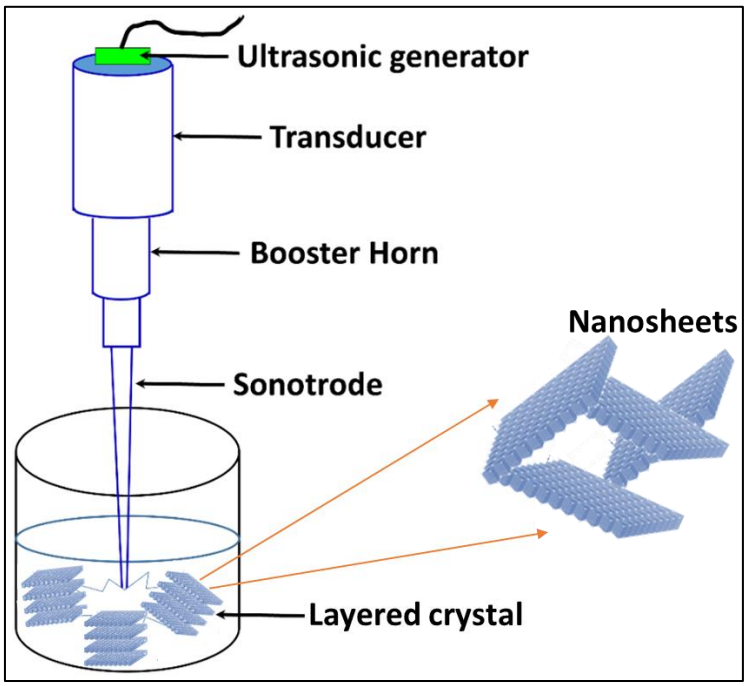

Fig. 2.4: Schematic representation of ultrasonication process.

(c) Intercalative exfoliation process:

Intercalation-exfoliation processes are typically chosen to produce 2D INs of multilayer compounds. The primary prerequisite for synthesizing 2D INs is highly crystalline layered inorganic crystals. These crystals are often made using crystal growth and solid-state reaction processes. Protonation, ion exchange and subsequent aqueous sonication processes are typically used to produce exfoliated INs [26]. The synthesis of exfoliated INs involves the following methods.

Intercalation:

Firstly, the layered compounds are often made by calcining a mixture of precursor material and alkali metal salts in the solid form at higher temperatures. This results in incorporating alkali metal ions into the inter-layer space of layered compounds.

Protonation:

Alkali metal ions have an ion exchangeable character. The alkali metal ions in the interlayer gap of layered materials can be substituted by protons when they react with the acidic solution. This protonation procedure leads to a protonated layered compound.

Ion-exchange:

In protonated layered materials, sufficient electrostatic interaction exists between the host layers and the charge-balancing species. The interaction between the host and guest is decreased when the interlayer distance increases by intercalating bulky guest species like organic solvent molecules that substitute the interlayer protons.

Successive aqueous sonication or exfoliation:

Ion-exchanged layered materials by organic ions exposed to the exfoliation assisted by successive aqueous sonication, resulting in the exfoliation of layered inorganic crystals to produce INs. The intercalated bulky ions increase the inter-gallery space of the layered crystal with the aid of external forces such as mechanical agitation or ultrasonication. This expansion causes a decrease in the electrostatic interaction between the guest ions and host layers, which results in the separation of the entity into individual NSs [27]. The schematic model of intercalative exfoliation of cesium titanate is displayed in **Fig. 2.5**.

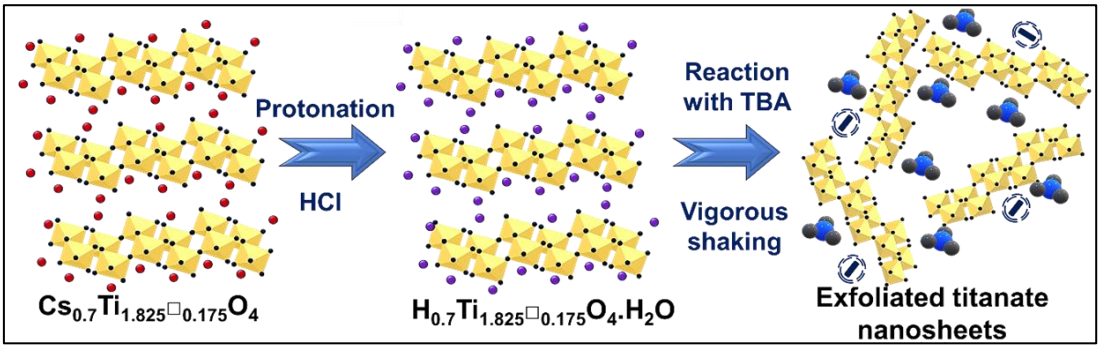

Fig. 2.5: Schematic depiction of the intercalative exfoliation process of cesium titanate.

2.4 Synthetic approaches for nanohybrids based on 2D NSs:

The various nanohybrid materials can be developed using exfoliated INs as the basic building blocks. Polycations, polyanions, inorganic nanoparticles (NPs), bioactive compounds, organic and inorganic ions and other guest species can be used to develop 2D INs-based nanohybrids [28]. The electrostatic interaction between exfoliated 2D NSs and hybridized species is a significant factor in producing hybrid materials. As a result, the interaction of NSs with various guest species is the fundamental building block of synthetic processes for hybrid materials. The 2D INs have a specific surface charge and can be hybridized with other species with an opposite surface charge. Negative surface charges on layered metal oxide and layered metal chalcogenides NSs cause them to be coupled with cationic species, whereas positive surface charges on LDH NSs cause them to be coupled with anionic species [29]. The schematic model of synthesis procedures and representative NSs-based hybrid structures is displayed in **Fig. 2.6**.

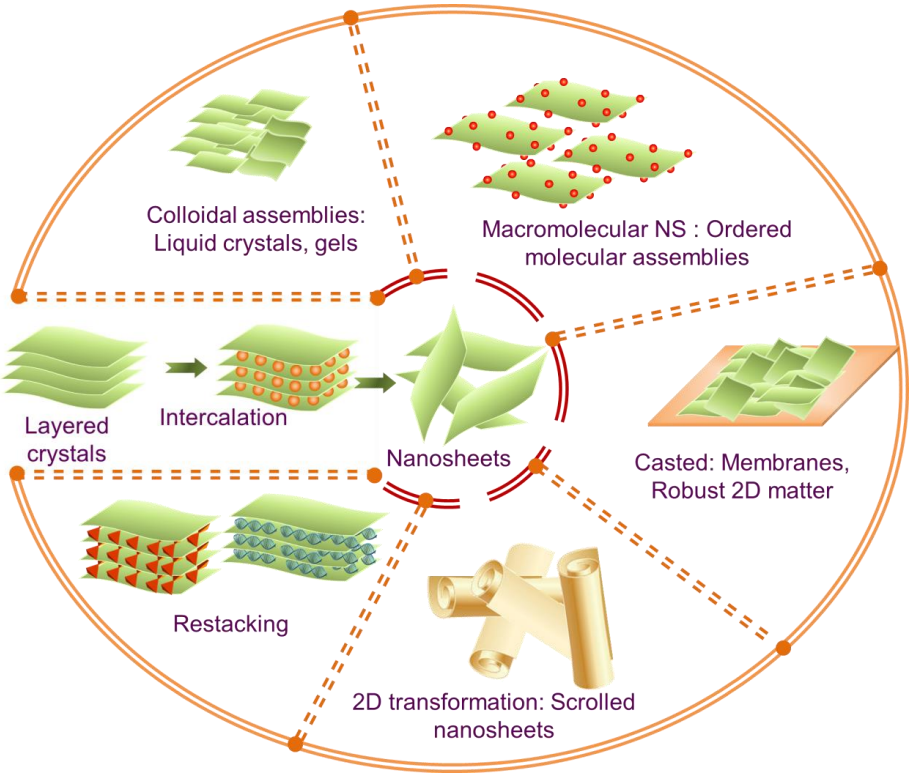

Fig. 2.6: Schematic model of synthesis procedures and representative NSs-based hybrid structures [30].

2.4.1 Ion exchange/intercalation:

Intercalation is one of the traditional synthesis methods for hetero-layered nanohybrids without exfoliating host inorganic crystals. During the intercalation process, the chosen guest species exchanges charge-balancing ions in the interlayer spacings of the layered host crystal. Because of the chemical interaction between the host crystal and guest species, the guest species are intercalated into the inter-lamellar spacing of the layered crystal. The intercalation method is supported by ion exchange, hydrogen bonding, neutralization, and electrochemical faradic reactions [31]. Since the intercalation process is diffusion-controlled, the host layer charge density, the guest species size, and their arrangement are the determining factors for the resulting intercalated nanohybrids. Ultrasonication, microwave radiation assistance, elevated temperature, pressure, and other external stimuli are frequently helpful in accelerating the intercalation hybridization process.

2.4.2 Exfoliation-reassembling:

Although the intercalation process is typically employed to produce hetero-layered nanohybrids, this method has potential drawbacks, including the need for highly transferable guest species and uncontrolled intercalated chemical composition. The exfoliation-reassembling strategy offers a versatile method for restacking oppositely

charged INs and charge-balancing guest species from their initially separated colloidal states [32]. The exfoliation-restacking method can accurately control the chemical composition and restacking pattern of INs-based nanohybrids. This facility enables the synthesis of innovative INs-based nanohybrids with high control over pore structure and surface morphology. The exfoliation-reassembling approach develops various crystal forms, including pillared, core-shell, interstratified and hollow materials [33].

2.4.3 Anchored assembly:

Since 2D INs produced from their highly crystalline bulk crystals can serve as 2D micromats for the direct growth of NPs or the adsorption of various functional guest species. Exfoliated 2D INs can offer nucleation and anchoring sites for the growth of functional NPs. Functional guest NPs can anchored on the 2D INs directly or through adsorption. Homogenous adsorption and controlled growth of guest NPs on the 2D INs surface are the key factors to consider when producing IN-based anchored assemblies [34]. Nanohybrid electrodes based on INs can be developed by anchoring in which uniform and homogeneous growth of guest materials is achieved without self-aggregation of NSs.

2.4.4 Layer-by-layer film deposition:

Layer-by-layer deposition is one of the most efficient and sophisticated methods for synthesizing INs-based thin films. The electrostatic surface charge on NSs is the foundation for the layer-by-layer deposition. This method is beneficial for explicit control over film thickness and the specific stacking sequence required for the growth of INs-based hybrids on a nanometer scale. In this method, the phenomena of charge compensation among NSs and guest species play a critical role. The charge compensation mechanism in the layer-by-layer method to synthesize INs hybridized with guest species can be realized by dipping the desired substrate into electrostatically charged INs suspension so that INs can get adsorbed on the substrate, followed by dipping it in suspension with oppositely charged guest species. The number of deposition cycles can be varied to obtain the desired film thickness. Additionally, this technique enables the control stacking pattern of INs and guest species at the nanometer scale. The layer-by-layer deposition allows for the fabrication of multi-layered hybrid films containing oppositely charged INs and several guest species, including polyelectrolytes, NPs, proteins, NSs, dyes and biomolecules [35].

The various synthesis methods for INs-based hybrids are shown in **Fig. 2.7**.

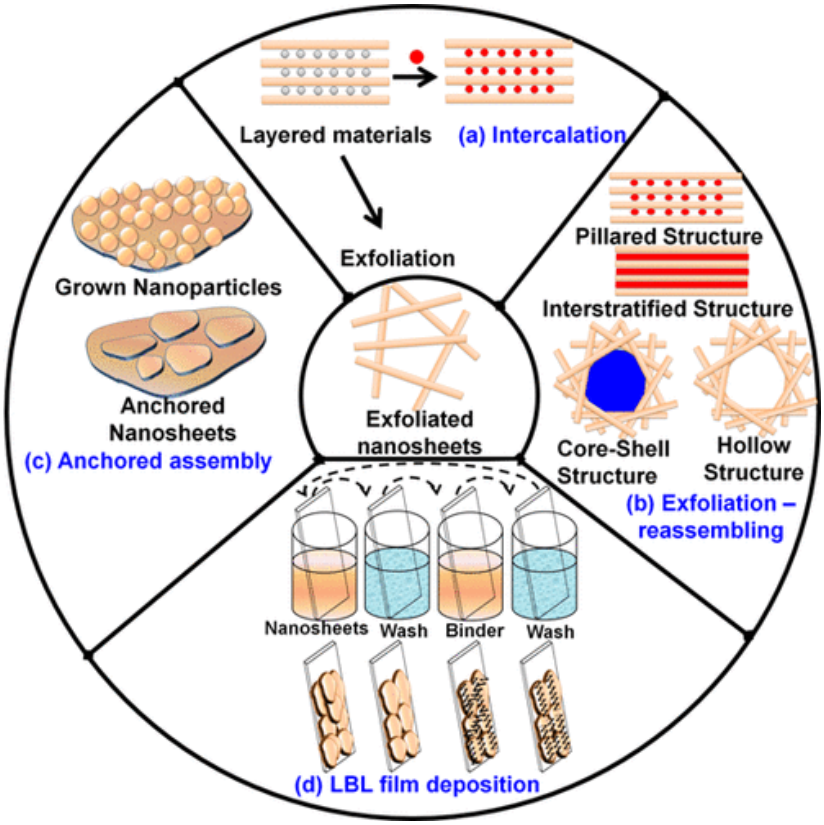

Fig. 2.7: Schematic representation of synthesis methods for fabrication of 2D INs and their nanohybrids: (a) intercalation, (b) exfoliation-reassembling, (c) anchored assembly and (d) layer-by-layer deposition [33].

2.5 Material characterization techniques:

The physicochemical properties of materials play a crucial role in their applications. The various material characterization techniques play a vital role in probing physicochemical properties. Also, investigating the properties of materials using different characterization techniques plays a significant role in optimizing their performance in various applications. The physicochemical properties of materials can be investigated with various characterization techniques like XRD, FTIR spectroscopy, Raman spectroscopy, XPS, FESEM, EDS, and UV-vis spectroscopy. The present section deals with explanation of various characterization techniques used to analyze materials.

2.5.1 XRD:

The structural analysis of materials (crystalline nature, phase identification, estimation of lattice parameters and crystallite size) is carried out with the XRD technique [36,37]. The schematic of the XRD diffractometer and a photograph of the XRD equipment (Rigaku miniflex-600 X-Ray diffractometer) are shown in **Fig. 2.8**.

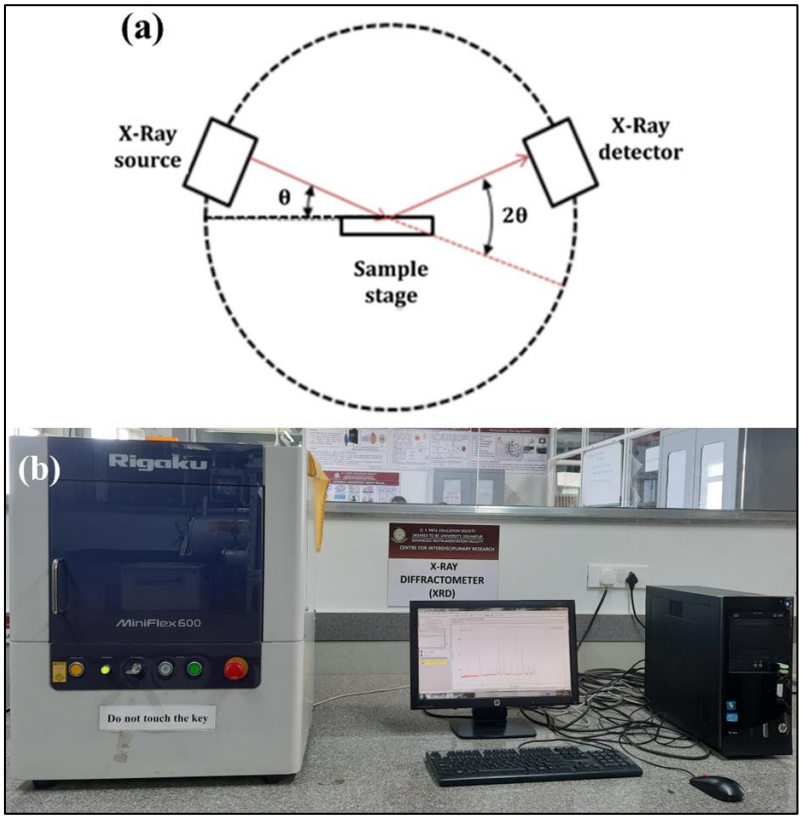

Fig. 2.8: (a) Schematic of XRD diffractometer and (b) Photograph of XRD instrument.

Working principle:

XRD technique depends on the principle of Bragg's law of X-ray diffraction [33]. When monochromatic X-rays are incident on a crystalline material at an angle 'θ', the X-rays are diffracted by a set of parallel lattice planes separated by interplanar spacing 'd'. When the path difference between two X-rays is a multiple of the wavelength, constructive interference will happen, as shown in **Fig. 2.9**.

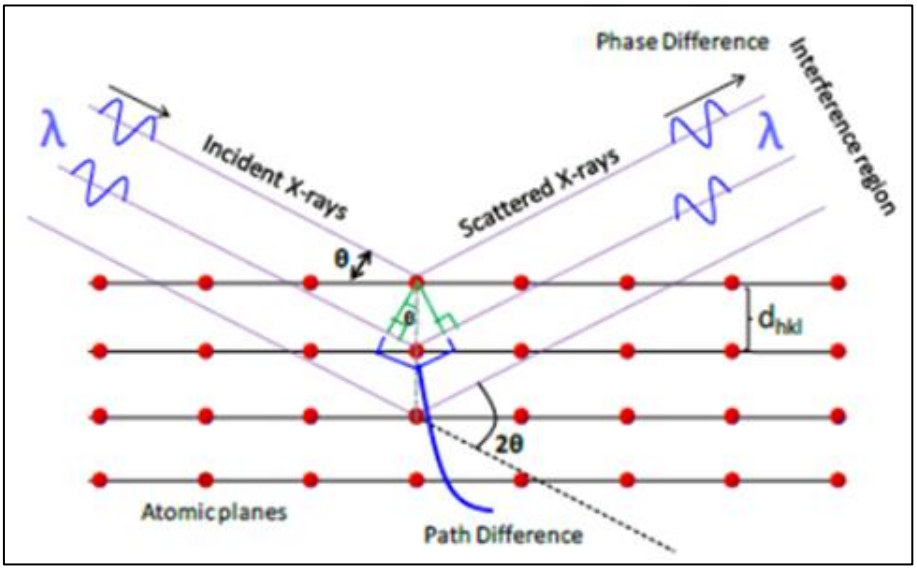

Fig. 2.9: Schematic representation of Bragg's law for X-ray diffraction [37].

Bragg's equation governs the X-ray diffraction phenomena, which can be thought of as the diffraction of X-rays from the parallel lattice planes of the material.

$$2dsin\theta = n\lambda \quad (2.7)$$

where d is interplanar spacing, λ is X-ray wavelength, θ is diffraction angle, and n denotes the order of diffraction.

Furthermore, the crystallite size of the material can be calculated using Scherrer's formula (equation 2.8) from the full width at half maximum (FWHM) of the most intense XRD peak.

$$D = \frac{K\lambda}{\beta \cos\theta} \quad (2.8)$$

where D is crystallite size, λ is X-ray wavelength, β is FWHM of XRD peak in radians, θ is Braggs angle, and K denotes shape factor. The value of the shape factor lies between 0.89 and 1.39, but it is taken as nearly 1 for most cases [38].

Advantages of XRD:

XRD technique is the most convenient and least expensive technique. It is commonly used for crystal structure identification and phase analysis. It does not require an evacuated chamber.

Disadvantages of XRD:

X-rays interact very strongly with only heavy elements as compared to lighter elements. XRD technique is unsuitable for examining the chemical composition of elements present in the material. It does not give an idea about the chemical bonding nature of materials.

In the current study, the XRD technique is applied to investigate the crystal structure, lattice parameters and crystallite size of pristine materials and nanohybrid thin films.

2.5.2 UV-vis spectroscopy:

The optical characteristics and band gap energy of the materials are investigated with UV-vis spectroscopy [39]. The ray diagram of the UV-vis spectroscopy is shown in **Fig. 2.10**.

Working principle:

The UV-Vis-NIR double-beam spectrophotometer relies on the principle of interaction of UV or visible light with chemical compounds. When the chemical compound absorbs the light, it undergoes excitation and de-excitation processes, resulting in the production of UV-visible spectrum [40].

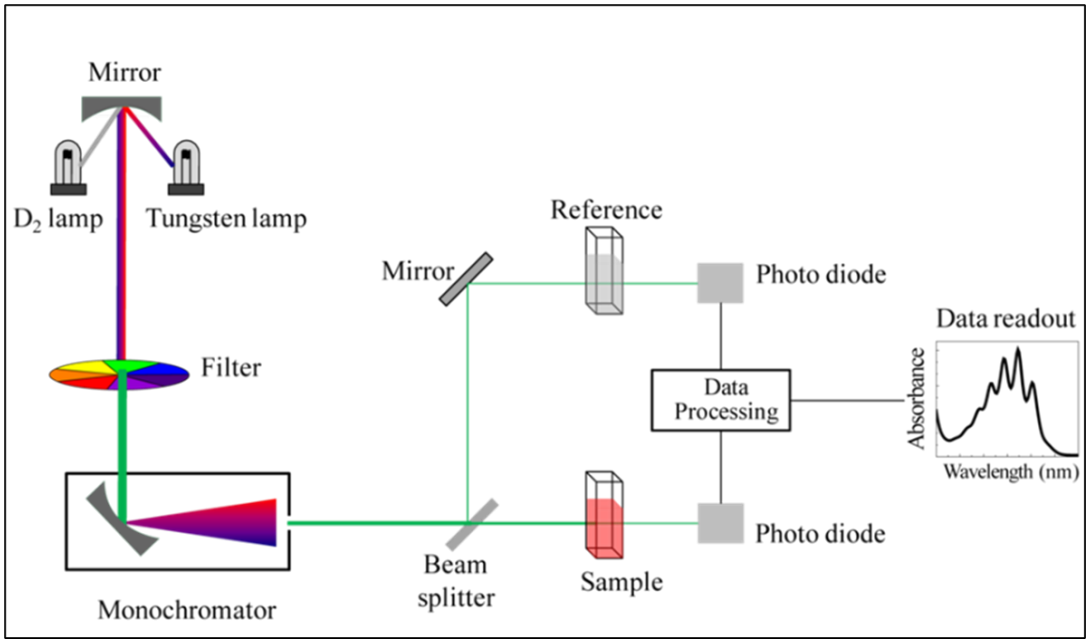

Fig. 2.10: Ray diagram of UV-Vis-NIR spectrophotometer [41].

UV-vis-NIR double beam spectrophotometer consists of two light sources: 1) for UV light (deuterium lamp) and 2) for visible light (tungsten lamp). The analysis is made by measuring the light intensity after passing through sample (I) and then comparing it to the initial light intensity before passing through a sample (I_0). The proportion of both intensities (I/I_0) gives the percentage transmittance of a compound. Again, absorbance (A) is calculated from transmittance (T) as represented in the following equation.

$$A = -logT = -log\frac{I}{I_0} \tag{2.9}$$

The band gap energy (E_g) of material is estimated from absorbance using the following relation,

$$E_g = \frac{hc}{\lambda_g} = \frac{1240}{\lambda_g}\ (eV) \tag{2.10}$$

where λ_g is the wavelength of light, h is Planck's constant and c is the velocity of light in air, respectively.

Advantages of UV-vis spectroscopy:

UV-vis spectrometer is simple to handle and use. Both qualitative and quantitative analyses can be performed by using UV-vis spectroscopy. It can be useful for analyzing the degradation of dyes and drugs. Samples in both forms (solid and liquid) can be analyzed with it. It covers the entire range of UV and visible light spectrum.

Disadvantages of UV-vis spectroscopy:

Only molecules that contain chromophores are examined by using UV-vis spectroscopy. Various parameters like pH, temperature, contaminants, and impurities

can all impact the absorption spectrum. In the case of reading a liquid sample, cuvette handling may have an impact.

The current study uses UV-vis spectroscopy to study the optical properties and band gap energy of pristine materials and nanohybrid thin films. In addition, the photocatalytic dye degradation performance is evaluated with UV-vis spectroscopy.

2.5.3 FTIR spectroscopy:

The chemical bonding nature and presence of functional groups in materials are investigated by FTIR spectroscopy. The spontaneous alignment of dipole moment in compounds is examined with FTIR spectroscopy, which provides evidence of inter-atomic forces within the crystal lattice. The ray diagram and photograph of FTIR spectrometer (Alpha (II) Bruker model)) is displayed in **Fig. 2.11**.

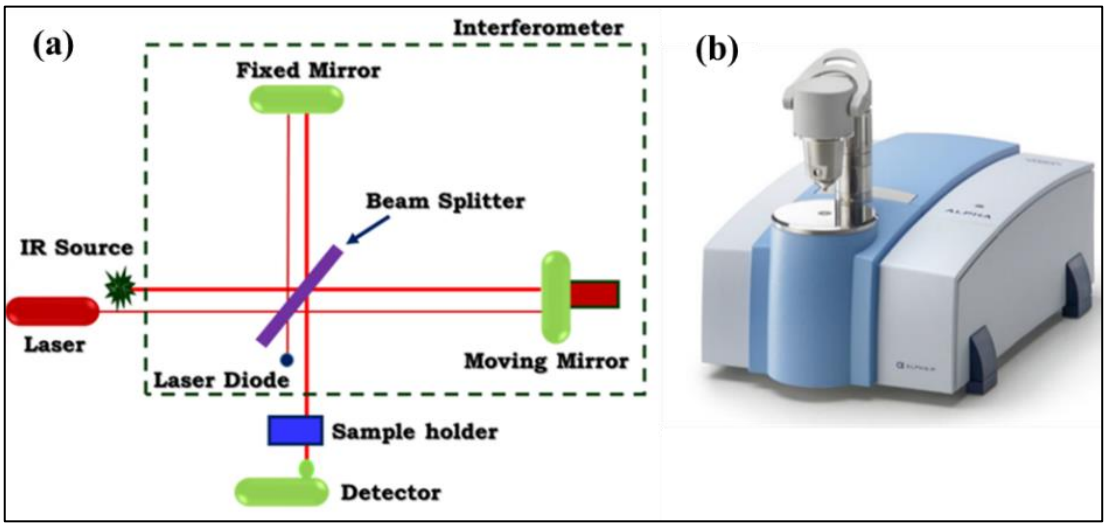

Fig. 2.11: (a) Ray diagram and (b) photograph of FTIR Spectrometer [42].

Working principle:

The IR vibrational frequencies and inter-atomic forces are linked and used to analyze the existing functional groups in compounds. The Planck-Einstein relation is used to determine the energy transfer between various energy states of molecules (equation 2.11),

$$\Delta E = h\nu \tag{2.11}$$

When radiation is emitted, the value of ΔE is negative, while ΔE is positive when the molecule absorbs energy. When the condition in the above equation is fulfilled, the resulting signal at the detector gives a unique vibration spectrum (intensity versus frequency) characteristic of a molecule. Any organic or inorganic molecule can vibrate in six different ways: (i) symmetric stretching, (ii) anti-symmetric stretching, (iii) wagging, (iv) rocking, (v) scissoring and (vi) twisting [40]. Also, molecules or atoms

raise different spectra based on the energy levels in the transition. Hence, the following equation represents the total energy contribution (E_{tot}) [42],

$$E_{tot}=E_{elect}+E_{vib}+E_{rot}+E_{trans} \quad (2.12)$$

where E_{elect} is electronic, E_{vib} is vibrational, E_{rot} is rotational, and E_{trans} is the translation energy.

Advantages of FTIR spectroscopy:

FTIR spectroscopy is an easy, fast and highly sensitive technique. It is highly sensitive to IR active molecules. It has a simpler mechanical design. It can provide qualitative and quantitative chemical information. It is a relatively inexpensive technique.

Disadvantages of FTIR spectroscopy:

Detection of atoms or monoatomic ions is impossible by using FTIR spectroscopy. It cannot detect symmetric molecules. Water is a strong IR absorber; therefore, aqueous solutions are challenging to examine using FTIR spectroscopy.

This study uses FTIR spectroscopy to inspect the functional groups and chemical bonding nature of pristine materials and nanohybrid thin films.

2.5.4 Raman spectroscopy:

The functional groups that are present in the material can be determined by Raman spectroscopy.

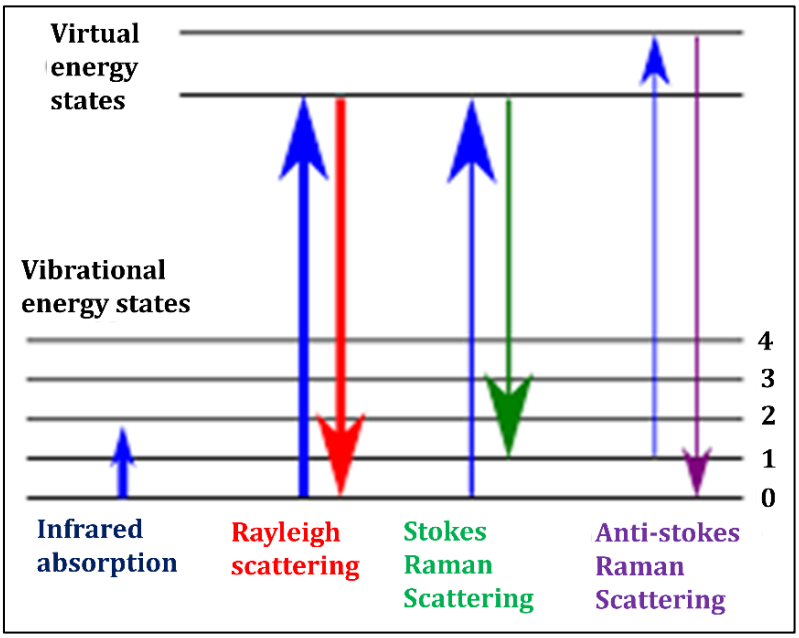

Fig. 2.12: Energy level diagram of Raman spectroscopy [43].

Working principle:

The inelastic scattering of monochromatic light, often known as Raman scattering, is the foundation of Raman spectroscopy. When monochromatic light strikes a material, it absorbs some of the light while most of the light passes through it. At the same time, the substance scatters a minimal amount of light in all directions. When the scattering occurs perpendicular to incident light (99% of the scattered light has the same frequency as incident light), then Rayleigh scattering is observed. On the other hand, Raman scattering is observed when scattered light (1%) has frequencies different from the incident light [44,45].

The schematic showing vibrational energy level diagram of Raman spectroscopy is represented in **Fig. 2.12**. When an electron in the material interacts with the incident monochromatic light, the electron makes a transition to a virtual state of energy by absorbing energy and again comes to the original energy level by losing energy. Rayleigh scattering occurs when the incident energy of photons equals the energy lost by the electron, and the electron returns to its initial level by emitting one photon. The energy lost by the electron is not always the same as the energy absorbed from incident light. Sometimes, electrons lose energy from the virtual state and fall to a distinct vibrational level from their original level. Thus, Raman scattering is observed when the emitted photon has a frequency other than the incident photon. Based on the final vibrational level of electrons, Raman scattering is again divided into two categories. When the frequency of the scattered photon is lower than that of the incident photon, Stokes lines can be seen (happen when an electron absorbs energy). On the other hand, anti-Stokes lines are observed when the frequency of the produced photons is higher than that of the incident photon (electrons release energy). Raman shift (Δ) is positive for stokes lines and negative for anti-stokes lines [46-48].

Advantages of Raman spectroscopy:

Raman spectroscopy can analyze a variety of organic and inorganic compounds. It is precise, like a chemical fingerprint of a material. It can be used on any surface since it analyses dispersed light, including opaque substrates. It shows low sensitivity to water and temperature.

Disadvantages of Raman spectroscopy:

Raman spectroscopy is unsuitable for use with metals or alloys. The instrumentation for detection must be highly sensitive and optimized. It might be

obscured by the fluorescence of impurities or the sample itself. Sample destruction is possible due to sample heating by intense laser light.

The current study uses Raman spectroscopy analysis to study the chemical bonding nature of pristine materials and nanohybrid thin films.

2.5.5 XPS:

The surface chemical composition and oxidation states of the elements present in the material are investigated using the XPS technique. The schematic of the ray diagram of XPS is depicted in **Fig. 2.13**.

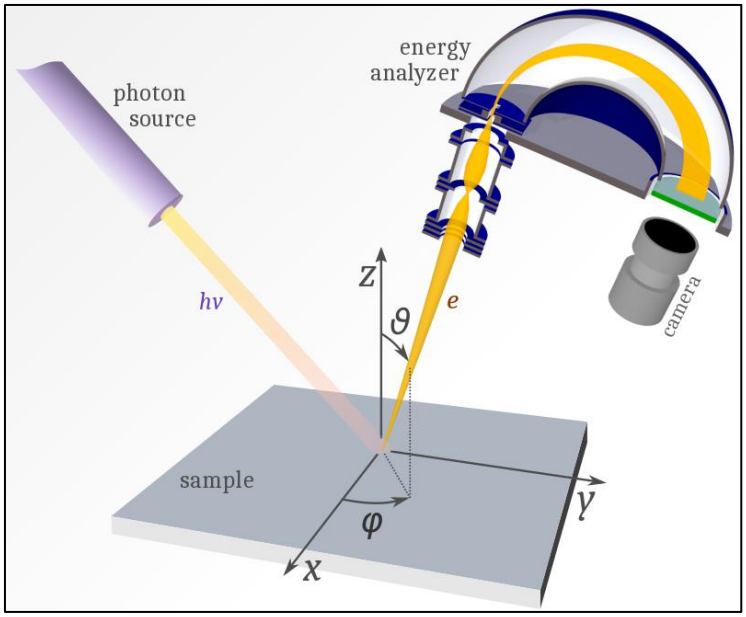

Fig. 2.13: Schematic representation of ray diagram of XPS [49].

Working principle:

The photoelectric effect serves as the basis for XPS [50]. When an X-ray beam strikes the sample surface, the atom absorbs this energy and inner shell electrons are ejected. The kinetic energy (KE) of ejected photoelectrons is linked with the binding energy (BE) of photoelectrons as given in the following equation,

$$KE = h\nu - \mathrm{BE} - \varphi_s \quad (2.13)$$

where hν, BE, and φ_s are photon energy, BE of atomic orbital and work function of the electron, respectively [51].

The monochromatic X-rays are generated from the monochromator in a very high vacuum. When the monochromatic X-rays are incident on the sample surface, electrons are emitted from the material. These emitted photoelectrons are collected at the detector (the detector measures the count and KE of emitted photoelectrons). Finally,

the measured KE is represented in the spectrum, in which particular energy is characteristic of the element [52].

The chemical composition and oxidation states of the elements present in the sample are evaluated with the plot of emitted photoelectrons count as a function of BE.

Advantages of XPS:

XPS is non-destructive technique. Quantitative measurements are attained by using the XPS technique. It is a surface-sensitive (10 to 100 Å) technique. It gives information regarding chemical bonding and elemental mapping. It provides information about the oxidation states of elements and their chemical composition.

Disadvantages of XPS:

XPS is a very expensive technique. It requires a very high vacuum, and its processing is slow. Hydrogen and helium cannot be detected by using XPS. It provides inadequate lateral resolution.

The current study uses XPS to study the chemical composition and oxidation states of elements present in pristine materials and nanohybrid thin films.

2.5.6 EDS:

The chemical composition of elements present in the compound is estimated with EDS. The schematic diagram of the X-ray emission mechanism in the EDS is shown in **Fig. 2.14**.

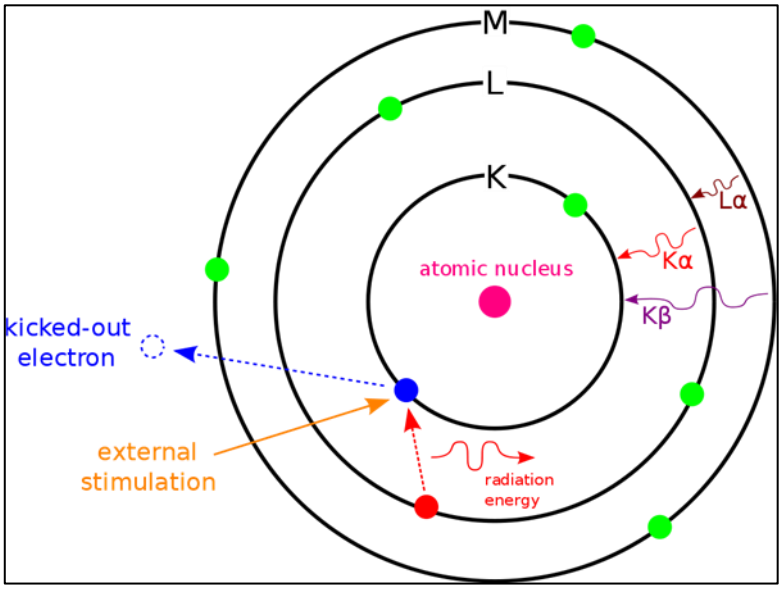

Fig. 2.14: Schematic representation of the X-ray emission mechanism in the EDS [53].

Working principle:

When the highly energetic electrons are incident on the sample surface, atoms absorb this energy and eject the core-shell electrons. To fill the vacancy generated in the

core-shell, a transition of higher energy electrons takes place with the emission of radiation in the form of photons. The energy released in this procedure is characteristic of each element; hence, it is utilized to determine the elements present in the material. The spectrum of counts of ejected electrons as a function of X-ray energy is plotted to determine the elemental composition of materials [54,55].

Advantages of EDS:

EDS has high detection efficiency. It can able to scan areas (raster scan) and single spots. It can map a wide spatial range from 1 mm^2 to μm^2. EDS is the most widely used technique in electron microscopes. It shows elemental coverage for almost all elements.

Disadvantages of EDS:

EDS is a destructive analysis in many cases. The EDS peaks have poor energy resolution. Surface sensitivity makes bulk analysis more difficult when using EDS. Quantitative examination of diverse materials frequently yields incorrect results.

In the current work, EDS estimates the chemical composition of elements in pristine materials and nanohybrid thin films.

2.5.7 FESEM:

FESEM analysis is used to observe the surface morphology of the materials. The schematic of the ray diagram of FESEM is represented in **Fig. 2.15**.

Working principle:

In FESEM, the cathode (electron gun) is heated to generate a high-energy electron (primary electron) beam. The potential difference between cathode and anode allows the generated electrons to accelerate to the surface of a material. Electromagnetic lenses are used to focus the beam of electrons in a sharp spot. The sample is inserted into a specific holder and injected into the high vacuum section of the microscope via the sample exchange chamber. To restrict the interaction of high-energy electrons with gas molecules in the air and to attain high resolution, FESEM is always carried out in a high vacuum. When the focused beam of electrons is bombarded on the surface of a sample, it penetrates the sample up to a few micrometers, causing various interactions to occur. Secondary electrons are generated when the primary electron beam collides with the sample surface. A positively charged electron detector collects these secondary electrons, creating a 3D picture of the sample surface [56].

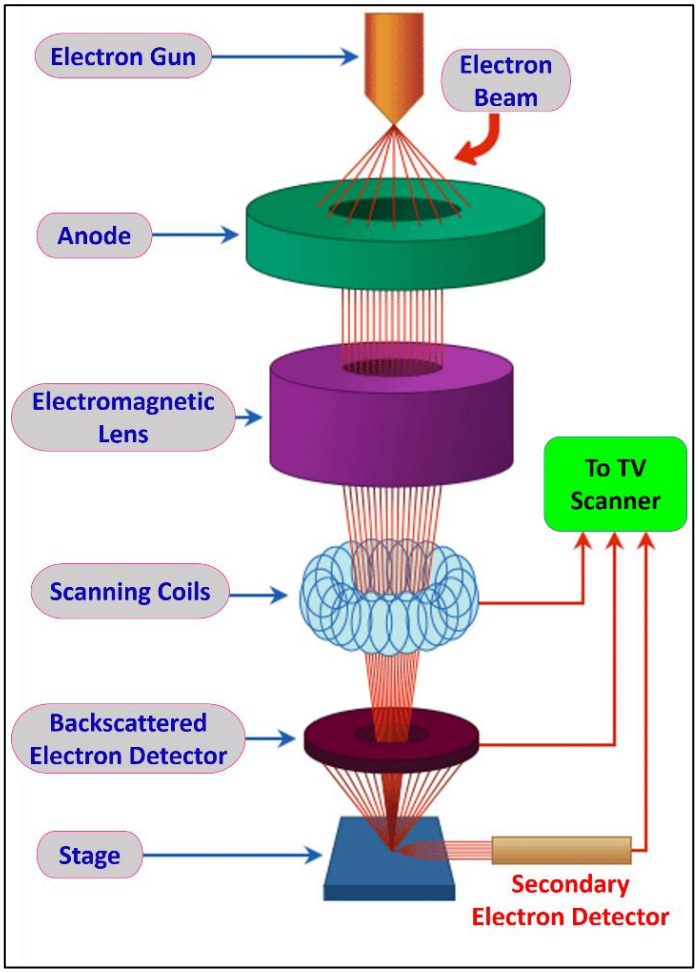

Fig. 2.15: Schematic of ray diagram of FESEM [56].

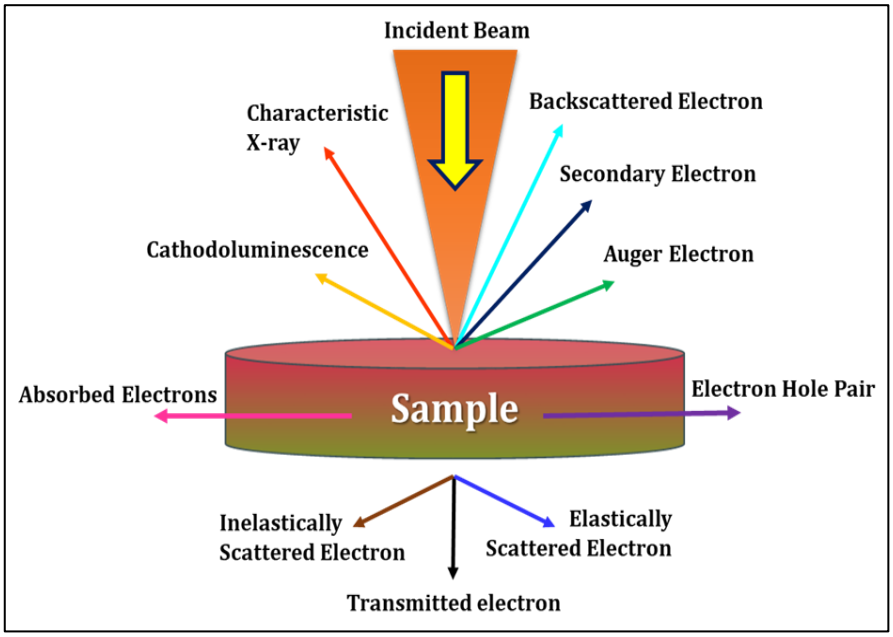

Fig. 2.16: Schematic representation of the different emission processes of electrons during scanning [57].

Advantages of FESEM:

FESEM magnifies objects more than 5,00,000 X. It can generate data in a digital format. It is possible to study a more considerable depth of field by using FESEM. It gives detailed 3D and topographical imaging.

Disadvantages of FESEM:

FESEM is expensive and requires ample space. It is affected by magnetic fields. Scattering of electrons from beneath the sample surface carries a negligible danger of radiation exposure. It is limited to solid samples.

In the current study, the FESEM analysis scrutinizes the surface morphology, thickness, and pore size of synthesized pristine materials nanohybrid thin films.

2.6 Photocatalytic dye degradation measurements:

Over the past few decades, environmental pollution from the ever-increasing industrial dye contamination has become a challenging concern. Heterogeneous semiconductor photocatalysis has received significant attention for the degradation of such contaminants. Photocatalysis accelerates precise oxidation and reduction processes under exposure to light irradiations [58].

The photocatalytic dye degradation performance of pristine and nanohybrid thin-film photocatalysts is studied with UV-vis spectroscopy (explained in **Chapter 2, Section 2.5.2**) using Carry win UV 5000 spectrophotometer. The photocatalytic activity of pristine and nanohybrid thin-film photocatalysts was estimated for the photodegradation of MB and Rh-B dyes under visible light illumination (light intensity = 100 mW cm^{-2}) using a quartz photoreactor. During the photocatalytic dye degradation experiments, the light obtained from the xenon lamp was calibrated by passing through the infrared (IR) water filter followed by AM 1.5 G and optical cut-off (420 nm) filters. The photocatalytic dye degradation setup used for testing is depicted in **Fig. 2.17**.

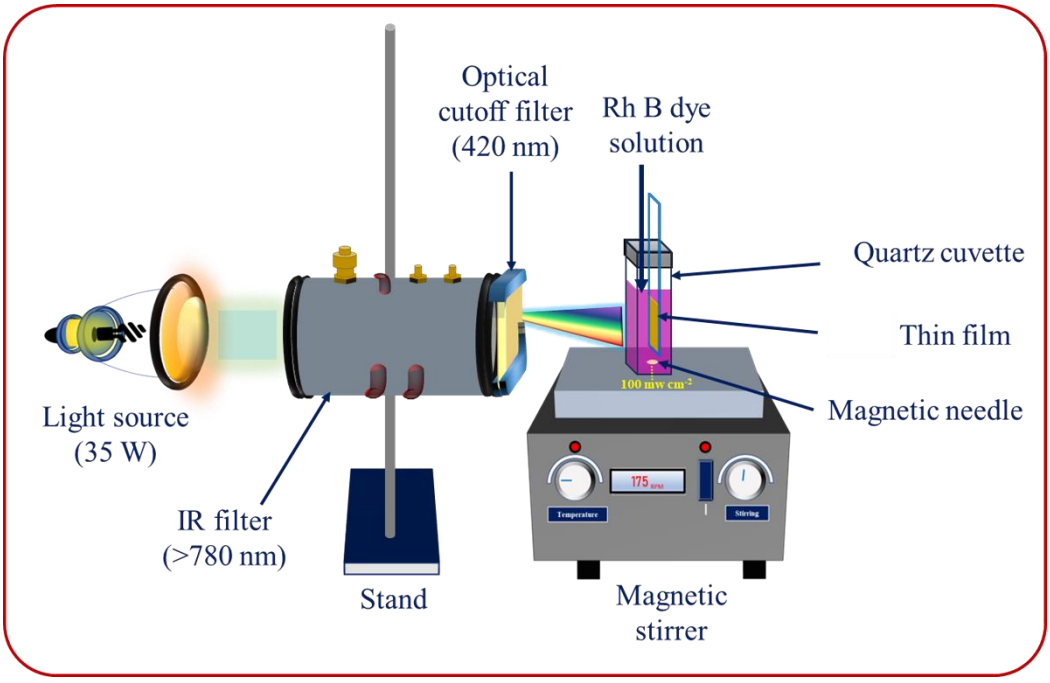

Fig. 2.17: Schematic representation of photocatalytic dye degradation setup.

The photocatalytic dye degradation performance of the pristine materials and nanohybrid thin films is evaluated with UV-vis absorption spectroscopy analysis. The photocatalytic performance of synthesized materials is inspected with a percentage degradation study using the formula [59],

$$\text{dye degradation } (\%) = \frac{C_0 - C_t}{C_0} \times 100 \quad (2.14)$$

where C_0 denotes the initial absorption and C_t denotes the absorption at time t.

The pseudo-first-order kinetic model is employed to explore dye degradation dynamics. The following equation describes a pseudo-first-order reaction [60]:

$$q_t = (1 - e^{-k_1 t}) \quad (2.15)$$

where k_1 and t are rate constant and time, q_e denotes adsorption at equilibrium and q_t is adsorption at time t.

Furthermore, a recyclability study was conducted to check the stability of nanohybrid thin films.

2.7 References:

1. R.L. Singh, P.K. Singh, R.P. Singh, Enzymatic decolorization and degradation of azo dyes: A review, J. Int. Biodeter. Biodeger 104 (2015) 21-31.
2. T.B. Gelaw, B.K. Sarojini, A.K. Kodoth, Review of the advancements on polymer/metal oxide hybrid nanocomposite-based adsorption assisted photocatalytic materials for dye removal, Chem. Eur. J. 6 (2021) 9300-9310.
3. L. Wang, T. Sasaki, Titanium oxide nanosheets: Graphene analogues with versatile functionalities, Chem. Rev. 114 (2014) 9455-9486.
4. I. Gurrappa, L. Binder, Electrodeposition of nanostructured coatings and their characterization- A review, Sci. Technol. Adv. Mater. 9 (2008) 043001.

5. T.P. Niesen, M.R. De Guire, Review: Deposition of ceramic thin films at low temperatures from aqueous solutions, J. Electroceram. 6 (2001) 169-207.
6. C.D. Lokhande, Chemical deposition of metal chalcogenide thin films, Mater. Chem. Phys. 27 (1991) 1-43.
7. D. Suthar, S. Chuhadiya, R. Sharma, S. Himanshu, M.S. Dhaka, An overview on the role of ZnTe as an efficient interface in CdTe thin film solar cells: A review, Mater. Adv. 3 (2022) 8081-8107.
8. G. Hodes, "Chemical Solution Deposition of Semiconductor Films", Marcel Dekker Inc., New York, (2001).
9. R.S. Mane, C.D. Lokhande, Chemical deposition method for metal chalcogenide thin films, Mater. Chem. Phys. 65 (2000) 1-31.
10. J. George, "Preparation of thin films", Marcel Dekker, Inc., New York, (1992).
11. K.L. Chopra, I. Kaur, "Thin film device application", Plenum Press, New York, (1983).
12. M.-W. Lee, Sequential ionic layer adsorption reaction (SILAR): A facile, low-cost growth method for ternary semiconductors for solar cells, AIP Conf. Proc. 2221 (2020) 020003.
13. H.M. Pathan, C.D. Lokhande, Deposition of metal chalcogenide thin films by successive ionic layer adsorption and reaction (SILAR) method, Bull. Mater. Sci. 27 (2004) 85-111.
14. V.R. Shinde, T.P. Gujar, C.D. Lokhande, R.S. Mane, S.H. Han, Development of morphological dependent chemically deposited nanocrystalline ZnO films for liquified petroleum gas (LPG) sensor, Sens. Act. B 123 (2007) 882-887.
15. L. Besra, M. Liu, A review on fundamentals and applications of electrophoretic deposition (EPD), Prog. Mater. Sci. 52 (2007) 1-61.
16. P. Amrollahi, J.S. Krasinski, R. Vaidyanathan, L. Tayebi, D. Vashaee, (2016) Electrophoretic deposition (EPD): Fundamentals and application from nano-to microscale structures. In M. Aliofkhazraei, A. Makhlouf (Eds), Handbook of Nanoelectrochemistry (pp. 561-591), Switzerland, Springer.
17. P. Sarkar, P.S. Nicholson, Electrophoretic deposition (EPD): Mechanisms, kinetics, and application to ceramics, J. Am. Ceram. Soc. 89 (1996) 1987-2002.
18. C. Tan, X. Cao, X.-J. Wu, Q. He, J. Yang, X. Zhang, J. Chen, W. Zhao, S. Han, G.-H. Nam, M. Sindoro, H. Zhang, Recent advances in ultrathin two-dimensional nanomaterials, Chem. Rev. 117 (2017) 6225-6331.
19. C. Murugana, V. Sharma, R.K. Murugan, G. Malaimegud, A. Sundaramurthy, Two-dimensional cancer theranostic nanomaterials: Synthesis, surface functionalization and applications in photothermal therapy, J. Control. Release 299 (2019) 1-20.
20. M. Yi, Z. Shen, A review on mechanical exfoliation for the scalable production of graphene, J. Mater. Chem. A. 3 (2015) 11700-11715.
21. S.M. Oh, S.B. Patil, X. Jin, S.-J. Hwang, Recent applications of 2D inorganic nanosheets for emerging energy storage system, Chem. Eur. J. 24 (2018) 4757-4773.
22. K. Fukuda, J. Sato, T. Saida, W. Sugimoto, Y. Ebina, T. Shibata, M. Osada, T. Sasaki, Fabrication of ruthenium metal nanosheets via topotactic metallization of exfoliated ruthenate nanosheets, Inorg. Chem. 52 (2013) 2280-2282.
23. J.N. Coleman, Two-dimensional nanosheets produced by liquid exfoliation of layered materials, Science 331 (2011) 568-571.
24. J.T. Han, J.I. Jang, H. Kim, J.Y. Hwang, H.K. Yoo, J.S. Woo, S. Choi, H.Y. Kim, H.J. Jeong, S.Y. Jeong, K.-J. Baeg, K. Cho, G.-W. Lee, Extremely efficient liquid exfoliation and dispersion of layered materials by unusual acoustic cavitation, Sci. Rep. 4 (2014) 5133.

25. S. Xiong, X. Chen, Y. Liu, T. Fan, Q. Wang, H. Zhang, T. Chen, Black phosphorus as a versatile nanoplatform: From unique properties to biomedical applications, J. Innov. Opt. Health Sci. 13 (2020) 2030008.
26. Z.J. Chen, B.Z. Lin, Y.L. Chen, K.Z. Zhang, B. Li, H. Zhu, Pillaring and photocatalytic properties of mesoporous α-Fe_2O_3/titanate nanocomposites via an exfoliation and restacking route, J. Phys. Chem. Solids 71 (2010) 841-847.
27. M. Osada, T. Sasaki, Exfoliated oxide nanosheets: New solution to nanoelectronics, J. Mater. Chem. 19 (2009) 2503-2511.
28. Y. Matsumoto, U. Unal, Y. Kimura, S. Ohashi, K. Izawa, Synthesis and photoluminescent properties of titanate layered oxides intercalated with lanthanide cations by electrostatic self-assembly methods, J. Phys. Chem. B 109 (2005) 12748-12754.
29. F. Leroux, J.P. Besse, Polymer interleaved layered double hydroxide: A new emerging class of nanocomposites, Chem. Mater. 13 (2001) 3507-3515.
30. S.P. Kulkarni, A.S. Patil, V.V. Patil, U.M. Patil, J.L. Gunjakar, (2021) Nanosheet-derived porous materials and coatings for energy storage applications. In F.I. Ezema, C.D. Lokhande, R. Jose (Eds) Chemically deposited nanocrystalline metal oxide thin films (pp. 431-467), Switzerland, Springer.
31. J.H. Choy, Intercalative route to heterostructured nanohybrid, J. Phys. Chem. Solids 65 (2004) 373-383.
32. K. Akatsuka, G. Takanashi, Y. Ebina, M. Haga, T. Sasaki, Electronic band structure of exfoliated titanium-and/or niobium-based oxide nanosheets probed by electrochemical and photoelectrochemical measurements, J. Phys. Chem. C 116 (2012) 12426-12433.
33. J.L. Gunjakar, I.Y. Kim, J.M. Lee, Y.K. Jo, S.J. Hwang, Exploration of nanostructured functional materials based on hybridization of inorganic 2D nanosheets, J. Phys. Chem. C 118 (2014) 3847-3863.
34. J.L. Gunjakar, A.I. Inamdar, B.H. Hou, S. Cha, S.M. Pawar, A.A. Talha, H.S. Chavan, J. Kim, S. Cho, S. Lee, Y. Jo, H. Kim, H. Im, Direct growth of 2D nickel hydroxide nanosheets intercalated with polyoxovanadate anions as a binder-free supercapacitor electrode, Nanoscale 10 (2018) 8953-8961.
35. Y.R. Lee, I.Y. Kim, T.W. Kim, J.M. Lee, S.J. Hwang, Mixed colloidal suspensions of reduced graphene oxide and layered metal oxide nanosheets: Useful precursors for the porous nanocomposites and hybrid films of graphene/metal oxide, Chem. Eur. J. 18 (2012) 2263-2271.
36. B.D. Cullity, S.R. Stock, "Elements of X-rays diffraction", 3rd Edn., Prentice Hall, New York, 2001.
37. B.D. Cullity, "Elements of X-rays diffraction", 2nd Edn., Addison-Wesley, London, 1978.
38. R. Vilar, "Laser Surface Modification of Biomaterials: Techniques and Applications", Woodhead Publishing, United Kingdom, 2016.
39. H.-H. Perkampus, "UV-VIS spectroscopy and its applications", Springer Science & Business Media, 2013.
40. S. Patel, A. Raulji, D. Patel, D. Panchal, M. Dalwadi, U. Upadhyay, A review on UV visible spectroscopy, Int. J. Pharm. Res. 7 (2022) 1144-1151.
41. https://commons.wikimedia.org/wiki/File:Schematic_of_UV_visible_spectrophotometer.png
42. J. Preudhomme, P. Tarte, Infrared studies of spinels-III: The normal II–III spinels, Spectrochim. Acta 27 (1971) 1817-1835.
43. https://en.wikipedia.org/wiki/Raman_spectroscopy

44. E.B. Hanlon, R. Manoharan, T.-W. Ko, K.E. Shafer, J.T. Motz, M. Fitzmaurice, J.R. Kramer, I. Itzkan, R.R. Dasari, M.S. Feld, Prospects for in vivo Raman spectroscopy, Phys. Med. Biol. 45 (2000) R1-R59.
45. G.S. Bumbrah, R.M. Sharm, Raman spectroscopy-Basic principle, instrumentation and selected applications for the characterization of drugs of abuse, Egypt. J. Forensic Sci. 6 (2016) 209-215.
46. R.S. Das, Y.K. Agrawal, Raman spectroscopy: Recent advancements, techniques and applications, Vib. Spectrosc. 57 (2011) 163-176.
47. R.R. Jones, D.C. Hooper, L. Zhang, D. Wolverson, V.K. Valev, Raman techniques: Fundamentals and frontiers, Nanoscale Res. Lett. 14 (2019) 231.
48. N.B. Colthup, L.H. Daly, S.E. Wiberley, Introduction to Infrared and Raman spectroscopy, 3rd ed., Academic Press, 542, 1990.
49. https://en.wikipedia.org/wiki/Photoemission_spectroscopy
50. S. Kerber, T. Barr, G. Mann, W. Brantley, E. Papazoglou, The complementary nature of x-ray photoelectron spectroscopy and angle-resolved x-ray diffraction Part I: Background and theory, J. Mater. Eng. Perform. 7 (1998) 329-333.
51. https://www.slideshare.net/faheemmaqsood/xray-photoelecctron-spectroscopy-xps
52. https://epm.univie.ac.at/research/low-dimensional-quantum solids/methods/, X-Ray Photoemission Spectroscopy.
53. https://chem.libretexts.org/Courses/Franklin_and_Marshall_College/Introduction_o_Materials_Characterization__CHM_412_Collaborative_Text/Spectroscopy/Energy-Dispersive_X ray_Spectroscopy_%28EDS%29
54. https://www.globalsino.com/EM/page4661.html
55. https://en.wikipedia.org/wiki/Energy-dispersive_X-ray_spectroscopy
56. https://www.nanoimages.com/sem-technology-overview/sem_img2/, FE-SEM image
57. https://www.azom.com/article.aspx?ArticleID=16146, Interaction electron beam with sample
58. H. Anwer, A. Mahmood, J. Lee, K.-H. Kim, J.-W. Park, A.C.K. Yip, Photocatalysts for degradation of dyes in industrial effluents: Opportunities and challenges, Nano Res. 12 (2019) 955-972.
59. L. Karimi, S. Zohoori, M.E. Yazdanshenas, Photocatalytic degradation of azo dyes in aqueous solutions under UV irradiation using nano-strontium titanate as the nanophotocatalyst, J. Saudi Chem. Soc. 18 (2014) 581-588.
60. E.D. Revellame, D.L. Fortela, W. Sharp, R. Hernandez, M.E. Zappi, Adsorption kinetic modeling using pseudo-first order and pseudo-second order rate laws: A review, Cleaner Engg. and Technol. 1 (2020) 100032.

CHAPTER-3

Synthesis and Characterizations of NS-titanate-$BiVO_4$ Nanohybrids by CBD: Application in Photocatalytic Dye Degradation

CHAPTER-3

Synthesis and Characterizations of NS-titanate-$BiVO_4$ Nanohybrids by CBD: Application in Photocatalytic Dye Degradation

3.1 Introduction:

The contamination of water resources due to toxic dye effluents is a significant issue in modern society [1]. Among the various techniques developed for toxic dye removal, photocatalysis has attracted considerable research attention as it is a cost-effective and environmentally friendly process [2,3]. A wide range of nanostructured semiconductive materials are being developed and investigated as photocatalysts [4-10]. The need for hybridization to improve the photocatalytic activity of semiconducting materials is explained in **Chapters 1-2, Sections 1.3-2.4**.

Recently, advanced 2D MONs have been widely explored as basic building blocks for the development of various lattice-engineered nanohybrids owing to their fascinating characteristics [11,12]. The 2D NS-titanate produced by the soft-chemical exfoliation protocol from their bulk layered crystals are unique due to their highly anisotropic 2D morphology, negative surface charge, suitable band structure for the oxidation of H_2O and reduction of hydroxide ions with high chemical stability [13,14]. These NSs can be useful candidates for synthesizing nanohybrids since all the constituent ions in the sub-nanometer-thick 2D NSs come in contact with the surface, and their electronic structure can be dramatically altered through interaction with hybridized guest species. In addition, the narrow bandgap (~2.4 eV) $BiVO_4$ is one of the highly studied photocatalysts owing to its high efficiency, high photostability, low toxicity, low photo corrosion, high optical absorption coefficient (10^4-10^5 cm^{-1} at 350-520 nm), suitable band positions for water splitting and promising flat band potential (<200mV) favorable to hydrogen evolution reaction [15,16].

Consequently, the exfoliated NS-titanate can be the best choice for hybridization with $BiVO_4$. The hybridization of $BiVO_4$ with NS-titanate leads to improved photocatalytic activity because of the strong electronic coupling between the hybridized species, expanded surface area by the development of mesoporous house-of-card type structure and tunable chemical composition to achieve the desired photo-physicochemical properties [17]. Moreover, NS-titanate can act as macromolecules with negative surface charge and thus can be used as a precursor for depositing titanate thin films. As compared to others, the CBD method for the deposition of $BiVO_4$ layers on the surface of NS-titanate thin films can be treated as an effective method for the synthesis of NS-titanate-$BiVO_4$ nanohybrid thin films because the CBD method is simple, inexpensive and appropriate for large-area deposition carried out at low

temperatures with a variety of substrates. It offers numerous advantages, like easy control over film thickness, preparative parameters and growth. It can able to deposit materials with flexible chemical compositions that allow tuning the physicochemical properties of the deposited material.

From this insight, in this chapter, we demonstrated the novel approach for synthesizing intimately coupled NS-titanate-$BiVO_4$ nanohybrid thin films by combining EPD and CBD methods. Furthermore, the $BiVO_4$ and NS-titanate-$BiVO_4$ nanohybrid thin films are thoroughly analyzed for their functionalities in photocatalytic dye degradation application. Conclusionally, the importance of the hybridization of $BiVO_4$ with NS-titanate on the visible-light-driven photocatalytic degradation of MB and Rh-B dyes is explored together with their physicochemical characteristics.

3.2 Synthesis and characterizations of NS-titanate-$BiVO_4$ nanohybrids:

3.3 Experimental details:

3.3.1 Chemicals:

Titanium dioxide (TiO_2), cesium carbonate (Cs_2CO_3), bismuth nitrate pentahydrate ($Bi(NO_3)_3.5H_2O$), sodium metavanadate ($NaVO_3$), ethylenediamine tetraacetic acid (EDTA) disodium salt ($C_{10}H_{14}N_2Na_2O_8$), sodium hydroxide (NaOH), hydrochloric acid (HCl), tetra-butyl ammonium hydroxide (TBAOH) and ethanol (C_2H_5OH) were obtained from Sigma-Aldrich and used as received.

3.3.2 Synthesis of NS-titanate-$BiVO_4$:

The NS-titanate-$BiVO_4$ nanohybrid thin films were synthesized by a combination of EPD and CBD methods. The synthesis of NS-titanate-$BiVO_4$ nanohybrid thin films is comprised of the following steps:

(a) Synthesis of pristine NS-titanate:

The wide band gap and chemically stable NS-titanate were synthesized from their host cesium titanate crystals ($Cs_{0.7}Ti_{1.825}\square_{0.175}O_4$) by ion-exchange and exfoliation protocol, as displayed in **Fig. 3.1** [18-20]. The host crystals of cesium titanate were synthesized by a solid-state reaction of an intimate mixture of Cs_2CO_3 and TiO_2 (molar ratio of 1:5.3) at 800°C (20 h). The calcination process was repeated twice to get a highly crystalline pure phase. Initially, the protonated titanate ($H_{0.7}Ti_{1.825}\square_{0.175}O_4.H_2O$) was obtained by reaction of cesium titanate powder with 1 M HCl at ambient temperature for 4 days. The HCl solution was exchanged with a fresh one daily during protonation.

Afterwards, the solution was centrifuged, and the obtained protonated titanate was thoroughly washed with DDW and air-dried to eliminate the acidic residue. The layered protonated titanate was exfoliated into individual NS-titanate by intercalating TBA molecules into the inter-gallery space of protonic titanate. For this, the weighted amount of protonated titanate was reacted with an aqueous solution of TBAOH. The solution was shaken vigorously for 15 days, which produced the colloidal suspension of exfoliated NS-titanate.

(b) Synthesis of pristine NS-titanate thin films by EPD:

The well-cleaned indium-doped tin oxide (ITO) coated glass substrates were used to deposit NS-titanate thin films. The ITO-coated glass substrates were cleaned in an ultrasonic bath using ethanol, DDW, acetone, and DDW. The well-cleaned ITO-coated glass substrates were kept in DDW before use.

NS-titanate thin films by EPD were obtained from the dialyzed colloidal NS-titanate suspension. The colloidal suspension of NS-titanate (with pH of 12-12.5) was dialyzed for 10 h using a dialysis membrane (Dialysis Membrane-135, average flat width-33.12 mm, average diameter-23.8 mm, Capacity approx.-4.45 ml cm^{-1}) in DDW to attain a pH of 8. The NS-titanate dialysis solution and absolute ethanol were mixed in the 1:3 volume proportion for EPD. Uniform NS-titanate thin films were deposited on ITO-coated glass substrates using a specially designed cylindrical graphite EPD cell and applying the potential of 10 V DC across the ITO and graphite cell. Herein, graphite cell and ITO substrates act as a cathode and anode, respectively. The deposition time of EPD was adjusted to a range of 5 to 15 min, and the films were air-dried. Further, the EPD-deposited NS-titanate thin films were annealed at 220℃ for 2 h in the air to remove TBA and improve adherence. The annealed NS-titanate thin films coated at 5, 10 and 15-min deposition times are represented as Ti-1, Ti-2, and Ti-3, respectively.

(c) Synthesis of NS-titanate-$BiVO_4$ nanohybrid thin films:

The narrow band gap $BiVO_4$ was deposited over the EPD-deposited NS-titanate thin films by the facile CBD method. A chemical bath for the deposition of $BiVO_4$ comprising an aqueous solution of 25 mM $Bi(NO_3)_3 \cdot 5H_2O$ complexed with disodium EDTA salt (25 mM) under constant stirring. The aqueous solution of 25 mM $NaVO_3$ was prepared as a vanadium precursor. The chemical bath was obtained by mixing vanadium precursor solution into the bismuth complex under constant stirring. The pH

of the bath was adjusted at 5.5 using an aqueous solution of 1 M NaOH and kept at 85°C under continuous stirring for 1 h to obtain a transparent pale-yellow color solution.

Further, the obtained solution was allowed to cool down at room temperature and used as a deposition solution. The NS-titanate coated (Ti-1, Ti-2 and Ti-3) ITO substrates were placed in the above deposition bath. The deposition vessel was closed and placed in a water bath at 85°C for 10 h, leading to the direct growth of $BiVO_4$ on NS-titanate thin films. After the deposition, NS-titanate-$BiVO_4$-coated ITO substrates were removed from the bath, washed with DDW, and air-dried. The schematic representation of the NS-titanate-$BiVO_4$ thin film deposition process is shown in **Fig. 3.1**. Subsequently, the as-prepared NS-titanate-$BiVO_4$ nanohybrid thin films were annealed at 400°C for 2 h. The annealed NS-titanate-$BiVO_4$ nanohybrid thin films deposited on Ti-1, Ti-2 and Ti-3 thin films are represented as C-BT1, C-BT2 and C-BT3, respectively.

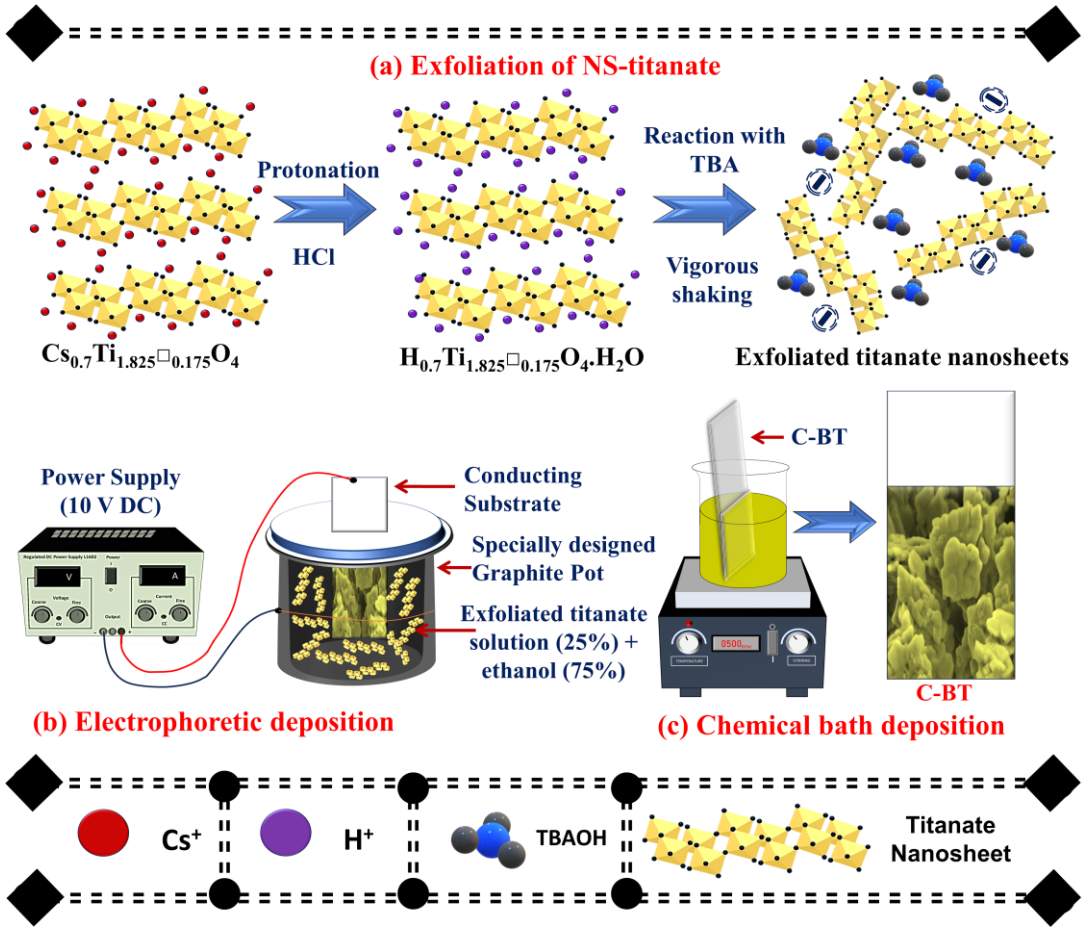

Fig. 3.1: Schematic representation of (a) exfoliation of NS-titanate, (b) EPD of NS-titanate thin films and (c) CBD method for the synthesis of NS-titanate-$BiVO_4$ nanohybrid thin films.

3.4 Characterizations of NS-titanate-$BiVO_4$ nanohybrids:

The crystal structures of pristine NS-titanate, $BiVO_4$ and NS-titanate-$BiVO_4$ nanohybrid thin films were studied with XRD analysis using Rigaku miniflex 600 Diffractometer (Cu k_α radiation: λ= 1.54 Å). The chemical bonding features of pristine NS-titanate and $BiVO_4$ thin films compared to NS-titanate-$BiVO_4$ nanohybrid thin films were probed with FT-IR spectra recorded on αT Bruker spectrometer. The chemical bonding of present nanohybrid thin films was further explored by micro-Raman spectroscopy collected on a FLEX G spectrometer (Tokyo Instrument, Japan) having an excitation wavelength of 532 nm. The oxidation states of elements present on the surface of stated thin films were investigated with XPS recorded on Thermo Scientific using Al K_α (1486.6 eV) X-ray source. The surface morphology and spatial elemental distribution of the synthesized nanohybrid thin films were scrutinized with FESEM technique using JEOL JSM-7900 F electron microscope equipped with EDS-elemental mapping analysis. The optical properties and band structure of the nanohybrid thin films were investigated with UV-vis DRS using a Jasco spectrometer.

Note: The C-BT2 nanohybrid thin film shows improved photocatalytic dye degradation performance. Therefore, all the optimized C-BT2 nanohybrid thin film characterizations are compared with the pristine materials.

3.4.1 XRD analysis:

The crystal structures of the pristine NS-titanate, $BiVO_4$ and NS-titanate-$BiVO_4$ nanohybrid (C-BT2) thin films were investigated with XRD analysis, as represented in **Fig. 3.2**. The cesium titanate ($Cs_{0.7}Ti_{1.825}\square_{0.175}O_4$) (**Fig. 3.2(a)**) shows a highly intense (020), (040), (060) and (200) diffraction peaks corresponding to lepidocrocite-type layered structure with orthorhombic symmetry (JCPDS: 84-1226) [21,22]. Its protonated derivative ($H_{0.7}Ti_{1.825}\square_{0.175}O_4.H_2O$) also displays sharp (020), (060), and (200) diffraction peaks slightly shifted toward the lower Braggs angles signifying the lattice expansion due to intercalation of water molecules in the inter-gallery space of layered crystals [23,24]. Additionally, signature (hkl) peaks (130), (150), and (051) matching with the in-plane host structure are present, demonstrating that the in-plane host structure remains intact after the protonation process [21]. The XRD pattern of pristine NS-titanate thin film (**Fig. 3.2(b)**) shows a broad diffraction peak centered at 10° corresponds to the (020) plane of lepidocrocite type NS-titanate with orthorhombic symmetry having an interplanar spacing of 0.88 nm [21]. The presence of this peak

indicates the layer-by-layer stacking of titanate NSs. Moreover, the diffraction peaks marked by the '*' correspond to the ITO substrate. The pristine $BiVO_4$ thin film displays typical Braggs reflections corresponding to the monoclinic scheelite $BiVO_4$ phase (I2/a) (JCPDS no.: 14-0688). Remarkably, the apparent peak splitting is observed at 2θ equal to 18.5°, 35° and 46°, clearly indicating the formation of $BiVO_4$ in the monoclinic scheelite phase [25]. On the other hand, the C-BT2 nanohybrid thin film displays diffraction peaks corresponding to both lepidocrocite type NS-titanate (marked with circles) and monoclinic scheelite $BiVO_4$ (marked with squares). It shows a broad (020) diffraction plane corresponding to the lepidocrocite type NS-titanate with orthorhombic symmetry. It also shows typical Braggs reflections with apparent peak splitting at 18.5°, 35° and 46 °, corresponding to the monoclinic scheelite $BiVO_4$ phase. Present XRD features related to the NS-titanate and $BiVO_4$ confirm the formation of NS-titanate and $BiVO_4$ in lepidocrocite-type layered structure and monoclinic scheelite-type structure, respectively. This clearly indicates the growth of monoclinic scheelite $BiVO_4$ over electrophoretically deposited NS-titanate thin films.

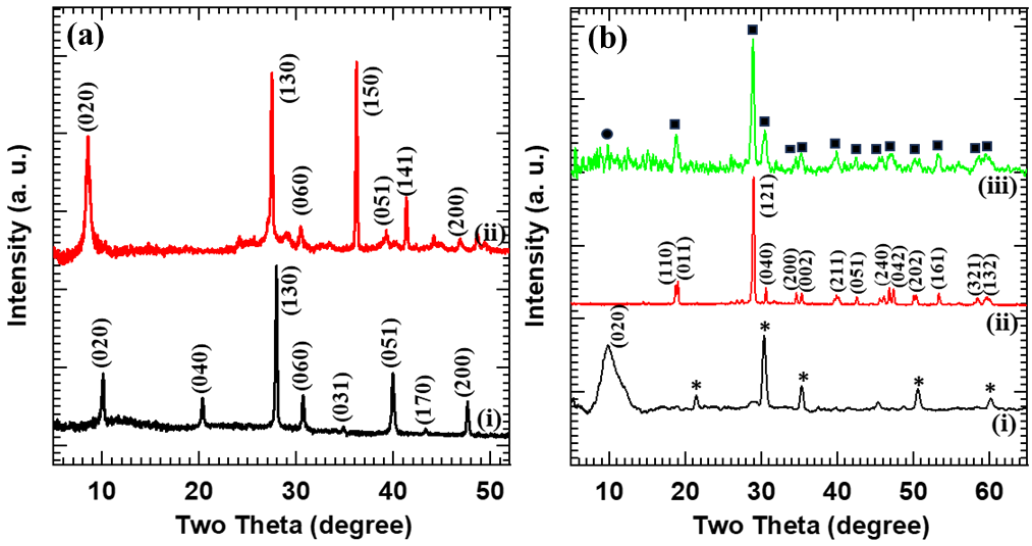

Fig. 3.2: (a) XRD patterns of (i) cesium titanate, (ii) protonated titanate and (b) XRD patterns of (i) NS-titanate, (ii) $BiVO_4$, (iii) C-BT2 nanohybrid thin films (In the XRD pattern of (iii), circles and squares represent the Bragg reflections of NS-titanate and monoclinic scheelite $BiVO_4$, respectively).

3.4.2 FTIR analysis:

The chemical bonding nature and microscopic structural features of NS-titanate-$BiVO_4$ nanohybrid thin film compared to the pristine NS-titanate and $BiVO_4$ thin films were probed with FTIR spectroscopy. As represented in **Fig. 3.3**, the pristine NS-titanate

thin film exhibits the signature absorption peaks *v*1 (482.17 cm^{-1}) and *v*2 (657.5 cm^{-1}) corresponding to the Ti-O bending mode and Ti-O-Ti stretching mode of the layered TiO_2, respectively [26,27]. The absorption peaks *v*3 (1108.51 cm^{-1}) and *v*4 (1381 cm^{-1}) are attributed to the stretching vibrations of the C-O group in primary alcohol and bending vibrations of the -CH_2- group in alkyl chain, respectively [28]. The absorption peaks *v*5 (1630 cm^{-1}) and *v*6 (3446.87 cm^{-1}) are linked with the bending vibrations of water molecules and stretching vibrations of hydroxyl groups, respectively [29]. The pristine $BiVO_4$ thin film shows sharp absorption peaks *v*7 (413 cm^{-1}) and *v*8 (482 cm^{-1}) corresponding to the Bi-O bending and the VO_4^{3-} stretching vibrations, respectively [30,31]. The absorption peaks *v*9 (741 cm^{-1}) and *v*10 (829 cm^{-1}) are assigned to the asymmetric and symmetric stretching of VO_4^{3-}, respectively [32]. The absorption peak *v*11 (3451.11 cm^{-1}) is associated with the stretching vibrations of hydroxyl groups [32].

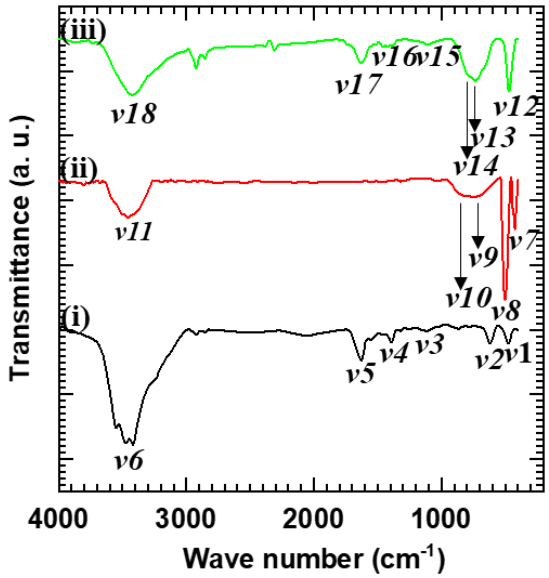

Fig. 3.3: FTIR spectra of (i) NS-titanate, (ii) $BiVO_4$ and (iii) C-BT2 nanohybrid thin films.

On the other hand, the NS-titanate-$BiVO_4$ nanohybrid thin film displays absorption peaks *v*12 (482.17 cm^{-1}), *v*13 (736 cm^{-1}), *v*14 (788 cm^{-1}), *v*15 (1105 cm^{-1}), *v*16 (1387cm^{-1}), *v*17 (1625 cm^{-1}) and *v*18 (3427 cm^{-1}). The peak *v*12 is assigned to the Ti-O bending mode of the layered TiO_2 [26]. The absorption peaks *v*13 and *v*14 are attributed to the asymmetric and symmetric stretching vibration of the V-O bond, respectively [32]. The mild absorption peaks *v*15 and *v*16 correspond to the stretching vibrations of the C-O group in primary alcohol and bending vibrations of the -CH_2- group in the alkyl chain, respectively [28]. The absorption peaks *v*17 and *v*18 are linked with the bending vibrations of water molecules and stretching vibrations of hydroxyl

groups, respectively [29]. The present FTIR analysis shows the chemical bonding features matching with both lepidocrocite-type NS-titanate and monoclinic scheelite-type $BiVO_4$. These spectral features clearly highlight the successful growth of monoclinic scheelite $BiVO_4$ over lepidocrocite-type NS-titanate thin films.

3.4.3 Raman analysis:

The chemical bonding nature of synthesized thin films was further probed with Raman spectroscopy, as shown in **Fig. 3.4**. The micro-Raman spectrum of NS-titanate shows several Raman peaks related to the Ti-O vibrations in NS-titanate. The micro-Raman spectrum of NS-titanate shows the spectral features P_1 (279.2 cm^{-1}) and P_2 (446.88 cm^{-1}) are assigned to the degenerate modes of the TiO_6 octahedron with Ag symmetry [33]. The sharp and intense Raman peak P_3 (708 cm^{-1}) is attributed to the symmetric Ti-O vibrations [34-36]. The mild Raman peak P_4 (919.46 cm^{-1}) is attributed to the stretching modes of shorter Ti-O bonds, which stick out into the interlayer spacings of NS-titanate [35-36]. These Raman peaks indicate deposition of well-developed 2D lepidocrocite-type layered NS-titanate. Similarly, $BiVO_4$ thin film shows the Raman peaks P_5 (131 cm^{-1}) and P_6 (212 cm^{-1}) are ascribed to the external rotation or translation modes of $BiVO_4$ [37]. Also, $BiVO_4$ displays characteristic Raman peaks P_7 (325 cm^{-1}) and P_8 (367 cm^{-1}), corresponding to the asymmetric (Bg symmetry) and symmetric (Ag symmetry) bending modes of the VO_4 tetrahedron, respectively [38]. The peaks P_9 (710 cm^{-1}) and P_{10} (826 cm^{-1}) are assigned to the asymmetric and symmetric (V-O) stretching modes of $BiVO_4$, respectively [37-39].

On the other hand, the NS-titanate-$BiVO_4$ nanohybrid thin film shows the Raman peak related to the NS-titanate and $BiVO_4$. The Raman peaks P_{11} (134 cm^{-1}) and P_{12} (219 cm^{-1}) originated due to the Ti-O vibrations with Ag symmetry. The Raman peaks P_{13} (334 cm^{-1}), P_{14} (373 cm^{-1}) and P_{15} (828 cm^{-1}) are assigned to the B_g asymmetric bending of the VO_4 tetrahedron, Ag symmetric bending mode of the VO_4 tetrahedron and symmetric (V-O) stretching modes, respectively [37-39]. The present work is related to the exfoliation of layered titanate that leads to exfoliated ultrathin monolayers of 2D NS-titanate. During the NS-titanate-$BiVO_4$ nanohybrid thin film formation, titanate NSs are uniformly coated with $BiVO_4$. Due to the low thickness of NS-titanate thin film, the Raman spectrum of C-BT2 nanohybrid thin film majorly displays Raman peaks corresponding to the $BiVO_4$. All the Raman peaks of NS-titanate are not active due to

the relatively thick $BiVO_4$ coating on NS-titanate that constrained Raman active vibrations of NS-titanate. The observed characteristic Raman features are related to chemical bonding in EPD-deposited NS-titanate and CBD-deposited $BiVO_4$ thin films. These spectral features provide strong evidence for the successful growth of $BiVO_4$ over EPD-deposited NS-titanate thin films.

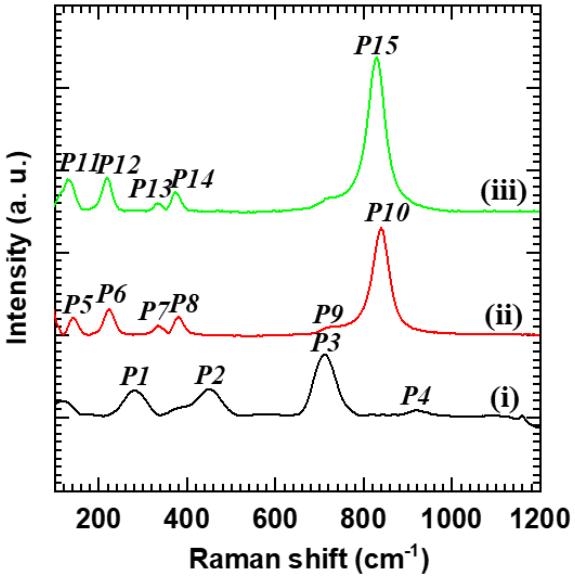

Fig. 3.4: Micro-Raman spectra of (i) NS-titanate, (ii) $BiVO_4$ and (iii) C-BT2 nanohybrid thin films.

3.4.4 XPS analysis:

The surface chemical compositions and different oxidation states of the NS-titanate-$BiVO_4$ nanohybrid thin film compared to pristine NS-titanate and $BiVO_4$ thin films were investigated with XPS analysis. The survey and high-resolution Ti 2p, Bi 4f, V2p, O 1s XPS spectra of the pristine NS-titanate, $BiVO_4$ and NS-titanate-$BiVO_4$ nanohybrid thin films are plotted in **Fig. 3.5** and **Fig. 3.6**. The survey XPS spectrum of C-BT2 nanohybrid thin film (**Fig. 3.5**) displays the spectral features at BE of the Ti, Bi, V and O elements, representing the presence of stated elements in C-BT2 thin film. As represented in high-resolution Ti 2p spectra (**Fig. 3.6(a)**), the pristine NS-titanate and NS-titanate-$BiVO_4$ nanohybrid thin films show two spectral features, P (464.1 eV) and Q (458.36 eV), correspond to the spin-orbit splitting of Ti $2p_{1/2}$ and Ti $2p_{3/2}$, respectively [40,41]. The position of peaks with BE difference of 20 eV indicates the +4 oxidation state of Ti in present samples. As shown in high-resolution Bi 4f spectra (**Fig. 3.6(b)**), the pristine $BiVO_4$ and NS-titanate-$BiVO_4$ nanohybrid thin films display intense peak doublet R (164.2 eV) and S (158.9 eV) ascribed to the Bi $4f_{5/2}$ and Bi $4f_{7/2}$, respectively that confirms the Bi^{3+} state in $BiVO_4$ [42]. As plotted in high-resolution V 2p spectra

(**Fig. 3.6(c)**), the pristine $BiVO_4$ and NS-titanate-$BiVO_4$ nanohybrid thin films exhibit two sharp peaks, A (523.01 eV) and B (515.4 eV) assigned to the spin-orbit splitting of V $2p_{1/2}$ and V $2p_{3/2}$, respectively [43]. This indicates the presence of V^{5+} in pristine $BiVO_4$ and NS-titanate-$BiVO_4$ nanohybrid. The high-resolution O 1s spectra (**Fig. 3.6(d)**) show an intense peak M (529.5 eV) assigned to the oxygen from the pristine NS-titanate, $BiVO_4$ and NS-titanate-$BiVO_4$ lattice, respectively [42]. For NS-titanate thin film, peak M is ascribed to Ti-O bonding. For $BiVO_4$ thin film, peak M corresponds to Bi-O and V-O bonding. On the other hand, for NS-titanate-$BiVO_4$ thin film, peak R is attributed to the Ti-O, Bi-O and V-O bonding. Interestingly, the Ti 2p, Bi 4f, V 2p and O 1s XPS spectra of the C-BT2 nanohybrid thin film slightly shift towards lower BEs after hybridization, suggesting an increase in electron density [44]. The intimate electronic coupling between NS-titanate and $BiVO_4$ resulted in the enhanced electron density on the NS-titanate-$BiVO_4$ nanohybrid. The obtained XPS features indicate the presence of Ti, Bi and V in Ti^{4+}, Bi^{3+} and V^{5+} states in NS-titanate-$BiVO_4$ nanohybrid thin film, respectively. These spectral features highlight the effective hybridization between NS-titanate and $BiVO_4$ in NS-titanate-$BiVO_4$ nanohybrid thin film.

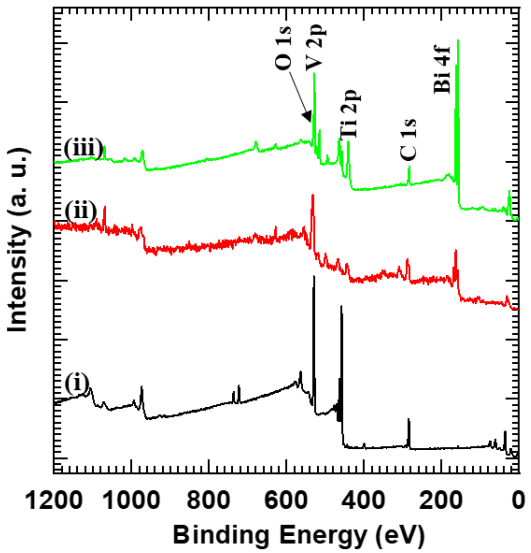

Fig. 3.5: Survey XPS spectra of (i) NS-titanate, (ii) $BiVO_4$ and (iii) C-BT2 nanohybrid thin films.

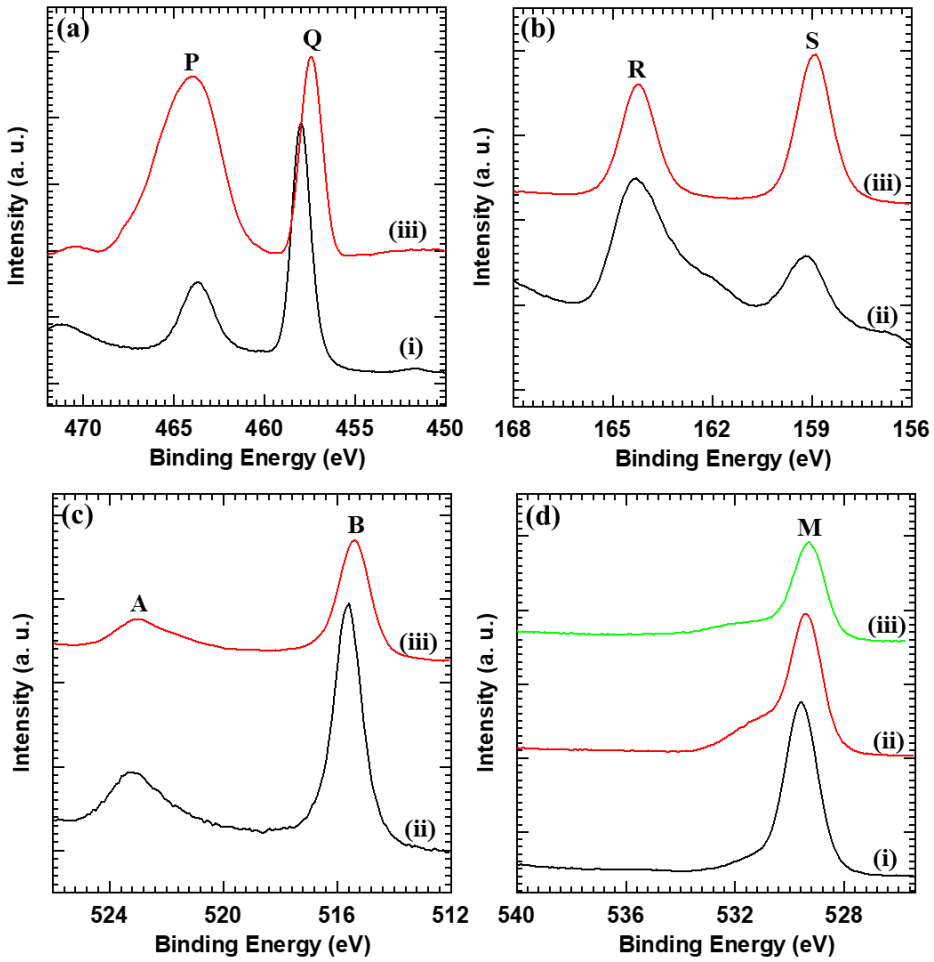

Fig. 3.6: (a) Ti 2p, (b) Bi 4f, (c) V 2p and (d) O 1s Core-level XPS spectra of (i) NS-titanate, (ii) $BiVO_4$ and (iii) C-BT2 nanohybrid thin films.

3.4.5 FESEM analysis:

The surface morphological features of the NS-titanate-$BiVO_4$ nanohybrid thin film in comparison with pristine NS-titanate and $BiVO_4$ thin films were probed with FESEM analysis, as displayed in **Fig. 3.7**. The electrophoretically deposited NS-titanate thin film (**Fig. 3.7(a)**) shows deposited titanate NSs laying parallel to the ITO substrate surface. The lateral sheet size of titanate NSs is in the range of 500 to 600 nm. The NSs are randomly aggregated on the ITO substrate surface, creating a porous structure of NS-titanate thin film. $BiVO_4$ thin film (**Fig. 3.7(b)**) demonstrates interconnected nanoparticle morphology with a particle size range of 75 to 95 nm [45].

Interestingly, significant morphological changes are observed in $BiVO_4$ after NS-titanate-$BiVO_4$ nanohybrid thin film formation. The observed change of interconnected nanoparticle morphology to highly smooth $BiVO_4$ deposit is attributed to the provision of NS-titanate nucleation sites for the smooth growth of $BiVO_4$. The NS-titanate-$BiVO_4$ nanohybrid thin film displays randomly deposited nanoplates

composed of NS-titanate uniformly covered with smooth $BiVO_4$ deposit. The edge-to-face interaction of randomly deposited interconnected nanoplates makes a mesoporous house-of-cards type structure, as revealed in **Fig. 3.7(c-d)**. A close topographical inspection of hybrid nanoplates reveals lateral size in the range of 650 to 750 nm and thickness in the 75 to 100 nm range. Considering lateral dimensions (~500 to 600 nm) and thickness (0.8 nm) of electrophoretically deposited NS-titanate, one can judge the deposition of smooth $BiVO_4$ on electrophoretically deposited NS-titanate. Such a hybrid structure can enable intimate electronic coupling between the NS-titanate and $BiVO_4$, which is highly beneficial in special electron-hole pair separation for solar-assisted photo-functional applications. A similar type of morphology is generally obtained for 2D NSs-based nanohybrids, which is advantageous for various applications [46-48].

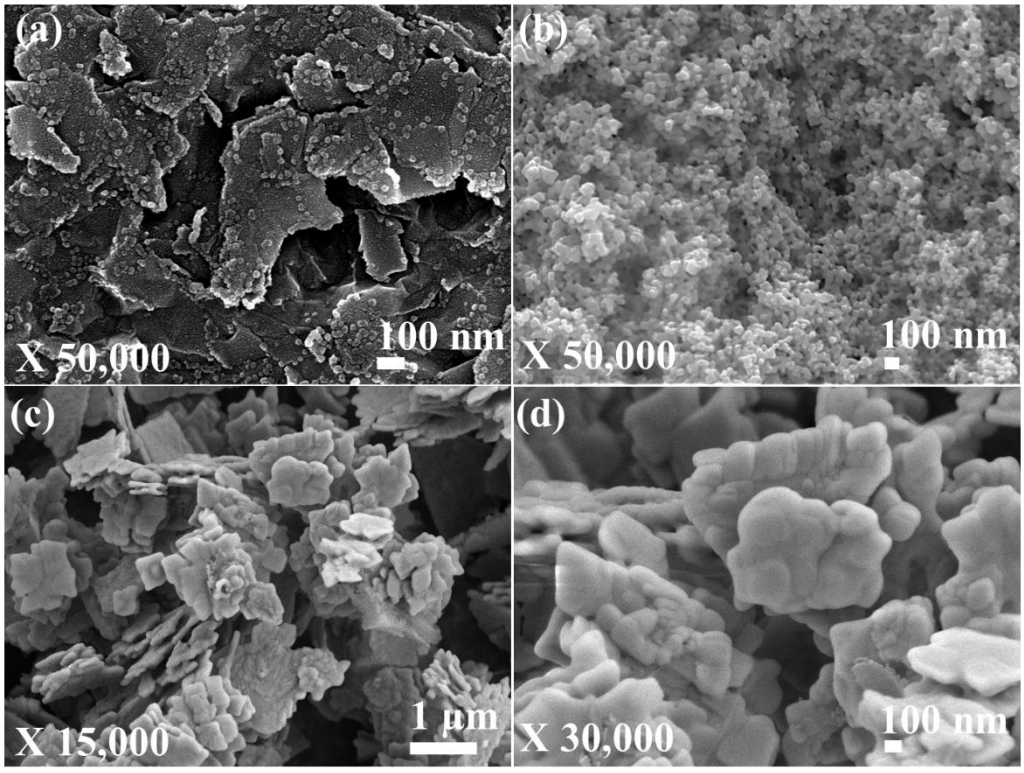

Fig. 3.7: FESEM micrographs of (a) NS-titanate, (b) $BiVO_4$ and (c-d) C-BT2 nanohybrid thin films.

3.4.6 EDS analysis:

Further, the distribution of constituent elements and chemical composition in NS-titanate-$BiVO_4$ nanohybrid thin films was investigated using elemental mapping and EDS study, as represented in **Fig. 3.8** and **Fig. 3.9**. The nanohybrid thin film displays a uniform distribution of titanium (Ti), bismuth (Bi), vanadium (V) and oxygen (O) elements with a Bi/V ratio of 1 over the whole mapping region, indicating the uniform

growth of $BiVO_4$ on the surface of the NS-titanate thin film. Due to the high thickness of $BiVO_4$ thin film, the Ti composition is observed lower in the hybrid sample. However, the upper layer $BiVO_4$ shows deposition of stoichiometric $BiVO_4$ with a Bi/V ratio of 1.

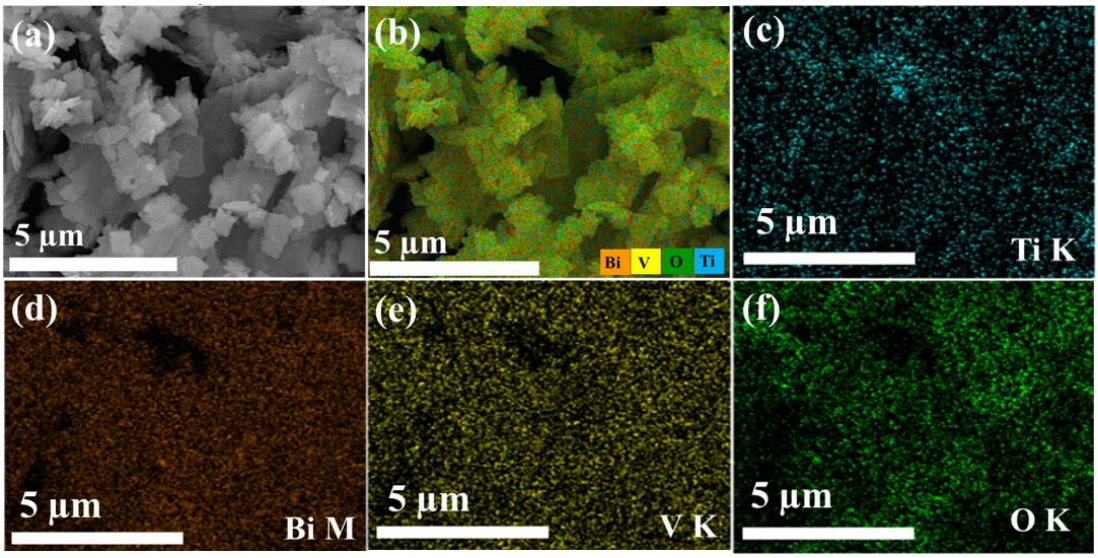

Fig. 3.8: (a) FESEM image and (b-f) EDS elemental maps of C-BT2 nanohybrid thin film.

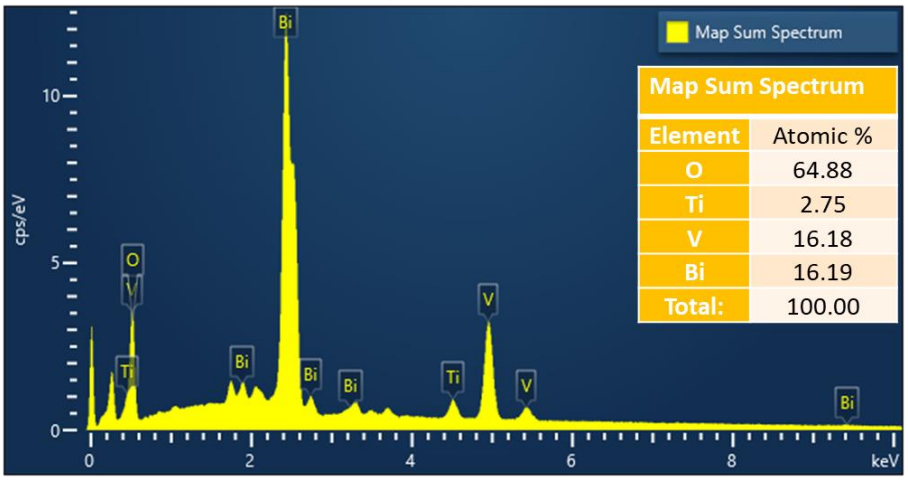

Fig. 3.9: EDS spectrum of C-BT2 nanohybrid thin film.

3.4.7 UV-vis DRS analysis:

The band structure and optical characteristics of NS-titanate-$BiVO_4$ nanohybrid thin film compared with pristine NS-titanate and $BiVO_4$ thin films were investigated with UV-vis DRS. As plotted in **Fig. 3.10**, the pristine $BiVO_4$ thin film displays prominent absorption in the visible region of the solar spectrum with bandgap energy of 2.3 eV assigned to the transition of electrons from hybrid Bi 6s/O 2p orbital to V 3d orbital [49]. The NS-titanate thin film shows a notable spectral difference compared to the optical profile of $BiVO_4$ thin film. It shows remarkable absorption in the UV region

with a bandgap energy of 3.17 eV. On the other hand, upon hybridization of NS-titanate with $BiVO_4$, the resultant nanohybrid thin film shows significant absorption in the visible region with a bandgap of 2.39 eV, clearly demonstrating the efficient electronic coupling between NS-titanate and $BiVO_4$. The observed results provide strong evidence for the superior visible light harvesting capability of NS-titanate-$BiVO_4$ nanohybrid thin film [46,47]. The strong visible light absorption ability of NS-titanate-$BiVO_4$ nanohybrid thin films makes them potential candidates for visible-light-driven photocatalysis applications.

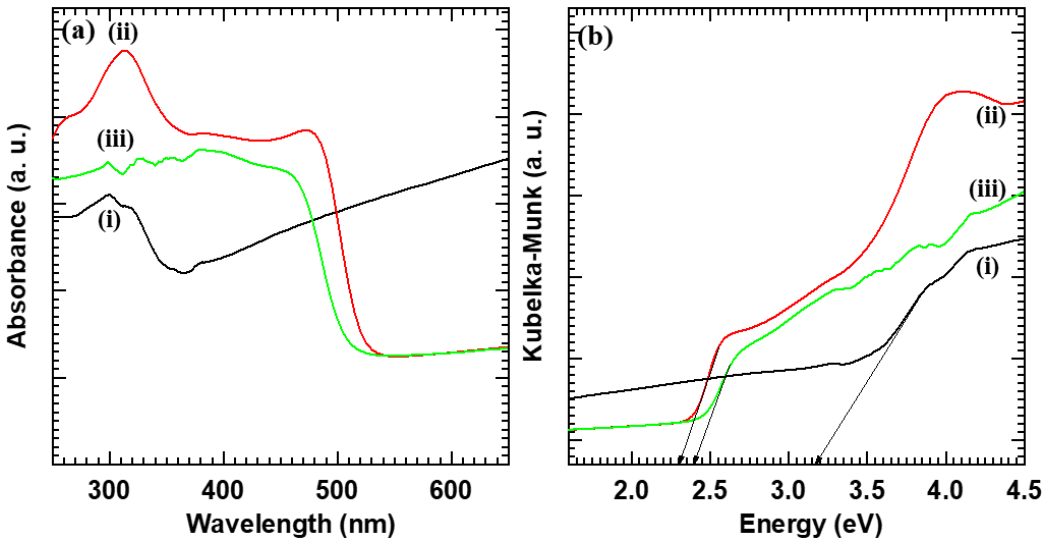

Fig. 3.10: (a) UV-vis absorbance spectra and (b) UV-vis DRS of (i) NS-titanate, (ii) $BiVO_4$, (iii) C-BT2 nanohybrid thin films.

3.5 Dye degradation Performance of NS-titanate-$BiVO_4$ nanohybrids:

The photocatalytic properties of NS-titanate-$BiVO_4$ nanohybrid thin films compared with pristine NS-titanate and $BiVO_4$ thin films were estimated for photodegradation of MB and Rh-B dyes under visible light illumination (light intensity = 100 mW cm^{-2}). In a typical experiment, the pristine NS-titanate or $BiVO_4$ or NS-titanate-$BiVO_4$ nanohybrid thin film (area: 1 cm^2) was kept vertically in the quartz photoreactor filled with 3 ml of dye solution (concentration: 50 µm). This solution was left to equilibrate with the target dye molecules for 30 min in a dark condition to assess the adsorption-desorption equilibrium of dye molecules on the catalyst surface. All the photocatalytic measurements were conducted at ambient conditions. During the photocatalytic experiments, the light obtained from the xenon lamp (light intensity of 100 mW cm^{-2}) was simulated by the AM 1.5 G and 420 nm optical cut-off filters. The

simulated light was focused on the quartz photoreactor. During the experiment, the photocatalyst thin film (NS-titanate or $BiVO_4$ or NS-titanate-$BiVO_4$ nanohybrid thin film) was withdrawn at specific time periods, and the change in concentration of dye solution was measured with UV-vis spectrophotometer (Carry 60 UV-vis: Agilent Technology). The change in concentration of MB and Rh-B dyes was observed by absorbance measurement at representative wavelengths of 664 and 553 nm, respectively. The photocatalytic degradation efficiency of NS-titanate, $BiVO_4$ and NS-titanate-$BiVO_4$ nanohybrid thin films was estimated from the analysis of UV-vis absorption spectra using the following equation,

$$\text{Percentage degradation} = \frac{C_0 - C_t}{C_0} \times 100 \quad (3.1)$$

where C_0 is absorption at the initial time, and C_t denotes absorption at time t.

Furthermore, the pseudo-first-order kinetic models were used to investigate photocatalytic degradation kinetics. The following relation represents a pseudo-first-order reaction,

$$\ln\left(\frac{C_0}{C_t}\right) = kt \quad (3.2)$$

where C_0, C_t, and k denote absorption at the initial time, absorption at a time 't', and rate constant, respectively.

3.5.1 Percentage degradation study for MB and Rh-B:

The photoactivity of NS-titanate-$BiVO_4$ nanohybrid thin films is investigated with photocatalytic degradation of MB and Rh-B as target dyes in the presence of visible light irradiations. The photodegradation performances of pristine NS-titanate and $BiVO_4$ thin films are also evaluated to study the effect of hybridization on photocatalytic activity. The photodegradation performance of NS-titanate-$BiVO_4$ nanohybrid thin films in comparison with pristine NS-titanate and $BiVO_4$ thin films is calculated using equation (3.1) and plotted in **Fig. 3.13** (their respective UV-vis absorbance spectra are shown in **Fig. 3.11 and Fig. 3.12**) [50]. The pristine NS-titanate, $BiVO_4$ and NS-titanate-$BiVO_4$ nanohybrid thin films display decrease in absorption at characteristic wavelengths of 664 and 553 nm with respect to irradiation time, demonstrating the superior degradation of MB and RhB, respectively. The NS-titanate thin film exhibited negligible photocatalytic performance of 10% and 6% for MB and Rh-B under visible light due to its wide band gap energy. On the other hand, the pristine $BiVO_4$ thin film displays superior photocatalytic activity for the photodegradation of both MB and Rh-B

dyes. The photocatalytic activity of pristine $BiVO_4$ is remarkably improved upon hybridization with NS-titanate. The optimized C-BT2 nanohybrid thin film photocatalyst demonstrated outstanding photoactivity for the photodegradation of MB and Rh-B dyes with photodegradation rates of 85.1 and 97%, respectively, which are higher than that of pristine $BiVO_4$ thin film (54 and 70%). It is concluded that the present NS-titanate-$BiVO_4$ nanohybrid thin films with enhanced photoactivity can be considered highly active visible-light-driven photocatalysts for the photodegradation of dyes.

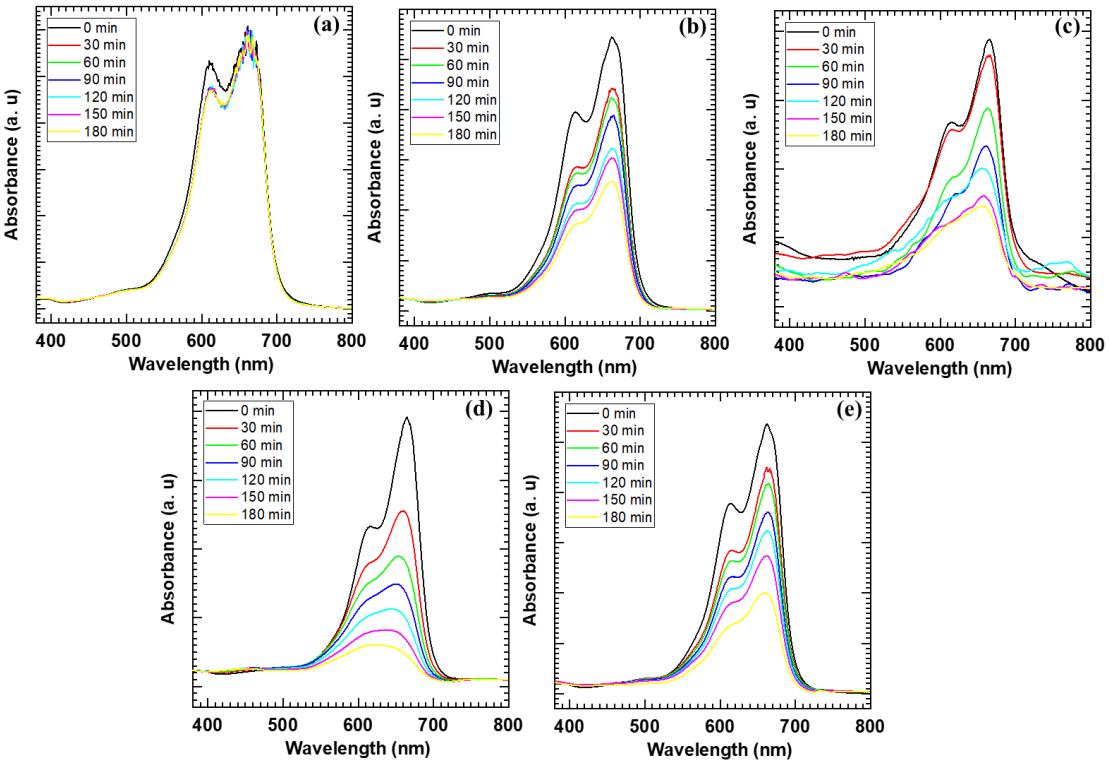

Fig. 3.11: UV-vis absorption spectra of the MB solution in the presence of (a) NS-titanate, (b) $BiVO_4$, (c) C-BT1-, (d) C-BT2- and (e) C-BT3 nanohybrid thin film photocatalysts.

The improvement of photocatalytic degradation activity of $BiVO_4$ upon hybridization with highly stable NS-titanate can be ascribed to the exceptional electronic coupling between NS-titanate and $BiVO_4$, which leads to the enhanced electron density beneficial for the effective photocatalytic reactions. The surface expansion that occurs during hybridization by creating a highly porous house-of-cards type structure can contribute to increased photocatalytic activity by giving rise to more reaction sites and effective electron-hole transport. Furthermore, in a hybrid structure, electron-hole recombination is depressed due to the spatial separation of photoinduced holes and electrons caused by the intimate electronic coupling between NS-titanate and $BiVO_4$, leading to improved photocatalytic activity. In conclusion, the exceptional

photocatalytic activity of present nanohybrid thin films can ascribed to the strong visible light harvesting ability, reduced electron-hole recombination, high photostability and mesoporous house-of-cards type structure of NS-titanate-$BiVO_4$ nanohybrid thin films.

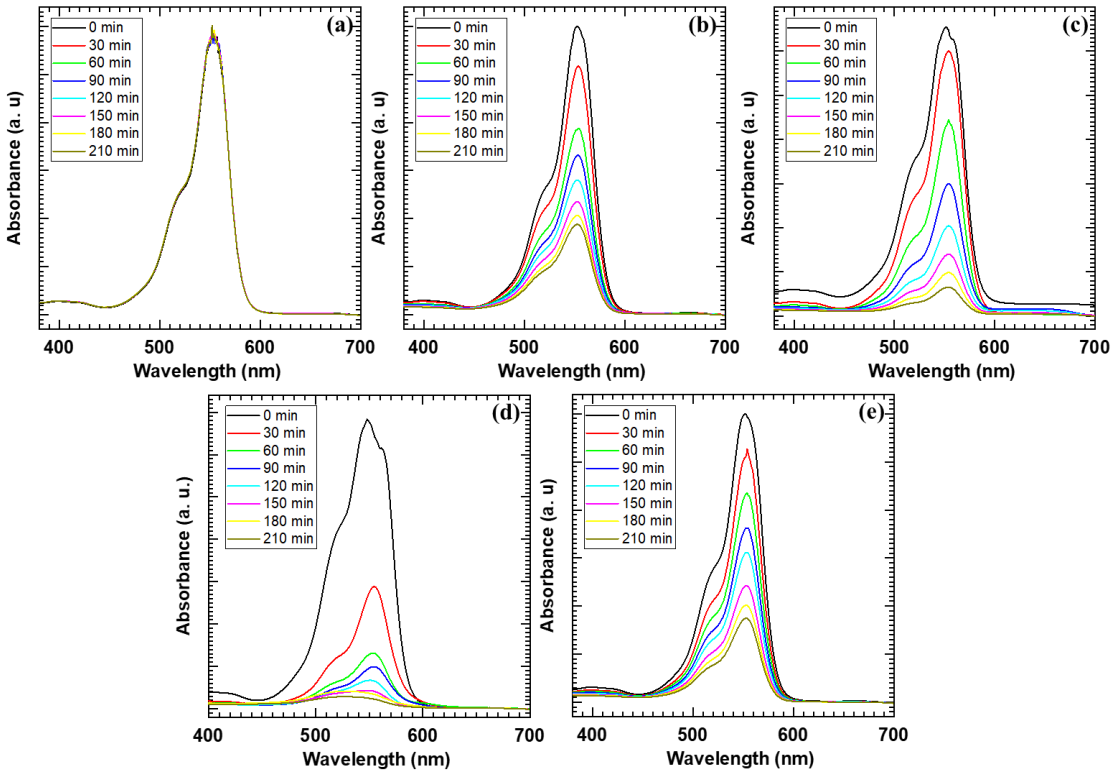

Fig. 3.12: UV-vis absorption spectra of the Rh-B solution in the presence of (a) NS-titanate, (b) $BiVO_4$, (c) C-BT1-, (d) C-BT2- and (e) C-BT3 nanohybrid thin film photocatalysts.

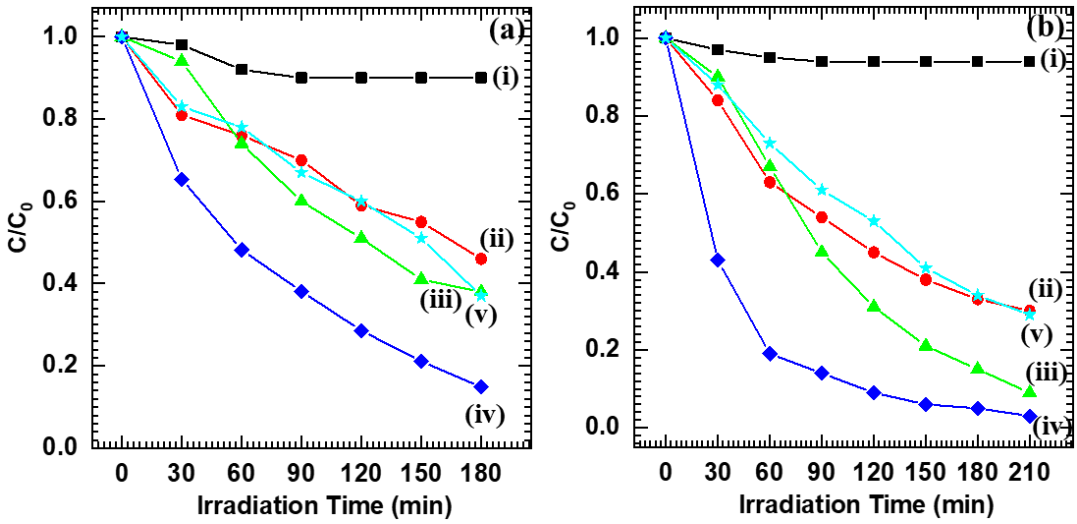

Fig. 3.13: (a) MB and (b) Rh-B degradation performance of (i) NS-titanate, (ii) $BiVO_4$, (iii) C-BT1-, (iv) C-BT2-, (v) C-BT3 nanohybrid thin film photocatalysts.

3.5.2 Rate kinetics study for MB and Rh-B:

The photocatalytic decomposition of MB and Rh-B was further studied to probe the kinetics using a pseudo-first-order rate kinetic model [51]. The pseudo-first-order reaction kinetics of MB and Rh-B dyes are represented in **Fig. 3.14**. The k and linear correlation coefficient (R^2) values of all tested photocatalysts for MB and Rh-B photodegradation are summarized in **Table 3.1**. Among all tested photocatalysts, the C-BT2 nanohybrid thin film shows improved k values (0.0105 and 0.0167 min^{-1} for MB and Rh-B, respectively), confirming the highest photocatalytic performance. The improved k-value for C-BT2 nanohybrid thin film is attributed to the strong visible light harvesting ability, reduced electron-hole recombination, high photostability and mesoporous house-of-cards type morphology beneficial for effective photocatalytic reactions.

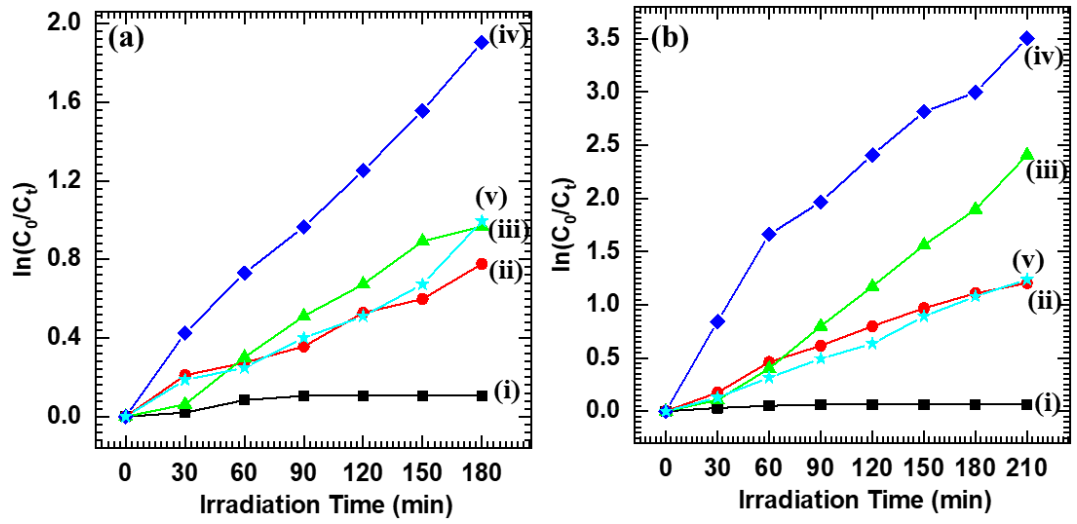

Fig. 3.14: Pseudo-first-order kinetics of (a) MB and (b) Rh-B for (i) NS-titanate, (ii) $BiVO_4$, (iii) C-BT1-, (iv) C-BT2-, (v) C-BT3 nanohybrid thin film photocatalysts.

Table 3.1: k and R^2 values of all tested photocatalysts.

Sample	MB		Rh-B	
	k (min^{-1})	R^2	k (min^{-1})	R^2
NS-titanate	0.0005	0.9995	0.0003	0.9997
$BiVO_4$	0.0043	0.9957	0.0057	0.9943
C-BT1	0.0053	0.9947	0.0114	0.9886
C-BT2	0.0105	0.9895	0.0167	0.9833
C-BT3	0.0055	0.9945	0.0059	0.9941

3.5.3 Recyclability study for MB and Rh-B:

The stability of the C-BT2 hybrid thin film for photocatalytic degradation of MB and Rh-B dyes is evaluated for five consecutive cycles, as shown in **Fig. 3.15**. The C-BT2 hybrid thin film is recovered from the dye solution, washed with DDW, dried at room temperature and then used for the subsequent photocatalytic degradation tests. The present C-BT2 hybrid thin film photocatalyst demonstrated good recycling performance for MB and Rh-B degradation, with photodegradation rates of 67.5 and 78.8% after 180 and 210 min of visible light exposure. The C-BT2 nanohybrid retains its photocatalytic activity with only decrement for five repetitive degradation cycles, signifying the good photostability of the present nanohybrid photocatalyst. The slight decrease in degradation performance after five consecutive cycles is ascribed to the adsorption of dye molecules on the surface of the C-BT2 nanohybrid thin film and the detachment of loosely bounded catalyst particles from the film surface.

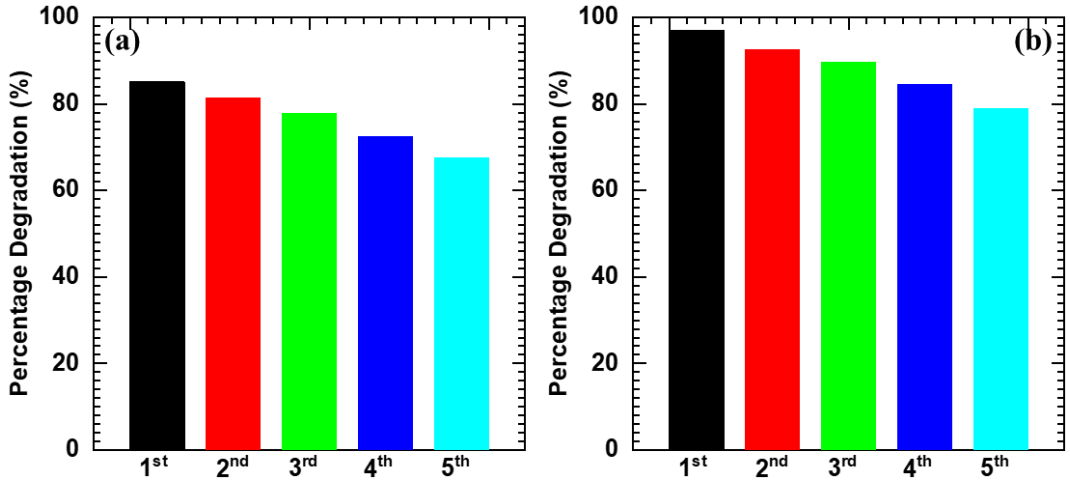

Fig. 3.15: Recyclability of C-BT2 nanohybrid thin film for (a) MB and (b) Rh-B dyes.

The above results confirmed that the C-BT2 nanohybrid thin film has the highest photocatalytic activity towards the photodegradation of MB and Rh-B dyes under visible light illumination.

3.6 Photocatalytic Dye Degradation Mechanism:

The band positions of NS-titanate and $BiVO_4$ thin films are estimated from the cyclic voltammetry (CV) measurements, as shown in **Fig. 3.16** [45, 52-53]. **Fig. 3.16(a)** shows the CV curve of NS-titanate thin film. The onset potential of the reduction peak of NS-titanate is observed at -1.27 V vs Ag/AgCl, corresponding to the 3.39 eV (vs Vacuum). Thus, the lowest edge of the CB of NS-titanate is located at 3.39 eV (vs

Vacuum) (i.e., -1.11 eV vs NHE). Judging from the bandgap energy (3.17 eV) of NS-titanate thin film, its VB position is located at 6.56 eV (vs Vacuum) (i.e., 2.06 eV vs NHE). Similarly, as shown in **Fig. 3.16(b)**, the onset potential of the reduction peak of $BiVO_4$ is observed at the -0.26 V vs Ag/AgCl, corresponding to the 4.39 eV (vs Vacuum). Thus, the lowest edge of the CB of $BiVO_4$ is located at 4.39 eV (vs Vacuum) (i.e., -0.11 eV vs NHE). The bandgap energy of $BiVO_4$ thin film is 2.33 eV; therefore, its VB position is located at 6.72 eV (vs Vacuum) (i.e., -2.22 eV vs NHE).

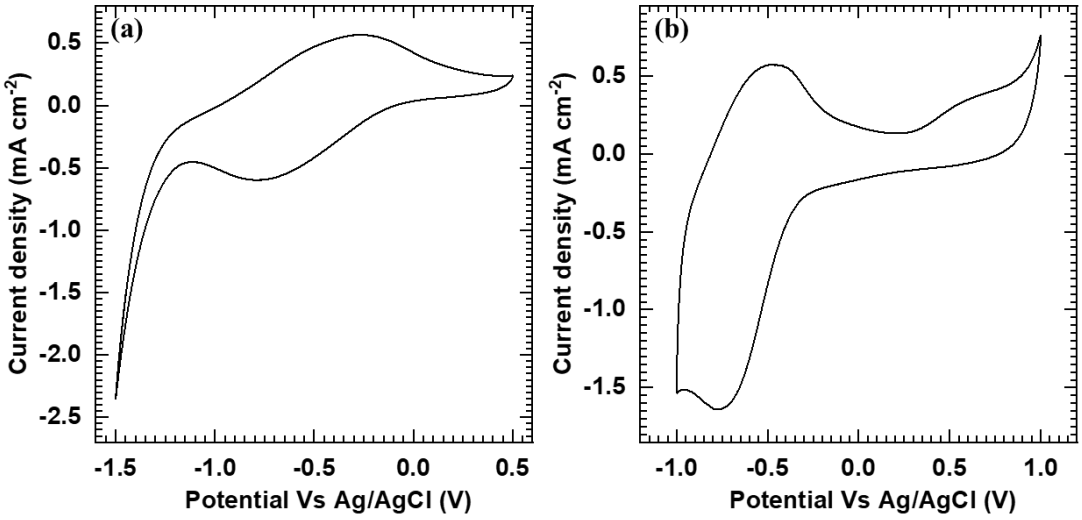

Fig. 3.16: CV curves of (a) NS-titanate and (b) $BiVO_4$ thin films.

The electron transfer between NS-titanate and $BiVO_4$ in the NS-titanate-$BiVO_4$ nanohybrid thin film is investigated with band structure estimated from the CV measurements and UV-vis DRS [46]. The photocatalytic dye degradation mechanism is mainly based on the photoinduced charge separation and transport to the semiconductor surface upon exposure to visible light [54]. When photons having energy equal to or greater than the bandgap of $BiVO_4$ (2.33 eV) are incident on the NS-titanate-$BiVO_4$ nanohybrid thin film, electrons from the VB of $BiVO_4$ are excited to its CB, which results in the formation of electron-hole pairs. As shown in **Fig. 3.17**, the NS-titanate shows a higher position of lower CB edge than the lower CB edge of $BiVO_4$, and $BiVO_4$ shows a higher position of higher VB edge than the higher VB edge of NS-titanate. The photogenerated electrons from the CB of $BiVO_4$ can migrate into the VB of NS-titanate, leading to the spatial separation of electrons and holes with a reduction in electron-hole recombination. The holes present at the VB of $BiVO_4$ generated hydroxyl radicals (OH*) when reacted with water molecules. Generated OH* radicals are strong oxidizing agents that can degrade the target organic (MB and Rh-B) molecules. On the other hand,

superoxide radicals ($*O_2^-$) are produced from the reaction of O_2 with photogenerated electrons from the CB of $BiVO_4$. As represented in equation (3.6), hydroperoxyl radicals (HOO*) are generated from protonation of superoxide radicals. Finally, H_2O_2 generated from hydroperoxyl radicals dissociates into OH* radicals, which can degrade the target organic molecules [55]. Due to the attack of OH* radicals on target MB and Rh-B molecules, various intermediate products are formed, and finally, they dissociate into CO_2 and H_2O. In the case of MB, Azure B, Azure A, Azure C and Thionine intermediate products are produced by de-methylation reactions in which the N-C bond between the methyl group and N atom is broken [56]. On the other hand, in the case of Rh-B, the N-deethylation reaction followed by decarboxylation and deamination results in the formation of aromatic compounds such as O-xylene, Benzoic acid and Phthalic acid via chromophore cleavage [57]. The schematic representation of the photocatalytic degradation mechanism over NS-titanate-$BiVO_4$ nanohybrid thin films is shown in **Fig. 3.17**.

$$NS - titanate - BiVO_4 + h\nu \rightarrow e^- + h^+ \quad (3.3)$$

$$h^+ + OH^-/H_2O \rightarrow OH^* + H^+ \quad (3.4)$$

$$O_2 + e^- \rightarrow O_2^{*-} \quad (3.5)$$

$$O_2^{*-} + H^+ \rightarrow HOO^* \quad (3.6)$$

$$2HOO^* \rightarrow H_2O_2 + O_2 \quad (3.7)$$

$$H_2O_2 \rightarrow 2OH^* \quad (3.8)$$

$$Dye + OH^* \rightarrow CO_2 + H_2O \quad (3.9)$$

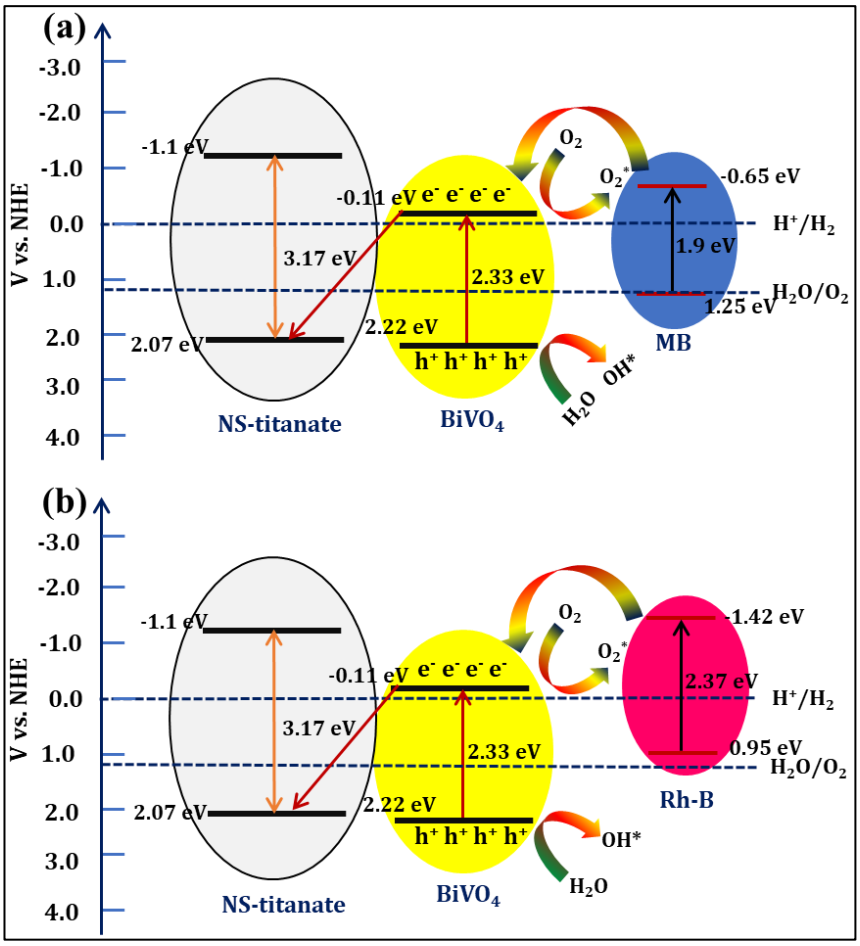

Fig. 3.17: Scheme of photocatalytic degradation mechanism of (a) MB and (b) Rh-B dyes over NS-titanate-$BiVO_4$ nanohybrid thin films.

3.7 Conclusions:

In this chapter, NS-titanate thin films are deposited using the EPD method. The EPD-deposited NS-titanate thin film shows the formation of lepidocrocite-type NS-titanate with orthorhombic symmetry. The NS-titanate thin film shows aggregated NSs morphology, creating a porous structure of NS-titanate thin film. The NS-titanate thin film shows wide-bandgap energy with remarkable absorption in the UV region, beneficial for coupling with narrow-bandgap $BiVO_4$. On the other hand, $BiVO_4$ thin films are deposited using the facile CBD method. Structural and chemical bonding analysis of $BiVO_4$ thin film confirms the highly crystalline growth of monoclinic scheelite $BiVO_4$. The $BiVO_4$ thin film displays porous nanoparticle morphology and effective visible light response, advantageous for superior photocatalytic performance. Further, the highly porous NS-titanate-$BiVO_4$-nanohybrid thin films are synthesized by depositing CBD-deposited $BiVO_4$ layer over EPD-deposited NS-titanate thin films. The

well-crystalline uniform deposition of monoclinic scheelite $BiVO_4$ on NS-titanate is evidenced by XRD and FESEM analysis. The NS-titanate-$BiVO_4$ nanohybrid thin films show randomly deposited nanoplates composed of NS-titanate uniformly covered with smooth $BiVO_4$ deposit, creating the house-of-cards type morphology. The nanohybrid thin films show a strong visible light absorption, indicating their visible light harvesting nature, which is useful for photocatalytic applications. The optimized C-BT2 nanohybrid photocatalyst demonstrated outstanding photoactivity for photodegradation of MB and Rh-B dyes with photodegradation rates of 85.1 and 97%, respectively, which are higher than that of pristine $BiVO_4$ (54 and 70%). The exceptional photocatalytic activity of present nanohybrids can be attributed to the strong visible light harvesting ability, reduced electron-hole recombination, high photostability and mesoporous house-of-cards type structure. The present experimental findings highlight the effectiveness of 2D layered MONs coupling with narrow bandgap semiconductors in developing chemically stable photocatalysts for efficient visible-light-driven photocatalysis.

3.8 References:

1. H. Anwer, A. Mahmood, J. Lee, K.-H. Kim, J.-W. Park, A.C.K. Yip, Photocatalysts for degradation of dyes in industrial effluents: Opportunities and challenges, Nano Res. 12 (2019) 955-972.
2. A. Rafiq, M. Ikram, S. Ali, F. Niaz, M. Khan, Q. Khan, M. Maqbool, Photocatalytic degradation of dyes using semiconductor photocatalysts to clean industrial water pollution, J. Ind. Eng. Chem. 97 (2021) 111-128.
3. M.I. Din, R. Khalid, J. Najeeb, Z. Hussain, Fundamentals and photocatalysis of methylene blue dye using various nano catalytic assemblies- A critical review, J. Clean. Prod. 298 (2021) 126567.
4. W.S. Koe, J.W. Lee, W.C. Chong, Y.L. Pang, L.C. Sim, An overview of photocatalytic degradation: Photocatalysts, mechanisms and development of photocatalytic membrane, Environ. Sci. Pollut. Res. 27 (2020) 2522-2565.
5. U.G. Akpan, B.H. Hameed, Parameters affecting the photocatalytic degradation of dyes using TiO_2-based photocatalysts: A review, J. Hazard. Mater. 170 (2009) 520-529.
6. Y. Zhao, Y. Li, L. Sun, Recent advances in photocatalytic decomposition of water and pollutants for sustainable application, Chemosphere 276 (2021) 130201.
7. D. Chen, Y. Cheng, N. Zhou, P. Chen, Y. Wang, K. Li, S. Huo, P. Cheng, P. Peng, R. Zhang, L. Wang, H. Liu, Y. Liu, R. Ruan, Photocatalytic degradation of organic pollutants using TiO_2-based photocatalysts: A review, J. Clean. Prod. 268 (2020) 121725.
8. S. Dong, J. Feng, M. Fan, Y. Pi, L. Hu, X. Han, M. Liu, J. Sun, J. Sun, Recent developments in heterogeneous photocatalytic water treatment using visible light-responsive photocatalysts: A review, RSC Adv. 5 (2015) 14610-14630.
9. K. Su, H. Liu, Z. Gao, P. Fornasiero, F. Wang, Nb_2O_5-based photocatalysts, Adv. Sci. 8 (2021) 2003156.

10. S. Goktas, A. Goktas, A comparative study on recent progress in efficient ZnO based nanocomposite and heterojunction photocatalysts: A review, J. Alloys Compd. 863 (2021) 158734.
11. J.L. Gunjakar, I.Y. Kim, J.M. Lee, Y.K. Jo, S.-J. Hwang, Exploration of nanostructured functional materials based on hybridization of inorganic 2D nanosheets, J. Phys. Chem. C 118 (2014) 3847-3863.
12. D.-H. Park, S.-J. Hwang, J.-M. Oh, J.-H. Yang, J.-H. Choy, Polymer-inorganic supramolecular nanohybrids for red, white, green and blue applications, Prog. Polym. Sci. 38 (2013) 1442-1486.
13. L. Wang, T. Sasaki, Titanium oxide nanosheets: Graphene analogues with versatile functionalities, Chem. Rev. 114 (2014) 9455-9486.
14. Y. Takezawa, H. Imai, Bottom-up synthesis of titanate nanosheets with hierarchical structures and a high specific surface area, Small 2 (2006) 390-393.
15. J.H. Kim, J.S. Lee, Elaborately modified $BiVO_4$ photoanodes for solar water splitting, Adv. Mater. 31 (2019) 1806938.
16. A. Malathi, J. Madhavan, M. Ashokkumar, P. Arunachalam, A review on $BiVO_4$ photocatalyst: Activity enhancement methods for solar photocatalytic applications, Appl. Catal. A: Gen. 555 (2018) 47-74.
17. H.N. Kim, T.W. Kim, I.Y. Kim, S.-J. Hwang, Cocatalyst-free photocatalysts for efficient visible-light-induced H_2 production: Porous assemblies of CdS quantum dots and layered titanate nanosheets, Adv. Funct. Mater. 21 (2011) 3111-3118.
18. T. Sasaki, M. Watanabe, Osmotic swelling to exfoliation: Exceptionally high degrees of hydration of a layered titanate, J. Am. Chem. Soc. 120 (1998) 4682-4689.
19. T. Sasaki, M. Watanabe, H. Hashizume, H. Yamada, H. Nakazawa, Macromolecule-like aspects for a colloidal suspension of an exfoliated titanate: Pairwise association of nanosheets and dynamic reassembling process initiated from it, J. Am. Chem. Soc. 118 (1996) 8329-8335.
20. T. Sasaki, S. Nakano, S. Yamauchi, M. Watanabe, Fabrication of titanium dioxide thin flakes and their porous aggregate, Chem. Mater. 9 (1997) 602-608.
21. Y. Matsumoto, A. Funatsu, D. Matsuo, U. Unal, K. Ozawa, Electrochemistry of titanate (IV) layered oxides, J. Phys. Chem. B 105 (2001) 10893-10899.
22. S.B. Patil, H.J. Kim, H.-K. Lim, S.M. Oh, J. Kim, J. Shin, H. Kim, J.W. Choi, S.-J. Hwang, Exfoliated 2D lepidocrocite titanium oxide nanosheets for high sulfur content cathodes with highly stable Li-S battery performance, ACS Energy Lett. 3 (2018) 412-419.
23. J.H. Choy, H.-C. Lee, H. Jung, H. Kim, H. Boo, Exfoliation and restacking route to anatase-layered titanate nanohybrid with enhanced photocatalytic activity, Chem. Mater. 14 (2002) 2486-2491.
24. H. Jung, H.-C. Lee, S.-M. Paek, S.-J. Hwang, J.-H. Choy, A novel hetero-structured RuS_2-titanate nanohybrid, J. Phys. Chem. Solids 67 (2006) 1248-1251.
25. S. Sun, W. Wang, L. Zhou, H. Xu, Efficient methylene blue removal over hydrothermally synthesized starlike $BiVO_4$, Ind. Eng. Chem. Res. 48 (2009) 1735-1739.
26. S.W. Hong, A. Kim, J.H. Choi, H. Jung, J.K. Park, Intercalation of conjugated polyelectrolytes in layered titanate nanosheets for enhancement in photocatalytic activity, J. Solid State Chem. 269 (2019) 291-296.
27. L.S. Chougala, M.S. Yatnatti, R.K. Linganagoudar, R.R. Kamble, J.S. Kadadevarmath, A simple approach on synthesis of TiO_2 nanoparticles and its application in dye sensitized solar cells, J. Nano- Electron. Phys. 9 (2017) 040051-040056.

28. R. Chroma, M. Vilkova, I. Shepa, P. Makos-Chelstowska, V. Andruch, Investigation of tetrabutylammonium bromide-glycerol-based deep eutectic solvents and their mixtures with water by spectroscopic techniques, J. Mol. Liq. 330 (2021) 115617.
29. Y. Geng, P. Zhang, S. Kuang, Fabrication and enhanced visible-light photocatalytic activities of $BiVO_4/Bi_2WO_6$ composites, RSC Adv. 4 (2014) 46054-46059.
30. M. Mousavi-Kamazani, Facile hydrothermal synthesis of egg-like $BiVO_4$ nanostructures for photocatalytic desulfurization of thiophene under visible light irradiation, J. Mater. Sci. Mater. Electron. 30 (2019) 17735-17740.
31. L. Zhang, Z. Dai, G. Zheng, Z. Yao, J. Mu, Superior visible light photocatalytic performance of reticular $BiVO_4$ synthesized via a modified sol-gel method, RSC Adv. 8 (2018) 10654-10664.
32. P. Pookmanee, S. Kojinok, R. Puntharod, S. Sangsrichan, S. Phanichphant, Preparation and characterization of $BiVO_4$ powder by the sol-gel method, Ferroelectrics 456 (2013) 45-54.
33. W. Hu, L. Li, G. Li, Y. Liu, R.L. Withers, Atomic-scale control of TiO_6 octahedra through solution chemistry towards giant dielectric response, Sci. Rep. 4 (2014) 6582.
34. Y. Mao, M. Kanungo, T. Hemraj-Benny, S.S. Wong, Synthesis and growth mechanism of titanate and titania one-dimensional nanostructures self-assembled into hollow micrometer-scale spherical aggregates, J. Phys. Chem. B 110 (2006) 702-710.
35. A. Kudo, T. Kondo, Photoluminescent and photocatalytic properties of layered cesium titanates, $Cs_2Ti_nO_{2n+1}$ (n=2,5,6), J. Mater. Chem. 7 (1997) 777-780.
36. T. Gao, H. Fjellvag, P. Norby, Raman scattering properties of a protonic titanate $H_xTi_{2-x/4}\square_{x/4}O_4 \cdot H_2O$ (□, vacancy; x=0.7) with lepidocrocite-type layered structure, J. Phys. Chem. B 112 (2008) 9400-9405.
37. T.D. Nguyen, Q.T.P. Bui, T.B. Le, T.M. Altahtamouni, K.B. Vu, D.V.N. Vo, N.T.H. Le, T.D. Luu, S.S. Hong, K.T. Lim, Co^{2+} substituted for Bi^{3+} in $BiVO_4$ and its enhanced photocatalytic activity under visible LED light irradiation, RSC Adv. 9 (2019) 23526-23534.
38. T.S. Dabodiya, P. Selvarasu, A.V. Murugan, Tetragonal to monoclinic crystalline phases change of $BiVO_4$ via microwave-hydrothermal reaction: In correlation with visible-light-driven photocatalytic performance, Inorg. Chem. 58 (2019) 5096-5110.
39. A. Helal, S.M. El-Sheikh, J. Yu, A.I. Eid, S.A. El-Haka, S.E. Samra, Novel synthesis of $BiVO_4$ using homogeneous precipitation and its enhanced photocatalytic activity, J. Nanopart. Res. 22 (2020) 132.
40. E. Zhang, Y. Pan, T. Lu, Y. Zhu, W. Dai, Novel synthesis of S-doped anatase TiO_2 via hydrothermal reaction of Cu-Ti amorphous alloy, Appl. Phys. A 126 (2020) 606.
41. X. Zhu, G. Wen, H. Liu, S. Han, S. Chen, Q. Kong, W. Feng, One-step hydrothermal synthesis and characterization of Cu-doped TiO_2 nanoparticles / nanobucks / nanorods with enhanced photocatalytic performance under simulated solar light, J. Mater. Sci. Mater. Electron. 30 (2019) 13826-13834.
42. Z. Jiang, Y. Liu, T. Jing, B. Huang, X. Zhang, X. Qin, Y. Dai, M.-H. Whangbo, Enhancing the photocatalytic activity of $BiVO_4$ for oxygen evolution by Ce doping: Ce^{3+} ions as hole traps, J. Phys. Chem. C 120 (2016) 2058-2063.
43. Y. Deng, L. Tang, G. Zeng, C. Feng, H. Dong, J. Wang, H. Feng, Y. Liu, Y. Zhou, Y. Pang, Plasmonic resonance excited dual Z-scheme $BiVO_4/Ag/Cu_2O$ nanocomposite: Synthesis and mechanism for enhanced photocatalytic performance in recalcitrant antibiotics degradation, Environ. Sci.: Nano 4 (2017) 1494-1511.

44. R.B. Shinde, A.S. Patil, S.V. Sadavar, Y.M. Chitare, V.V. Magdum, N.S. Padalkar, U.M. Patil, S.T. Kochuveedu, V.G. Parale, H.-H. Park, C.D. Lokhande, J.L. Gunjakar, Polyoxotungstate intercalated self-assembled nanohybrids of Zn-Cr-LDH for room temperature Cl_2 sensing, Sens. Actuators B: Chem. 352 (2022) 131046.
45. S.P. Kulkarni, Y.M. Chitare, V.V. Magdum, P.D. Sawant, S.V. Talekar, S.A. Pawar, U.M. Patil, K.V. Gurav, D.B. Malavekar, A.U. Pawar, J.L. Gunjakar, Chemically synthesized facet-controlled visible light active $BiVO_4$ thin films for photoelectrochemical water splitting, Appl. Phys. A 129 (2023) 876.
46. J.L. Gunjakar, T.W. Kim, H.N. Kim, I.Y. Kim, S.-J. Hwang, Mesoporous layer-by-layer ordered nanohybrids of layered double hydroxide and layered metal oxide: Highly active visible light photocatalysts with improved chemical stability, J. Am. Chem. Soc. 133 (2011) 14998-15007.
47. J.L. Gunjakar, I.Y. Kim, J.M. Lee, N.-S. Lee, S.-J. Hwang, Self-assembly of layered double hydroxide 2D nanoplates with graphene nanosheets: An effective way to improve the photocatalytic activity of 2D nanostructured materials for visible light-induced O_2 generation, Energy Environ. Sci. 6 (2013) 1008-1017.
48. J.L. Gunjakar, T.W. Kim, I.Y. Kim, J.M. Lee, S.-J. Hwang, Highly efficient visible-light-induced O_2 generation by self-assembled nanohybrids of inorganic nanosheets and polyoxometalate nanoclusters, Sci. Rep. 3 (2013) 2080.
49. K.K. Dey, S. Gahlawat, P.P. Ingole, $BiVO_4$ optimized to nano-worm morphology for enhanced activity towards photoelectrochemical water splitting, J. Mater. Chem. A 7 (2019) 21207-21221.
50. M. Yan, Y. Wu, Y. Yan, X. Yan, F. Zhu, Y. Hua, W. Shi, Synthesis and characterization of novel $BiVO_4/Ag_3VO_4$ heterojunction with enhanced visible-light-driven photocatalytic degradation of dyes, ACS Sustainable Chem. Eng. 4 (2016) 757-766.
51. H.R. Choe, J.H. Kim, A. Ma, H. Jung, H.Y. Kim, K.M. Nam, Understanding reaction kinetics by tailoring metal co-catalysts of the $BiVO_4$ photocatalyst, ACS Omega 4 (2019) 16597-16602.
52. K. Saruwatari, H. Sato, T. Idei, J. Kameda, A. Yamagishi, A. Takagaki, K. Domen, Photoconductive properties of organic-inorganic hybrid films of layered perovskite-type niobate, J. Phys. Chem. B 109 (2005) 12410-12416.
53. N. Sakai, Y. Ebina, K. Takada, T. Sasaki, Electronic band structure of titania semiconductor nanosheets revealed by electrochemical and photoelectrochemical studies, J. Am. Chem. Soc. 126 (2004) 5851-5858.
54. M.A. Rauf, S.S. Ashraf, Fundamental principles and application of heterogeneous photocatalytic degradation of dyes in solution, Chem. Eng. J. 151 (2009) 10-18.
55. A. Ajmal, I. Majeed, R.N. Malik, H. Idriss, M.A. Nadeem, Principles and mechanisms of photocatalytic dye degradation on TiO_2 based photocatalysts: A comparative overview, RSC Adv. 4 (2014) 37003-37026.
56. C. Yang, W. Dong, G. Cui, Y. Zhao, X. Shi, Xi. Xia, B. Tang, W. Wang, Highly efficient photocatalytic degradation of methylene blue by P2ABSA-modified TiO_2 nanocomposite due to the photosensitization synergetic effect of TiO_2 and P2ABSA, RSC Adv. 7 (2017) 23699-23708.
57. A.M. Cruz, U.M.G. Perez, Photocatalytic properties of $BiVO_4$ prepared by the co-precipitation method: Degradation of rhodamine B and possible reaction mechanisms under visible irradiation, Mater. Res. Bull. 45 (2010) 135-141.

CHAPTER-4

Synthesis and Characterizations of NS-titanate-$BiVO_4$ Nanohybrids by SILAR: Application in Photocatalytic Dye Degradation

CHAPTER-4

Synthesis and Characterizations of NS-titanate-$BiVO_4$ Nanohybrids by SILAR: Application in Photocatalytic Dye Degradation

4.1 Introduction:

As introduced in previous chapters, natural water sources are getting highly polluted due to the high discharge of toxic dye contaminants, which significantly impact human and aquatic ecosystems [1-3]. The heterogeneous photocatalysis using semiconducting photocatalysts has been treated as a potential approach for removing highly toxic inorganic and organic compounds from contaminated water [4,5]. As previously explained in **Chapters 1-3**, **Sections 1.3**, **2.4, and 3.1**, enormous research efforts have been focused on enhancing the photocatalytic activity of semiconducting materials by improving charge carrier transfer, effective electron-hole pair separation and shifting of absorption edge towards a visible region of the solar spectrum [6-9]. Compared to others, a strategy of coupling wide-band gap semiconductor photocatalysts with narrow-band gap semiconductors can be effective; it can promote easy charge separation, leading to improved visible-light-driven photocatalytic activity [10-14].

Numerous chemical and physical methods were explored for synthesizing hybrid photocatalysts for visible-light-driven photocatalytic applications [15-18]. Compared to others, the SILAR method has attracted intense research attention to deposit hybrid thin films due to its certain advantages such as low-cost fabrication, facile control of preparative parameters, large area deposition, better orientation of crystallites with pinhole free and uniform deposition on a variety of substrates [19-22]. As explained in **Chapter 3**, **Section 3.1**, the exfoliated NS-titanate coupled with $BiVO_4$ can be the best choice for hybridization. It has been reported that interconnected $BiVO_4$ nanoparticles with improved visible light harvesting activity were deposited by the SILAR method, wherein the type of anionic precursor was varied to achieve the 3D interconnected $BiVO_4$ nanoparticles morphology [23]. The SILAR-deposited $BiVO_4$ photoanodes display excellent visible-light-driven PEC performance.

In this context, in the present chapter, the novel approach for the synthesis of highly porous NS-titanate-$BiVO_4$ nanohybrid thin films by a combination of EPD and SILAR methods is explored for photocatalytic dye degradation application. The photoactivity of NS-titanate-$BiVO_4$ nanohybrid thin films is explored for the degradation of MB and Rh-B dyes, along with their structural and physicochemical features.

4.2 Synthesis and characterizations of NS-titanate-$BiVO_4$ nanohybrids:

4.3 Experimental details:

4.3.1 Chemicals:

TiO_2, Cs_2CO_3, $Bi(NO_3)_3.5H_2O$, $NaVO_3$, HCl, acetic acid (CH_3COOH), TBAOH and C_2H_5OH were purchased from Sigma-Aldrich and used as received.

4.3.2 Synthesis of NS-titanate-$BiVO_4$:

The NS-titanate-$BiVO_4$ nanohybrid thin films were deposited by a combination of EPD and SILAR methods. Initially, thin films of pristine NS-titanate were obtained from the dialyzed colloidal suspension of NS-titanate by the EPD method similar to that described in **Chapter 3, Section 3.2**. $BiVO_4$ layers were deposited over the EPD-deposited NS-titanate thin films by the SILAR method.

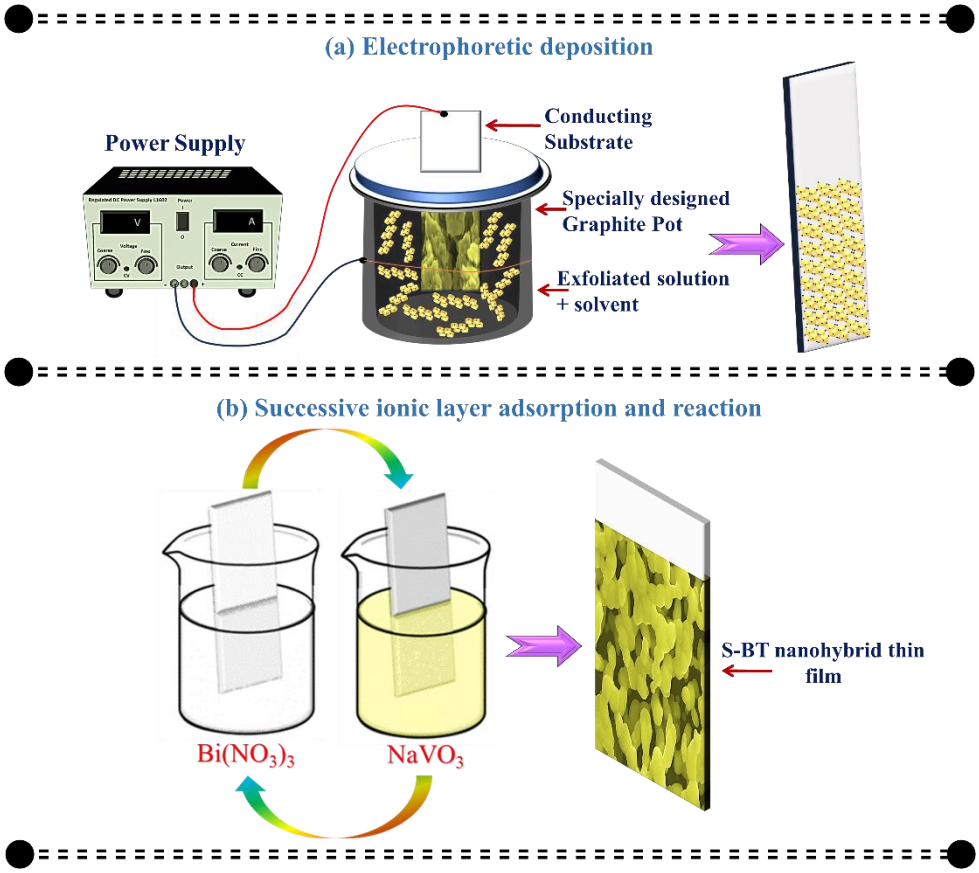

Fig. 4.1: Schematic representation of (a) EPD of NS-titanate thin films and (b) SILAR method for depositing NS-titanate-$BiVO_4$ nanohybrid thin films.

Deposition of $BiVO_4$ by SILAR method was carried out by immersion of NS-titanate coated (Ti-1, Ti-2 and Ti-3) ITO substrates into separately placed cationic (Bi) and anionic (V) precursors (two-beaker process). A cationic precursor for the deposition of $BiVO_4$ was prepared from an aqueous solution of 0.025 M $Bi(NO_3)_3 \cdot 5H_2O$ dissolved in 1 M acetic acid ($V_{acetic\ acid}$:V_{DDW} = 1:19, pH 1.5). An anionic precursor was prepared

from the aqueous solution of 0.025 M $NaVO_3$ (pH 6.8). One deposition cycle of SILAR was completed by successive immersion of NS-titanate coated ITO substrates into a cationic (Bi) bath for 20 s and then immersing into an anionic (V) bath for the next 20 s. Repetitions of such 15-deposition cycles result in the direct growth of $BiVO_4$ on NS-titanate thin films. After the deposition, NS-titanate-$BiVO_4$ nanohybrid thin films were washed with DDW and air dried. The schematic representation of the NS-titanate-$BiVO_4$ nanohybrid thin films deposition process is displayed in **Fig. 4.1**. Subsequently, the as-prepared NS-titanate-$BiVO_4$ nanohybrid thin films were annealed at 400℃ for 2 h. The annealed NS-titanate-$BiVO_4$ nanohybrid thin films synthesized on Ti-1, Ti-2 and Ti-3 thin films are represented as S-BT1, S-BT2 and S-BT3, respectively.

4.4 Characterizations of NS-titanate-$BiVO_4$ nanohybrids:

The physicochemical characteristics of NS-titanate-$BiVO_4$ nanohybrid thin films compared to pristine NS-titanate and $BiVO_4$ were studied with various characterization techniques, as described in **Chapter 3, Section 3.4**.

Note: The S-BT2 nanohybrid thin film shows improved photocatalytic dye degradation performance. Therefore, all the optimized S-BT2 nanohybrid thin film characterizations are compared with the pristine materials.

4.4.1 XRD analysis:

The development of the crystal structure of pristine $BiVO_4$ upon hybridization with NS-titanate was analyzed using XRD analysis. The XRD patterns of S-BT2 nanohybrid thin film compared to the pristine NS-titanate and $BiVO_4$ thin films are shown in **Fig. 4.2**. As described in **Chapter 3, Section 3.4.1**, the pristine NS-titanate thin film displays broad diffraction peak centered at 10° corresponds to the (020) plane of lepidocrocite type NS-titanate with orthorhombic symmetry. The pristine SILAR deposited $BiVO_4$ thin film (**Fig. 4.2(ii)**) shows typical Bragg reflections matching with the monoclinic scheelite $BiVO_4$ structure (I2/a) (JCPDS no.: 14-0688). Interestingly, the apparent peak splitting is observed at 2θ equal to 18.5°, 35° and 46°, clearly signifying the formation of $BiVO_4$ in the monoclinic scheelite phase [24]. However, the NS-titanate-$BiVO_4$ nanohybrid thin film (**Fig. 4.2(iii)**) shows diffraction peaks matching with both lepidocrocite type NS-titanate (denoted by squares) and monoclinic scheelite-type $BiVO_4$ (denoted by circles). It shows (020) diffraction peak matching with the lepidocrocite type NS-titanate with orthorhombic symmetry having interplanar spacing of 0.88 nm [25-28]. This peak is attributed to the layer-by-layer stacking of titanate

nanosheets over the ITO substrate. In addition, it shows typical Braggs reflections and characteristic peak splitting (18.5°, 35° and 46°) corresponding to the monoclinic scheelite $BiVO_4$ structure with space group (I2/a) (JCPDS no.: 14-0688) [23]. Present XRD results provide strong evidence of the formation of NS-titanate and $BiVO_4$ in lepidocrocite-type layered phase and monoclinic scheelite-type phase, respectively. This indicates the effective growth of monoclinic scheelite $BiVO_4$ phase over EPD-deposited NS-titanate thin films.

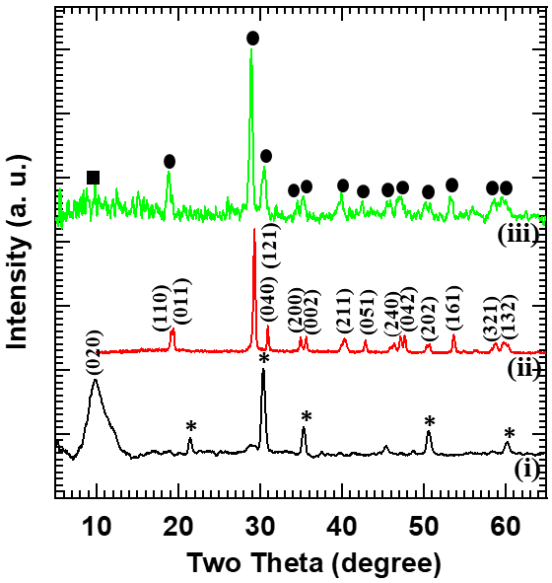

Fig. 4.2: XRD patterns of (i) NS-titanate, (ii) $BiVO_4$ and (iii) S-BT2 nanohybrid thin films (asterisk, squares and circles denote the Bragg reflections of ITO, NS-titanate and monoclinic scheelite-type $BiVO_4$, respectively).

4.4.2 FTIR analysis:

The microscopic structural characteristics and chemical bonding nature of the pristine NS-titanate, $BiVO_4$ and NS-titanate-$BiVO_4$ nanohybrid thin films were investigated using FTIR spectroscopy. As described in **Chapter 3, Section 3.4.2**, the pristine NS-titanate thin film displays characteristic IR features (*v*1 to *v*6) related to NS-titanate. As represented in **Fig. 4.3**, the pristine SILAR-deposited $BiVO_4$ thin film exhibits sharp absorption peaks *v*7 (413 cm^{-1}) and *v*8 (482 cm^{-1}) assigned to the Bi-O bending vibrations and the stretching vibrations of VO_4^{3-}, respectively [29-30]. The absorption peaks *v*9 (741 cm^{-1}) and *v*10 (829 cm^{-1}) correspond to the asymmetric and symmetric stretching vibrations of VO_4^{3-}, respectively [31]. The absorption peaks *v*11 (3451.11 cm^{-1}) and *v*12 (3446.87 cm^{-1}) are linked with the bending vibrations of water molecules and stretching vibrations of hydroxyl groups, respectively [32].

On the contrary, the NS-titanate-$BiVO_4$ nanohybrid thin film shows absorption peaks *v*13 (482.17 cm^{-1}), *v*14 (737 cm^{-1}), *v*15 (788 cm^{-1}), *v*16 (1105 cm^{-1}), *v*17 (1630 cm^{-1}) and *v*18 (3431 cm^{-1}) linked with the NS-titanate and $BiVO_4$. The absorption peak *v*13 corresponds to the Ti-O bending mode of the layered TiO_2 [33-34]. The absorption peaks *v*14 and *v*15 are assigned to the asymmetric and symmetric stretching vibrations of VO_4^{3-}, respectively [31]. The absorption peak at *v*16 is attributed to the stretching vibrations of the C-O group in the alkyl chain of TBA [35]. The absorption peaks *v*17 and *v*18 are assigned to the bending vibrations of water molecules and stretching vibrations of hydroxyl groups, respectively [31]. These IR features closely match with the chemical bonding features of SILAR-deposited $BiVO_4$ and EPD-deposited NS-titanate thin films. The observed spectral features confirm the successful growth of monoclinic scheelite $BiVO_4$ phase over EPD-deposited NS-titanate thin films.

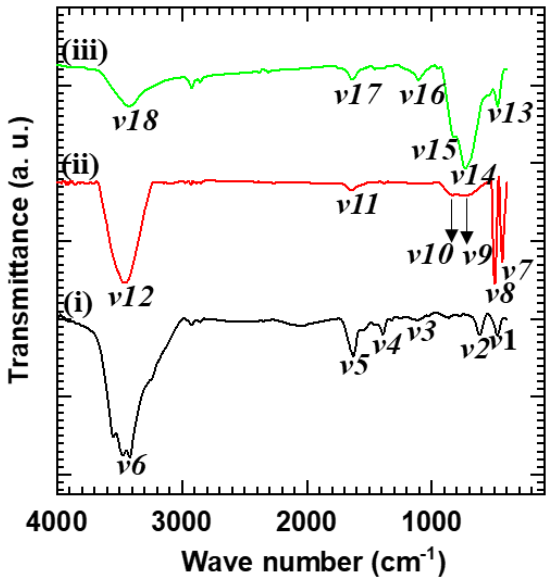

Fig. 4.3: FTIR spectra of (i) NS-titanate, (ii) $BiVO_4$ and (ii) S-BT2 nanohybrid thin films.

4.4.3 Raman analysis:

The chemical bonding nature of the pristine NS-titanate, $BiVO_4$ and NS-titanate-$BiVO_4$ nanohybrid thin films were further probed with micro-Raman spectroscopy as shown in **Fig. 4.4**. As described in **Chapter 3, Section 3.4.3**; the pristine NS-titanate thin film shows several Raman peaks (P_1 to P_4) related to the Ti-O vibrations in NS-titanate. The micro-Raman spectrum of SILAR-deposited $BiVO_4$ shows the spectral features P_5 (131 cm^{-1}) and P_6 (212 cm^{-1}) at lower frequency regions that are assigned to the external rotation or translation modes of $BiVO_4$ [36]. Also, it displays characteristics Raman bands P_7 (325.5 cm^{-1}) and P_8 (369 cm^{-1}), corresponding to the asymmetric (Bg

symmetry) and symmetric (Ag symmetry) bending modes of the VO_4 tetrahedron, respectively [37]. The peaks P_9 (710 cm^{-1}) and P_{10} (826 cm^{-1}) are assigned to the asymmetric and symmetric (V-O) stretching modes of $BiVO_4$, respectively [36-38].

Alternatively, the NS-titanate-$BiVO_4$ nanohybrid thin film exhibits the Raman peaks associated with the NS-titanate and $BiVO_4$. The Raman peaks P_{11} (134 cm^{-1}) and P_{12} (219 cm^{-1}) are ascribed to the Ti-O vibrations with Ag symmetry [39-41]. The Raman peak present at P_{13} (350.25 cm^{-1}) is the superposition of the two Raman peaks P_7 and P_8, corresponding to the asymmetric (Bg symmetry) and symmetric (Ag symmetry) bending modes of the VO_4 tetrahedron, respectively [37]. However, the sharp and intense Raman peak centered around P_{14} (821.11 cm^{-1}) is linked with the symmetric (V-O) stretching mode [36-38]. The Raman spectrum of the S-BT2 nanohybrid thin film mostly shows Raman peaks corresponding to the $BiVO_4$ because of the extremely thin thickness of the NS-titanate thin film. All the Raman peaks of NS-titanate are not active owing to the comparatively thick $BiVO_4$ deposition on NS-titanate restricting the Raman active vibrations of NS-titanate. The present Micro-Raman features are linked with the chemical bonding characteristics of EPD-deposited NS-titanate and SILAR-deposited $BiVO_4$ thin films. These spectral features signify the successful growth of monoclinic scheelite $BiVO_4$ phase on the surface of EPD-deposited NS-titanate thin films.

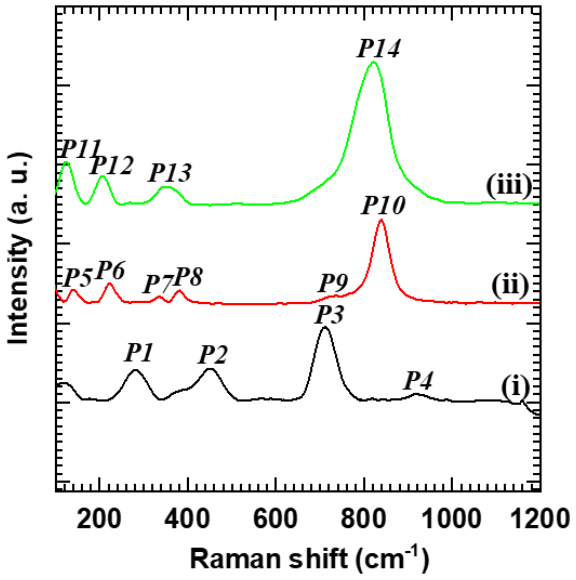

Fig. 4.4: Micro-Raman spectra of (i) NS-titanate, (ii) $BiVO_4$ and (iii) S-BT2 nanohybrid thin films.

4.4.4 XPS analysis:

The surface compositions and chemical oxidation states of the NS-titanate-$BiVO_4$ nanohybrid thin film compared with pristine NS-titanate and $BiVO_4$ thin films were analyzed with XPS analysis. The survey and Ti 2p, Bi 4f, V 2p, O 1s core-level XPS spectra of the NS-titanate, $BiVO_4$ and NS-titanate-$BiVO_4$ nanohybrid thin films are shown in **Fig. 4.5** and **Fig. 4.6**. The survey XPS spectrum of NS-titanate-$BiVO_4$ nanohybrid thin film (**Fig. 4.5**) shows the spectral features at BE corresponding to the Ti, Bi, V and O elements representing the existence of above elements in S-BT2 thin film.

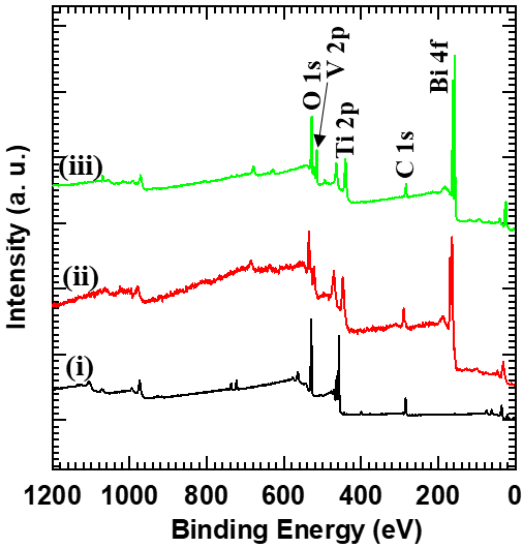

Fig. 4.5: Survey XPS spectra of (i) NS-titanate, (ii) $BiVO_4$ and (iii) S-BT2 nanohybrid thin films.

As displayed in high-resolution Ti 2p spectra (**Fig. 4.6(a)**), the pristine NS-titanate and NS-titanate-$BiVO_4$ nanohybrid thin films commonly exhibit spectral features A (464.1 eV) and B (458.36 eV) are assigned to the spin-orbit splitting of Ti $2p_{1/2}$ and Ti $2p_{3/2}$, respectively [42,43]. The presence of these spectral features with BE difference of 5.74 eV confirms the presence of Ti^{+4} state in the above samples. In case of S-BT2 thin film, the Ti 2p peaks broaden due to the change in the chemical and electronic environment of Ti atoms. This can affect the BE of electrons, leading to a spreading in the observed XPS peaks [44]. As shown in high-resolution Bi 4f spectra (**Fig. 4.6(b)**), the pristine $BiVO_4$ and NS-titanate-$BiVO_4$ nanohybrid thin films display two strong peaks, P (164.2 eV) and Q (158.9 eV), which are assigned to the Bi $4f_{5/2}$ and Bi $4f_{7/2}$, respectively which indicates the presence of Bi^{3+} state in stated samples [45].

As plotted in high-resolution V 2p spectra (**Fig. 4.6(c)**), the pristine $BiVO_4$ and NS-titanate-$BiVO_4$ nanohybrid thin films commonly exhibit spectral features R (516.4 eV) and S (520.8 eV) owing to the spin-orbit coupling of V $2p_{3/2}$ and V $2p_{1/2}$, respectively [46]. This indicates the presence of V^{5+} in pristine $BiVO_4$ and NS-titanate-$BiVO_4$ nanohybrid thin film. The high-resolution O 1s XPS spectra in **Fig. 4.6(d)** show an intense peak M (529.5 eV) ascribed to the oxygen from the pristine NS-titanate, $BiVO_4$ and NS-titanate-$BiVO_4$ lattice, respectively [45]. For NS-titanate thin film, peak M is attributed to Ti-O bonding. For $BiVO_4$ thin film, peak M is ascribed to Bi-O and V-O bonding. Conversely, for NS-titanate-$BiVO_4$ thin film, peak R corresponds to the Ti-O, Bi-O and V-O bonding.

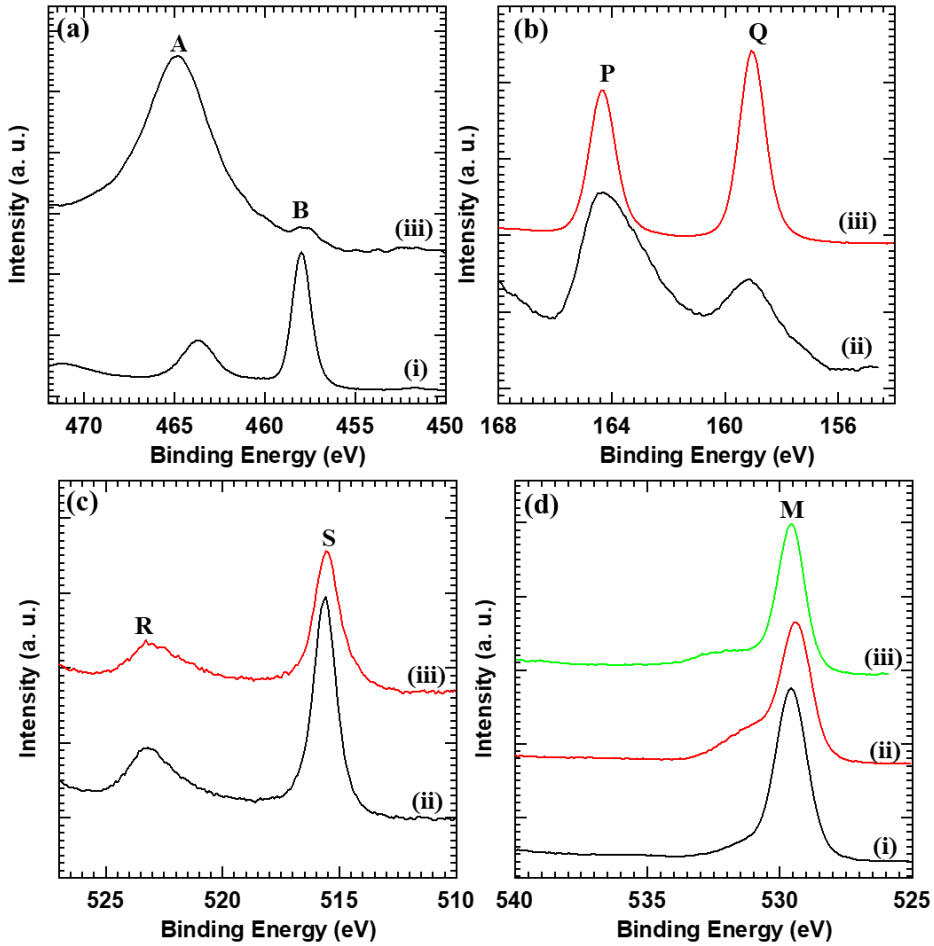

Fig. 4.6: (a) Ti 2p, (b) Bi 4f, (c) V 2p, (d) O 1s core-level XPS spectra of (i) NS-titanate, (ii) $BiVO_4$ and (iii) S-BT2 nanohybrid thin films.

Notably, after hybridization, the Ti 2p, Bi 4f, V 2p, and O 1s XPS spectra of S-BT2 nanohybrid thin film slightly shifted towards lower BEs due to the increased electron density on NS-titanate-$BiVO_4$ nanohybrid. A strong electronic coupling

between NS-titanate and $BiVO_4$ causes the increased electron density on the NS-titanate-$BiVO_4$ nanohybrid. The observed XPS results highlight the presence of Ti^{4+}, Bi^{3+} and V^{5+} states of Ti, Bi and V in NS-titanate-$BiVO_4$ nanohybrid thin film, respectively. The presence of these spectral features confirms the intimate electronic coupling between NS-titanate and $BiVO_4$ in NS-titanate-$BiVO_4$ nanohybrid thin film.

4.4.5 FESEM analysis:

The surface morphologies of the pristine NS-titanate, $BiVO_4$ and NS-titanate-$BiVO_4$ nanohybrid thin films were scrutinized with FESEM analysis, as shown in **Fig. 4.7**. As represented in **Fig. 4.7(a)**, the EPD deposited NS-titanate thin film display NSs morphology with titanate NSs deposited parallel to the surface of ITO substrate. $BiVO_4$ thin film (**Fig. 4.7(b)**) shows interconnected nanoparticle morphology with an average size within the 150-200 nm range. The interconnection of $BiVO_4$ nanoparticles forms a highly porous structure. Such interconnected nanoparticle morphology is commonly observed for $BiVO_4$ synthesized by chemical methods [23, 47]. The development of a highly porous structure due to interconnected $BiVO_4$ nanoparticles can promote the effective charge (electrons and holes) transport to its surface and enable expanded surface area that is useful for photocatalytic activity.

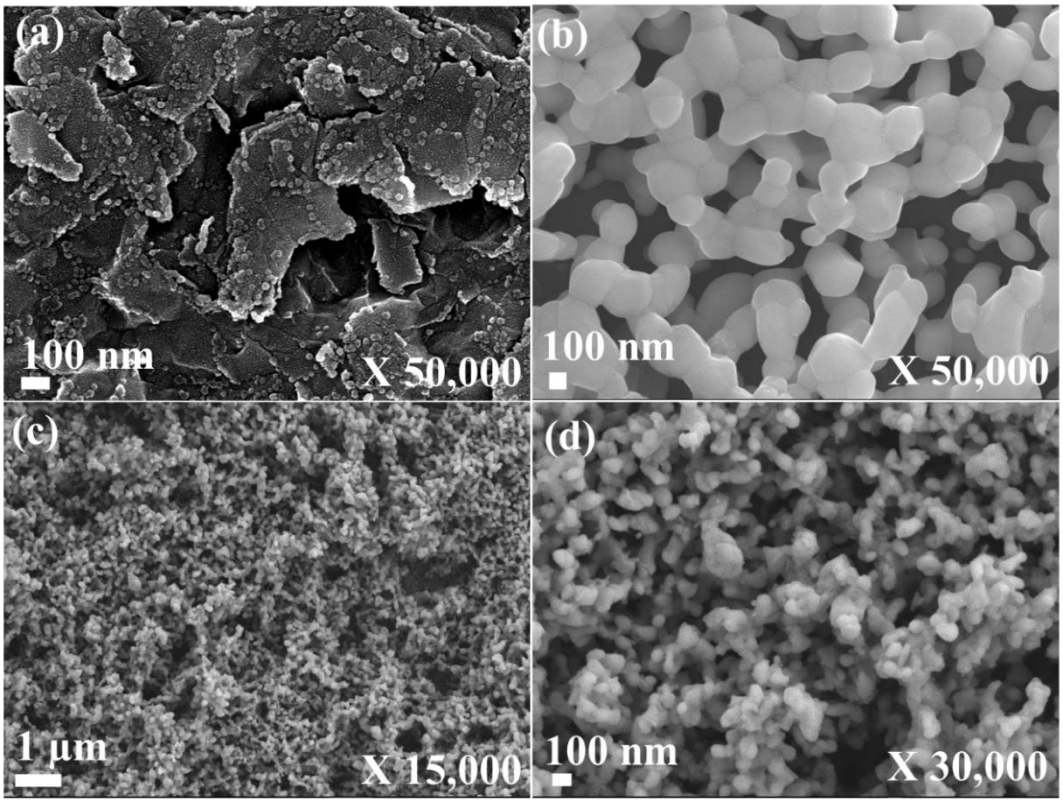

Fig. 4.7: FESEM micrographs of (a) NS-titanate, (b) $BiVO_4$ and (c-d) S-BT2 nanohybrid thin films.

On the other hand, the NS-titanate-$BiVO_4$ nanohybrid thin film **(Fig. 4.7(c-d))** shows the mesoporous morphology composed of a 3D network of $BiVO_4$ nanoparticles deposited on the surface of randomly oriented titanate nanosheets. The FESEM images of S-BT2 nanohybrid thin film show 3D network-type structure of $BiVO_4$ nanoparticles. Due to the large thickness of $BiVO_4$ thin film, only $BiVO_4$ morphology can be visible. The close inspection of these FESEM micrographs shows that the average particle size of NS-titanate-$BiVO_4$ nanohybrid is in the range of 75-95 nm. Interestingly, the 3D network-type structure of $BiVO_4$ nanoparticles forms mesopores of sizes in the range of 100 to 150 nm within the voids of 3D network-type structure. Such a mesoporous structure can allow expanded surface area with effective electronic coupling between the NS-titanate and $BiVO_4$, which is highly advantageous in easy charge separation and transport for photocatalytic applications. This type of highly porous structure is usually detected for 2D NSs-based nanohybrids and is advantageous for solar-assisted photo-functional applications [48-50].

4.4.6 EDS analysis:

Additionally, the distribution of constituent elements and chemical compositions of NS-titanate-$BiVO_4$ nanohybrid thin film were scrutinized with elemental mapping and EDS analysis, as displayed in **Fig. 4.8** and **Fig. 4.9**. The S-BT2 nanohybrid thin film exhibits the homogeneous distribution of Ti, Bi, V and O elements with a Bi/V ratio of ~1 over the entire mapping region, demonstrating the uniform growth of $BiVO_4$ on the surface of NS-titanate thin film. Due to the larger thickness of $BiVO_4$ thin film, the Ti content is observed to be very low in the NS-titanate-$BiVO_4$ thin film.

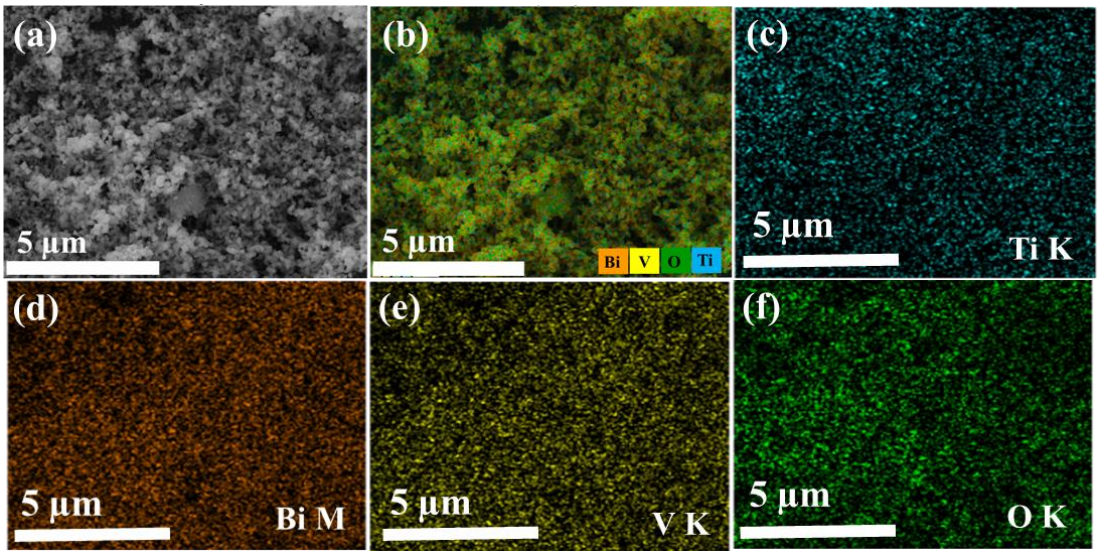

Fig. 4.8: (a) FESEM image and (b-f) EDS elemental maps of S-BT2 nanohybrid thin film.

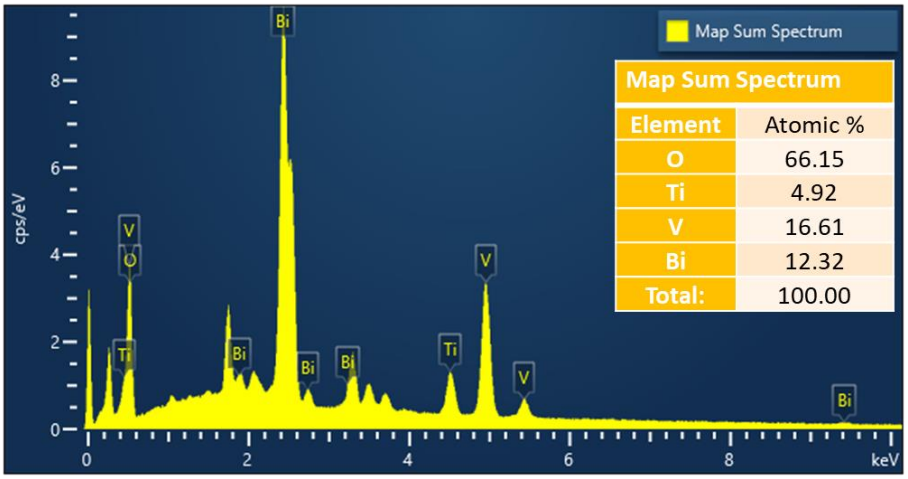

Fig. 4.9: EDS spectrum of S-BT2 nanohybrid thin film.

4.4.7 UV-vis DRS analysis:

The electronic band structure and optical properties of the present NS-titanate-$BiVO_4$ nanohybrid thin film, compared to the pristine NS-titanate and $BiVO_4$ thin films, were examined with UV-vis DRS. As plotted in **Fig. 4.10**, the pristine $BiVO_4$ thin film shows significant absorption of visible light with band gap energy of 2.45 eV. $BiVO_4$ is indirect band gap material with VB and CB comprised of hybrid Bi 6s/O 2p and V 3d orbitals, respectively [51]. Conversely, the NS-titanate thin film shows prominent absorption in the UV region with a band gap energy of 3.17 eV. Interestingly, the hybridization of NS-titanate with $BiVO_4$ leads to the shifting of the absorption edge of the resultant nanohybrid thin film in the visible region of the solar spectrum with a band gap of 2.28 eV, clearly highlighting the effective electronic coupling between NS-titanate and $BiVO_4$. Summarizing the results of UV-vis DRS, the visible light harvesting ability of $BiVO_4$ is boosted by the electronic coupling with the NS-titanate. The effective visible light absorption ability of NS-titanate-$BiVO_4$ nanohybrid thin films makes them potential photocatalysts for solar-assisted photocatalysis applications [48,49].

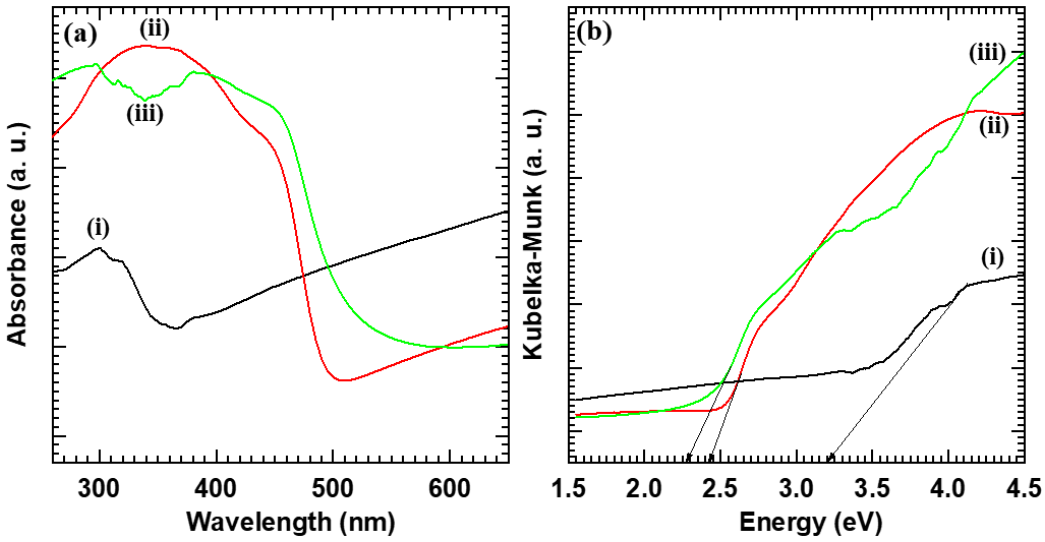

Fig. 4.10: (a) UV-vis absorbance spectra and (b) UV-vis DRS of (i) NS-titanate, (ii) $BiVO_4$, (iii) S-BT2 nanohybrid thin films.

4.5 Dye degradation Performance of NS-titanate-$BiVO_4$ nanohybrids:

The photocatalytic dye degradation performance of NS-titanate-$BiVO_4$ nanohybrid thin films compared to pristine $BiVO_4$ thin film was estimated with UV-vis spectroscopy, as explained in **Chapter 3, Section 3.5**.

4.5.1 Percentage degradation study for MB and Rh-B:

The photoactivity of the synthesized NS-titanate-$BiVO_4$ nanohybrid thin films is detected by measurement of the photocatalytic degradation of MB and Rh-B as target dyes under visible light illumination. To examine the effect of hybridization on photocatalytic activity, the photodegradation performances of pristine NS-titanate (explained in **Chapter 3, Section 3.5.1**) and $BiVO_4$ thin films are also evaluated. The photodegradation performance of NS-titanate-$BiVO_4$ nanohybrid thin films is estimated and represented in **Fig. 4.13** (their respective UV-vis absorbance spectra are represented in **Fig. 4.11 and Fig. 4.12**). The pristine $BiVO_4$ and NS-titanate-$BiVO_4$ nanohybrid thin films show decrease in absorption at the characteristic wavelengths of 664 and 553 nm with respect to irradiation time, representing the effective degradation of MB and RhB, respectively. The photocatalytic activity of pristine $BiVO_4$ is remarkably improved upon hybridization with NS-titanate. The optimized S-BT2 nanohybrid thin film photocatalyst demonstrated outstanding photoactivity for photodegradation of MB and Rh-B dyes with photodegradation rates of 92.1 and 91.3%, respectively, remarkable than pristine $BiVO_4$ (61.2 and 70.3%). The above results indicate that the present NS-titanate $BiVO_4$

nanohybrid thin films with enhanced photocatalytic activity can be considered highly effective visible-light-driven photocatalysts for photocatalytic application.

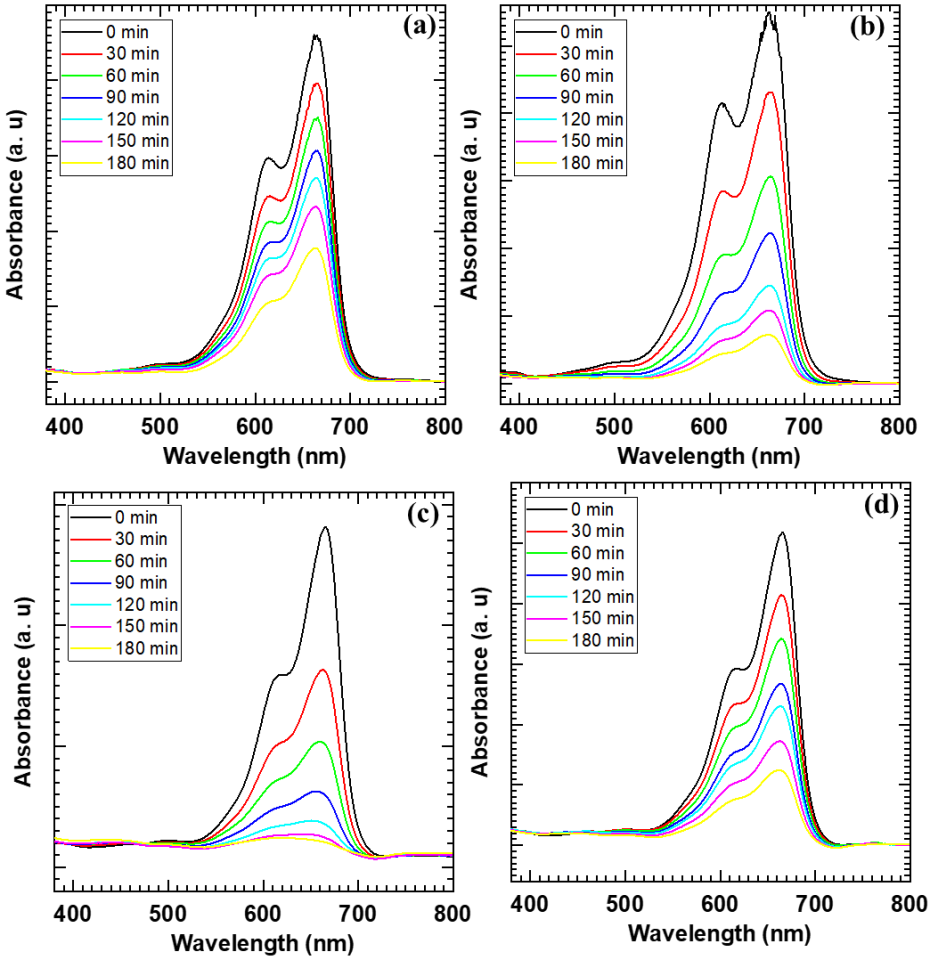

Fig. 4.11: UV-vis absorption spectra of the MB solution in the presence of (a) $BiVO_4$, (b) S-BT1, (c) S-BT2 and (d) S-BT3 nanohybrid thin film photocatalysts.

The superior photoactivity of present nanohybrid thin films can be attributed to the effective electronic coupling between hybridized species, resulting in decreased electron-hole recombination, which is beneficial for effective photocatalytic reactions. The mesoporous 3D network-type structure can allow expanded surface area with effective electronic coupling between hybridized species, leading to improved photocatalytic activity by giving rise to more reaction sites and effective charge separation and transport to catalytic sites. Conclusionally, the improved photoactivity of present nanohybrid thin films can be ascribed to the effective electronic coupling with minimal electron-hole recombination, strong visible light harvesting ability and mesoporous 3D network-type morphology.

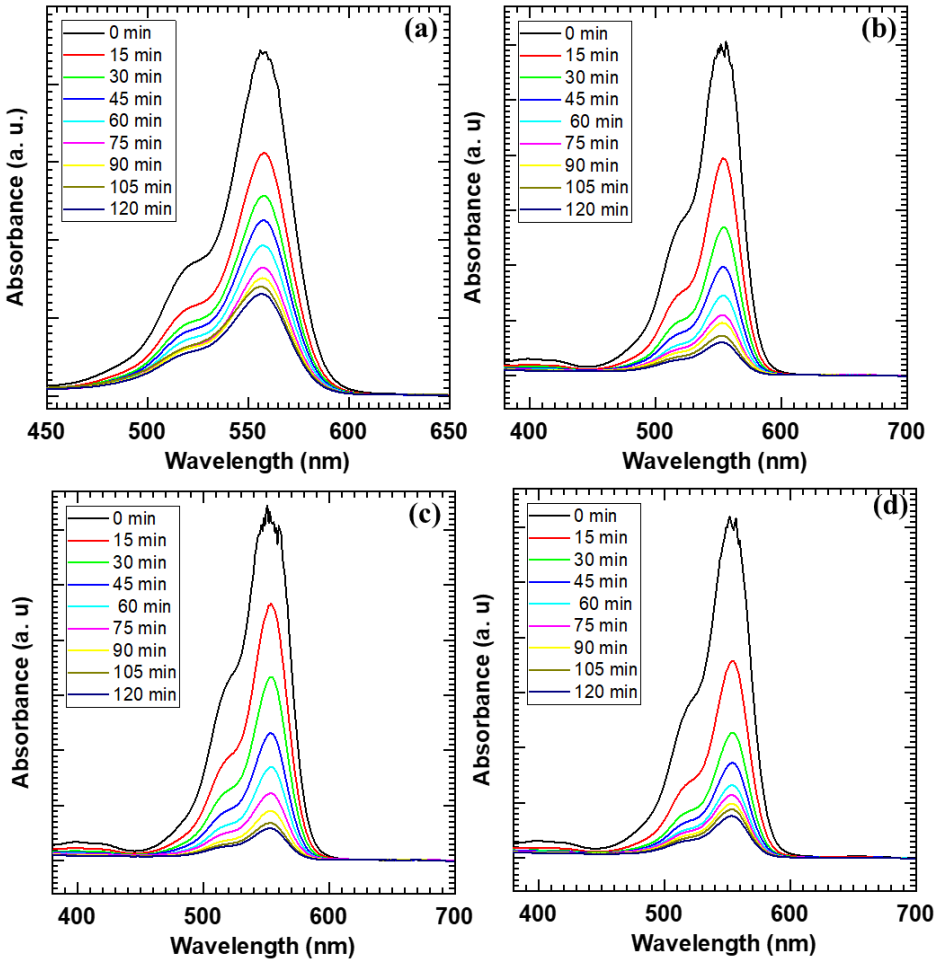

Fig. 4.12: UV-vis absorption spectra of the Rh-B solution in the presence of (a) $BiVO_4$, (b) S-BT1, (c) S-BT2 and (d) S-BT3 nanohybrid thin film photocatalysts.

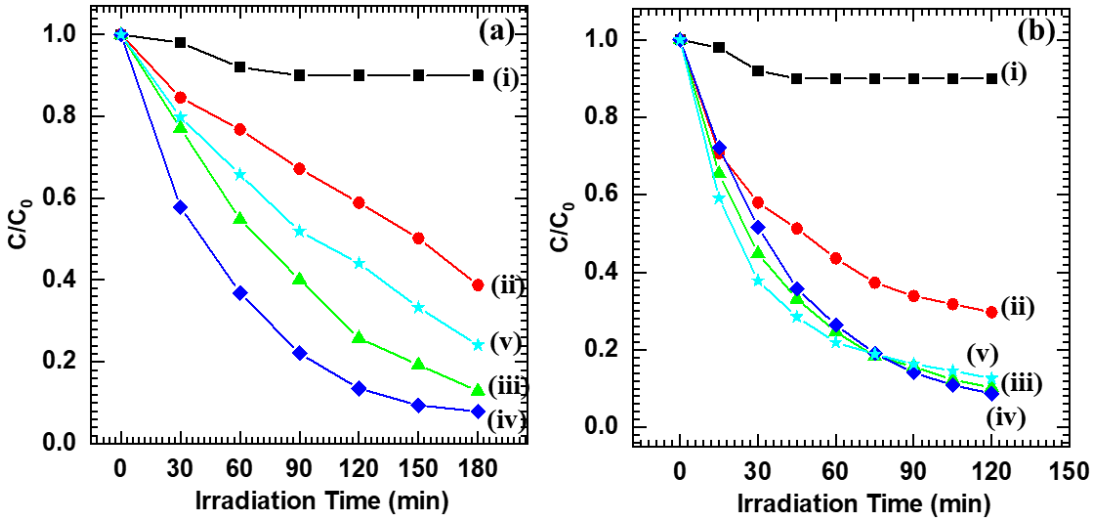

Fig. 4.13: (a) MB and (b) Rh-B degradation performance of (i) NS-titanate, (ii) $BiVO_4$, (iii) S-BT1, (iv) S-BT2, (v) S-BT3 nanohybrid thin film photocatalysts.

4.5.2 Rate kinetics study for MB and Rh-B:

The photodegradation performance of MB and Rh-B was further evaluated by their kinetics using a pseudo-first-order rate kinetic model. The pseudo-first-order reaction kinetics of MB and Rh-B dyes are represented in **Fig. 4.14**. The values of k and R^2 for all tested samples for photocatalytic degradation of MB and Rh-B dyes are noted in **Table 4.1**. Compared with other photocatalysts, S-BT2 nanohybrid thin film displays a higher k value, confirming the highest photocatalytic performance. The highest k values obtained for the S-BT2 nanohybrid thin film photocatalyst are 0.0141 and 0.0203 min^{-1} for MB and Rh-B dyes, respectively. The higher k-value for S-BT2 nanohybrid thin film photocatalyst is ascribed to the effective electronic coupling with minimal electron-hole recombination, strong visible light harvesting ability and mesoporous 3D network-type morphology, which is highly advantageous in effective charge separation and transport for photocatalytic applications.

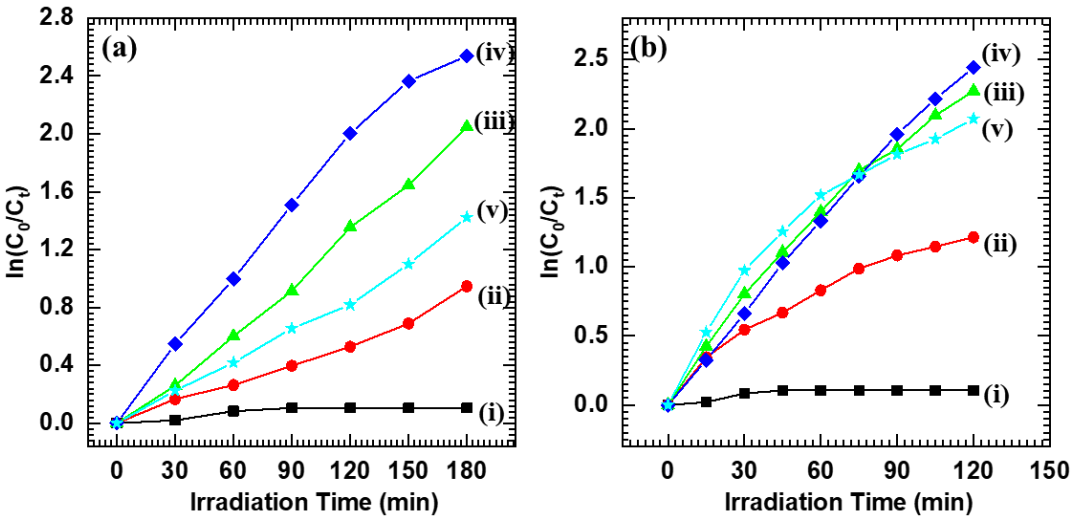

Fig. 4.14: Pseudo-first-order kinetics of (a) MB and (b) Rh-B for (i) NS-titanate, (ii) $BiVO_4$, (iii) S-BT1, (iv) S-BT2, (v) S-BT3 nanohybrid thin film photocatalysts.

Table 4.1: k and R^2 values of all tested photocatalysts.

Sample	MB		Rh-B	
	k (min^{-1})	R^2	k (min^{-1})	R^2
NS-titanate	0.0006	0.9994	0.0008	0.9992
$BiVO_4$	0.0053	0.9947	0.0101	0.9899
S-BT1	0.0114	0.9886	0.0189	0.9811
S-BT2	0.0141	0.9859	0.0203	0.9797
S-BT3	0.0079	0.9921	0.0173	0.9827

4.5.3 Recyclability study for MB and Rh-B:

Additionally, the recyclability of the S-BT2 nanohybrid thin film photocatalyst for photodegradation of MB and Rh-B dyes is confirmed by the course of five consecutive degradation tests, as represented in **Fig. 4.15**. During each experiment, the S-BT2 nanohybrid thin film is withdrawn from the dye solution, cleaned with DDW, dried at ambient conditions and used for the succeeding cycles. The optimized S-BT2 nanohybrid thin film photocatalyst exhibited good recycling ability for degradation of both MB and Rh-B dyes with photodegradation rates of 68.1 and 69.2% under 180 and 120 min of visible light illumination, respectively. The S-BT2 nanohybrid thin film retains its photoactivity with only gradual decrement for five repetitive degradation cycles, signifying the high photostability of the present S-BT2 nanohybrid thin film photocatalyst. The gradual decrement in degradation activity over the subsequent five cycles is ascribed to the detachment of overgrown SILAR-deposited $BiVO_4$ nanoparticles from the surface of the hybrid film or the adsorption of dye molecules on the surface of S-BT2 thin film. The results highlighted the effectiveness of S-BT2 nanohybrid thin film as an effective visible-light-driven photocatalyst for the photodegradation of MB and Rh-B dyes.

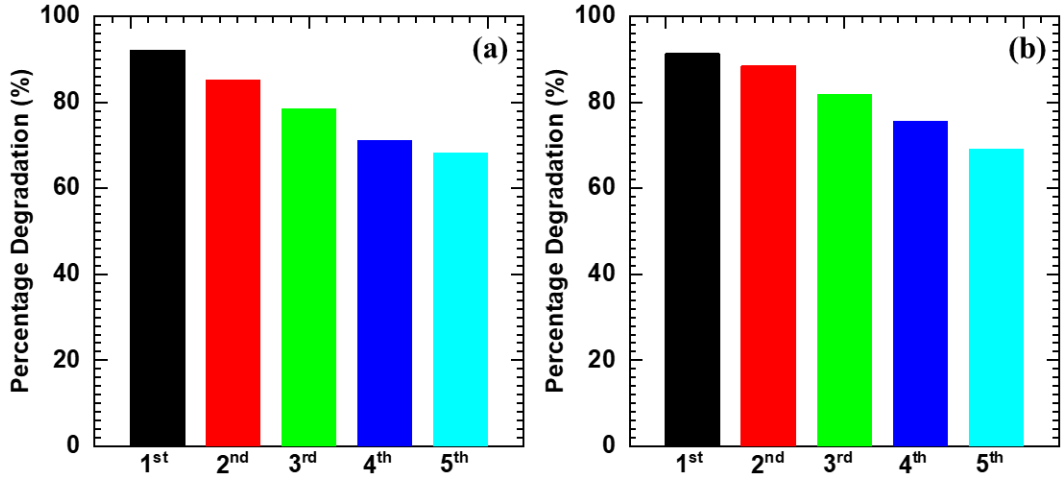

Fig. 4.15: Recyclability of S-BT2 nanohybrid thin film for (a) MB and (b) Rh-B dyes.

4.6 Photocatalytic Dye Degradation Mechanism:

To study the electron transfer between NS-titanate and $BiVO_4$, the electronic band structure of NS-titanate-$BiVO_4$ nanohybrid thin film is mapped from CV measurements and UV-vis DRS. The band positions of SILAR deposited $BiVO_4$ thin

film are estimated from the onset potential of the CV measurements and band gap energy determined from UV-vis DRS, as shown in **Fig. 4.16** [48, 52-53]. The onset potential of the reduction peak of $BiVO_4$ is seen at -0.31 V vs Ag/AgCl, corresponding to the lowest edge of CB at 4.35 eV vs vacuum (-0.15 eV vs NHE). As the band gap energy of $BiVO_4$ thin film is 2.45 eV, the position of the upper edge of the VB of $BiVO_4$ is located at 6.8 eV vs vacuum (2.3 eV vs NHE).

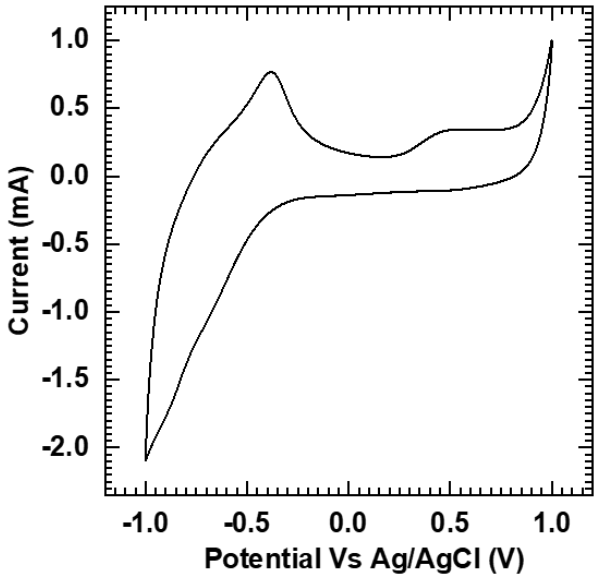

Fig. 4.16: CV curve of $BiVO_4$ thin film.

The photocatalytic dye degradation mechanism is based on the photoinduced charge separation and transport to the semiconductor surface upon the light incidence, as shown in **Fig. 4.17** [54]. When photons having energy equal to or greater than band gap of $BiVO_4$ are incident on NS-titanate-$BiVO_4$ nanohybrid thin film, its VB electrons are excited to CB, resulting in the generation of electron-hole pairs. From **Fig. 4.17**, it is seen that the CB position of NS-titanate is quite higher than that of $BiVO_4$ and VB position of $BiVO_4$ is higher than that of NS-titanate. Consequently, the photogenerated electrons from the CB of $BiVO_4$ can transfer towards the VB of NS-titanate, resulting in effective electronic coupling with the reduction in electron-hole recombination. The holes present at the VB of $BiVO_4$ react with water molecules to form OH* radicals. Generated OH* radicals are strong oxidizing agents that can degrade the adsorbed target dye molecules. Alternatively, the photogenerated electrons from the CB of $BiVO_4$ react with O_2 molecules to form $*O_2^-$ radicals. Further, the protonation of $*O_2^-$ radicals produces HOO* radicals. Finally, H_2O_2 produced from HOO* radicals split into OH* radicals, which can decompose the target dye molecules [55].

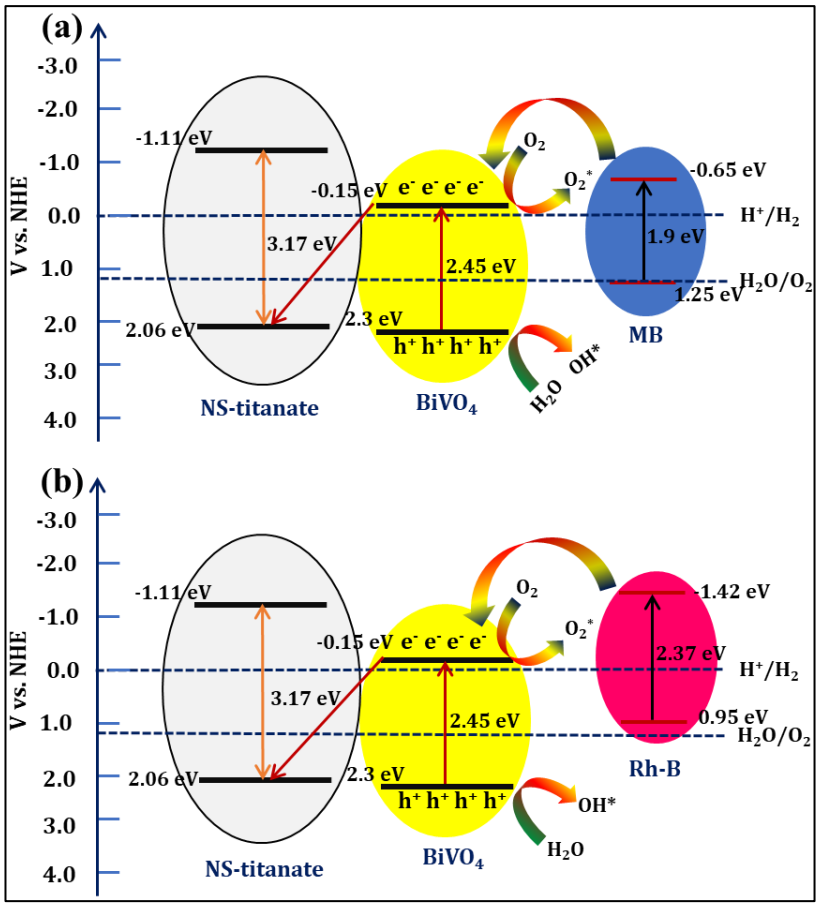

Fig. 4.17: Schematic diagram of photocatalytic dye degradation mechanism of (a) MB and (b) Rh-B over NS-titanate-$BiVO_4$ nanohybrid thin film.

4.7 Conclusions:

In the present chapter, $BiVO_4$ thin films are deposited using the cost-effective SILAR method. The structural and chemical bonding analysis of $BiVO_4$ thin film shows the highly crystalline growth of monoclinic scheelite $BiVO_4$ on ITO substrate. The $BiVO_4$ thin film displays highly porous interconnected nanoparticle morphology and narrow band gap energy with visible light absorption, beneficial for effective photocatalytic reactions. Further, the NS-titanate-$BiVO_4$ nanohybrid thin films are deposited by deposition of $BiVO_4$ thin films on EPD-deposited NS-titanate thin films by the SILAR method. The structural and chemical bonding analysis confirms the well-crystalline and uniform growth of monoclinic scheelite $BiVO_4$ on NS-titanate thin films. The morphological features show the mesoporous morphology composed of a 3D network of $BiVO_4$ nanoparticles deposited on the surface of randomly oriented titanate NSs. The optical study displays the effective visible light absorption ability of NS-titanate-$BiVO_4$ nanohybrid thin films, making them potential photocatalysts for solar-

assisted photocatalysis applications. The optimized S-BT2 nanohybrid thin film photocatalyst demonstrated outstanding photoactivity for photodegradation of MB and Rh-B dyes with photodegradation rates of 92.1 and 91.3%, respectively, remarkable than pristine $BiVO_4$ (61.2 and 70.3%). The superior photoactivity of nanohybrid thin films can be ascribed to the effective hybridization between NS-titanate and $BiVO_4$, strong visible light harvesting nature, notable electron-hole separation and mesoporous 3D network-type structure beneficial for effective photocatalytic reactions. The present nanohybridization approach can be further extended to synthesize several other 2D layered MONs-based nanohybrid thin films for various applications.

4.8 References:

1. J. Zia, F. Fatima, U. Riaz, A comprehensive review on photocatalytic activity of polythiophene based nanocomposites against degradation of organic pollutants, Catal. Sci. Technol. 11 (2021) 6630-6648.
2. V. Katheresan, J. Kansedo, S.Y. Lau, Efficiency of various recent wastewater dye removal methods: A review, J. Environ. Chem. Eng. 6 (2018) 4676-4697.
3. V. Selvaraj, T.S. Karthika, C. Mansiya, M. Alagar, An over review on recently developed techniques, mechanisms and intermediate involved in the advanced azo dye degradation for industrial applications, J. Mol. Struct. 1224 (2021) 129195.
4. J. Lan, Y. Wang, B. Huang, Z. Xiao, P. Wu, Application of polyoxometalates in photocatalytic degradation of organic pollutants, Nanoscale Adv. 3 (2021) 4646-4658.
5. W.S. Koe, J.W. Lee, W.C. Chong, Y.L. Pang, L.C. Sim, An overview of photocatalytic degradation: Photocatalysts, mechanisms and development of photocatalytic membrane, Environ. Sci. Pollut. Res. 27 (2020) 2522-2565.
6. K.P. Gopinath, N.V. Madhav, A. Krishnan, R. Malolan, G. Rangarajan, Present applications of titanium dioxide for the photocatalytic removal of pollutants from water: A review, J. Environ. Manage. 270 (2020) 110906.
7. R.P. Souza, T.K.F.S. Freitas, F.S. Domingues, O. Pezoti, E. Ambrosio, A.M. Ferrari-Lima, J.C. Garcia, Photocatalytic activity of TiO_2, ZnO and Nb_2O_5 applied to degradation of textile wastewater, J. Photochem. Photobiol. A: Chem. 329 (2016) 9-17.
8. M. Samadi, M. Zirak, A. Naseri, M. Kheirabadi, M. Ebrahimi, A.Z. Moshfegh, Design and tailoring of one-dimensional ZnO nanomaterials for photocatalytic degradation of organic dyes: A review, Res. Chem. Intermed. 45 (2019) 2197-2254.
9. O. Monfort, T. Roch, M. Gregor, L. Satrapinskyy, D. Raptis, P. Lianos, G. Plesch, Photooxidative properties of various $BiVO_4/TiO_2$ layered composite films and study of their photocatalytic mechanism in pollutant degradation, J. Environ. Chem. Eng. 5 (2017) 5143-5149.
10. A.P. Singh, B.R. Mehta, A. Held, L. Mayrhofer, M. Moseler, Band edge engineering in $BiVO_4/TiO_2$ nanohybrid: Enhanced photoelectrochemical performance through improved charge transfer, ACS Catal. 6 (2016) 5311-5318.
11. M. Ni, M.K.H. Leung, D.Y.C. Leung, K. Sumathy, A review and recent developments in photocatalytic water-splitting using TiO_2 for hydrogen production, Renew. Sustain. Energy Rev. 11 (2007) 401-425.

12. S. Biswas, M.F. Hossain, T. Takahashi, Y. Kubota, A. Fujishima, Photocatalytic activity of high-vacuum annealed CdS-TiO_2 thin film, Thin Solid Films 516 (2008) 7313-7317.
13. D.S. Bhachu, S. Sathasivam, C.J. Carmalt, I.P. Parkin, PbO modified TiO_2 thin films; A route to visible light photocatalysts, Langmuir 30 (2014) 624-630.
14. C. Xia, H. Wang, J.K. Kim, J. Wang, Rational design of metal oxide-based nanohybrid for efficient photocatalytic and photoelectrochemical systems, Adv. Funct. Mater. 31 (2021) 2008247.
15. M.J.F. Calvete, G. Piccirillo, C.S. Vinagreiro, M.M. Pereira, Hybrid materials for heterogeneous photocatalytic degradation of antibiotics, Coord. Chem. Rev. 395 (2019) 63-85.
16. S. Zhong, Y. Xi, S. Wu, Q. Liu, L. Zhao, S. Bai, Hybrid cocatalysts in semiconductor-based photocatalysis and photoelectrocatalysis, J. Mater. Chem. A 8 (2020) 14863-14894.
17. Y.K. Jo, J.M. Lee, S. Son, S.-J. Hwang, 2D inorganic nanosheet-based hybrid photocatalysts: Design, applications, and perspectives, J. Photochem. Photobiol. C: Photochem. Rev. 40 (2019) 150-190.
18. J.L. Gunjakar, I.Y. Kim, J.M. Lee, Y.K. Jo, S.-J. Hwang, Exploration of nanostructured functional materials based on hybridization of inorganic 2D nanosheets, J. Phys. Chem. C 118 (2014) 3847-3863.
19. G. Odling, N. Robertson, $BiVO_4$-TiO_2 composite photocatalysts for dye degradation formed using the SILAR method, Chem. Phys. Chem. 17 (2016) 2872-2880.
20. V.S. Kumbhar, H. Lee, J. Lee, K. Lee, Interfacial growth of the optimal $BiVO_4$ nanoparticles onto self-assembled WO_3 nanoplates for efficient photoelectrochemical water splitting, J. Colloid Interface Sci. 557 (2019) 478-487.
21. T. Stoll, G. Zafeiropoulos, I. Dogan, H. Genuit, R. Lavrijsen, B. Koopmans, M.N. Tsampas, Visible-light-promoted gas-phase water splitting using porous WO_3/$BiVO_4$ photoanodes, Electrochem. Commun. 82 (2017) 47-51.
22. L. Yan, W. Zhao, Z. Liu, 1D ZnO/$BiVO_4$ heterojunction photoanodes for efficient photoelectrochemical water splitting, Dalton Trans. 45 (2016) 11346-11352.
23. S.P. Kulkarni, V.V. Magdum, Y.M. Chitare, P.D. Sawant, S.V. Talekar, S.A. Pawar, A.U. Pawar, D.B. Malavekar, S.D. Sartale, A.A. Ghfar, J.L. Gunjakar, Modified successive ionic layer adsorption and reaction for interconnected bismuth vanadate nanograins: Highly active visible light harvesting photoanodes, J. Photochem. Photobiol. A: Chem. 454 (2024) 115737.
24. K.K. Dey, S. Gahlawat, P.P. Ingole, $BiVO_4$ optimized to nano-worm morphology for enhanced activity towards photoelectrochemical water splitting, J. Mater. Chem. A 7 (2019) 21207-21221.
25. Y. Matsumoto, A. Funatsu, D. Matsuo, U. Unal, K. Ozawa, Electrochemistry of titanate (IV) layered oxides, J. Phys. Chem. B 105 (2001) 10893-10899.
26. S.B. Patil, H.J. Kim, H.-K. Lim, S.M. Oh, J. Kim, J. Shin, H. Kim, J.W. Choi, S.-J. Hwang, Exfoliated 2D lepidocrocite titanium oxide nanosheets for high sulfur content cathodes with highly stable Li-S battery performance, ACS Energy Lett. 3 (2018) 412-419.
27. J.H. Choy, H.-C. Lee, H. Jung, H. Kim, H. Boo, Exfoliation and restacking route to anatase-layered titanate nanohybrid with enhanced photocatalytic activity, Chem. Mater. 14 (2002) 2486-2491.
28. H. Jung, H.-C. Lee, S.-M. Paek, S.-J. Hwang, J.-H. Choy, A novel hetero-structured RuS_2 titanate nanohybrid, J. Phys. Chem. Solids 67 (2006) 1248-1251.

29. M. Mousavi-Kamazani, Facile hydrothermal synthesis of egg-like $BiVO_4$ nanostructures for photocatalytic desulfurization of thiophene under visible light irradiation, J. Mater. Sci. Mater. Electron. 30 (2019) 17735-17740.
30. L. Zhang, Z. Dai, G. Zheng, Z. Yao, J. Mu, Superior visible light photocatalytic performance of reticular $BiVO_4$ synthesized via a modified sol-gel method, RSC Adv. 8 (2018) 10654-10664.
31. P. Pookmanee, S. Kojinok, R. Puntharod, S. Sangsrichan, S. Phanichphant, Preparation and characterization of $BiVO_4$ powder by the sol-gel method, Ferroelectrics 456 (2013) 45-54.
32. Y. Geng, P. Zhang, S. Kuang, Fabrication and enhanced visible-light photocatalytic activities of $BiVO_4/Bi_2WO_6$ composites, RSC Adv. 4 (2014) 46054-46059.
33. S.W. Hong, A. Kim, J.H. Choi, H. Jung, J.K. Park, Intercalation of conjugated polyelectrolytes in layered titanate nanosheets for enhancement in photocatalytic activity, J. Solid State Chem. 269 (2019) 291-296.
34. L.S. Chougala, M.S. Yatnatti, R.K. Linganagoudar, R.R. Kamble, J.S. Kadadevarmath, A simple approach on synthesis of TiO_2 nanoparticles and its application in dye-sensitized solar cells, J. Nano-Electron. Phys. 9 (2017) 40051-40056.
35. R. Chroma, M. Vilkova, I. Shepa, P. Makos-Chelstowska, V. Andruch, Investigation of tetrabutylammonium bromide-glycerol-based deep eutectic solvents and their mixtures with water by spectroscopic techniques, J. Mol. Liq. 330 (2021) 115617.
36. T.D. Nguyen, Q.T.P. Bui, T.B. Le, T.M. Altahtamouni, K.B. Vu, D.V.N. Vo, N.T.H. Le, T.D. Luu, S.S. Hong, K.T. Lim, Co^{2+} substituted for Bi^{3+} in $BiVO_4$ and its enhanced photocatalytic activity under visible LED light irradiation, RSC Adv. 9 (2019) 23526-23534.
37. X. Tian, Y. Zhu, W. Zhang, Z. Zhang, R. Hua, Preparation and photocatalytic properties of Mo-doped $BiVO_4$, J. Mater. Sci. Mater. Electron. 30 (2019) 19335-19342.
38. T.S. Dabodiya, P. Selvarasu, A.V. Murugan, Tetragonal to monoclinic crystalline phases change of $BiVO_4$ via microwave-hydrothermal reaction: In correlation with visible-light-driven photocatalytic performance, Inorg. Chem. 58 (2019) 5096-5110.
39. W. Hu, L. Li, G. Li, Y. Liu, R.L. Withers, Atomic-scale control of TiO_6 octahedra through solution chemistry towards giant dielectric response, Sci. Rep. 4 (2014) 6582.
40. A. Kudo, T. Kondo, Photoluminescent and photocatalytic properties of layered cesium titanates, $Cs_2Ti_nO_{2n+1}$ (n=2,5,6), J. Mater. Chem. 7 (1997) 777-780.
41. T. Gao, H. Fjellvag, P. Norby, Raman scattering properties of a protonic titanate $H_xTi_{2-x/4}\square_{x/4}O_4 \cdot H_2O$ (□, vacancy; x=0.7) with lepidocrocite-type layered structure, J. Phys. Chem. B 112 (2008) 9400-9405.
42. E. Zhang, Y. Pan, T. Lu, Y. Zhu, W. Dai, Novel synthesis of S-doped anatase TiO_2 via hydrothermal reaction of Cu-Ti amorphous alloy, Appl. Phys. A 126 (2020) 606.
43. X. Zhu, G. Wen, H. Liu, S. Han, S. Chen, Q. Kong, W. Feng, One-step hydrothermal synthesis and characterization of Cu-doped TiO_2 nanoparticles/nanobucks/nanorods with enhanced photocatalytic performance under simulated solar light, J. Mater. Sci. Mater. Electron. 30 (2019) 13826-13834.
44. P.S. Bagus, E. Ilton, C.J. Nelin, Extracting chemical information from XPS spectra: A perspective, Catal. Lett. 148 (2018) 1785-1802.
45. M. Zalfani, B.V. Schueren, Z.-Y. Hu, J.C. Rooke, R. Bourguiga, M. Wu, Y. Li, G.V. Tendeloo, B.-L. Su, Novel 3DOM $BiVO_4/TiO_2$ nanocomposites for highly enhanced photocatalytic activity, J. Mater. Chem. A 3 (2015) 21244-21256.

46. Y. Chen, Y. Liu, X. Xie, C. Li, Y. Si, M. Zhang, Q. Yan, Synthesis of flower-like $BiVO_4$/BiOI core/shell nanohybrid photocatalyst for tetracycline degradation under visible-light irradiation, J. Mater. Sci. Mater. Electron. 30 (2019) 9311-9321.
47. S.P. Kulkarni, Y.M. Chitare, V.V. Magdum, P.D. Sawant, S.V. Talekar, S.A. Pawar, U.M. Patil, K.V. Gurav, D.B. Malavekar, A.U. Pawar, J.L. Gunjakar, Chemically synthesized facet-controlled visible light active $BiVO_4$ thin films for photoelectrochemical water splitting, Appl. Phys. A 129 (2023) 876.
48. J.L. Gunjakar, T.W. Kim, H.N. Kim, I.Y. Kim, S.-J. Hwang, Mesoporous layer-by-layer ordered nanohybrids of layered double hydroxide and layered metal oxide: Highly active visible light photocatalysts with improved chemical stability, J. Am. Chem. Soc. 133 (2011) 14998-15007.
49. J.L. Gunjakar, I.Y. Kim, J.M. Lee, N.-S. Lee, S.-J. Hwang, Self-assembly of layered double hydroxide 2D nanoplates with graphene nanosheets: An effective way to improve the photocatalytic activity of 2D nanostructured materials for visible light-induced O_2 generation, Energy Environ. Sci. 6 (2013) 1008-1017.
50. J.L. Gunjakar, T.W. Kim, I.Y. Kim, J.M. Lee, S.-J. Hwang, Highly efficient visible-light-induced O_2 generation by self-assembled nanohybrids of inorganic nanosheets and polyoxometalate nanoclusters, Sci. Rep. 3 (2013) 2080.
51. D. Chen, Z. Xie, Y. Tong, Y. Huang, Review on $BiVO_4$-based photoanodes for photoelectrochemical water oxidation: The main influencing factors, Energy Fuels 36 (2022) 9932-9949.
52. K. Saruwatari, H. Sato, T. Idei, J. Kameda, A. Yamagishi, A. Takagaki, K. Domen, Photoconductive properties of organic-inorganic hybrid films of layered perovskite-type niobate, J. Phys. Chem. B 109 (2005) 12410-12416.
53. N. Sakai, Y. Ebina, K. Takada, T. Sasaki, Electronic band structure of titania semiconductor nanosheets revealed by electrochemical and photoelectrochemical studies, J. Am. Chem. Soc. 126 (2004) 5851-5858.
54. M.A. Rauf, S.S. Ashraf, Fundamental principles and application of heterogeneous photocatalytic degradation of dyes in solution, Chem. Eng. J. 151 (2009) 10-18.
55. A. Ajmal, I. Majeed, R.N. Malik, H. Idriss, M.A. Nadeem, Principles and mechanisms of photocatalytic dye degradation on TiO_2 based photocatalysts: A comparative overview, RSC Adv. 4 (2014) 37003-37026.

CHAPTER-5

Synthesis and Characterizations of NS-hexaniobate-$BiVO_4$ Nanohybrids by CBD: Application in Photocatalytic Dye Degradation

CHAPTER-5

Synthesis and Characterizations of NS-hexaniobate-$BiVO_4$ Nanohybrids by CBD: Application in Photocatalytic Dye Degradation

5.1 Introduction:

The need and benefits of nanohybridization for improving the photocatalytic performance of $BiVO_4$ thin films are described in the previous chapters (**Chapter 1, Section 1.3, Chapter 2, Section 2.4** and **Chapter 3, Section 3.1**). In recent years, research interest in the nanostructured semiconductor photocatalysts is extended to 2D NSs materials due to unusually high anisotropy in their crystal structure, morphology, large surface area and thin thickness, which render them advantageous candidates for the synthesis of nanohybrid materials with unique physicochemical properties [1]. Similar to NS-titanate, the 2D NS-hexaniobate evokes high research interest as macromolecules for the hybrid photocatalysts due to their highly anisotropic 2D morphology, ultrathin thickness, high surface area, electrostatic surface charged, high mechanical flexibility, suitable band positions for the reduction of hydroxide ions as well as oxidation of water molecules and high chemical stability [1-3]. On this background, hybridization between narrow bandgap $BiVO_4$ and wide bandgap 2D NS-hexaniobate can enable expanded surface area, superior visible light harvesting ability and improved electronic coupling useful for visible-light-induced photocatalytic dye degradation.

The present chapter deals with the synthesis of NS-hexaniobate-$BiVO_4$ nanohybrid thin films by depositing $BiVO_4$ layers over EPD-deposited NS-hexaniobate thin films by CBD method. The effect of the hybridization of $BiVO_4$ with NS-hexaniobate on the visible-light-induced photocatalytic degradation of MB and Rh-B dyes is explored together with their structural and physicochemical features. The present nanohybridization strategy is novel because the efficient 2D nanohybrid photocatalyst based on layered NS-hexaniobate and $BiVO_4$ has not yet been realized in practical application.

5.2 Synthesis and characterizations of NS-hexaniobate-$BiVO_4$ nanohybrids:

5.3 Experimental details:

5.3.1 Chemicals:

Niobium pentoxide (Nb_2O_5), potassium carbonate (K_2CO_3), $Bi(NO_3)_3.5H_2O$, $NaVO_3$, $C_{10}H_{14}N_2Na_2O_8$, NaOH, HCl, TBAOH and C_2H_5OH were purchased from Sigma-Aldrich and used as received.

5.3.2 Synthesis of NS-hexaniobate-$BiVO_4$:

The NS-hexaniobate-$BiVO_4$ nanohybrid thin films were synthesized by deposition of $BiVO_4$ on NS-hexaniobate thin films. The CBD and EPD were used to

deposit $BiVO_4$ and NS-hexaniobate thin films, respectively. The synthesis of NS-hexaniobate-$BiVO_4$ nanohybrid thin films is comprised of the following steps.

(a) Synthesis of pristine NS-hexaniobate:

The wide band gap and chemically stable NS-hexaniobate were synthesized from highly crystalline potassium hexaniobate ($K_4Nb_6O_{17}$) host crystals by ion exchange and exfoliation process [4]. The host crystals of potassium hexaniobate were synthesized by solid-state reaction of an intimate mixture of K_2CO_3 and Nb_2O_5 (molar ratio of 2:3) at 1050℃ (24 h). The corresponding protonic hexaniobate ($H_xK_{4-x}Nb_6O_{17}$) was prepared by reaction of potassium hexaniobate powder with an aqueous solution of 1 M HCl at ambient temperature for four days. The HCl solution was exchanged with a fresh one daily throughout this proton exchange process. Afterwards, the protonated solid was centrifuged, thoroughly washed with DDW and air-dried to eliminate the acidic residue. The layered proton-exchanged hexaniobate was delaminated into individual NS-hexaniobate by intercalating TBA molecules into the interlayer space of protonic hexaniobate. For this, the weighted amount of protonic hexaniobate was reacted with an aqueous solution of TBAOH. The solution was shaken vigorously for two days, which produced the colloidal suspension of exfoliated NS-hexaniobate. A schematic representation of the intercalation-exfoliation protocol for synthesizing NS-hexaniobate is shown in **Fig. 5.1**.

(b) Synthesis of pristine NS-hexaniobate thin films:

The well-cleaned ITO-coated glass substrates were used for deposition. The ITO substrate cleaning procedure is described in **Chapter 3, Section 3.3.2**.

Initially, the colloidal suspension of NS-hexaniobate (with pH of 12-12.5) was dialyzed for 14 h using a dialysis membrane (Dialysis Membrane-135, average flat width-33.12 mm, average diameter-23.8 mm, Capacity approx.-4.45 ml cm^{-1}) in DDW to reach a pH of 8. The NS-hexaniobate thin films were obtained from the dialyzed NS-hexaniobate colloidal suspension by EPD method. The dialyzed NS-hexaniobate colloidal suspension and absolute ethanol were mixed in the 1:3 volume proportion for the EPD. The NS-hexaniobate thin films were deposited on ITO-coated glass substrates using a specially designed cylindrical-shaped graphite EPD cell by applying the potential of 15 V DC across the ITO and graphite cell electrodes. The graphite cell and ITO substrate can act as a cathode and anode, respectively. The deposition time of EPD was adjusted to a range of 5 to 15 min. The obtained NS-hexaniobate thin films were

annealed at 230°C for 1 h in the air to improve adherence and remove TBA content. The annealed NS-hexaniobate thin films deposited at 5, 10 and 15-min deposition times are denoted as Nb-1, Nb-2 and Nb-3, respectively.

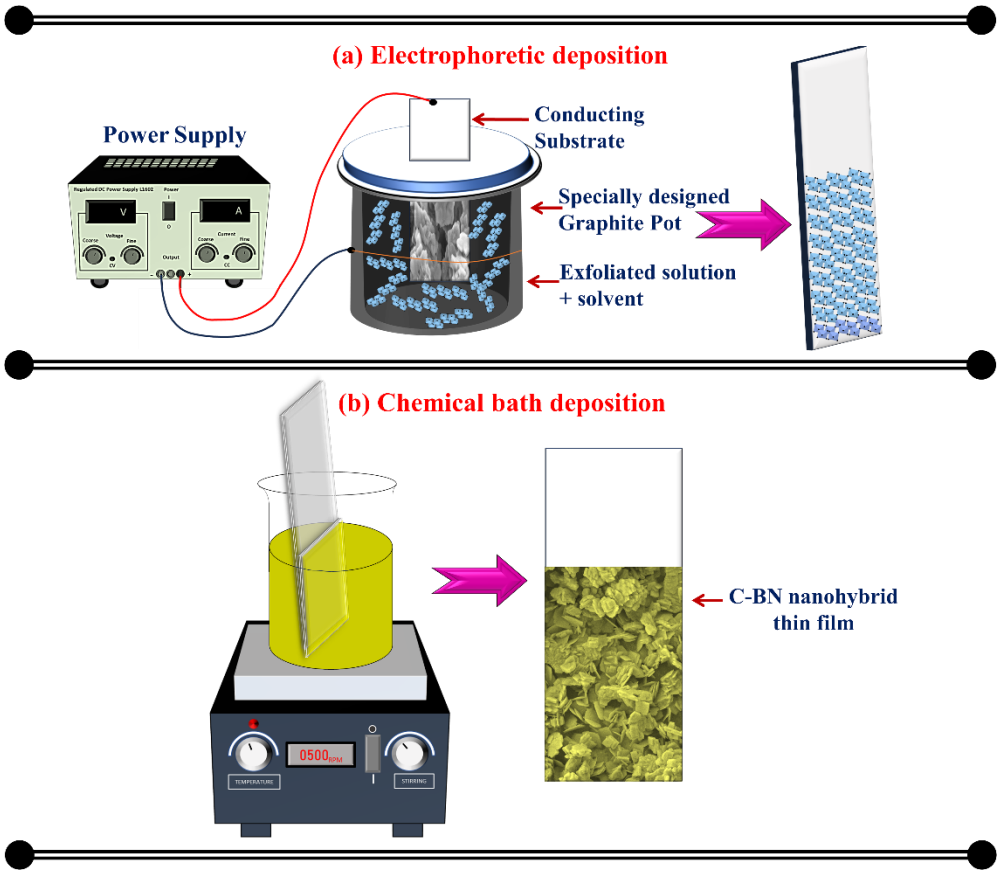

Fig. 5.1: Schematic model of (a) EPD of NS-hexaniobate thin films and (b) CBD method for depositing NS-hexaniobate-$BiVO_4$ nanohybrid thin films.

(c) Synthesis of NS-hexaniobate-$BiVO_4$ nanohybrid thin films:

$BiVO_4$ thin films were deposited using the CBD method on EPD-deposited NS-hexaniobate thin films as described in **Chapter 3, Section 3.3.2** [5]. The chemical bath for the deposition of $BiVO_4$ comprised an aqueous solution of 25 mM $Bi(NO_3)_3 \cdot 5H_2O$ complexed with EDTA disodium salt (25 mM) under constant stirring. The aqueous stock solution of 25 mM $NaVO_3$ was prepared as another precursor. The CBD bath was obtained by mixing vanadium stock solution into the bismuth complex under constant stirring. The final pH of the bath was adjusted to 5.5 using an aqueous solution of 1 M NaOH. Afterward, the bath was maintained at 85°C under constant stirring for 1 h to obtain a transparent pale-yellow color solution.

The obtained solution was cooled to room temperature and used as a deposition solution. The NS-hexaniobate-coated ITO substrates (Nb-1, Nb-2 and Nb-3) were immersed vertically in the above deposition bath, and the whole bath was kept in the water bath at a constant temperature of 85°C for 10 h. After 10 h, the direct growth of $BiVO_4$ on NS-hexaniobate thin films was observed. Subsequently, the NS-hexaniobate-$BiVO_4$-coated ITO substrates were removed from the bath, washed with DDW and air-dried. The schematic representation of the NS-hexaniobate-$BiVO_4$ thin film deposition process is shown in **Fig. 5.1**. The as-deposited NS-hexaniobate-$BiVO_4$ nanohybrid thin films were annealed in a muffle furnace at 400°C for 2 h. The annealed NS-hexaniobate-$BiVO_4$ nanohybrid thin films deposited on Nb-1, Nb-2 and Nb-3 thin films are denoted as C-BN1, C-BN2 and C-BN3, respectively.

5.4 Characterizations of NS-hexaniobate-$BiVO_4$ nanohybrids:

The NS-hexaniobate-$BiVO_4$ nanohybrid thin films were characterized by different physicochemical characterization techniques, as explained in **Chapter 3, Section 3.4**.

Note: The C-BN2 nanohybrid thin film shows improved photocatalytic dye degradation performance. Therefore, all the optimized C-BN2 nanohybrid thin film characterizations are compared with the pristine materials.

5.4.1 XRD analysis:

The crystallographic properties of the synthesized materials were probed by using XRD analysis. The XRD patterns of NS-hexaniobate-$BiVO_4$ nanohybrid thin film (C-BN2) compared with the pristine NS-hexaniobate and $BiVO_4$ thin films are shown in **Fig. 5.2**. As represented in **Fig. 5.2(a)**, the potassium hexaniobate ($K_4Nb_6O_{17}$) displays a highly intense series of (020), (040), (220), (002), (0 10 0), (063) and (400) diffraction peaks matching with the highly crystalline well-ordered layered orthorhombic structure (JCPDS: 76-0977) [5,6]. Its protonated product ($H_xK_{4-x}Nb_6O_{17}$) also shows an intense series of (020), (040), (002), (0 10 0) and (400) diffraction peaks. Additionally, minor signature (hkl) peaks (140), (041), (220), (240) and (063) matching with the in-plane host structure are discernible, demonstrating that the in-plane host structure remains intact after the proton-exchange process [6-9]. The present XRD features confirm the formation of a well-crystalline layered protonated hexaniobate with orthorhombic structure. The XRD pattern of pristine NS-hexaniobate thin film (**Fig. 5.2(b)**) shows a high-intensity broad (020) diffraction peak corresponding to the well-

ordered stacking of lamellar NS-hexaniobate with the orthorhombic structure. The interplanar spacing of the (020) diffraction peak is 0.87 nm [6]. Additionally, the diffraction peaks denoted by the asterisk '*' match with the ITO substrate. Remarkably, no other peak corresponding to the different phases of Nb_2O_5 is present, indicating the high thermal stability of NS-hexaniobate thin films. As described in **Chapter 3, Section 3.4.1**, the pristine CBD deposited $BiVO_4$ thin film shows typical Braggs reflections and characteristic peak splitting (18.5°, 35° and 46°) corresponding to the monoclinic scheelite $BiVO_4$ structure with space group (I2/a) (JCPDS no.: 14-0688) [10].

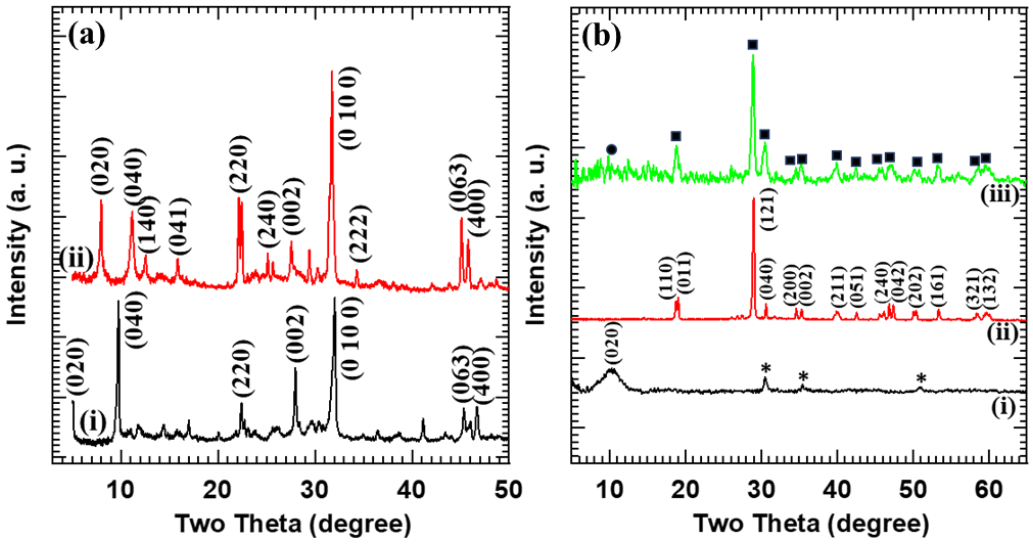

Fig. 5.2: (a) XRD patterns of (i) potassium hexaniobate, (ii) protonated hexaniobate and (b) XRD patterns of (i) NS-hexaniobate, (ii) $BiVO_4$, (iii) C-BN2 nanohybrid thin films (asterisk, circles and squares denote the Bragg reflections of ITO, NS-hexaniobate and monoclinic scheelite-type $BiVO_4$, respectively).

On the contrary, the C-BN2 nanohybrid thin film exhibits diffraction peaks corresponding to well-ordered lamellar NS-hexaniobate (denoted by circles) and monoclinic scheelite-type $BiVO_4$ (denoted by squares). It shows a broad (020) diffraction peak matching with the well-ordered stacking of lamellar NS-hexaniobate. It also shows typical Braggs reflections and characteristic peak splitting (18.5°, 35° and 46°) matching with the monoclinic scheelite $BiVO_4$. Present XRD results related to the NS-hexaniobate and $BiVO_4$ clearly indicate the formation of NS-hexaniobate and $BiVO_4$ in orthorhombic and monoclinic scheelite-type structures, respectively. This confirms the growth of monoclinic scheelite $BiVO_4$ over EPD-deposited lamellar NS-hexaniobate thin films.

5.4.2 FTIR analysis:

The chemical bonding nature and microscopic structural properties of NS-hexaniobate-$BiVO_4$ nanohybrid thin films compared to the pristine NS-hexaniobate and $BiVO_4$ thin films were investigated with FTIR spectroscopy, as shown in **Fig. 5.3**. The FTIR spectrum of pristine NS-hexaniobate thin film shows absorption peaks *v*1 (576 cm^{-1}) and *v*2 (901.25 cm^{-1}) corresponding to the stretching vibrations of the terminal Nb-O and asymmetric stretching vibrations of the Nb-O bridge in central NbO_6 octahedron, respectively [11-14]. The absorption peaks *v*3 (1626.25 cm^{-1}) and *v*4 (3449.66 cm^{-1}) correspond to the bending vibrations of water molecules and stretching vibrations of hydroxyl groups, respectively [15]. As described in **Chapter 3, Section 3.4.2**, the pristine $BiVO_4$ thin film displays sharp absorption peaks *v*5 (413 cm^{-1}) and *v*6 (482 cm^{-1}) linked with the bending vibrations of Bi-O and the stretching vibrations of VO_4^{3-}, respectively [16,17]. The absorption peaks *v*7 (741 cm^{-1}) and *v*8 (829 cm^{-1}) are assigned to the asymmetric and symmetric stretching vibrations of VO_4^{3-}, respectively [18]. The absorption peak *v*9 (3451.15 cm^{-1}) is associated with the stretching vibrations of hydroxyl groups [15].

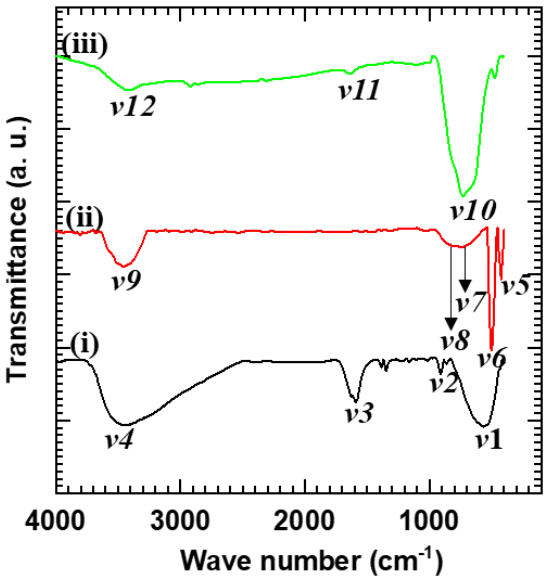

Fig. 5.3: FTIR spectra of (i) NS-hexaniobate, (ii) $BiVO_4$ and (iii) C-BN2 nanohybrid thin films.

On the other hand, the NS-hexaniobate-$BiVO_4$ nanohybrid thin film shows absorption peaks *v*10 (733.75 cm^{-1}), *v*11 (1626.25 cm^{-1}) and *v*12 (3444.55 cm^{-1}) related to the NS-hexaniobate and $BiVO_4$. The high-intensity broad absorption peak *v*10 originated from the superposition of metal-oxygen peaks of stretching vibrations of the

terminal Nb-O in central NbO_6 octahedron, asymmetric stretching vibrations of VO_4^{3-} and symmetric stretching vibrations of VO_4^{3-} [11, 18-19]. The absorption peaks *v*11 and *v*12 are ascribed to the bending vibrations of water molecules and stretching vibrations of hydroxyl groups, respectively [15]. The present FTIR features are well-matched with the chemical bonding characteristics of EPD-deposited NS-hexaniobate and CBD-deposited $BiVO_4$ thin films. These spectral features demonstrate the successful growth of monoclinic scheelite $BiVO_4$ phase over EPD-deposited NS-hexaniobate thin films.

5.4.3 Raman analysis:

The chemical bonding of NS-hexaniobate-$BiVO_4$ nanohybrid thin film as compared to pristine $BiVO_4$ and NS-hexaniobate thin films was further probed with micro-Raman analysis. As shown in **Fig. 5.4**, the NS-hexaniobate thin film shows a sharp Raman peak around P_1 (92.33 cm^{-1}) assigned to the internal bending modes of O-Nb-O groups [20]. The Raman peaks P_2 (219.55 cm^{-1}) and P_3 (250.43 cm^{-1}) are ascribed to the lattice vibration mode of highly distorted NbO_6 octahedra and Nb-O-Nb angular deformation modes, respectively [12, 21]. The Raman peaks centered within the frequency range of 500-700 cm^{-1}, P_4 (616.71 cm^{-1}) and P_5 (657.73 cm^{-1}) are attributed to the stretching of longer Nb-O bonds [20]. The Raman peak at higher frequency P_6 (895.86 cm^{-1}) corresponds to the Nb-O terminal stretching mode of highly distorted NbO_6 octahedra [21]. As described in **Chapter 3, Section 3.4.3**, the pristine $BiVO_4$ thin film shows Raman peaks P_7 (131 cm^{-1}) and P_8 (212 cm^{-1}), which are ascribed to the external modes (rotation or translation) of $BiVO_4$ [22,23]. The Raman peaks P_9 (325 cm^{-1}) and P_{10} (367 cm^{-1}) are assigned to the asymmetric (B_g symmetry) and symmetric (A_g symmetry) bending modes of the VO_4 tetrahedron, respectively [24]. The sharp and highly intense Raman peaks centered around P_{12} (826 cm^{-1}) and the shoulder P_{11} (710 cm^{-1}) are attributed to the symmetric and asymmetric (V-O) stretching modes of $BiVO_4$, respectively [22-24].

On the other hand, the NS-hexaniobate-$BiVO_4$ nanohybrid thin film displays Raman peaks attributed to the NS-hexaniobate and $BiVO_4$. The sharp and intense Raman peak around P_{13} (92.33 cm^{-1}) is assigned to the internal bending modes of O-Nb-O groups [20]. The Raman peaks P_{14} (131 cm^{-1}) and P_{15} (212 cm^{-1}) are ascribed to the external modes (rotation or translation) of $BiVO_4$ [22,23]. The Raman peaks P_{16} (325 cm^{-1}) and P_{17} (367 cm^{-1}) are assigned to the asymmetric (B_g symmetry) and symmetric (A_g symmetry) bending modes of the VO_4 tetrahedron, respectively [24]. The Raman

peaks P_{18} (710 cm^{-1}) and P_{19} (826 cm^{-1}) are attributed to the asymmetric and symmetric (V-O) stretching modes of $BiVO_4$, respectively [22-24]. These characteristic Raman features are associated with the lattice vibrational modes of EPD-deposited NS-hexaniobate and CBD-deposited $BiVO_4$ thin films. The present spectral features provide strong evidence of the successful growth of monoclinic scheelite $BiVO_4$ over EPD-deposited NS-hexaniobate thin films.

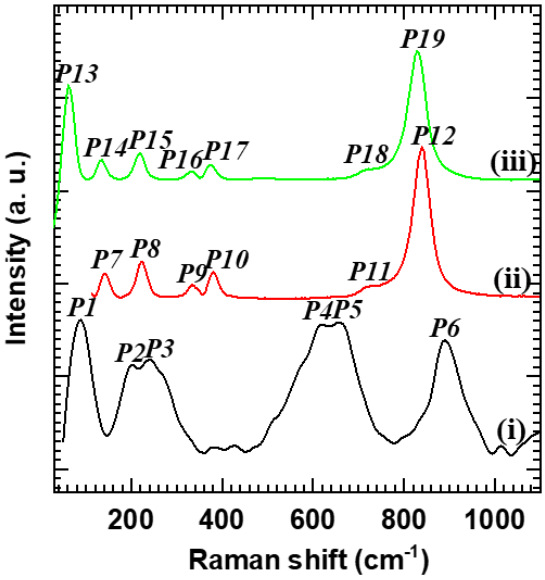

Fig. 5.4: Micro-Raman spectra of (i) NS-hexaniobate, (ii) $BiVO_4$ and (iii) C-BN2-nanohybrid thin films.

5.4.4 XPS analysis:

The effect of the hybridization of NS-hexaniobate and $BiVO_4$ on the chemical bonding characteristics of present NS-hexaniobate-$BiVO_4$ nanohybrid thin films was inspected with XPS analysis. The survey XPS spectrum of C-BN2 nanohybrid thin film (**Fig. 5.5**) shows the spectral features at BE of the Nb, Bi, V and O elements, indicating the presence of stated elements in C-BN2 nanohybrid thin film. As plotted in **Fig. 5.6(a)**, the core level Nb 3d XPS spectra of pristine NS-hexaniobate and NS-hexaniobate-$BiVO_4$ nanohybrid thin films display two sharp peaks P (207.1 eV) and Q (209.7 eV) corresponds to the spin-orbit splitting of Nb $3d_{5/2}$ and Nb $3d_{3/2}$, respectively [12]. The position of peaks (P and Q) and their BE difference of 2.6 eV indicate that Nb in its pentavalent state is present in the above samples [25]. **Fig. 5.6(b)** shows the Bi 4f core-level XPS spectra of the pristine $BiVO_4$ and NS-hexaniobate-$BiVO_4$ nanohybrid thin films. The spectra display peaks A (164 eV) and B (157.5 eV) corresponding to Bi $4f_{5/2}$ and Bi $4f_{7/2}$ states, respectively, which confirms the presence of Bi^{3+} ions in pristine

$BiVO_4$ and NS-hexaniobate-$BiVO_4$ nanohybrid thin films [26]. As shown in **Fig 5.6(c)**, the V 2p core-level XPS spectra of $BiVO_4$ and NS-hexaniobate-$BiVO_4$ nanohybrid thin films show spectral features C (523.1 eV) and D (515.5 eV) corresponding to the spin-orbit coupling of V $2p_{1/2}$ and V $2p_{3/2}$, respectively with BE difference of 7.28 eV, which confirms the presence of pentavalent state of V in pristine $BiVO_4$ and NS-hexaniobate-$BiVO_4$ nanohybrid thin films [27]. The O 1s core-level XPS spectra of pristine NS-hexaniobate, $BiVO_4$ and NS-hexaniobate-$BiVO_4$ nanohybrid thin films (**Fig. 5.6(d)**) exhibit an intense peak R (529.5 eV), which is attributed to presence of oxygen in core levels of pristine NS-hexaniobate, $BiVO_4$ and NS-hexaniobate-$BiVO_4$ nanohybrid thin films [26]. For NS-hexaniobate thin film, peak R is ascribed to Nb-O bonding. For the $BiVO_4$ thin film, peak R corresponds to Bi-O and V-O bonding. On the other hand, for NS-hexaniobate-$BiVO_4$ thin film, peak R is attributed to the Nb-O, Bi-O and V-O bonding. The observed XPS features underscore strong evidence of the presence of Bi^{3+}, V^{5+} and Nb^{5+} states of Bi, V and Nb in NS-hexaniobate-$BiVO_4$ nanohybrid thin film, respectively. This indicates the effective hybridization of NS-hexaniobate and $BiVO_4$ in NS-hexaniobate-$BiVO_4$ nanohybrid thin film.

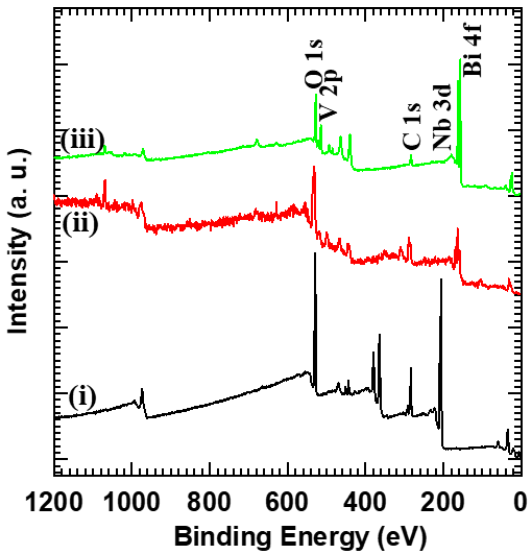

Fig. 5.5: Survey XPS spectra of (i) NS-hexaniobate, (ii) $BiVO_4$ and (iii) C-BN2 nanohybrid thin films.

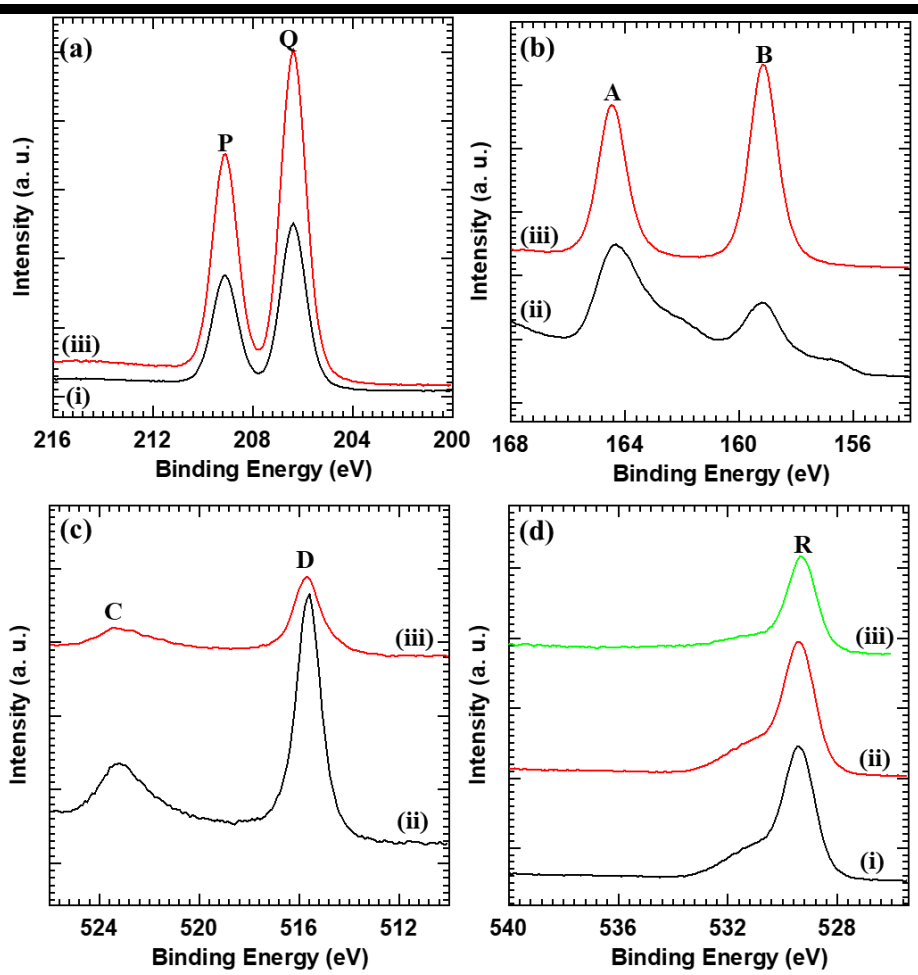

Fig. 5.6: (a) Nb 3d, (b) Bi 4f, (c) V 2p, (d) O 1s core-level XPS spectra of (i) NS-hexaniobate, (ii) $BiVO_4$ and (iii) C-BN2 nanohybrid thin films.

5.4.5 FESEM analysis:

The surface morphology, shape and size of present NS-hexaniobate-$BiVO_4$ nanohybrid thin film, as compared to pristine NS-hexaniobate and $BiVO_4$ thin films, were studied with FESEM analysis, as shown in **Fig. 5.7**. The EPD-deposited NS-hexaniobate thin film (**Fig. 5.7(a)**) displays the hexaniobate nanoscrolls laying parallel to the surface of ITO substrate. The lateral dimensions of the nanoscrolls are between 600 to 700 nm. The nanoscrolls are randomly aggregated on the surface of the ITO substrate to form a porous structure of NS-hexaniobate thin film. The CBD-deposited $BiVO_4$ thin film (**Fig. 5.7(b)**) shows interconnected nanoparticle morphology with an average particle size within the range of 75-95 nm [5].

Conversely, the NS-hexaniobate-$BiVO_4$ nanohybrid thin film (**Fig. 5.7(c-d)**) exhibits highly porous nanoclusters composed of randomly aggregated NSs, creating the slit-shaped porous. The edge-to-face interaction of deposited NSs forms the highly porous aggregated NSs network, creating the house-of-cards type morphology. A close

examination of the present FESEM discloses that the average lateral size of NS-hexaniobate-$BiVO_4$ nanohybrid ranges between 650-750 nm. Such a high surface area porous structure improves the photocatalytic activity of photocatalysts by providing more active sites, enhancing light absorption, and enabling improved diffusion of charge carriers to catalytic sites by minimizing charge recombination rate via spatial electron-hole separation, leading to the superior photocatalytic reactions. This type of porous morphology is usually reported for 2D NSs-based nanohybrids, which is crucial for solar-driven photo-functional applications [28-31].

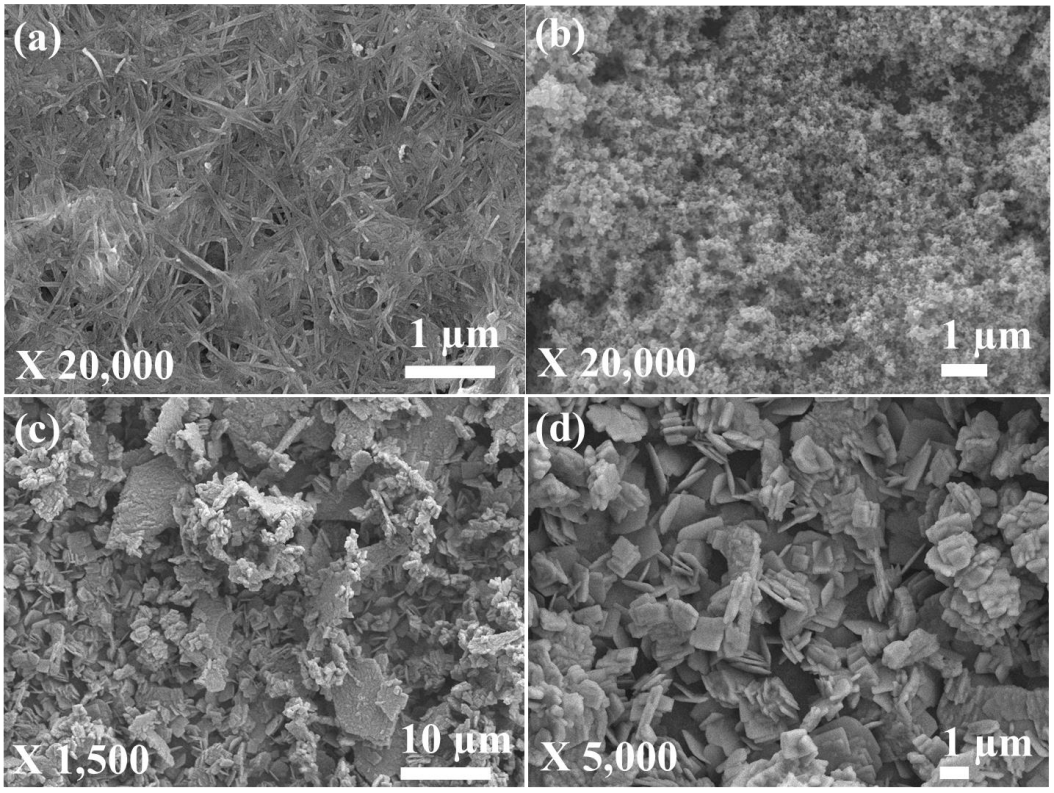

Fig. 5.7: FESEM micrographs of (a) NS-hexaniobate, (b) $BiVO_4$ and (c-d) C-BN2 nanohybrid thin films.

5.4.6 EDS analysis:

The chemical composition and the distribution of constituent elements of NS-hexaniobate-$BiVO_4$ nanohybrid thin film were probed with EDS and elemental mapping analysis, as shown in **Fig. 5.8** and **Fig. 5.9**. The NS-hexaniobate-$BiVO_4$ nanohybrid thin film shows the uniform distribution of niobium (Nb), bismuth (Bi), vanadium (V) and oxygen (O) elements at the nanometer scale with Bi/V ratio of ~1, confirming the uniform growth of $BiVO_4$ on the surface of NS-hexaniobate thin film without any special phase separation. Due to the large thickness of CBD deposited $BiVO_4$ thin film, the Nb

composition appears lower in the C-BN2 nanohybrid thin film. However, the upper layer $BiVO_4$ displays uniform deposition of stoichiometric $BiVO_4$ with Bi/V ratio of 0.97.

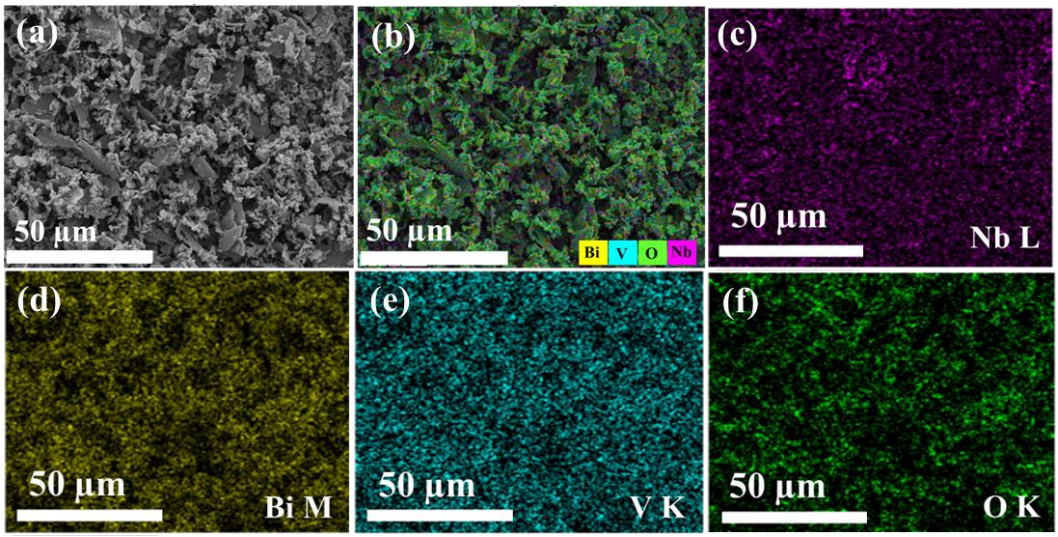

Fig. 5.8: (a) FESEM image and (b-f) EDS elemental maps of C-BN2 nanohybrid thin film.

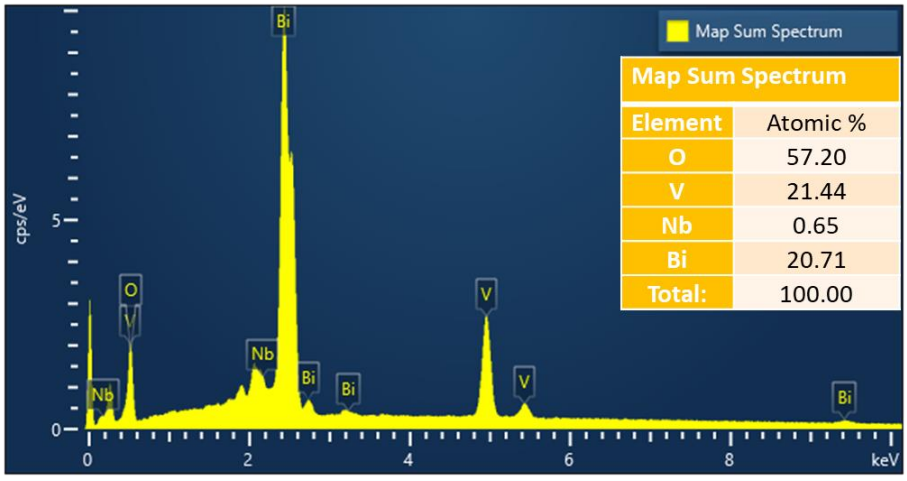

Fig. 5.9: EDS spectrum of C-BN2 nanohybrid thin film.

5.4.7 UV-vis DRS analysis:

The electronic structure and optical properties of NS-hexaniobate-$BiVO_4$ nanohybrid thin film compared to pristine NS-hexaniobate and $BiVO_4$ thin films were examined using UV-vis DRS analysis. As represented in **Chapter 3, Section 3.4.7**, the pristine $BiVO_4$ thin film shows strong visible light absorption with band gap energy of 2.33 eV, which can be ascribed to the transition of electrons from hybrid Bi 6s-O 2p orbital to V 3d orbital of $BiVO_4$ [32]. In contrast, the pristine NS-hexaniobate thin film (**Fig. 5.10**) displays prominent absorption in the UV region of the solar spectrum with a

band gap energy of 3.2 eV. On the other hand, the NS-hexaniobate-$BiVO_4$ nanohybrid thin film shows a quite similar type of optical behavior as that of pristine $BiVO_4$ thin film. Compared with the pristine $BiVO_4$, the NS-hexaniobate-$BiVO_4$ nanohybrid thin film causes a more prominent absorption of visible light with a band gap energy of 2.29 eV, highlighting its superior optical characteristics. This observation demonstrates that the NS-hexaniobate-$BiVO_4$ nanohybrid thin films can be highly effective photocatalysts for visible-light-driven photocatalytic dye degradation. The improved visible light harvesting nature of present nanohybrid thin films can be attributed to the effective electronic coupling between NS-hexaniobate and $BiVO_4$ [28-30].

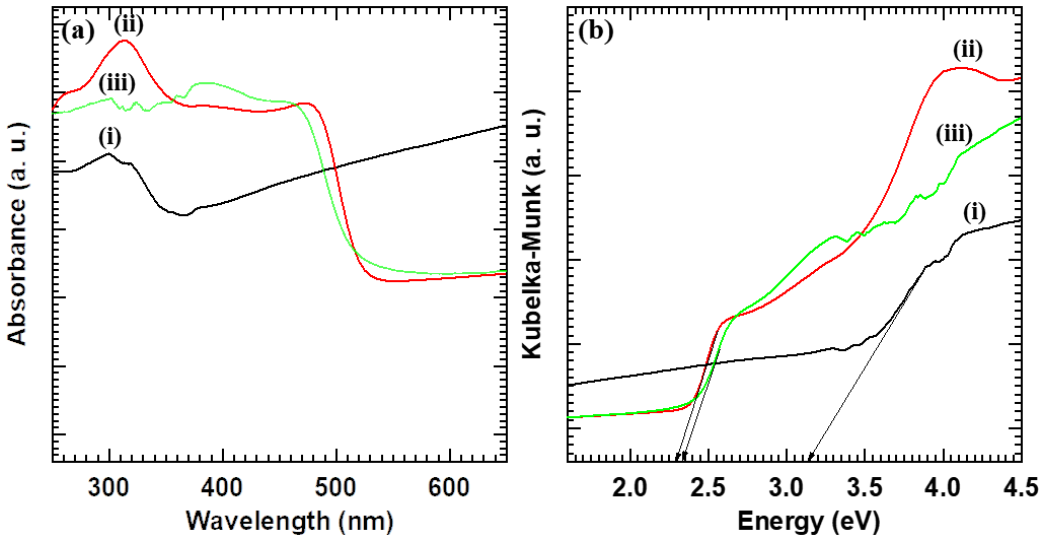

Fig. 5.10: (a) UV-vis absorbance spectra and (b) UV-vis DRS of (i) NS-hexaniobate, (ii) $BiVO_4$, (iii) C-BN2 nanohybrid thin films.

5.5 Dye degradation Performance of NS-hexaniobate-$BiVO_4$ nanohybrids:

The photocatalytic dye degradation activity of pristine NS-hexaniobate and NS-hexaniobate-$BiVO_4$ nanohybrid thin films was studied, as explained in **Chapter 3, Section 3.5**.

5.5.1 Percentage degradation study for MB and Rh-B:

The photoactivity of NS-hexaniobate-$BiVO_4$ nanohybrid thin films is examined with photocatalytic degradation of MB and Rh-B dyes under visible light illumination. To analyze the effect of hybridization on photocatalytic activity, the photocatalytic dye degradation performance of pristine NS-hexaniobate thin films is also measured. The photodegradation performance of pristine $BiVO_4$ thin film is explained in **Chapter 3, Section 3.5.1**. The UV-vis absorption spectra of pristine NS-hexaniobate and NS-

hexaniobate-$BiVO_4$ nanohybrid thin films for MB and Rh-B degradation are shown in **Fig. 5.11** and **Fig. 5.12**.

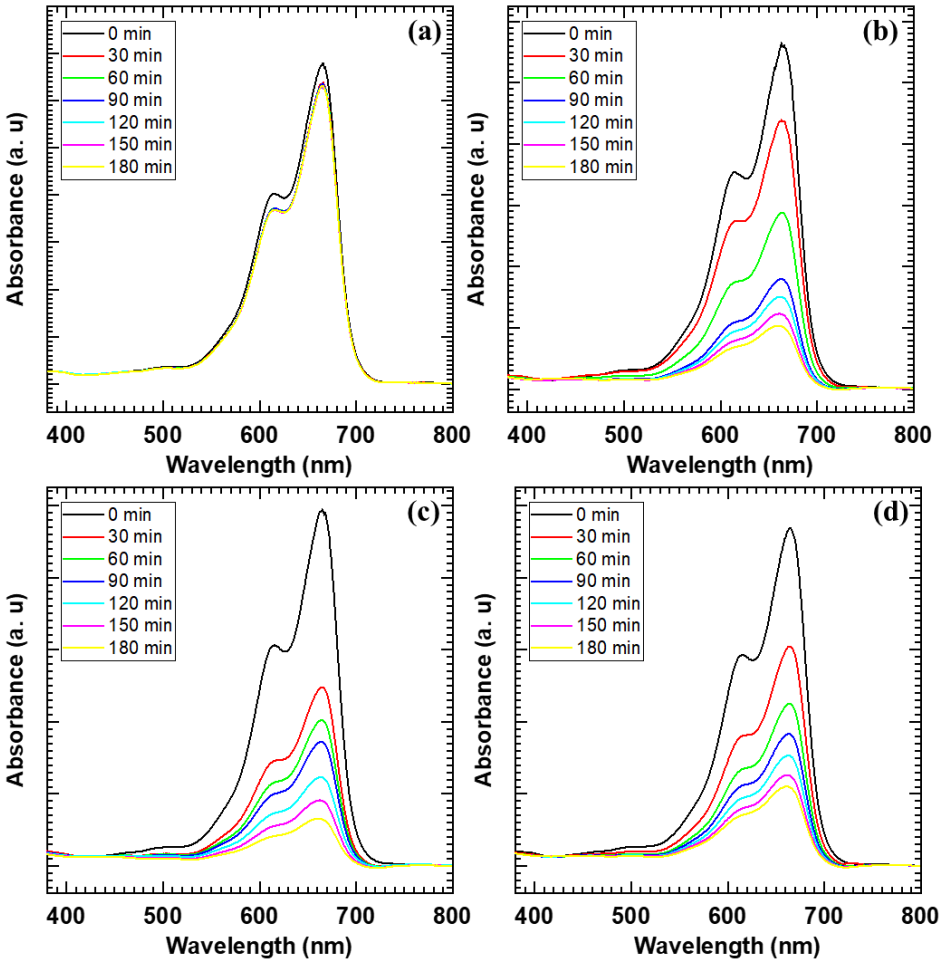

Fig. 5.11: UV-vis absorption spectra of the MB solution in the presence of (a) NS-hexaniobate, (b) C-BN1, (c) C-BN2 and (d) C-BN3 nanohybrid thin film photocatalysts.

The pristine NS-hexaniobate and NS-hexaniobate-$BiVO_4$ nanohybrid thin films display decrease in absorption at the characteristic wavelengths of 664 and 553 nm with respect to irradiation time, highlighting the effective degradation of MB and RhB, respectively. The photocatalytic degradation performance of pristine NS-hexaniobate and NS-hexaniobate-$BiVO_4$ nanohybrid thin films were calculated and graphically shown in **Fig. 5.13** [33]. The pristine NS-hexaniobate thin film shows minor photocatalytic degradation performance of 7.2% and 12.2% for MB and Rh-B, respectively, in visible light because of its wide band gap energy. On the contrary, the pristine $BiVO_4$ thin film exhibited superior photocatalytic degradation of MB and Rh-B dyes compared to NS-hexaniobate thin film. The photocatalytic activity of pristine $BiVO_4$ is further enhanced after hybridization with NS-hexaniobate. The optimized C-

BN2 nanohybrid thin film shows excellent photocatalytic degradation activity for both dyes (MB and Rh-B) with photodegradation rates of 87.3 and 92.8%, respectively, which are more significant than that of pristine $BiVO_4$ (54 and 70%). Although the pristine $BiVO_4$ is a highly active photocatalyst for visible light-induced photocatalytic degradation of MB and Rh-B dyes, the present NS-hexaniobate-$BiVO_4$ nanohybrid thin films with exceptional photoactivity can be considered highly effective visible-light-induced photocatalysts for photodegradation of MB and Rh-B dyes.

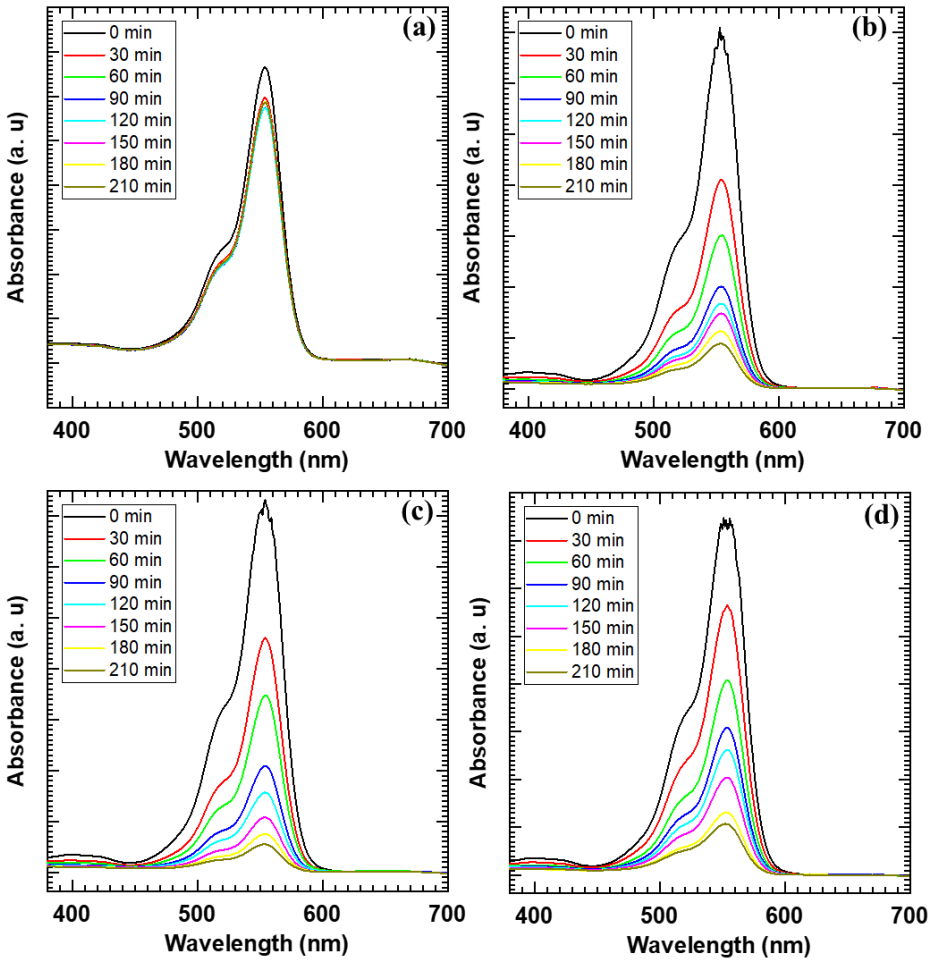

Fig. 5.12: UV-vis absorption spectra of the Rh-B solution in the presence of (a) NS-hexaniobate, (b) C-BN1, (c) C-BN2 and (d) C-BN3 nanohybrid thin film photocatalysts.

The enhanced photocatalytic degradation performance of $BiVO_4$ after hybridization with highly stable NS-hexaniobate can be linked with the intimate electronic coupling between NS-hexaniobate and $BiVO_4$, which facilitates enhanced electron density on NS-hexaniobate-$BiVO_4$ nanohybrid advantageous for effective photocatalytic reactions. The expanded surface area obtained after hybridization by forming a highly porous house-of-cards type morphology can promote efficient

electron-hole transport and plenty of reaction sites, which boost photocatalytic activity. Conclusionally, the superior photocatalytic activity of present nanohybrid thin films can be attributed to the effective electronic coupling with easy charge transport, high photostability, strong visible light harvesting ability, expanded surface area and highly porous house-of-cards type structure useful for visible-light-driven photocatalytic dye degradation.

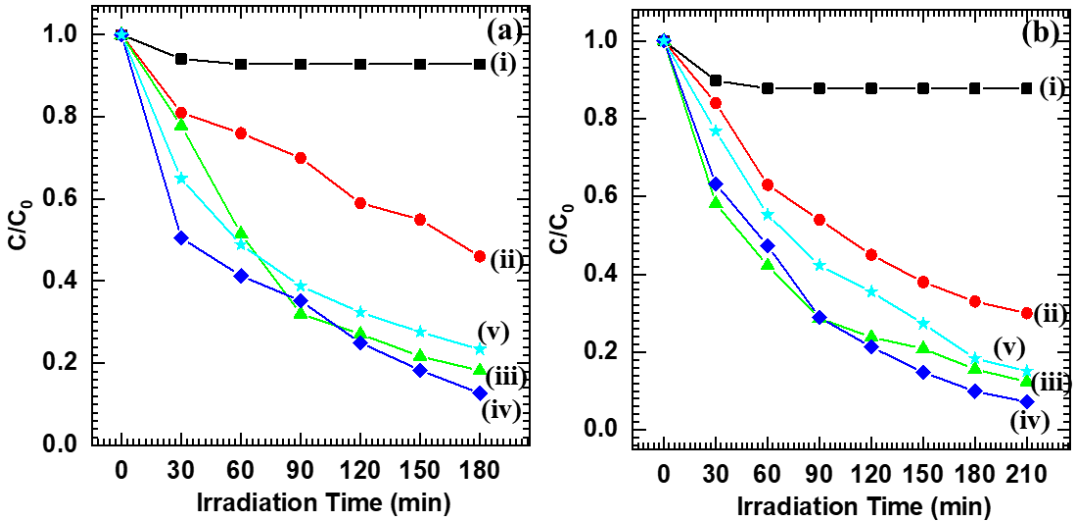

Fig. 5.13: (a) MB and (b) Rh-B degradation performance of (i) NS-hexaniobate, (ii) $BiVO_4$, (iii) C-BN1, (iv) C-BN2, (v) C-BN3 nanohybrid thin film photocatalysts.

5.5.2 Rate kinetics study for MB and Rh-B:

The photoactivity of NS-hexaniobate-$BiVO_4$ nanohybrids for MB and Rh-B degradation was further described by their kinetics using a pseudo-first-order rate kinetic model [34]. The pseudo-first-order reaction kinetics for MB and Rh-B dyes are graphically shown in **Fig. 5.14**. The k and R^2 values of all tested thin-film photocatalysts for MB and Rh-B degradation are enlisted in **Table 5.1**. Compared with other photocatalysts, C-BN2 nanohybrid thin film shows improved k values, signifying the maximum photocatalytic activity. The highest k values obtained for the C-BN2 nanohybrid thin film for MB and Rh-B degradation are 0.0115 and 0.0146 min^{-1}, respectively. The high k value obtained for C-BN2 nanohybrid thin film can be ascribed to the effective electronic coupling between hybridized species with easy charge transport, high photostability, strong visible light harvesting ability, and expanded surface area obtained by highly porous house-of-cards type structure.

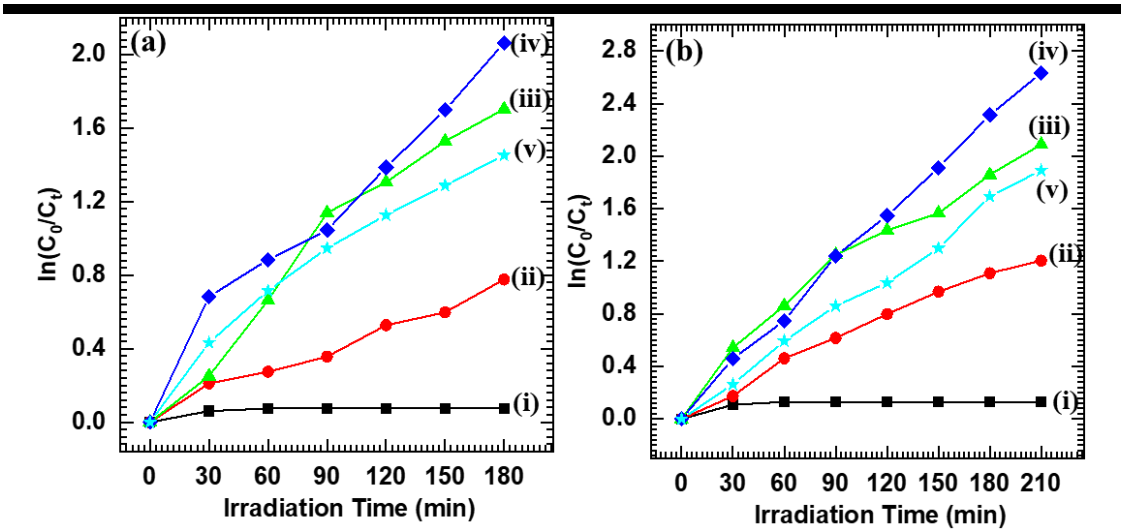

Fig. 5.14: Pseudo-first-order kinetics of (a) MB and (b) Rh-B for (i) NS-hexaniobate, (ii) $BiVO_4$, (iii) C-BN1, (iv) C-BN2, (v) C-BN3 nanohybrid thin film photocatalysts.

Table 5.1: k and R^2 values of all tested photocatalysts.

Sample	MB		Rh-B	
	k (min^{-1})	**R^2**	**k (min^{-1})**	**R^2**
NS-hexaniobate	0.0004	0.9996	0.0007	0.9993
$BiVO_4$	0.0043	0.9957	0.0067	0.9933
C-BN1	0.0095	0.9905	0.0116	0.9884
C-BN2	0.0115	0.9885	0.0146	0.9854
C-BN3	0.0081	0.9919	0.0105	0.9895

5.5.3 Recyclability study for MB and Rh-B:

The photostability of C-BN2 nanohybrid thin film for photocatalytic degradation of MB and Rh-B dyes is estimated for five consecutive degradation cycles, as displayed in **Fig. 5.15**. The C-BN2 nanohybrid thin film is separated from the dye (MB/Rh-B) solution, washed with DDW, dried at room temperature, and used for subsequent cycles. The present C-BN2 nanohybrid thin film shows superior recycling performance for MB and Rh-B photodegradation with degradation rates of 66.8 and 71.5% within 180 and 210 min of visible light exposure, respectively. The C-BN2 nanohybrid thin film retains its photocatalytic activity with a negligible decrease for five repetitive degradation cycles, suggesting its superior photostability. The negligible decrement in degradation performance after five consecutive cycles is attributed to the adsorption of dye

molecules on the surface of the C-BN2 nanohybrid thin film and the detachment of loosely bound photocatalyst particles from the film surface.

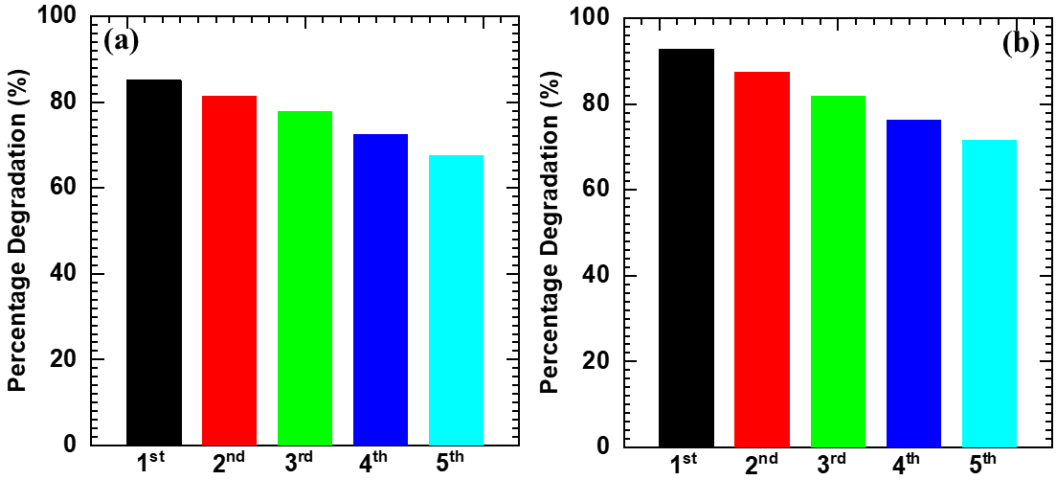

Fig. 5.15: Recyclability of C-BN2 nanohybrid thin film for (a) MB and (b) Rh-B dyes.

5.6 Photocatalytic Dye Degradation Mechanism:

The electron transfer between NS-hexaniobate and $BiVO_4$ in the NS-hexaniobate-$BiVO_4$ nanohybrid thin films is investigated with electronic band structure [28, 35-36]. The photocatalytic dye degradation mechanism (schematically represented in **Fig. 5.16**) is mainly based on the photoinduced charge separation and transport to the semiconductor surface upon exposure to visible light irradiation [37]. When photons having energy equal to or greater than the band gap of $BiVO_4$ are incident on the NS-hexaniobate-$BiVO_4$ nanohybrids, then electrons from the VB of $BiVO_4$ are excited to the CB and electron-hole pairs are generated. It is observed that the NS-hexaniobate shows a higher position of CB (-0.44 eV vs NHE) and VB (2.76 eV vs NHE) as compared to CB and VB of $BiVO_4$. The photogenerated electrons from the CB of $BiVO_4$ can transferred into the VB of NS-hexaniobate, resulting in the effective electron-hole pair separation with depressed electron-hole recombination. The holes at the VB of $BiVO_4$ generate OH* radicals when reacting with H_2O molecules. Generated OH* radicals are strong oxidizing agents that can degrade adsorbed dye (MB and Rh-B) molecules. On the other hand, $*O_2^-$ radicals are produced from the reaction of O_2 with photogenerated electrons from CB of $BiVO_4$. Again, HOO* radicals are generated from the protonation of $*O_2^-$ radicals. Finally, H_2O_2 generated from HOO* radicals dissociates into OH* radicals, which can degrade the target dye molecules [38].

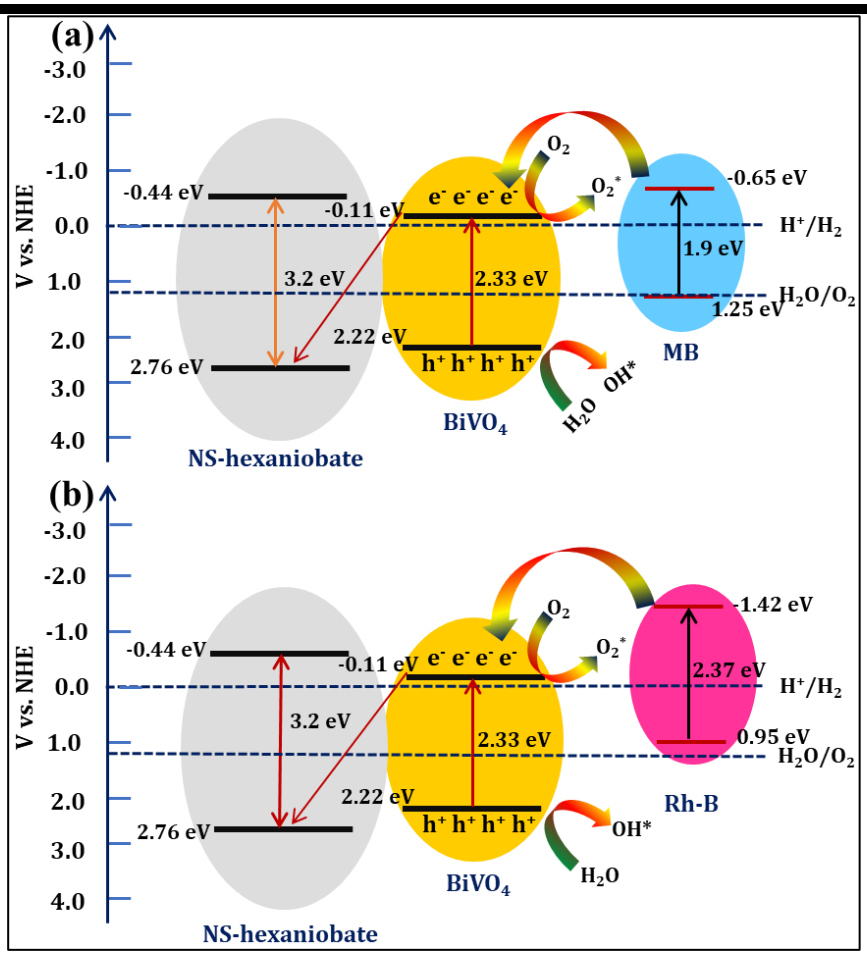

Fig. 5.16: Schematic representation of photodegradation mechanism of (a) MB and (b) Rh-B dyes over NS-hexaniobate-$BiVO_4$ nanohybrids.

5.7 Conclusions:

In the present chapter, NS-hexaniobate thin films are deposited on ITO substrates using the EPD method. The EPD-deposited NS-hexaniobate thin film shows well-crystalline growth of lamellar NS-hexaniobate with orthorhombic structure. The NS-hexaniobate thin film shows nanoscroll morphology, forming a porous structure of NS-hexaniobate thin film. Although the NS-hexaniobate thin film displays prominent absorption in the UV region due to its wide-bandgap energy, it is the best choice for coupling with narrow-bandgap $BiVO_4$. Further, the NS-hexaniobate-$BiVO_4$ nanohybrid thin films are synthesized by depositing $BiVO_4$ layers over EPD-deposited NS-hexaniobate thin films by CBD method. The well-crystalline uniform deposition of monoclinic scheelite $BiVO_4$ on NS-hexaniobate thin films is evidenced by XRD analysis. In addition, the NS-hexaniobate-$BiVO_4$ nanohybrid thin films show effective electronic coupling between NS-hexaniobate and $BiVO_4$ with easy charge transport,

strong visible light harvesting ability, high photostability and a highly porous randomly aggregated NSs network creating the house-of-cards type morphology beneficial for visible-light-induced photocatalytic dye degradation. The best optimized NS-hexaniobate-$BiVO_4$ nanohybrid thin film shows superior photocatalytic activity for visible-light-driven photodegradation of MB and Rh-B dyes with photodegradation rates of 87.3 and 92.8%, respectively, higher than that of pristine $BiVO_4$. The improved photocatalytic degradation performance of hybrid photocatalysts is attributed to the effective electronic coupling with easy charge transport, high photostability, strong visible light harvesting ability, expanded surface area and highly porous house-of-cards type structure beneficial for effective photocatalytic reactions. The present results highlight the expediency of hybridization in enhancing the photocatalytic activity of pristine $BiVO_4$ by minimizing its charge recombination rate and improving chemical stability.

5.8 References:

1. M.A. Bizeto, A.L. Shiguihara, V.R.L. Constantino, Layered niobate nanosheets: Building blocks for advanced materials assembly, J. Mater. Chem. 19 (2009) 2512-2525.
2. C.H.B. Silva, A.M.D.C. Ferreira, V.R.L. Constantino, M.L.A. Temperini, Hybrid materials of polyaniline and acidic hexaniobate nanoscrolls: High polaron formation and improved thermal properties, J. Mater. Chem. A 2 (2014) 8205-8214.
3. S. Adireddy, T. Rostamzadeh, C.E. Carbo, J.B. Wiley, Particle placement and sheet topological control in the fabrication of Ag-hexaniobate nanocomposites, Langmuir 31 (2015) 480-485.
4. G.B. Saupe, C.C. Waraksa, H.-N. Kim, Y.J. Han, D.M. Kaschak, D.M. Skinner, T.E. Mallouk, Nanoscale tubules formed by exfoliation of potassium hexaniobate, Chem. Mater. 12 (2000) 1556-1562.
5. S.P. Kulkarni, Y.M. Chitare, V.V. Magdum, P.D. Sawant, S.V. Talekar, S.A. Pawar, U.M. Patil, K.V. Gurav, D.B. Malavekar, A.U. Pawar, J.L. Gunjakar, Chemically synthesized facet-controlled visible light active $BiVO_4$ thin films for photoelectrochemical water splitting, Appl. Phys. A 129 (2023) 876.
6. R. Ma, Y. Kobayashi, W.J. Yngblood, T.E. Mallouk, Potassium niobate nanoscrolls incorporating rhodium hydroxide nanoparticles for photocatalytic hydrogen evolution, J. Mater. Chem. 18 (2008) 5982-5985.
7. H. Hayashi, Y. Hakuta, Y. Kurata, Hydrothermal synthesis of potassium niobate photocatalysts under subcritical and supercritical water conditions, J. Mater. Chem. 14 (2004) 2046-2051.
8. K. Maeda, M. Eguchi, W.J. Youngblood, T.E. Mallouk, Niobium oxide nanoscrolls as building blocks for dye-sensitized hydrogen production from water under visible light irradiation, Chem. Mater. 20 (2008) 6770-6778.
9. R. Abe, K. Shinohara, A. Tanaka, M. Hara, J.N. Kondo, K. Domen, Preparation of porous niobium oxides by soft-chemical process and their photocatalytic activity, Chem. Mater. 9 (1997) 2179-2184.

10. G.P. Nagabhushana, G. Nagaraju, G.T. Chandrappa, Synthesis of bismuth vanadate: Its application in H_2 evolution and sunlight-driven photodegradation, J. Mater. Chem. A 1 (2013) 388-394.
11. Q.Q. Wang, B.Z. Lin, B.H. Xu, X.L. Li, Z.J. Chen, X.T. Pian, Preparation and photocatalytic properties of mesoporous SnO_2-hexaniobate layered nanocomposite, Microporous Mesoporous Mater. 130 (2010) 344-351.
12. B.N. Nunes, C. Haisch, A.V. Emeline, D.W. Bahnemann, A.O.T. Patrocinio, Photocatalytic properties of layer-by-layer thin films of hexaniobate nanoscrolls, Catal. Today 326 (2019) 60-67.
13. B.-H. Xu, B.-Z. Lin, Q.-Q. Wang, X.-T. Pian, O. Zhang, L.-M. Fu, Anatase TiO_2-pillared hexaniobate mesoporous nanocomposite with enhanced photocatalytic activity, Microporous Mesoporous Mater. 147 (2012) 79-85.
14. S. Elumalai, S. Vadivel, M. Yoshimura, Interlayer-modified two-dimensional layered hexaniobate $K_4Nb_6O_{17}$ as an anode material for lithium-ion batteries, Mater. Adv. 2 (2021) 1957-1961.
15. N.S. Padalkar, S.V. Sadavar, R.B. Shinde, A.S. Patil, U.M. Patil, V.V. Magdum, Y.M. Chitare, S.P. Kulkarni, R.N. Bulakhe, V.G. Parale, J.L. Gunjakar, 2D-2D nanohybrids of Ni-Cr-layered double hydroxide and graphene oxide nanosheets: Electrode for hybrid asymmetric supercapacitors, Electrochim. Acta 424 (2022) 140615.
16. M. Mousavi-Kamazani, Facile hydrothermal synthesis of egg-like $BiVO_4$ nanostructures for photocatalytic desulfurization of thiophene under visible light irradiation, J. Mater. Sci. Mater. Electron. 30 (2019) 17735-17740.
17. L. Zhang, Z. Dai, G. Zheng, Z. Yao, J. Mu, Superior visible light photocatalytic performance of reticular $BiVO_4$ synthesized via a modified sol-gel method, RSC Adv. 8 (2018) 10654-10664.
18. P. Pookmanee, S. Kojinok, R. Puntharod, S. Sangsrichan, S. Phanichphant, Preparation and characterization of $BiVO_4$ powder by the sol-gel method, Ferroelectrics 456 (2013) 45-54.
19. L.A. Faustino, B.L. Souza, B.N. Nunes, A.-T. Duong, F. Sieland, D.W. Bahnemann, A.O.T. Patrocinio, Photocatalytic CO_2 reduction by Re(I) polypyridyl complexes immobilized on niobates nanoscrolls, ACS Sustainable Chem. Eng. 6 (2018) 6073-6083.
20. B.N. Nunes, D.W. Bahnemann, A.O.T. Patrocinio, Photoinduced H_2 evolution by hexaniobate sheets grafted with metal ions: The fate of photogenerated carriers, ACS Appl. Energy Mater. 4 (2021) 3681-3692.
21. T.M.F. Marques, M.E. Strayer, A. Ghosh, A. Silva, O.P. Ferreira, K. Fujisawa, J.R.A. Cunha, G.J.P. Abreu, M. Terrones, T.E. Mallouk, B.C. Viana, Homogeneously dispersed CeO_2 nanoparticles on exfoliated hexaniobate nanosheets, J. Phys. Chem. Solids 111 (2017) 335-342.
22. G.S. Kamble, Y.-C. Ling, Solvothermal synthesis of facet-dependent $BiVO_4$ photocatalyst with enhanced visible-light-driven photocatalytic degradation of organic pollutant: Assessment of toxicity by zebrafish embryo, Sci. Rep. 10 (2020) 12993.
23. S. Gu, W. Li, F. Wang, H. Li, H. Zhou, Substitution of Ce(III,IV) ions for Bi in $BiVO_4$ and its enhanced impact on visible-light-driven photocatalytic activities, Catal. Sci. Technol. 6 (2016) 1870-1881.
24. L. Shi, C. Xu, X. Sun, H. Zhang, Z. Liu, X. Qu, F. Du, Facile fabrication of hierarchical $BiVO_4/TiO_2$ heterostructures for enhanced photocatalytic activities under visible-light irradiation, J. Mater. Sci. 53 (2018) 11329-11342.

25. R.B. Shinde, N.S. Padalkar, S.V. Sadavar, S.B. Kale, V.V. Magdum, Y.M. Chitare, S.P. Kulkarni, U.M. Patil, V.G. Parale, H.-H. Park, J.L. Gunjakar, 2D-2D lattice engineering route for intimately coupled nanohybrids of layered double hydroxide and potassium hexaniobate: Chemiresistive SO_2 sensor, J. Hazard. Mater. 432 (2022) 128734.
26. R. Ran, J.G. McEvoy, Z. Zhang, Synthesis and optimization of visible light active $BiVO_4$ photocatalysts for the degradation of RhB, Int. J. Photoenergy 2015 (2015) 612857.
27. J.L. Gunjakar, A.I. Inamdar, B. Hou, S.N. Cha, S.M. Pawar, A. Talha, H.S. Chavan, J. Kim, S. Cho, S. Lee, Y. Jo, H. Kim, H. Im, Direct growth of 2D nickel hydroxide nanosheets intercalated with polyoxovanadate anions as a binder-free supercapacitor electrode, Nanoscale 10 (2018) 8953-8961.
28. J.L. Gunjakar, T.W. Kim, H.N. Kim, I.Y. Kim, S.-J. Hwang, Mesoporous layer-by-layer ordered nanohybrids of layered double hydroxide and layered metal oxide: Highly active visible light photocatalysts with improved chemical stability, J. Am. Chem. Soc. 133 (2011) 14998-15007.
29. J.L. Gunjakar, I.Y. Kim, J.M. Lee, N.-S. Lee, S.-J. Hwang, Self-assembly of layered double hydroxide 2D nanoplates with graphene nanosheets: An effective way to improve the photocatalytic activity of 2D nanostructured materials for visible light-induced O_2 generation, Energy Environ. Sci. 6 (2013) 1008-1017.
30. J.L. Gunjakar, T.W. Kim, I.Y. Kim, J.M. Lee, S.-J. Hwang, Highly efficient visible-light-induced O_2 generation by self-assembled nanohybrids of inorganic nanosheets and polyoxometalate nanoclusters, Sci. Rep. 3 (2013) 2080.
31. J.M. Lee, J.L. Gunjakar, Y. Ham, I.Y. Kim, K. Domen, S.-J. Hwang, A linker-mediated self-assembly method to couple isocharged nanostructures: Layered double hydroxide-CdS nanohybrids with high activity for visible-light-induced H_2 generation, Chem. Eur. J. 20 (2014) 17004-17010.
32. H. Shi, H. Guo, S. Wang, G. Zhang, Y. Hu, W. Jiang, G. Liu, Visible light photoanode material for photoelectrochemical water splitting: A review of bismuth vanadate, Energy Fuels 36 (2022) 11404-11427.
33. B. Zhou, X. Zhao, H. Liu, J. Qua, C.P. Huang, Visible-light sensitive cobalt-doped $BiVO_4$ (Co-$BiVO_4$) photocatalytic composites for the degradation of methylene blue dye in dilute aqueous solutions, Appl. Catal. B: Environ. 99 (2010) 214-221.
34. S. Dong, Y. Cui, Y. Wang, Y. Li, L. Hu, J. Sun, J. Sun, Designing three-dimensional acicular sheaf shaped $BiVO_4$/reduced graphene oxide composites for efficient sunlight-driven photocatalytic degradation of dye wastewater, Chem. Eng. J. 249 (2014) 102-110.
35. K. Saruwatari, H. Sato, T. Idei, J. Kameda, A. Yamagishi, A. Takagaki, K. Domen, Photoconductive properties of organic-inorganic hybrid films of layered perovskite-type niobate, J. Phys. Chem. B 109 (2005) 12410-12416.
36. N. Sakai, Y. Ebina, K. Takada, T. Sasaki, Electronic band structure of titania semiconductor nanosheets revealed by electrochemical and photoelectrochemical studies, J. Am. Chem. Soc. 126 (2004) 5851-5858.
37. C.N.C. Hitam, A.A. Jalil, A review on exploration of Fe_2O_3 photocatalyst towards degradation of dyes and organic contaminants, J. Environ. Manage. 258 (2020) 110050.
38. K.P. Gopinath, N.V. Madhav, A. Krishnan, R. Malolan, G. Rangarajan, Present applications of titanium dioxide for the photocatalytic removal of pollutants from water: A review, J. Environ. Manage. 270 (2020) 110906.

CHAPTER-6

Synthesis and Characterizations of NS-hexaniobate-$BiVO_4$ Nanohybrids by SILAR: Application in Photocatalytic Dye Degradation

CHAPTER-6

Synthesis and Characterizations of NS-hexaniobate-$BiVO_4$ Nanohybrids by SILAR: Application in Photocatalytic Dye Degradation

6.1 Introduction:

With reference to the nanohybridization advantages described in **Chapter 1, Section 1.3, Chapter 2, Section 2.4** and **Chapter 3, Section 3.1** to enhance the photocatalytic degradation performance of $BiVO_4$ thin film photocatalyst, hybridization of NS-hexaniobate with $BiVO_4$ is explored in **Chapter 5**. Remarkably, the NS-hexaniobate evokes high research interest as macromolecules for the hybrid photocatalysts due to their highly anisotropic 2D morphology, ultrathin thickness, high surface area, electrostatic surface charged, high mechanical flexibility, suitable band positions for water splitting and high chemical stability. As compared to other deposition methods, the SILAR method has attracted intense research attention to deposit hybrid thin films due to its certain advantages, such as extremely low-cost fabrication, facile control of preparative parameters, large area deposition, better orientation of crystallites with pinhole-free and uniform deposition on a variety of substrates. Importantly, the SILAR method avoids unnecessary homogeneous precipitation that occurs in CBD and the wastage of chemicals. The development of NS-hexaniobate-$BiVO_4$ nanohybrid thin films can lead to high surface area porous morphology, high photo-conductivity, improved visible light harvesting ability and intimate electronic coupling between hybridized species useful for visible-light-induced photocatalytic dye degradation.

In the present chapter, the highly porous visible light active NS-hexaniobate-$BiVO_4$ nanohybrid thin films are synthesized by the deposition of $BiVO_4$ layers over EPD-deposited NS-hexaniobate thin films using the SILAR method. The visible-light-driven photocatalytic activity of NS-hexaniobate-$BiVO_4$ nanohybrid thin films is investigated for the photodegradation of MB and Rh-B dyes in addition to their physicochemical characterizations.

6.2 Synthesis and characterizations of NS-hexaniobate-$BiVO_4$ nanohybrids:

6.3 Experimental details:

6.3.1 Chemicals:

Nb_2O_5, K_2CO_3, $Bi(NO_3)_3.5H_2O$, $NaVO_3$, HCl, CH_3COOH, TBAOH and C_2H_5OH were purchased from Sigma-Aldrich and used as received.

6.3.2 Synthesis of NS-hexaniobate-$BiVO_4$:

The NS-hexaniobate-$BiVO_4$ nanohybrid thin films were deposited by a combination of EPD and SILAR methods. Initially, thin films of pristine NS-

hexaniobate were obtained from the dialyzed colloidal suspension of NS-hexaniobate by the EPD method described in **Chapter 5, Section 5.3**.

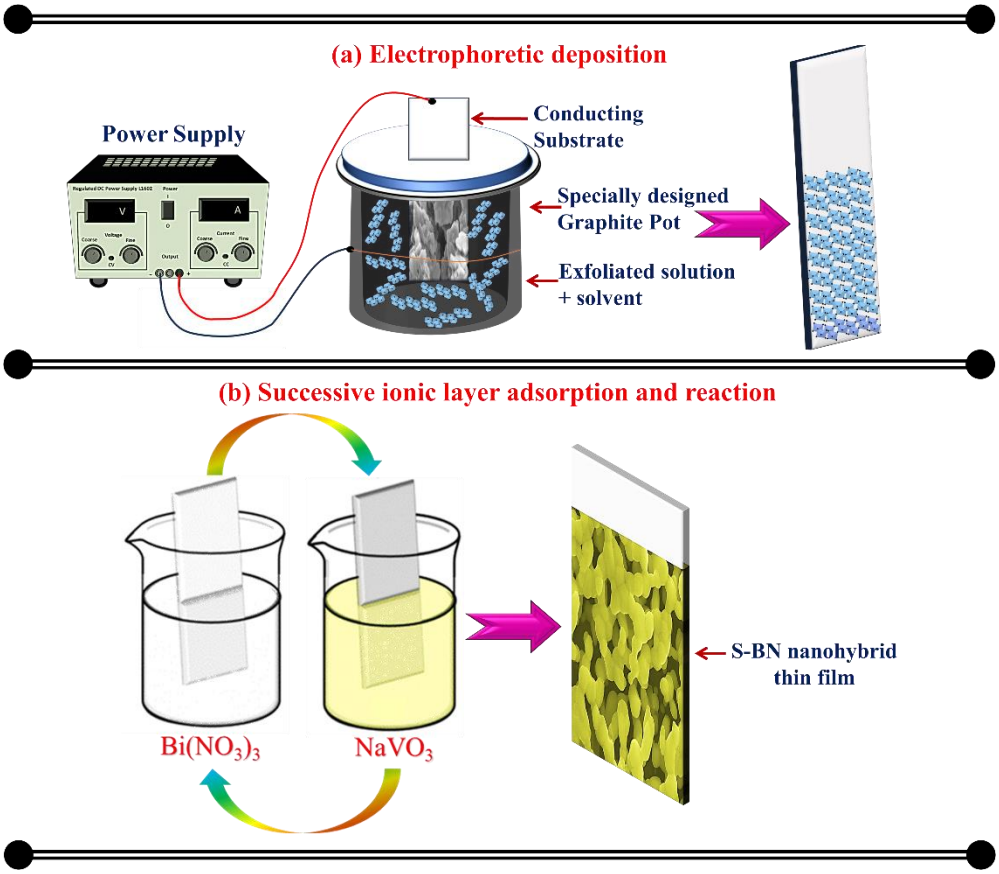

Fig. 6.1: Schematic representation of (a) EPD of NS-hexaniobate thin films and (b) SILAR method for depositing NS-hexaniobate-$BiVO_4$ nanohybrid thin films.

$BiVO_4$ layers were deposited over the EPD-deposited NS-hexaniobate thin films by the SILAR method as described in **Chapter 4, Section 4.3**. Deposition of NS-hexaniobate-$BiVO_4$ nanohybrid thin films by SILAR method was carried out by immersion of NS-hexaniobate coated (Nb-1, Nb-2 and Nb-3) ITO substrates into separately placed cationic (Bi) and anionic (V) precursors (two-beaker process). A cationic (Bi) precursor for the deposition of $BiVO_4$ was prepared from an aqueous solution of 25 mM $Bi(NO_3)_3 \cdot 5H_2O$ dissolved in 1 M acetic acid ($V_{acetic\ acid}$: V_{DDW} = 1:19, pH 1.5). An anionic (V) precursor was prepared from the aqueous solution of 25 mM $NaVO_3$ (pH 6.8). One deposition cycle of SILAR was completed by successive immersion of NS-hexaniobate-coated ITO substrates into a cationic (Bi) bath for 20 s and then immersing into an anionic (V) bath for the next 20 s. The deposition process was completed by repeating such 15-deposition cycles. After the deposition, NS-hexaniobate-$BiVO_4$ nanohybrid thin films were washed with DDW and air dried. The

schematic representation of the NS-hexaniobate-$BiVO_4$ nanohybrid thin film deposition process is displayed in **Fig. 6.1**. Subsequently, the as-prepared NS-hexaniobate-$BiVO_4$ nanohybrid thin films were annealed at 400°C for 2 h. The annealed NS-hexaniobate-$BiVO_4$ nanohybrid thin films deposited on Nb-1, Nb-2 and Nb-3 are represented as S-BN1, S-BN2 and S-BN3, respectively.

6.4 Characterizations of NS-hexaniobate-$BiVO_4$ nanohybrids:

The NS-hexaniobate-$BiVO_4$ nanohybrid thin films were characterized by numerous characterization techniques, as explained in **Chapter 3, Section 3.4**.

Note: The S-BN2 nanohybrid thin film shows improved photocatalytic dye degradation performance. Therefore, all the optimized S-BN2 nanohybrid thin film characterizations are compared with the pristine materials.

6.4.1 XRD analysis:

The development of the crystal structure of pristine $BiVO_4$ after hybridization with NS-hexaniobate was probed with the XRD technique. The XRD patterns of the S-BN2 nanohybrid thin film in comparison with the pristine NS-hexaniobate and $BiVO_4$ thin films are displayed in **Fig. 6.2**. As described in **Chapter 5, Section 5.4.1**, the pristine NS-hexaniobate thin film display a high-intensity broad (020) diffraction peak corresponding to the well-ordered stacking of lamellar NS-hexaniobate with the orthorhombic structure. As described in **Chapter 4, Section 4.4.1**, the SILAR deposited pristine $BiVO_4$ thin film shows typical Braggs reflections with apparent peak splitting at 18.5°, 35° and 46° corresponding to the monoclinic scheelite $BiVO_4$ structure (space group: I2/a) (JCPDS no.: 14-0688) [1]. On the other hand, the XRD pattern of S-BN2 nanohybrid thin film shows diffraction peaks matching with both well-ordered lamellar NS-hexaniobate (represented by circles) and monoclinic scheelite-type $BiVO_4$ (represented by squares). It shows a broad (020) diffraction peak at 10° matching with the well-ordered lamellar orthorhombic NS-hexaniobate having an interplanar spacing of 0.87 nm [2-5]. In addition, it displays typical Braggs reflections with apparent peak splitting at 18.5°, 35° and 46° corresponding to the monoclinic scheelite $BiVO_4$. Present XRD features related to NS-hexaniobate and $BiVO_4$ highlight the formation of NS-hexaniobate and $BiVO_4$ in orthorhombic and monoclinic scheelite phases, respectively. This confirms uniform and well-crystalline growth of SILAR-deposited $BiVO_4$ over EPD-deposited NS-hexaniobate thin films.

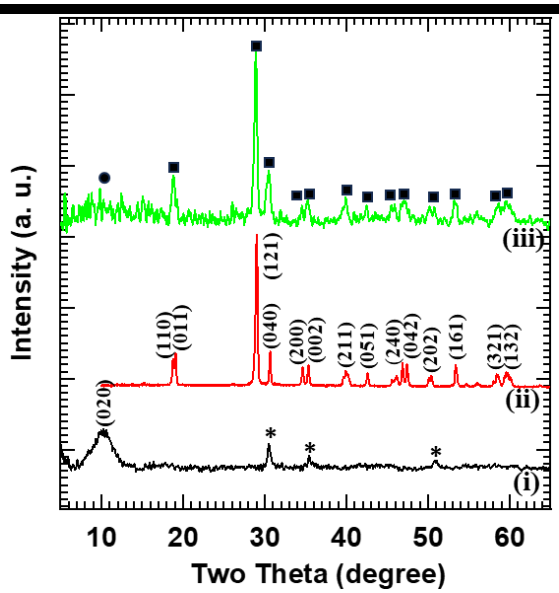

Fig. 6.2: XRD patterns of (i) NS-hexaniobate, (ii) $BiVO_4$ and (iii) S-BN2 nanohybrid thin films (asterisk, circles and squares represent the Bragg reflections of ITO, NS-hexaniobate and monoclinic scheelite-type $BiVO_4$, respectively).

6.4.2 FTIR analysis:

The chemical bonding features of NS-hexaniobate-$BiVO_4$ nanohybrid thin film in comparison with pristine NS-hexaniobate and $BiVO_4$ thin films were scrutinized with FTIR spectra, as represented in **Fig. 6.3**. As described in **Chapter 5, Section 5.4.2**, the pristine NS-hexaniobate thin film displays characteristic IR features ($v1$ to $v4$) related to NS-hexaniobate. As described in **Chapter 4, Section 4.4.2**, the SILAR deposited $BiVO_4$ thin film exhibits characteristic IR features ($v5$ to $v9$) corresponding to chemical bonding in $BiVO_4$. On the other hand, the NS-hexaniobate-$BiVO_4$ nanohybrid thin film displays absorption peaks $v10$ (733.75 cm^{-1}), $v11$ (1626.25 cm^{-1}) and $v12$ (3451.55 cm^{-1}) linked with the chemical bonding in NS-hexaniobate and $BiVO_4$ [6-13]. The absorption peak centered at $v10$ originated from the superposition of three peaks, $v1$ (576 cm^{-1}), $v7$ (741 cm^{-1}) and $v8$ (829 cm^{-1}), associated with the stretching vibrations of the terminal Nb-O in central NbO_6 octahedron, asymmetric stretching vibrations of VO_4^{3-} and symmetric stretching vibrations of VO_4^{3-}, respectively [8, 10-13]. The absorption peaks $v11$ and $v12$ are linked with the bending vibrations of water molecules and stretching vibrations of hydroxyl groups, respectively [9]. Obtained IR features closely match with the chemical bonding characteristics of SILAR-deposited $BiVO_4$ and EPD-deposited NS-hexaniobate thin films. These spectral features demonstrate the successful growth of $BiVO_4$ on the surface of EPD-deposited NS-hexaniobate thin films.

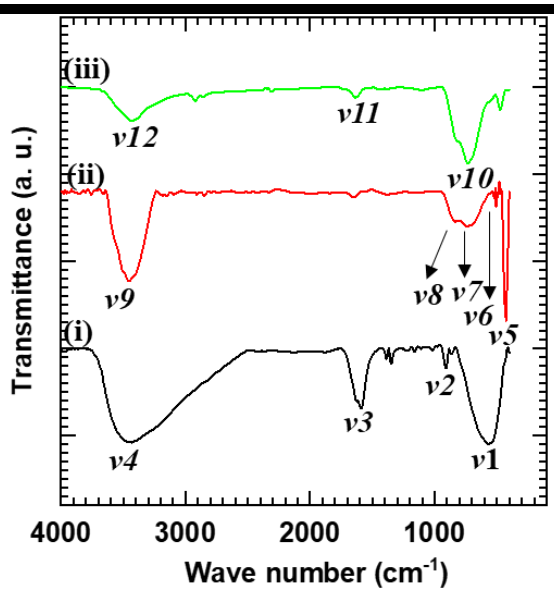

Fig. 6.3: FTIR spectra of (i) NS-hexaniobate, (ii) $BiVO_4$ and (iii) S-BN2 nanohybrid thin films.

6.4.3 Raman analysis:

The chemical bonding nature of NS-hexaniobate-$BiVO_4$ nanohybrid thin film as compared to pristine NS-hexaniobate and $BiVO_4$ thin films was further investigated with micro-Raman spectra displayed in **Fig. 6.4**. As described in **Chapter 5, Section 5.4.3**; the pristine NS-hexaniobate thin film shows characteristic Raman features (P_1 to P_6) related to lattice vibrational modes of NS-hexaniobate. As described in **Chapter 4, Section 4.4.3**, the micro-Raman spectrum of pristine $BiVO_4$ thin film displays characteristic Raman features (P_7 to P_{12}) corresponding to lattice vibrational modes of $BiVO_4$. On the other hand, the NS-hexaniobate-$BiVO_4$ nanohybrid thin film shows the Raman peaks related to the NS-hexaniobate and $BiVO_4$ [14-18]. The sharp Raman peak centered around P_{13} (92.33 cm^{-1}) corresponds to the internal bending modes of O-Nb-O groups [17,18]. The Raman peaks P_{14} (131 cm^{-1}) and P_{15} (212 cm^{-1}) are attributed to the external modes (rotation or translation) of $BiVO_4$ [14,15]. The Raman peak centered at P_{16} (367 cm^{-1}) is linked with the symmetric (A_g symmetry) bending modes of the VO_4 tetrahedron [18]. The Raman peaks P_{17} (710 cm^{-1}) and P_{18} (826 cm^{-1}) correspond to the asymmetric and symmetric (V-O) stretching modes of $BiVO_4$, respectively [14-16]. These characteristic Raman features match with the lattice vibrational modes of EPD-deposited NS-hexaniobate and SILAR-deposited $BiVO_4$. This clearly highlights the effective growth of SILAR-deposited $BiVO_4$ over EPD-deposited NS-hexaniobate thin films.

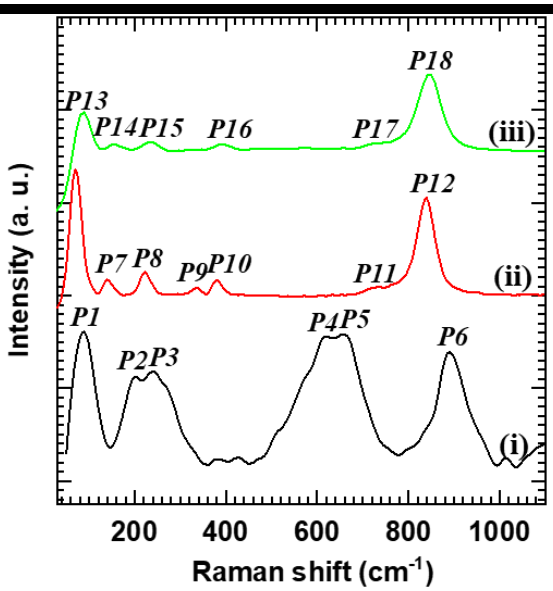

Fig. 6.4: Micro-Raman spectra of (i) NS-hexaniobate, (ii) $BiVO_4$ and (iii) S-BN2 nanohybrid thin films.

6.4.4 XPS analysis:

The effect of hybridization on the chemical states of NS-hexaniobate and $BiVO_4$ in the present NS-hexaniobate-$BiVO_4$ nanohybrid thin film was probed with the XPS technique. The survey XPS spectrum of NS-hexaniobate-$BiVO_4$ nanohybrid thin film (**Fig. 6.5**) displays the spectral features at BEs corresponding to the Nb, Bi, V and O elements representing the existence of the above elements in S-BN2 nanohybrid thin film.

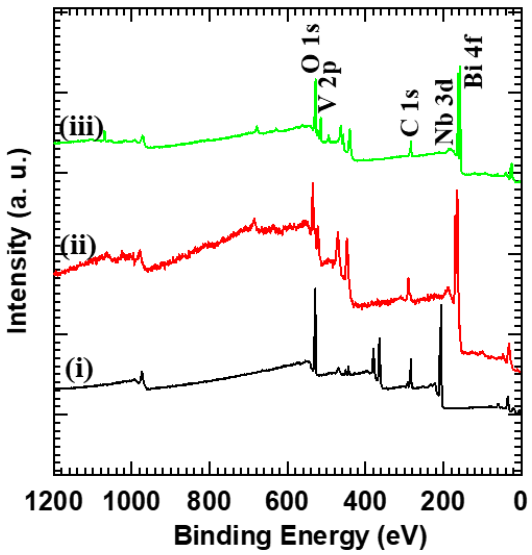

Fig. 6.5: Survey XPS spectra of (i) NS-hexaniobate, (ii) $BiVO_4$ and (iii) S-BN2 nanohybrid thin films.

The core level Nb 3d XPS spectra of pristine NS-hexaniobate and NS-hexaniobate-$BiVO_4$ nanohybrid thin films (**Fig. 6.6(a)**) exhibit two sharp peaks A (207.1 eV) and B (209.7 eV) matching with the spin-orbit coupling of Nb $3d_{5/2}$ and Nb $3d_{3/2}$, respectively [7]. The position of peaks and their BE difference of 2.6 eV confirm the presence of Nb in its +5 oxidation state in the above samples [19]. As displayed in **Fig. 6.6(b)**, the Bi 4f core-level XPS spectra of the pristine $BiVO_4$ and NS-hexaniobate-$BiVO_4$ nanohybrid thin films show spectral features C (164 eV) and D (157.5 eV) corresponding to the spin-orbit splitting of Bi $4f_{5/2}$ and Bi $4f_{7/2}$, respectively confirming the presence of bismuth in its trivalent state [20]. The V 2p core-level XPS spectra of pristine $BiVO_4$ and NS-hexaniobate-$BiVO_4$ nanohybrid thin films (**Fig. 6.6(c)**) show two peaks P (515.4 eV) and Q (522.1 eV) linked with the spin-orbit coupling of vanadium into V $2p_{3/2}$ and V $2p_{1/2}$ states, respectively. These spectral features are ascribed to the presence of pentavalent vanadium in present samples [21]. As shown in **Fig. 6.6(d)**, the high-resolution O 1s XPS spectra of pristine NS-hexaniobate, $BiVO_4$ and NS-hexaniobate-$BiVO_4$ nanohybrid thin films commonly display the intense peak R (530.1 eV) corresponds to the presence of oxygen in core levels of NS-hexaniobate, $BiVO_4$ and NS-hexaniobate-$BiVO_4$ nanohybrid, respectively [20]. In case of NS-hexaniobate thin film, peak R represents Nb-O bonding. For $BiVO_4$ thin film, peak R represents Bi-O and V-O bonding. In case of NS-hexaniobate-$BiVO_4$ thin film, peak R arises due to the Nb-O, Bi-O and V-O bonding. The observed XPS features provide strong evidence of the presence of Nb^{5+}, Bi^{3+} and V^{5+} states of Nb, Bi and V in NS-hexaniobate-$BiVO_4$ nanohybrid thin film, respectively. These spectral features highlight intimate electronic coupling between NS-hexaniobate and $BiVO_4$ in NS-hexaniobate-$BiVO_4$ nanohybrid thin film.

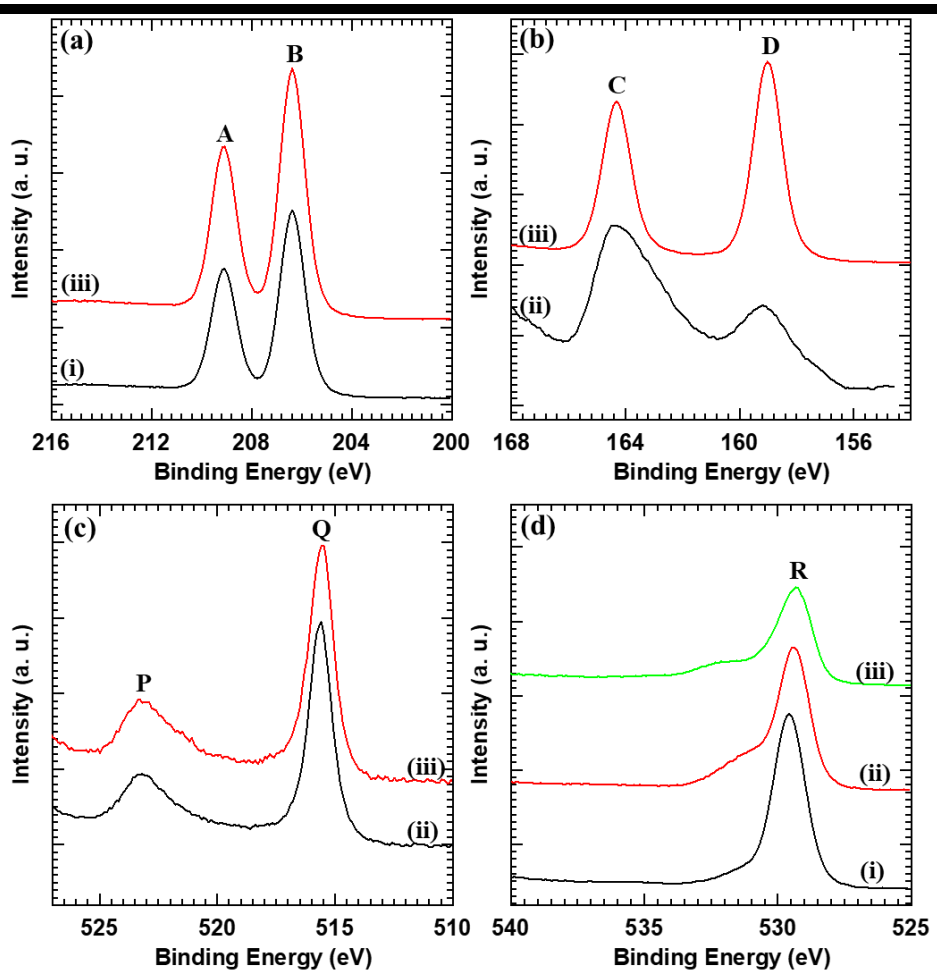

Fig. 6.6: (a) Nb 3d, (b) Bi 4f, (c) V 2p, (d) O 1s core-level XPS spectra of (i) NS-hexaniobate, (ii) $BiVO_4$ and (iii) S-BN2 nanohybrid thin films.

6.4.5 FESEM analysis:

The surface morphology of NS-hexaniobate-$BiVO_4$ nanohybrid thin film as compared to the pristine NS-hexaniobate and $BiVO_4$ thin films was probed with FESEM analysis as shown in **Fig. 6.7**. As explained in **Chapter 5, Section 5.4.5**, the EPD-deposited pristine NS-hexaniobate thin film (**Fig. 6.7(a)**) shows hexaniobate nanoscrolls laying parallel to the top of ITO substrate. As explained in **Chapter 4, Section 4.4.5**, the SILAR-deposited $BiVO_4$ thin film (**Fig. 6.7(b)**) displays the nanostructured (interconnected nanoparticles) morphology with particle size in the range of 150-200 nm. On the contrary, the NS-hexaniobate-$BiVO_4$ nanohybrid thin film (**Fig. 6.7(c-d)**) displays the formation of a highly porous 3D network-type structure composed of $BiVO_4$ nanoparticles deposited on the surface of hexaniobate nanoscrolls. The FESEM image of the S-BN2 nanohybrid thin film shows a 3D network-type structure of $BiVO_4$ nanoparticles. Due to the large thickness of $BiVO_4$ thin film, only $BiVO_4$ morphology can be seen in FESEM images. From the close inspection of the present FESEM, it is

observed that the average lateral size of NS-hexaniobate-$BiVO_4$ nanohybrid is in the range of 75-95 nm. Remarkably, the 3D network-type structure of $BiVO_4$ nanoparticles forms mesopores of 100 to 150 nm within the voids of the 3D network-type structure. Such a porous structure provides expanded surface area, which allows more active sites for effective photocatalytic reactions. The internal surfaces of the pores can capture light more effectively, which enhances the photocatalytic activity of the material. The porous structure enables effective electron-hole transport, leading to better diffusion of charge carriers from the photocatalytic sites and improving overall reaction efficiency. The porous structure may have lower electron-hole recombination due to the increased pathways of charge carriers to reach the surface without recombining. This type of highly porous structure is generally seen for 2D NSs-based nanohybrids and is favorable for solar-assisted photocatalytic applications [22-24].

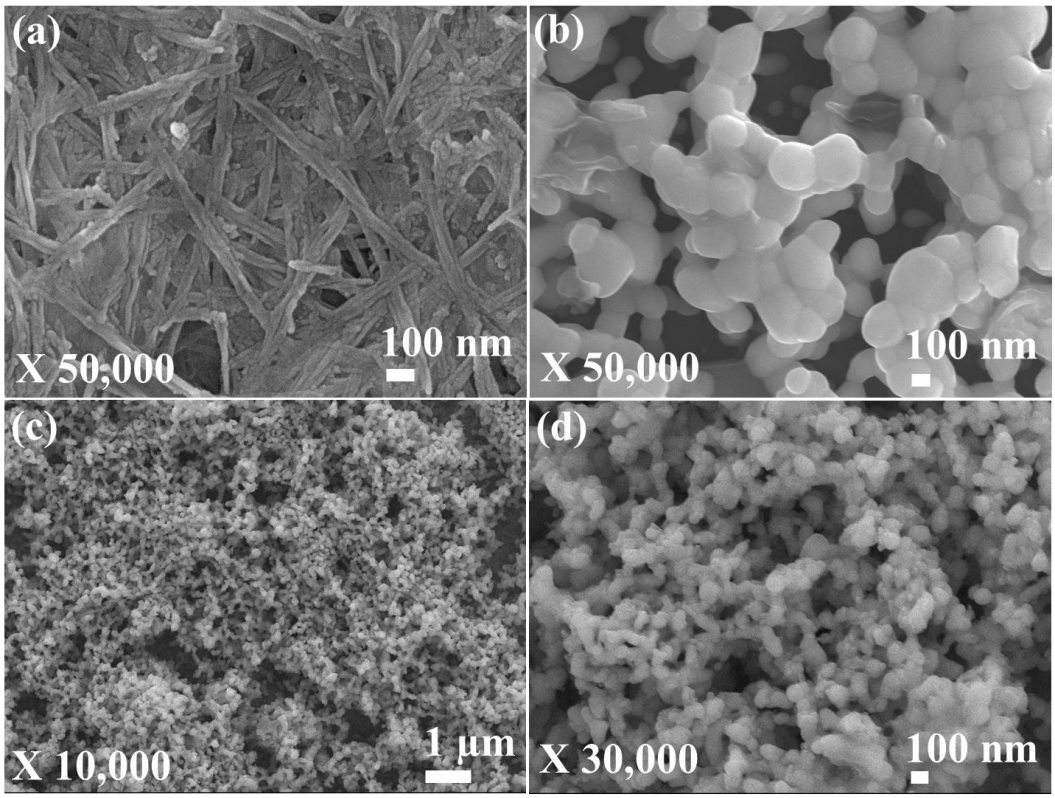

Fig. 6.7: FESEM micrographs of (a) NS-hexaniobate, (b) $BiVO_4$ and (c-d) S-BN2 nanohybrid thin films.

6.4.6 EDS analysis:

The hybridization between NS-hexaniobate and $BiVO_4$ in NS-hexaniobate-$BiVO_4$ thin film was further confirmed by EDS and elemental mapping analysis as represented in **Fig. 6.8** and **Fig. 6.9**. The NS-hexaniobate-$BiVO_4$ thin film shows the uniform distribution of constituent elements (Nb, Bi, V, O) in the nanometer scale

mapping region with a Bi/V ratio of ~1. It indicates the uniform growth of $BiVO_4$ on the surface of NS-hexaniobate thin film without any special phase separation. Very low Nb composition is seen in the EDS spectrum due to the larger thickness of the upper $BiVO_4$ layer.

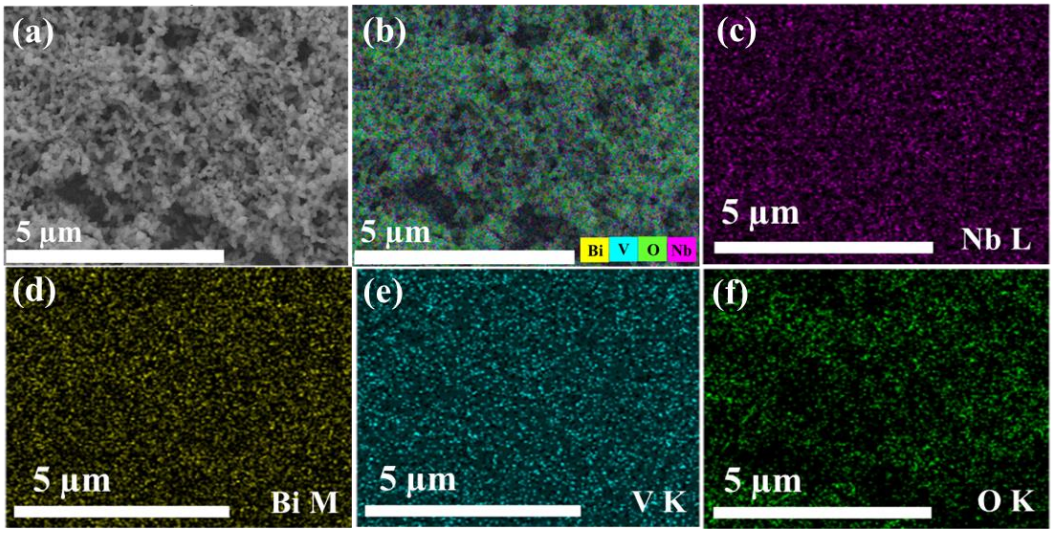

Fig. 6.8: (a) FESEM image and (b-f) EDS elemental maps of S-BN2 nanohybrid thin film.

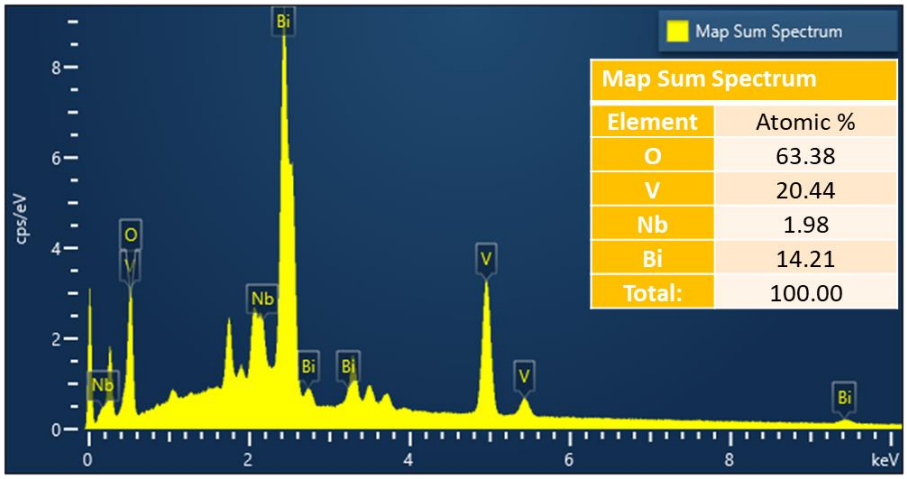

Fig. 6.9: EDS spectrum of S-BN2 nanohybrid thin film.

6.4.7 UV-vis DRS analysis:

The optical behavior of NS-hexaniobate-$BiVO_4$ nanohybrid thin film as compared to pristine NS-hexaniobate and $BiVO_4$ thin films was investigated with UV-vis absorbance and UV-vis DRS spectra represented in **Fig. 6.10**. As described in **Chapter 5, Section 5.4.7**; the pristine NS-hexaniobate thin film displays prominent absorption in the UV region of the solar spectrum with band gap energy of 3.2 eV. As represented in **Chapter 4, Section 4.4.7**, the pristine $BiVO_4$ thin film (band gap energy = 2.45 eV) is highly active in the visible spectrum. The transition of electrons from

hybrid Bi 6s-O 2p orbital to V 3d orbital of $BiVO_4$ is responsible for this visible region absorption [25]. Interestingly, the absorption profile of NS-hexaniobate-$BiVO_4$ displays significant absorption in the visible region upon hybridization. The NS-hexaniobate-$BiVO_4$ nanohybrid thin film shows significant absorption in the visible region with a band gap energy of 2.23 eV, clearly highlighting its visible light harvesting ability. The present results underscore the effective electronic coupling between NS-hexaniobate and $BiVO_4$. In addition, the charge transport characteristics of pristine $BiVO_4$ are modified due to the lower recombination rate of electron-hole pairs in a hybrid system. The present NS-hexaniobate-$BiVO_4$ nanohybrid thin films with strong visible light absorption ability are highly active for visible-light-driven photocatalytic applications [22-24].

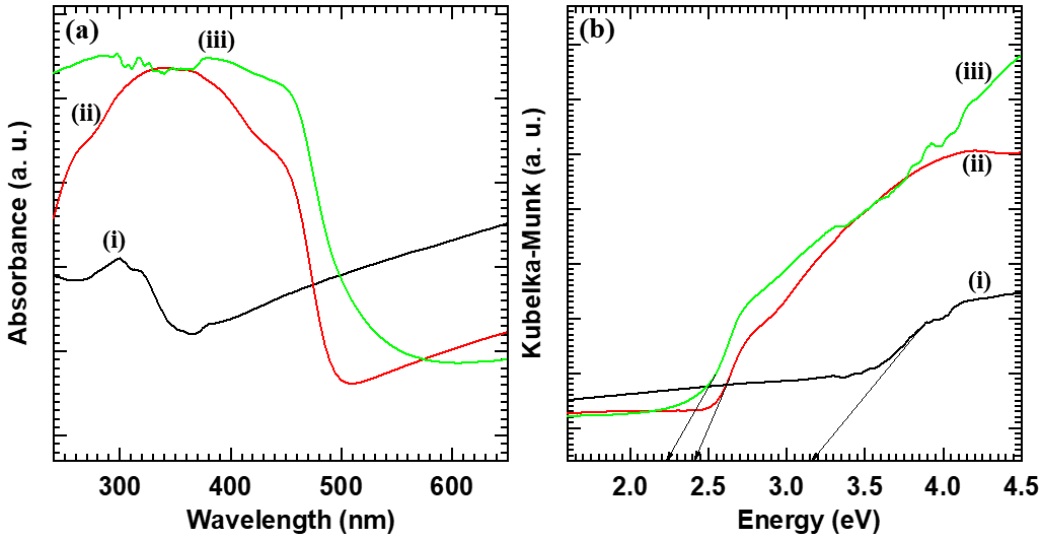

Fig. 6.10: (a) UV-vis absorbance spectra and (b) UV-vis DRS of (i) NS-hexaniobate, (ii) $BiVO_4$, (iii) S-BN2 nanohybrid thin films.

6.5 Dye degradation Performance of NS-hexaniobate-$BiVO_4$ nanohybrids:

The photocatalytic dye degradation activity of NS-hexaniobate-$BiVO_4$ nanohybrid thin films deposited by the SILAR method was studied with protocol explained in **Chapter 3, Section 3.5**.

6.5.1 Percentage degradation study for MB and Rh-B:

The photocatalytic activity of the NS-hexaniobate-$BiVO_4$ nanohybrid thin films is evaluated by monitoring the time-dependent photocatalytic degradation of MB and Rh-B as target dyes in the presence of visible light irradiations. To study the effect of hybridization on photocatalytic activity, the photocatalytic dye degradation performance

of pristine NS-hexaniobate (explained in **Chapter 5, Section 5.5.1**) and $BiVO_4$ thin films (explained in **Chapter 4, Section 4.5.1**) is compared with photodegradation performance of NS-hexaniobate-$BiVO_4$ nanohybrid thin films. The UV-vis absorption spectra of NS-hexaniobate-$BiVO_4$ nanohybrid thin films for MB and Rh-B degradation are shown in **Fig. 6.11** and **6.12**. The NS-hexaniobate-$BiVO_4$ thin films display decrease in absorption at characteristic wavelengths of 664 and 553 nm with respect to irradiation time, indicating superior degradation of MB and RhB, respectively. The photocatalytic degradation efficiency of NS-hexaniobate-$BiVO_4$ nanohybrid thin films is calculated and plotted in **Fig. 6.13** [26]. The photocatalytic activity of pristine $BiVO_4$ is significantly enhanced upon hybridization with NS-hexaniobate. All the NS-hexaniobate-$BiVO_4$ nanohybrid thin films exhibit improved photocatalytic performance compared to pristine $BiVO_4$. The best optimized S-BN2 nanohybrid thin film photocatalyst exhibited exceptional photocatalytic activity for degradation of both dyes (MB and Rh-B) with photodegradation rates of 85.5 and 88.8%, respectively, which are far superior to that of pristine $BiVO_4$ (61.2 and 70.3%). Although the pristine $BiVO_4$ is one of the highly active photocatalysts for visible-light-induced photocatalytic degradation, the present NS-hexaniobate-$BiVO_4$ nanohybrid thin films with improved photoactivity can be considered as highly effective photocatalysts for photodegradation of MB and Rh-B dyes.

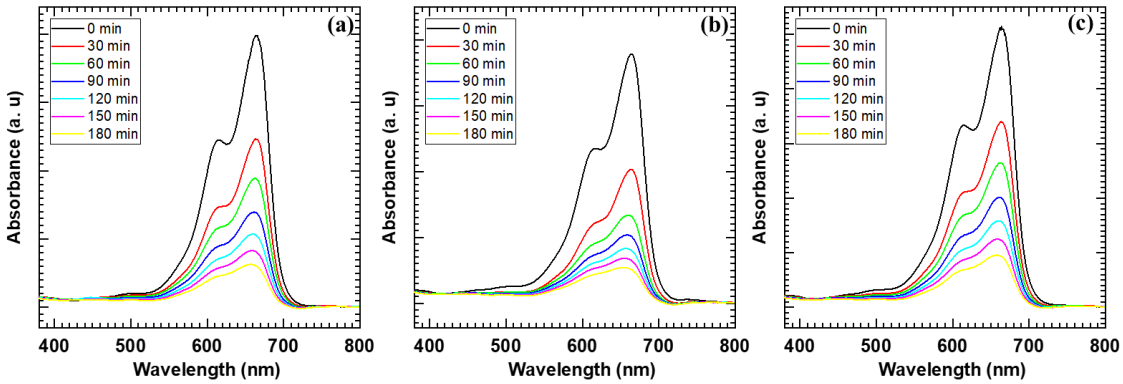

Fig. 6.11: UV-vis absorption spectra of the MB solution in the presence of (a) S-BN1, (b) S-BN2 and (c) S-BN3 nanohybrid thin film photocatalysts.

The excellent photocatalytic activity of present nanohybrid thin films can be ascribed to the effective electronic coupling between NS-hexaniobate and $BiVO_4$, promoting easy charge separation and transport of charges to catalytic sites to carry effective photocatalytic reactions. The highly porous 3D network-type structure can promote the expanded surface area with effective electronic coupling between

hybridized species, resulting in superior photocatalytic activity by giving rise to plenty of reaction sites and effective charge separation and transport. Conclusionally, the excellent photocatalytic activity of present nanohybrid thin films can be attributed to strong visible light harvesting nature, better photostability, and high surface area porous 3D network-type morphology beneficial for effective photocatalytic MB and Rh-B degradation reactions.

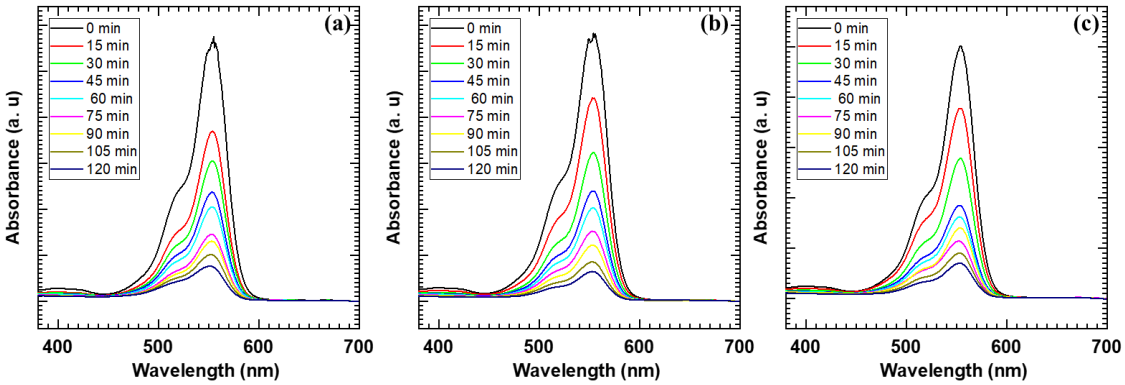

Fig. 6.12: UV-vis absorption spectra of the Rh-B solution in the presence of (a) S-BN1, (b) S-BN2 and (c) S-BN3 nanohybrid thin film photocatalysts.

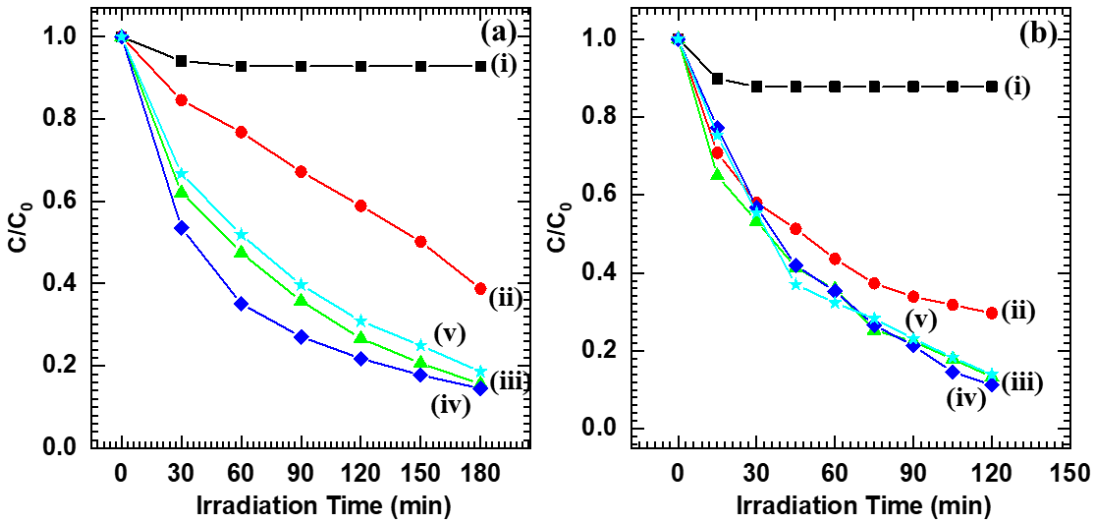

Fig. 6.13: (a) MB and (b) Rh-B degradation performance of (i) NS-hexaniobate, (ii) $BiVO_4$, (iii) S-BN1, (iv) S-BN2, (v) S-BN3 nanohybrid thin film photocatalysts.

6.5.2 Rate kinetics study for MB and Rh-B:

The photodegradation activity of MB and Rh-B dyes was further evaluated by their kinetics study using a pseudo-first-order rate kinetic model [27]. The pseudo-first-order reaction kinetics of MB and Rh-B dyes are displayed in **Fig. 6.14**. The values of k and R^2 for all tested photocatalysts for photodegradation of MB and Rh-B dyes are

summarized in **Table 6.1**. Compared with other photocatalysts, S-BN2 nanohybrid thin film exhibits a higher k value, confirming the improved photocatalytic performance. The highest k values obtained for the S-BN2 nanohybrid thin film are 0.0107 and 0.0182 min^{-1} for MB and Rh-B, respectively. The higher k-value obtained for S-BN2 nanohybrid thin film photocatalyst is attributed to the strong visible light harvesting nature, better photostability, and high surface area porous 3D network-type structure, which can enable exceptional electron-hole pair separation and transport of charges to catalytic sites beneficial for effective photocatalytic reactions.

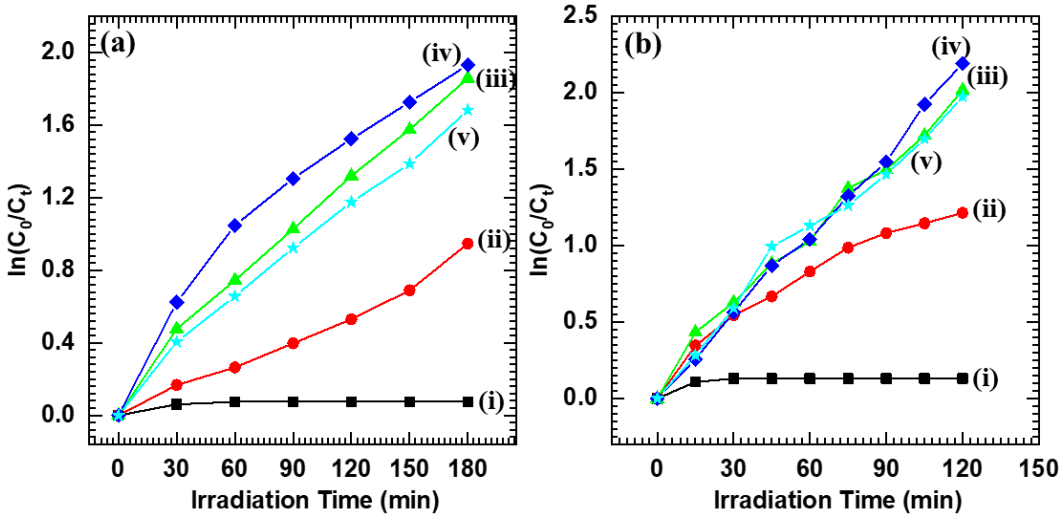

Fig. 6.14: Pseudo-first-order kinetics of (a) MB and (b) Rh-B for (i) NS-hexaniobate, (ii) $BiVO_4$, (iii) S-BN1, (iv) S-BN2, (v) S-BN3 nanohybrid thin film photocatalysts.

Table 6.1: k and R^2 values of all tested photocatalysts.

Sample	MB		Rh-B	
	k (min^{-1})	R^2	k (min^{-1})	R^2
NS-hexaniobate	0.0004	0.9996	0.0011	0.9989
$BiVO_4$	0.0052	0.9948	0.0101	0.9899
S-BN1	0.0103	0.9897	0.0168	0.9832
S-BN2	0.0107	0.9893	0.0182	0.9818
S-BN3	0.0093	0.9907	0.0164	0.9836

6.5.3 Recyclability study for MB and Rh-B:

In addition, the recyclability of the S-BN2 nanohybrid thin film for photocatalytic degradation of MB and Rh-B dyes is examined for the course of five consecutive degradation tests, as shown in **Fig. 6.15**. During each experiment, the S-

BN2 nanohybrid thin film is separated from the dye (MB/Rh-B) solution, cleaned with DDW, dried at ambient temperature, and used again for the subsequent cycles. The optimized S-BN2 nanohybrid thin film displayed superior recycling ability for photodegradation of both MB and Rh-B dyes, having degradation efficiency of 67.2 and 69.3% in visible light irradiation, respectively. The present S-BN2 nanohybrid thin film maintains its photocatalytic performance with only a slight drop for five repetitive degradation cycles, demonstrating its superior photostability. The mild decrement in degradation performance upon five consecutive degradation cycles is ascribed to the detachment of upper layer loosely bound $BiVO_4$ nanoparticles from the surface of the hybrid film or adsorption of dye molecules on the surface of S-BN2 nanohybrid thin film, which may lead to decrease in catalytic sites.

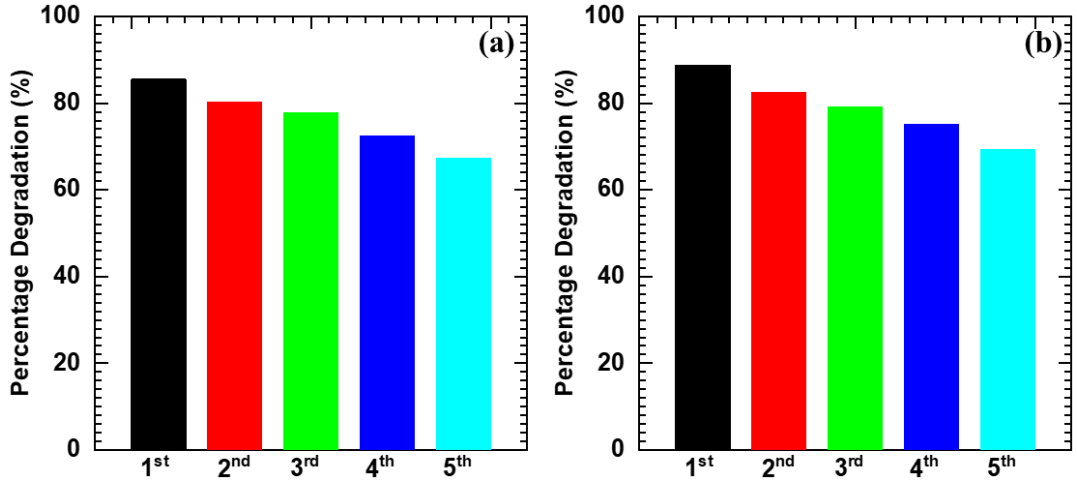

Fig. 6.15: Recyclability of S-BN2 nanohybrid thin film for (a) MB and (b) Rh-B dyes.

6.6 Photocatalytic Dye Degradation Mechanism:

The electron transfer between NS-hexaniobate and $BiVO_4$ in NS-hexaniobate-$BiVO_4$ nanohybrid thin films is investigated by electronic band structure [22, 28-29]. As shown in **Fig. 6.16**, the photocatalytic dye degradation mechanism is based on the photoinduced charge separation and transport to the semiconductor surface upon the light incidence [30]. When photons having energy equal to or greater than the band gap of $BiVO_4$ are incident on the NS-hexaniobate-$BiVO_4$ nanohybrid thin films, then electrons from the VB of $BiVO_4$ are excited to its CB, resulting in the formation of electron-hole pairs. It is seen that the NS-hexaniobate exhibits a higher position for CB and VB as compared to CB and VB of $BiVO_4$. The photogenerated electrons from the CB of $BiVO_4$ can migrate into the VB of NS-hexaniobate, leading to spatial separation

of electron-hole pairs with reduced electron-hole recombination. When water molecules interact with the holes present at the VB of $BiVO_4$, OH* radicals are produced. Generated OH* radicals are strong oxidizing agents that can degrade the adsorbed target MB and Rh-B dye molecules. On the contrary, when photogenerated electrons are reacted with O_2 molecules, $*O_2^-$ radicals are produced. Afterwards, the protonation of $*O_2^-$ radicals produces HOO* radicals. Ultimately, the H_2O_2 generated from HOO* radicals split into OH* radicals, which can degrade MB and Rh-B dye molecules [31].

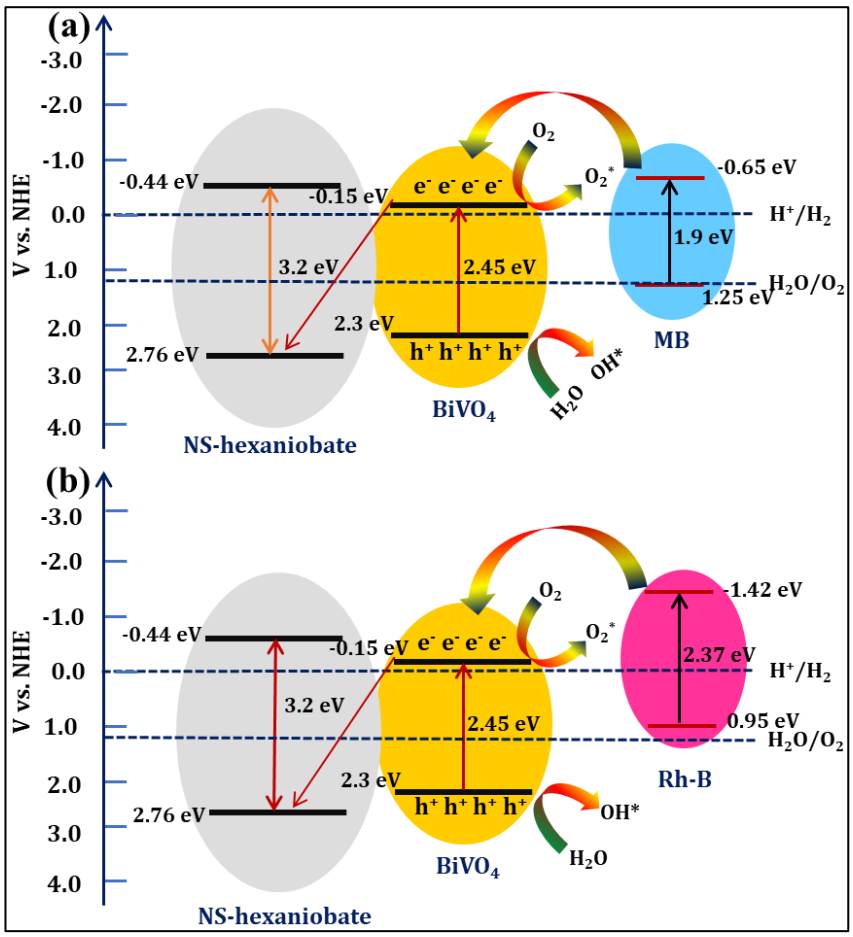

Fig. 6.16: Pictorial representation of photocatalytic degradation mechanism of (a) MB and (b) Rh-B dyes over NS-hexaniobate-$BiVO_4$ nanohybrid thin films.

6.7 Conclusions:

In the present chapter, the highly photoactive 2D NS-hexaniobate-$BiVO_4$ nanohybrid thin films are prepared by a combination of EPD and SILAR methods for photocatalytic dye degradation. The XRD analysis confirms the uniform and well-crystalline growth of $BiVO_4$ over EPD-deposited NS-hexaniobate thin films. The FESEM results show the formation of a highly porous 3D network-type structure

composed of $BiVO_4$ nanoparticles deposited on the surface of hexaniobate nanoscrolls, which is beneficial for effective charge transport. Optical analysis confirms the strong visible light absorption ability of the present NS-hexaniobate-$BiVO_4$ nanohybrid thin films effective for photocatalytic applications. The best optimized NS-hexaniobate-$BiVO_4$ nanohybrid thin film photocatalyst exhibited excellent photocatalytic activity for photodegradation of MB and Rh-B dyes with degradation efficiency of 85.5 and 88.8%, respectively, which is far superior to that of pristine $BiVO_4$. The excellent photocatalytic activity of present nanohybrid thin films can be ascribed to the effective electronic coupling between NS-hexaniobate and $BiVO_4$, strong visible light harvesting nature, better photostability, and highly porous 3D network-type morphology beneficial for improved photoactivity. Present results highlight the expediency of hybridization for further enhancing the photocatalytic activity of pristine materials.

6.8 References:

1. K.K. Dey, S. Gahlawat, P.P. Ingole, $BiVO_4$ optimized to nano-worm morphology for enhanced activity towards photoelectrochemical water splitting, J. Mater. Chem. A 7 (2019) 21207-21221.
2. R. Ma, Y. Kobayashi, W.J. Yngblood, T.E. Mallouk, Potassium niobate nanoscrolls incorporating rhodium hydroxide nanoparticles for photocatalytic hydrogen evolution, J. Mater. Chem. 18 (2008) 5982-5985.
3. H. Hayashi, Y. Hakuta, Y. Kurata, Hydrothermal synthesis of potassium niobate photocatalysts under subcritical and supercritical water conditions, J. Mater. Chem. 14 (2004) 2046-2051.
4. K. Maeda, M. Eguchi, W.J. Youngblood, T.E. Mallouk, Niobium oxide nanoscrolls as building blocks for dye-sensitized hydrogen production from water under visible light irradiation, Chem. Mater. 20 (2008) 6770-6778.
5. R. Abe, K. Shinohara, A. Tanaka, M. Hara, J.N. Kondo, K. Domen, Preparation of porous niobium oxides by soft-chemical process and their photocatalytic activity, Chem. Mater. 9 (1997) 2179-2184.
6. M. Mousavi-Kamazani, Facile hydrothermal synthesis of egg-like $BiVO_4$ nanostructures for photocatalytic desulfurization of thiophene under visible light irradiation, J. Mater. Sci. Mater. Electron. 30 (2019) 17735-17740.
7. G.P. Nagabhushana, G. Nagaraju, G.T. Chandrappa, Synthesis of bismuth vanadate: Its application in H_2 evolution and sunlight-driven photodegradation, J. Mater. Chem. A 1 (2013) 388-394.
8. P. Longchin, P. Pookmanee, S. Satienperakul, S. Sangsrichan, R. Puntharod, V. Kruefu, W. Kangwansupamonkon, S. Phanichphant, Characterization of bismuth vanadate ($BiVO_4$) nanoparticle prepared by solvothermal method, Integr. Ferroelectr. 175 (2016) 18-24.
9. S.V. Sadavar, N.S. Padalkar, R.B. Shinde, A.S. Patil, U.M. Patil, V.V. Magdum, Y.M. Chitare, S.P. Kulkarni, S.B. Kale, R.N. Bulakhe, D.S. Bhange, S.T. Kochuveedu, J.L. Gunjakar, Lattice engineering exfoliation-restacking route for 2D layered double hydroxide hybridized with 0D polyoxotungstate anions: Cathode for hybrid asymmetric supercapacitors, Energy Storage Mater. 48 (2022) 101-113.

10. Q.Q. Wang, B.Z. Lin, B.H. Xu, X.L. Li, Z.J. Chen, X.T. Pian, Preparation and photocatalytic properties of mesoporous SnO_2-hexaniobate layered nanocomposite, Microporous Mesoporous Mater. 130 (2010) 344-351.
11. B.N. Nunes, C. Haisch, A.V. Emeline, D.W. Bahnemann, A.O.T. Patrocinio, Photocatalytic properties of layer-by-layer thin films of hexaniobate nanoscrolls, Catal. Today 326 (2019) 60-67.
12. B.-H. Xu, B.-Z. Lin, Q.-Q. Wang, X.-T. Pian, O. Zhang, L.-M. Fu, Anatase TiO_2-pillared hexaniobate mesoporous nanocomposite with enhanced photocatalytic activity, Microporous Mesoporous Mater. 147 (2012) 79-85.
13. S. Elumalai, S. Vadivel, M. Yoshimura, Interlayer-modified two-dimensional layered hexaniobate $K_4Nb_6O_{17}$ as an anode material for lithium-ion batteries, Mater. Adv. 2 (2021) 1957-1961.
14. S. Nikam, S. Joshi, Irreversible phase transition in $BiVO_4$ nanostructures synthesized by a polyol method and enhancement in photodegradation of methylene blue, RSC Adv. 6 (2016) 107463-107474.
15. C. Hu, J. Xu, Y. Zhu, A. Chen, Z. Bian, H. Wang, Morphological effect of $BiVO_4$ catalysts on degradation of aqueous paracetamol under visible light irradiation, Environ. Sci. Pollut. Res. 23 (2016) 18421-18428.
16. M.R.S. Pelissari, N.F.A. Neto, L.P. Camargo, L.H.D. Antonia, Characterization and photoinduced electrocatalytic evaluation for $BiVO_4$ films obtained by the SILAR process, Electrocatalysis 12 (2021) 211-224.
17. B.N. Nunes, D.W. Bahnemann, A.O.T. Patrocinio, Photoinduced H_2 evolution by hexaniobate sheets grafted with metal ions: The fate of photogenerated carriers, ACS Appl. Energy Mater. 4 (2021) 3681-3692.
18. T.M.F. Marques, M.E. Strayer, A. Ghosh, A. Silva, O.P. Ferreira, K. Fujisawa, J.R.A. Cunha, G.J.P. Abreu, M. Terrones, T.E. Mallouk, B.C. Viana, Homogeneously dispersed CeO_2 nanoparticles on exfoliated hexaniobate nanosheets, J. Phys. Chem. Solids 111 (2017) 335-342.
19. R.B. Shinde, N.S. Padalkar, S.V. Sadavar, S.B. Kale, V.V. Magdum, Y.M. Chitare, S.P. Kulkarni, U.M. Patil, V.G. Parale, H.-H. Park, J.L. Gunjakar, 2D-2D lattice engineering route for intimately coupled nanohybrids of layered double hydroxide and potassium hexaniobate: Chemiresistive SO_2 sensor, J. Hazard. Mater. 432 (2022) 128734.
20. H. He, S.P. Berglund, A.J.E. Rettie, W.D. Chemelewski, P. Xiao, Y. Zhang, C.B. Mullins, Synthesis of $BiVO_4$ nanoflake array films for photoelectrochemical water oxidation, J. Mater. Chem. A 2 (2014) 9371-9379.
21. Z. Jiang, Y. Liu, T. Jing, B. Huang, X. Zhang, X. Qin, Y. Dai, M.-H. Whangbo, Enhancing the photocatalytic activity of $BiVO_4$ for oxygen evolution by Ce doping: Ce^{3+} ions as hole traps, J. Phys. Chem. C 120 (2016) 2058-2063.
22. J.L. Gunjakar, T.W. Kim, H.N. Kim, I.Y. Kim, S.-J. Hwang, Mesoporous layer-by-layer ordered nanohybrids of layered double hydroxide and layered metal oxide: Highly active visible light photocatalysts with improved chemical stability, J. Am. Chem. Soc. 133 (2011) 14998-15007.
23. J.L. Gunjakar, I.Y. Kim, J.M. Lee, N.-S. Lee, S.-J. Hwang, Self-assembly of layered double hydroxide 2D nanoplates with graphene nanosheets: An effective way to improve the photocatalytic activity of 2D nanostructured materials for visible light-induced O_2 generation, Energy Environ. Sci. 6 (2013) 1008-1017.

24. J.L. Gunjakar, T.W. Kim, I.Y. Kim, J.M. Lee, S.-J. Hwang, Highly efficient visible-light-induced O_2 generation by self-assembled nanohybrids of inorganic nanosheets and polyoxometalate nanoclusters, Sci. Rep. 3 (2013) 2080.
25. Z. Wang, X. Huang, X. Wang, Recent progresses in the design of $BiVO_4$-based photocatalysts for efficient solar water splitting, Catal. Today 335 (2019) 31-38.
26. K. Pingmuang, J. Chen, W. Kangwansupamonkon, G.G. Wallace, S. Phanichphant, A. Nattestad, Composite photocatalysts containing $BiVO_4$ for degradation of cationic dyes, Sci. Rep. 7 (2017) 8929.
27. K. Pingmuang, A. Nattestad, W. Kangwansupamonkon, G.G. Wallace, S. Phanichphant, J. Chen, Phase-controlled microwave synthesis of pure monoclinic $BiVO_4$ nanoparticles for photocatalytic dye degradation, Appl. Mater. Today 1 (2015) 67-73.
28. K. Saruwatari, H. Sato, T. Idei, J. Kameda, A. Yamagishi, A. Takagaki, K. Domen, Photoconductive properties of organic-inorganic hybrid films of layered perovskite-type niobate, J. Phys. Chem. B 109 (2005) 12410-12416.
29. N. Sakai, Y. Ebina, K. Takada, T. Sasaki, Electronic band structure of titania semiconductor nanosheets revealed by electrochemical and photoelectrochemical studies, J. Am. Chem. Soc. 126 (2004) 5851-5858.
30. M. Hasanpour, M. Hatami, Photocatalytic performance of aerogels for organic dyes removal from wastewaters: Review study, J. Mol. Liq. 309 (2020) 113094.
31. M.I. Din, R. Khalid, J. Najeeb, Z. Hussain, Fundamentals and photocatalysis of methylene blue dye using various nanocatalytic assemblies- A critical review, J. Clean. Prod. 298 (2021) 126567.

CHAPTER-7

Summary and Conclusions

Summary and conclusions:

In the current world, the problem of drinking water contamination has become more challenging. Much effort has been put into photocatalysis as a promising technology for removing extremely hazardous inorganic and organic compounds from polluted water. One of the most potential techniques for providing a clean aquatic environment for humans in modern society is the photocatalytic degradation of organic contaminants using highly efficient nanostructured semiconductor photocatalysts. The development of efficient oxidation processes, like photocatalysis, has been explored to address the hard-to-treat contaminants that may effectively degrade the recalcitrant compounds.

Researchers have developed a variety of inorganic compounds for visible-light-driven photocatalysis applications. Still, most of the inorganic photocatalyst systems ever developed are unsuitable for visible-light-photocatalysis owing to their wide band gap energy, lower photostability and inadequate band structure for reducing protons and oxidation of water. Among many nanocrystalline oxides, nanostructured TiO_2 and Nb_2O_5 have been considered as stable materials for photocatalysis. Bulk TiO_2 and Nb_2O_5-based composite materials are investigated for photocatalytic applications. However, their optimum performance is restricted by the difficulty in controlling crystallite size, the high recombination rate of excited electron-hole pairs and insufficient electronic coupling due to the large crystallites. A strategy to overcome this involves coupling wide band gap semiconductor photocatalysts with other narrow band gap materials, which can collect the holes/electrons or channelize them.

The 2D NS-titanate and NS-hexaniobate produced by the soft-chemical exfoliation protocol from their bulk layered crystals are unique due to their highly anisotropic 2D morphology, negative surface charge, suitable band structure for the oxidation of H_2O and reduction of hydroxide ions with high chemical stability. These NSs can be useful candidates for synthesizing nanohybrids since all the constituent ions in the sub-nanometer-thick 2D NSs come in contact with the surface, and their electronic structure can be dramatically altered through interaction with hybridized guest species. The coupling of 2D NS-titanate and NS-hexaniobate with narrow band gap materials will lead to the development of hybrid photocatalysts with strong visible light absorption ability, which makes them potential candidates for visible-light-driven photocatalysis applications.

Therefore, there is a strong need to design and develop novel types of layered NS-titanate and NS-hexaniobate-based hybrids, which can result in the development of mesoporous house-of-cards-type stacking structure and a controlled alteration in the electronic structure, which makes it possible to optimize the physicochemical characteristics and applicability of NSs based hybrid in solar assisted photocatalysis with high stability and efficiency. Specifically, NS-titanate and NS-hexaniobate are selected due to their highly anisotropic 2D morphology, suitable band structure for water-splitting reactions, and high chemical stability. $BiVO_4$ is chosen due to its narrow band gap energy, high photostability, low photo corrosion, and low environmental toxicity. Until now, no previous work has been on NS-titanate and NS-hexaniobate hybridized with $BiVO_4$ for photocatalytic applications.

Thus, the present work aims to develop highly porous NS-titanate-$BiVO_4$ and NS-hexaniobate-$BiVO_4$ nanohybrid thin films for photocatalytic dye degradation application. Four types of nanohybrid thin films are synthesized to accomplish this goal. In the first two nanohybrids, $BiVO_4$ hybridized with NS-titanate was synthesized by chemical methods like CBD and SILAR and employed as photocatalysts in photocatalytic dye degradation applications. Similarly, $BiVO_4$ hybridized with NS-hexaniobate was synthesized by CBD and SILAR methods and used in photocatalytic dye degradation. Further, the dye degradation performances of pristine $BiVO_4$ are compared with those of its nanohybrid thin films.

CHAPTER 1 deals with the essential preface to photocatalytic dye degradation and the significance of NS-titanate, NS-hexaniobate, $BiVO_4$ and their nanohybrid thin films for dye degradation application. The literature survey has included summarizing the preparation and photocatalytic dye degradation performance of pristine $BiVO_4$ and TiO_2/Nb_2O_5-based nanohybrids. The purpose of a thesis is covered at the end of chapter 1.

CHAPTER 2 explains the theoretical background of synthetic strategies, characterization techniques and photocatalytic dye degradation mechanisms. The theoretical background of the synthesis of the pristine $BiVO_4$ and its nanohybrid thin films by CBD and SILAR methods, as well as the synthesis of pristine NS-titanate and NS-hexaniobate thin films by EPD, are explained in this chapter. Chapter 2 also provides information about numerous characterization techniques, instruments and their theoretical background. Essential characterization techniques, including XRD, Micro-Raman, FT-IR spectroscopy, XPS, UV-vis spectroscopy, FESEM and EDS are covered

in the present chapter. Moreover, the last part describes the theoretical background of photocatalytic dye degradation. The photocatalytic dye degradation concepts, like percentage degradation, rate constant and pseudo-first-order reaction kinetics, have been explained in the present chapter.

CHAPTER 3 describes the synthesis, characterizations and photocatalytic dye degradation performance of NS-titanate-$BiVO_4$ (C-BT) nanohybrid thin films deposited by the CBD method. For the synthesis of C-BT nanohybrid thin films, initially, thin films of pristine NS-titanate were obtained from the colloidal suspension of NS-titanate by EPD method and over EPD deposited NS-titanate thin films $BiVO_4$ was coated by CBD method. Different characterization techniques such as XRD, Micro-Raman, FT-IR, XPS, UV-vis DRS and FESEM were employed to investigate the physicochemical properties of pristine materials and C-BT nanohybrid thin films.

The EPD-deposited NS-titanate thin film shows the formation of lepidocrocite-type NS-titanate with orthorhombic symmetry. The NS-titanate thin film shows aggregated NSs morphology, creating a porous structure of NS-titanate thin film. The NS-titanate thin film shows wide-bandgap energy with remarkable absorption in the UV region, which is beneficial for coupling with narrow-bandgap $BiVO_4$. On the other hand, the structural and chemical bonding analysis of $BiVO_4$ thin film deposited by CBD indicates the growth of monoclinic scheelite $BiVO_4$. The $BiVO_4$ thin film displays nanoparticle morphology and significant visible light absorption, which is advantageous for superior photocatalytic performance. The structural and morphological analysis of C-BT nanohybrid thin films confirms the well-crystalline uniform deposition of monoclinic scheelite $BiVO_4$ on NS-titanate. The C-BT nanohybrid thin films show randomly deposited nanoplates composed of NS-titanate uniformly covered with smooth $BiVO_4$ deposit, creating the house-of-cards type morphology. The C-BT nanohybrid thin films show a strong visible light absorption, indicating their visible light harvesting nature, which is useful for photocatalytic applications.

The photocatalytic dye degradation performance of C-BT nanohybrid thin films as compared to pristine NS-titanate and $BiVO_4$ thin films is described in this chapter. The photoactivity of C-BT nanohybrid thin films is evaluated with photocatalytic degradation of MB and Rh-B as target dyes for decomposition. The optimized C-BT2 nanohybrid photocatalyst demonstrated outstanding photoactivity for photodegradation of MB and Rh-B dyes with photodegradation rates of 85.1 and 97%, respectively, which

are higher than that of pristine $BiVO_4$ (54 and 70%). The present C-BT2 hybrid thin film photocatalyst demonstrated good recycling performance for MB and Rh-B degradation, with photodegradation rates of 67.5 and 78.8%, respectively. The exceptional photocatalytic activity of present nanohybrids can be attributed to the strong visible light harvesting ability, reduced electron-hole recombination, high photostability and mesoporous house-of-cards type structure. The photocatalytic degradation mechanism of MB and Rh-B dyes over C-BT nanohybrid thin films is proposed at the end of chapter 3.

CHAPTER 4 addresses the preparation, characterizations and photocatalytic dye degradation activity of NS-titanate-$BiVO_4$ (S-BT) nanohybrid thin films deposited by the SILAR method. For the synthesis of S-BT nanohybrid thin films, initially, thin films of pristine NS-titanate were obtained from the colloidal suspension of NS-titanate by EPD method and over EPD-deposited NS-titanate thin films, $BiVO_4$ was coated by SILAR method. Various physicochemical characterization techniques such as XRD, Micro-Raman, FT-IR, XPS, UV-vis DRS and FESEM were used to investigate the properties of S-BT nanohybrid thin films.

The structural and chemical bonding analysis of $BiVO_4$ thin film deposited by SILAR shows the highly crystalline growth of monoclinic scheelite $BiVO_4$ on ITO substrate. The $BiVO_4$ thin film displays highly porous interconnected nanoparticle morphology and narrow band gap energy with visible light absorption, which is beneficial for efficient photocatalytic reactions. The structural and chemical bonding analysis of S-BT nanohybrid thin films confirms the well-crystalline and uniform growth of monoclinic scheelite $BiVO_4$ on NS-titanate thin films. The morphological features show the mesoporous morphology composed of a 3D network of $BiVO_4$ nanoparticles deposited on the surface of randomly oriented titanate NSs. The optical study displays the effective visible light absorption ability of S-BT nanohybrid thin films, making them potential photocatalysts for solar-assisted photocatalysis applications.

The optimized S-BT2 nanohybrid thin film photocatalyst demonstrated outstanding photoactivity for photodegradation of MB and Rh-B dyes with photodegradation rates of 92.1 and 91.3%, respectively, remarkable than pristine $BiVO_4$ (61.2 and 70.3%). The optimized S-BT2 nanohybrid thin film photocatalyst exhibited good recycling ability for degradation of both MB and Rh-B dyes with photodegradation rates of 68.1 and 69.2% under 180 and 120 min of visible light illumination. The superior

photoactivity of nanohybrid thin films can be ascribed to the effective hybridization between NS-titanate and $BiVO_4$, strong visible light harvesting nature, notable electron-hole separation and mesoporous 3D network-type structure beneficial for effective photocatalytic reactions. The photocatalytic degradation mechanism of MB and Rh-B dyes over S-BT nanohybrid thin films is proposed at the end of chapter 4.

CHAPTER 5 describes the synthesis, characterizations and photocatalytic dye degradation performance of NS-hexaniobate-$BiVO_4$ (C-BN) nanohybrid thin films deposited by the CBD method. For the synthesis of C-BN nanohybrid thin films, initially, thin films of pristine NS-hexaniobate were obtained from the colloidal suspension of NS-hexaniobate by EPD method and over EPD deposited NS-hexaniobate thin films, $BiVO_4$ was coated by CBD method. Different characterization techniques such as XRD, Micro-Raman, FT-IR, XPS, UV-vis DRS and FESEM were employed to probe the physicochemical characteristics of C-BN nanohybrid thin films.

The EPD-deposited NS-hexaniobate thin film shows well-crystalline growth of lamellar NS-hexaniobate with orthorhombic structure. The NS-hexaniobate thin film shows nanoscroll morphology, forming a porous structure of the NS-hexaniobate thin film. Although the NS-hexaniobate thin film displays prominent absorption in the UV region due to its wide-bandgap energy, it is the best choice for coupling with narrow-bandgap $BiVO_4$. The structural analysis of C-BN nanohybrid thin films shows well-crystalline uniform deposition of monoclinic scheelite $BiVO_4$ on NS-hexaniobate thin films. The C-BN nanohybrid thin films show effective electronic coupling between NS-hexaniobate and $BiVO_4$ with easy charge transport, strong visible light harvesting ability, high photostability and a highly porous randomly aggregated NSs network creating the house-of-cards type morphology beneficial for visible-light-induced photocatalytic dye degradation.

The best optimized NS-hexaniobate-$BiVO_4$ nanohybrid thin film shows superior photocatalytic activity for visible-light-driven photodegradation of MB and Rh-B dyes with photodegradation rates of 87.3 and 92.8%, respectively, higher than that of pristine $BiVO_4$. The present C-BN2 nanohybrid thin film shows superior recycling performance for MB and Rh-B photodegradation with degradation rates of 66.8 and 71.5%, respectively. The improved photocatalytic degradation performance of hybrid photocatalysts is attributed to the effective electronic coupling with easy charge transport, high photostability, strong visible light harvesting ability, expanded surface

area and highly porous house-of-cards type structure beneficial for effective photocatalytic reactions. The photodegradation mechanism of MB and Rh-B dyes over C-BN nanohybrid thin films is proposed at the end of chapter 5.

CHAPTER 6 covers the preparation, characterizations and photocatalytic dye degradation activity of S-BN nanohybrid thin films deposited by the SILAR method. For the synthesis of S-BN nanohybrid thin films, initially, thin films of pristine NS-hexaniobate were obtained from the colloidal suspension of NS-hexaniobate by EPD method and over EPD deposited NS-hexaniobate thin films, $BiVO_4$ was coated by SILAR method. Various physicochemical characterization techniques such as XRD, Micro-Raman, FT-IR, XPS, UV-vis DRS and FESEM were employed to assess the properties of S-BN nanohybrid thin films.

The structural analysis of S-BN nanohybrid thin films confirms the uniform and well-crystalline growth of $BiVO_4$ over EPD-deposited NS-hexaniobate thin films. The morphological study shows the formation of a highly porous 3D network-type structure composed of $BiVO_4$ nanoparticles deposited on the surface of hexaniobate nanoscrolls, which is beneficial for effective charge transport. Optical analysis confirms the strong visible light absorption ability of the present S-BN nanohybrid thin films that are effective for photocatalytic applications.

The best optimized S-BN2 nanohybrid thin film photocatalyst exhibited excellent photocatalytic activity for photodegradation of MB and Rh-B dyes with degradation efficiency of 85.5 and 88.8%, respectively, which is far superior to that of pristine $BiVO_4$. The optimized S-BN2 nanohybrid thin film displayed superior recycling ability for photodegradation of both MB and Rh-B dyes, having degradation efficiency of 67.2 and 69.3%, respectively. The excellent photocatalytic activity of present nanohybrid thin films can be ascribed to the effective electronic coupling between NS-hexaniobate and $BiVO_4$, strong visible light harvesting nature, better photostability, and highly porous 3D network-type morphology beneficial for improved photoactivity. The photodegradation mechanism of MB and Rh-B dyes over S-BN nanohybrid thin films is proposed at the end of chapter 6.

All of the findings from the previous chapters are compiled in this ***CHAPTER 7***, after which conclusions are drawn. Finally, it is concluded that pristine $BiVO_4$ thin films deposited by both CBD and SILAR methods show good photocatalytic activity for the photodegradation of MB and Rh-B dyes. Also, EPD is the potential method for

depositing uniform NS-titanate and NS-hexaniobate thin films. It is concluded that simple chemical methods like CBD and SILAR are advantageous for synthesizing highly porous C-BT, S-BT, C-BN and S-BN nanohybrid thin films. These nanohybrid thin films are highly effective photocatalysts for visible-light-driven photocatalytic dye degradation. The comparative photocatalytic dye degradation performances of C-BT, S-BT, C-BN and S-BN nanohybrid thin films are summarised in **Table 7.1** and **Table 7.2**.

The photocatalytic dye degradation experimental findings in **Table 7.1** and **Table 7.2** indicate that the C-BT, S-BT, C-BN and S-BN nanohybrid thin films are effective for visible-light-driven photocatalysis. Interestingly, S-BT and C-BT nanohybrid thin-film photocatalysts demonstrated outstanding photoactivity for the photodegradation of MB and Rh-B dyes with 92.1 and 97% photodegradation rates, respectively. Also, both nanohybrid thin films maintain their photocatalytic performance with a slight decrement for five repetitive degradation cycles, signifying their high photostability. Consequently, it is concluded that NS-titanate-based nanohybrid thin films are better for visible-light-driven photocatalytic dye degradation than the other nanohybrid thin films.

Table 7.1: Comparative dye degradation performance of C-BT, S-BT, C-BN and S-BN nanohybrid thin-film photocatalysts for MB degradation.

Sr. No.	**Nanohybrid photocatalyst**	**MB**		
		degradation rate (%)	**K (min^{-1})**	**R^2**
1	C-BT	85.1	0.0105	0.9895
2	**S-BT**	**92.1**	**0.0141**	**0.9859**
3	C-BN	87.3	0.0115	0.9885
4	S-BN	85.5	0.0107	0.9893

Table 7.2: Comparative dye degradation performance of C-BT, S-BT, C-BN and S-BN nanohybrid thin film photocatalysts for Rh-B degradation.

Sr. No.	**Nanohybrid photocatalyst**	**Rh-B**		
		degradation rate (%)	**K (min^{-1})**	**R^2**
1	**C-BT**	**97**	**0.0167**	**0.9833**
2	S-BT	91.3	0.0203	0.9797
3	C-BN	92.8	0.0146	0.9854
4	S-BN	88.8	0.0182	0.9818

CHAPTER-8

80-Recommendations

CHAPTER-8

80-Recommendations

8.1 Recommendations:

Among the various photoactive materials, the narrow band gap (2.4 eV) $BiVO_4$ is a potential photocatalyst suitable for numerous photo-functional applications owing to its high efficiency, non-toxicity, low photo corrosion, high optical absorption coefficient (10^4-10^5 cm^{-1} at 350-520 nm), suitable band positions for water splitting reaction and promising flat band potential favorable to hydrogen evolution reaction. However, $BiVO_4$ suffers from high recombination rates of excitons and limited photostability. The hybridization strategy of coupling $BiVO_4$ with wide band gap photocatalyst materials is essential to overcome the above problems and enhance photocatalytic activity. Subsequently, four types of nanohybrid thin films were deposited (1. $BiVO_4$ hybridized with NS-titanate by CBD (C-BT nanohybrids), 2. $BiVO_4$ hybridized with NS-titanate by SILAR (S-BT nanohybrids), 3. $BiVO_4$ hybridized with NS-hexaniobate by CBD (C-BN nanohybrids) and 4. $BiVO_4$ hybridized with NS-hexaniobate by SILAR (S-BN nanohybrids)). Hybridization of $BiVO_4$ with NS-titanate and NS-hexaniobate leads to improved photocatalytic activity owing to the effective electronic coupling between the hybridized species, expanded surface area by the development of mesoporous house-of-cards type morphology and tunable chemical composition to achieve the desire photo-physicochemical properties.

Several recommendations are provided based on the research findings on synthesis, characterizations, and photocatalytic dye degradation activity of NS-titanate/NS-hexaniobate-$BiVO_4$ nanohybrid thin films. All the nanohybrid thin films display significant absorption of visible light and decreased electron-hole recombination, demonstrating the significant electronic coupling between hybridized species. Also, all the nanohybrid thin films show highly porous structures, tunable chemical compositions, and controlled modification of electronic structures that are beneficial for improved photocatalytic activity. In addition, the chemical stability and photocatalytic activity of $BiVO_4$ are significantly improved upon hybridization with highly stable NS-titanate and NS-hexaniobate. The resultant nanohybrid thin films (C-BT, S-BT, C-BN and S-BN) display improved photoactivity for visible-light-driven photocatalytic decomposition of MB and Rh-B dyes.

The comparative analysis of the visible-light-driven photodegradation performance of NS-titanate/NS-hexaniobate-$BiVO_4$ nanohybrid thin films indicates that S-BT and C-BT nanohybrid thin-film photocatalysts demonstrated outstanding

photoactivity for the photodegradation of MB and Rh-B dyes with photodegradation rates of 92.1 and 97%, respectively. Also, both nanohybrid thin films retain their photocatalytic activity with only a minor decrement for five repetitive degradation cycles, signifying their high photostability. From the above results, it is recommended that, among the tested NS-titanate/NS-hexaniobate-$BiVO_4$ nanohybrid thin films, the highly stable NS-titanate is the best choice for hybridization with visible light active $BiVO_4$.

8.2 Conclusions of the Research Work:

Here are some of the conclusions drawn from the present study:

1. Materials with narrow band gap energy are required to cover the maximum portion of the solar spectrum. Still, these semiconductor photocatalysts suffer from high recombination rates and limited photostability. To enhance the photocatalytic activity and overcome the above problems, a hybridization strategy of coupling narrow-band gap photocatalysts with wide-band gap materials is necessary. Specifically, NS-titanate and NS-hexaniobate are chosen due to their highly anisotropic 2D morphology, suitable band positions for reducing hydroxide ions and oxidizing H_2O molecules, and high stability. $BiVO_4$ is chosen due to its narrow band gap, high photostability, and low environmental toxicity.

2. The pristine $BiVO_4$ thin films are synthesized by using the facile CBD and SILAR methods. The photocatalytic performance of pristine $BiVO_4$ thin films is evaluated with photocatalytic degradation of both (MB and Rh-B) as target dyes in visible light illumination. $BiVO_4$ thin film deposited by CBD exhibited photodegradation performance of 54% and 70% for MB and Rh-B under 180 and 210 min of visible light exposure, respectively. On the other hand, $BiVO_4$ thin film deposited by SILAR demonstrated photocatalytic degradation performance of 61.2 and 70.3% for MB and Rh-B under 180 and 120 min of visible light illumination, respectively.

3. The C-BT nanohybrid thin films are synthesized by CBD of the $BiVO_4$ layer over EPD-deposited NS-titanate thin films. The C-BT nanohybrid thin films display significant absorption of visible light and decreased electron-hole recombination, demonstrating the effective electronic coupling between the hybridized species. Upon hybridization, the chemical stability of pristine $BiVO_4$ is significantly enhanced due to highly stable NS-titanate. The hybridization of NS-titanate with $BiVO_4$ leads to the

development of highly porous house-of-cards type morphology beneficial for improved photocatalytic activity. The resultant nanohybrid thin films are very effective for visible-light-driven photocatalytic degradation of both (MB and Rh-B) dyes with photodegradation rates of 85.1 and 97%, respectively, higher than that of pristine $BiVO_4$, which is one of the most prominent visible light active photocatalysts. These results underscore the superior photo-functionality of the C-BT nanohybrid thin films as effective visible-light-driven photocatalysts.

4. Highly porous S-BT nanohybrid thin films are synthesized via a combination of EPD and SILAR methods. The S-BT nanohybrid thin films demonstrate significant absorption of visible light, mesoporous 3D network type morphology, tunable chemical composition and controlled electronic structure modification beneficial for improved photocatalytic activity. The chemical stability and photocatalytic activity of pristine $BiVO_4$ are significantly improved upon hybridization with highly stable NS-titanate. The resultant nanohybrid thin films display improved photoactivity for photodegradation of both (MB and Rh-B) dyes with degradation rates of 92.1 and 91.3%, respectively, which are quite higher than that of pristine $BiVO_4$ demonstrating the effective hybridization between NS-titanate and $BiVO_4$. The present findings underscore the effectiveness of hybridizing 2D layered MONs with narrow band gap semiconductors in developing chemically stable photocatalysts for efficient visible-light-driven photocatalysis.

5. On a similar background, C-BN nanohybrid thin films are synthesized by the combination of EPD and CBD methods. The physicochemical characterizations of C-BN thin films confirm successful hybridization between NS-hexaniobate and $BiVO_4$ with the conservancy of NS-hexaniobate. Moreover, C-BN nanohybrid thin films display highly porous nanoclusters composed of randomly aggregated NSs networks, creating the house-of-cards type morphology. The optical study confirms the strong visible light harvesting nature of present nanohybrids, making them potential photocatalysts for the photodegradation of dyes. The optimized C-BN2 nanohybrid photocatalyst showed excellent photocatalytic activity for both (MB and Rh-B) dyes with photodegradation rates of 87.3 and 92.8%, respectively, which are greater than that of pristine $BiVO_4$ (54 and 70%). Also, the C-BN2 nanohybrid retains its photocatalytic activity with only a small decrement for five repetitive degradation

cycles, corresponding to the high photostability of a present nanohybrid thin film photocatalyst.

6. Highly porous nanohybrids of NS-hexaniobate and $BiVO_4$ are prepared by combining EPD and SILAR methods. The hybridization of layered NS-hexaniobate with $BiVO_4$ results in the development of highly porous S-BN nanohybrid thin films, which is beneficial for efficient visible-light-driven photocatalytic decomposition of MB and Rh-B dyes. The synthesized S-BN nanohybrid thin films show strong visible light harvesting ability, efficient electron-hole pair separation and mesoporous 3D network-type morphology advantageous for improved photocatalytic activity. The optimized S-BN2 nanohybrid thin film photocatalyst exhibited excellent photocatalytic activity for photodegradation of both dyes (MB and Rh-B) with degradation rates of 85.5 and 88.8%, respectively, which are far superior to that of pristine $BiVO_4$ (61.2 and 70.3%). Present results underscore the effective hybridization between NS-hexaniobate and $BiVO_4$.

It is concluded that the use of the EPD method is beneficial for synthesizing NS-titanate and NS-hexaniobate thin films. Also, the use of simple chemical methods like CBD and SILAR is useful for synthesizing 2D NSs-$BiVO_4$-based nanohybrid thin films (NS-titanate-$BiVO_4$ and NS-hexaniobate-$BiVO_4$) with highly porous structures, strong visible light harvesting ability and efficient electron-hole pair separation. Because of these characteristics, NS-titanate/NS-hexaniobate-$BiVO_4$-based nanohybrid thin films are highly active photocatalysts in photocatalytic dye degradation. According to the outcomes of physicochemical investigations, a conclusion is made that enlarged surface area, porous structure, strong visible light harvesting nature, and effective charge transfer between NS-titanate/NS-hexaniobate and $BiVO_4$ are beneficial for the improvement in photocatalytic dye degradation performance. The comparative study of the photocatalytic dye degradation performance of NS-titanate-$BiVO_4$ and NS-hexaniobate-$BiVO_4$ nanohybrids indicates that the S-BT2 and C-BT2 nanohybrid thin films demonstrate superior visible-light-driven photocatalytic dye degradation performance. From the above results, it is concluded that, among the tested NS-titanate/NS-hexaniobate-$BiVO_4$ nanohybrid thin films, the highly stable NS-titanate is the best choice for hybridization with visible light active $BiVO_4$.

8.3 Summary:

1. Pristine $BiVO_4$ thin films are synthesized by using CBD and SILAR methods.
2. Pristine NS-titanate and NS-hexaniobate thin films are synthesized by using the EPD method.
3. Pristine $BiVO_4$ thin films are highly active for visible-light-driven photodegradation of both MB and Rh-B dyes.
4. $BiVO_4$ thin film deposited by CBD exhibited visible-light-driven photodegradation performance of 54 and 70% for MB and Rh-B dyes, respectively.
5. $BiVO_4$ thin film deposited by SILAR exhibited visible-light-driven photodegradation performance of 61.2% and 70.3% for MB and Rh-B dyes, respectively.
6. Pristine NS-titanate and NS-hexaniobate thin films display negligible visible-light-induced photocatalytic performance towards MB (10 and 7.2%) and Rh-B (6 and 12.2%) degradation.
7. NS-titanate-$BiVO_4$ nanohybrid thin films are synthesized by using CBD and SILAR methods.
8. The optimized NS-titanate-$BiVO_4$ nanohybrid thin film synthesized by using CBD is very effective for visible-light-driven photodegradation of both (MB and Rh-B) dyes with degradation rates of 85.1 and 97%, respectively.
9. The optimized NS-titanate-$BiVO_4$ nanohybrid thin film synthesized by using SILAR displays improved photoactivity for photodegradation of both (MB and Rh-B) dyes with degradation rates of 92.1 and 91.3%, respectively.
10. NS-hexaniobate-$BiVO_4$ nanohybrid thin films are synthesized by using CBD and SILAR methods.
11. The optimized NS-hexaniobate-$BiVO_4$ nanohybrid thin film synthesized by using CBD showed excellent photodegradation of both (MB and Rh-B) dyes with photodegradation rates of 87.3 and 92.8%, respectively.
12. The optimized optimized NS-hexaniobate-$BiVO_4$ nanohybrid thin film synthesized by using SILAR exhibited excellent photocatalytic activity for photodegradation of both (MB and Rh-B) dyes with degradation rates of 85.5 and 88.8%, respectively.

8.4 Future Findings:

The present investigation significantly improved the photocatalytic dye degradation activity of $BiVO_4$ thin films by making NS-titanate-$BiVO_4$ and NS-

hexaniobate-$BiVO_4$ nanohybrid thin films and used as photocatalysts for photocatalytic dye degradation application. The expanded surface area porous morphology, versatile chemical composition and variable pore structure of nanohybrid thin films are beneficial for their improved photocatalytic performance as compared to their respective pristine materials. This research opens new horizons for exploring 2D layered MONs-based-nanohybrid thin film photocatalysts for various photo-functional applications. Moreover, the present nanohybridization strategy can be applicable to numerous other layered MONs, LDHs, and various other narrow band gap semiconductors to enhance the performance of nanohybrid materials further.

Although current research work confirmed cutting-edge breakthroughs for NS-titanate/NS-hexaniobate-$BiVO_4$-based nanohybrid thin film photocatalysts, few challenges endured to further increase their performance for various photo-functional applications. Consequently, the current research endeavours offer new findings to boost further the photocatalytic activity of 2D NSs-based nanohybrid thin films.

- The photocatalytic activity of nanohybrid thin film photocatalysts can be improved significantly via transition metal doping in NS-titanate, NS-hexaniobate or $BiVO_4$.
- To further enhance the performance of $BiVO_4$-based nanohybrid thin films, combinations of numerous other 2D MONs and various guest materials need to be explored.
- The direct deposition of exfoliated 2D MONs or LDH NSs and guest species by layer-by-layer method can be advantageous in synthesizing 2D NSs-based nanohybrid thin film photocatalysts on the substrate surface.
- The layer-by-layer deposition of two types of exfoliated 2D MONs or exfoliated NSs of LDH and 2D MONs will be challenging and can be useful for further performance improvement.
- The development of Z-scheme heterostructure photocatalysts based on $BiVO_4$ and other MONs need to be further explored.
- The development of nanohybrid photocatalysts via combinations of various host-guest materials by bandposition tuning will be challenging.
- The various carbon nanostructures, like carbon nanotubes and fullerene, can be hybridized with 2D MONs to tune further the electrical properties of 2D NSs-based nanohybrid thin films.
- The photocatalytic activity of nanohybrid photocatalysts can be further explored by use of various target molecules such as antibiotics and pesticide degradation.

- Further investigation is required into the details of the change of pore size and shape, the correlation between interlayer spacing and the interfacial characteristics of hybridized components and their impact on the 2D NSs-based nanohybrids performance.